Nanocomposites à base de g-C_3N_4 et $Zn_xCd_{1-x}S$ comme photocatalyseurs pour la production d'hydrogène à partir de l'eau sous la lumière solaire

Thèse

Mohammad Reza Gholipour

Doctorat en génie chimique

Philosophiae Doctor (Ph.D.)

Québec, Canada

Résumé

Le processus de photocatalyse est l'un des moyens prometteurs d'utiliser l'énergie solaire à grande échelle pour différents types d'applications tels que la production d'hydrogène comme énergie propre ou encore la purification de l'eau et l'air contre les polluants et les produits chimiques nocifs. Néanmoins, le pourcentage de l'énergie du rayonnement solaire utilisé est généralement inférieur à 1%, en raison de la faible absorption de la lumière solair, de la rapide recombinaison de charge « électron-trou paires » et de l'instabilité photochimique. La modification de la structure des semi-conducteurs et la création de photocatalyseurs nanocomposites peuvent aider à surmonter ces problèmes.

Le TiO_2 est le photocatalyseur le plus étudié en raison de ses propriétés physiques et chimiques imortantes dans le processus de photocatalyse. Bien que son faible coût encourage à l'utiliser à grande échelle, sa largeur de bande interdite (E_G =3.2 eV) importante, qui ne peut être activée que par irradiation UV, et sa vitesse de recombinaison des charges, ont limité son utilisation dans les applications industrielles. La création d'une hétérojonction entre TiO_2 et d'autres semiconducteurs actifs sous la lumière visible est l'un des moyens les plus prometteurs pour utiliser les propriétés du dioxyde de titane dans la région du visible. De plus, le nitrure de carbone graphitique (g-C_3N_4) a été largement étudié pour la production d'hydrogène sous irradiation lumineuse visible. Malgré le fait qu'il peut être actif dans la région du visible et réduire les protons pour générer de l'hydrogène, son efficacité est considérablement limitée en raison de son taux de recombinaison de charge élevé et de sa faible surface spécifique.

Nous avons synthétisé un photocatalyseur nanocomposite de g-C_3N_4 et TiO_2 afin d'améliorer la procédure de séparation des charges et donc de produire plus d'hydrogène. Des nanodisques de titanate uniformes (TND) avec un diamètre compris entre 12 et 35 nm ont été synthétisés à l'aide d'une méthode solvothermale. Les feuilles nanométriques de g-C_3N_4 ont été synthétisés par des techniques de sonication, puis ont été mélangées avec des TND. Après cela, une étape de calcination a non seulement généré des contacts intimes avec deux semi-conducteurs, mais aussi converti les TND en nanoparticules de TiO_2. En raison de la position des bandes de valence et de conduction des deux semi-conducteurs, les électrons photogénérés sont en mesure de passer du g-C_3N_4 au TiO_2. Grâce à l'ajout de Pt comme cocatalyseur ainsi que comme fournisseur de sites actifs, les électrons photoexcités sont en capacité de réduire les protons de l'eau et de générer du

dihydrogène. Cette hétérojonction pourrait produire plus du double l'hydrogène que le gC_3N_4 pur dans les mêmes conditions.

Nous avons créé une nouvelle forme de feuille nanométrique de g-C_3N_4 contenant des lacunes de carbone avec des trous dans tous les plans de feuille. Après la synthèse du matériau de vrac g-C_3N_4 à partir du dicyandiamide, le matériau obtenu a été chauffé à 650 ° C sous argon pendant 2 h. Après avoir refroidi, il a été calciné à nouveau à 500 ºC pendant 2 heures sous air. Ainsi, sa surface spécifique a été considérablement augmenté de 28 $m^2.g^{-1}$ de g-C_3N_4 à 160 $m^2.g^{-1}$. En outre, ces traitements par étapes ont introduit certains défauts tels que des lacunes de carbone à l'intérieur de la structure des feuilles nanométriques de g-C_3N_4. Ces derniers ont fourni des sites photocatalytiques hautement actifs pour l'évolution de l'hydrogène. Par conséquent, sa production d'hydrogène est dix fois supérieure à celle du g-C_3N_4 brut sous irradiation de la lumière visible. Il a montré une efficacité quantique très élevée de 29,2% et 21,3% à 400 nm et 420 nm, respectivement.

Enfin, nous avons généré une solution solide de zinc-cadmium ($Zn_xCd_{1-x}S$) par synthèse solvothermale en utilisant des précurseurs de glycérates métalliques de Cd et Zn. Ensuite, le matériau a été calciné (500 ºC pendant 4 heures) et traité avec H_2S à 450 ºC pendant 2 heures. Ainsi, une solution solide homogène de $Zn_xCd_{1-x}S$ avec structure cristallographique de wurtzite hexagonale a été formée. Il convient de mentionner que le semi-conducteur obtenu peut absorber une large partie du spectre visible, de plus, sa largeur de bande interdite est fortement affecté par le rapport Zn / Cd et varie entre 2,35 et 3,4 eV ($0 \leq x \leq 1$). Les meilleurs résultats pour l'évolution de l'hydrogène ont été obtenus à partir de l'échantillon $Zn_{30}Cd_{70}S$ avec dépôt de MoS_2 comme cocatalyseur. Il peut générer de l'hydrogène dans des longueurs d'onde les plus longues de la région de la lumière visible et ses rendements quantiques sont : 46,6% à 400 nm à 23,4% à 500 nm ainsi que 11,3% à 550 nm.

Abstract

Photocatalysis process is one of the promising ways to use solar energy in large scale for various kind of application including producing hydrogen as clean energy and purify water and air from harmful pollutants and chemicals. Nevertheless, the solar conversion efficiency of photocatalysts are usually below 1% because of weak sunlight absorption, high charge recombination and high photochemical instability. Modifying semiconductor structure and creating nanocomposite photocatalyst can help to overcome these issues.

TiO_2 is the most well-known photocatalysts because of its physical and chemical properties in photocatalysis process. Although its low cost encourages people to utilize it in large scale, its large band gap, which can only be activated under UV irradiation, and high rate of charge recombination, limited its usage in industrial applications. Creating an heterojunction between TiO_2 and others visible light active semiconductor, is one of the best way to take advantage of TiO_2 in visible region. Furthermore, graphitic carbon nitride (g-C_3N_4) has been widely investigated for its potential in hydrogen production under visible light irradiation. Despite the fact that it can activated in visible light region and reduce protons to generate hydrogen, its efficiency is considerably limited because of its high rate of charge recombination and low specific surface area.

We synthesized a nanocomposite photocatalyst of g-C_3N_4 and TiO_2 in order to increase charge separation procedure and so it can produce more hydrogen. Uniform titanate nanodisks (TNDs) with diameter between 12 and 35 nm were synthesized with a solvothermal method. Nanosheets of g-C_3N_4 were synthesized via sonication techniques and then were mixed with TNDs. After that, a calcination step not only made intimate contacts with two semiconductors, but also converted TNDs into TiO_2 nanoparticles. Due to the position of conduction band edges of two semiconductors, photogenerated electrons could transfer from g-C_3N_4 to TiO_2. There with a help of Pt as a cocatalyst and active sites provider, photoexcited electrons reduced protons from water and generated hydrogen. This heterojunction could produce more than double hydrogen as pristine g-C_3N_4 under the same conditions.

We created a novel g-C_3N_4 nanosheets with carbon vacancies and nanoholes throughout nanosheet planes. After synthesis g-C_3N_4 bulk material from dicyandiamide, the obtained material was heated to 650 ^oC under argon flow for 2 hr. After it cooled down, it was calcined again at 500 ^oC for 2 hr. As a result, its specific surface area increased significantly from 28 $m^2\ g^{-1}$ of bulk g-

C_3N_4 to 160 m^2 g^{-1}. Moreover, these stepwise treatments introduced some defects as carbon vacancies inside the structure of g-C_3N_4 nanosheets. They provided highly active photocatalytic sites for hydrogen evolution. Therefore, its hydrogen production was ten times higher than bulk material of g-C_3N_4 under visible light irradiation. It showed very high quantum efficiencies of 29.2% and 21.3% at 400 nm and 420 nm, respectively.

Finally, we generated zinc cadmium solid solution ($Zn_xCd_{1-x}S$) with synthesizing metal-glycerate of Cd and Zn via solvothermal method. Then, the material was calcined (500 ºC for 4 hr) and treated with H_2S at 450 ºC for 2hr. Thus, an homogeneous solid solution of $Zn_xCd_{1-x}S$ with hexagonal wurtzite crystal structure was formed. It should be mentioned that the obtained semiconductor could absorb a wide range of visible light energy and its band gap is strongly affected by Zn/Cd ratio and varies between 2.35 and 3.4 eV ($0 \leq x \leq 1$). The best results for hydrogen evolution was gained from $Zn_{30}Cd_{70}S$ sample with depositing MoS_2 as a cocatalyst. It could generate hydrogen in longer wavelengths of visible light region and its quantum efficiencies were: 46.6 % at 400 nm to 23.4% at 500 nm as well as 11.3% at 550 nm.

Tables of contents

List of Figures

List of Tables

Nomenclature

2D	Two dimensional
A	Reductant
AFM	Atomic force microscopy
AGCN	Nanosheet of g-C_3N_4 after argon treatment
BET	Brunauer-Emmett-Teller theory
BJH	Barrett-Joyner-Halenda theory
CIO	$CaIn_2O_4$ nanorod
Cd_RS	Hexagonal/Cubic CdS
CdS_R	Hexagonal CdS
D	Oxidant
eV	Electron Volt
FTIR	Fourier transform infrared spectroscopy
FTO	Fe-TiO_2 nanoparticle
GCN	Bulk g-C_3N_4
GT	Gas template
HRTEM	High-resolution transmission electron microscope
IUPAC	International Union of Pure and Applied Chemistry
LE	Liquid exfoliation
MOF	Metal organic framework
UMC	Coordinatively unsaturated metal center
MPs	Multicomponent photocatalyst
NHE	Normal hydrogen electrode
NP	Nanoparticle

NW	Nanowire
P	Pressure
PL	Photoluminescence
PMT	photomultiplier
QE	Quantum efficiency
SAED	Selected area election diffraction
SGCN	Nanosheet of g-C_3N_4 after second calcination
T	Temperature
TCD	Thermal conductivity detector
TEA	Triethanolamine
TEM	Transmission electron microscopy
TGA	Thermogravimetric analysis
TND	Titanate nanodisk
TNT	Titanate nanotube
TW	Tetrawatt
V_{pore}	total pore volume
UV	Ultraviolet
XPS	X-ray photoelectron spectroscopy
XRD	X-ray diffraction

Acknowledgment

Firstly, I would like to express my sincere gratitude to my advisor Prof. Trong On Do, for giving the opportunity to study at Université Laval and his great support of my Ph.D study. His motivation and immense knowledge guided me throughout this research project. Moreover, I would like to thank my co-supervisor, Dr. François Béland, who always inspires me with his precious advice and guidance for this work. I extremely grateful to both my supervisors for believing in me when I doubted myself the most.

This work could not be accomplished without the help of many other people. I would like to express my acknowledge to to Richard Janvier for electron microscopy analysis. In addition, I would like to thank Alain Adnot and Jean Frenette for XPS and XRD analyses. Moreover, I want to appreciate all Chemical Engineering department staffs, who assisted me greatly during my study at Université Laval.

I would like to appreciate all members of the Do research group, specially Cao Thang Dinh and Chinh Chien Nguyen, who gave me deeper insights in fundamental of nanomaterial and photocatalysis. Many Thanks to all my friends in Do research group: Amir Enferadi Kerenkan, Nhu Nang Vu, Manh Hiep Vu, Duc Trung Nguyen and specially Arnaud Gandon who helped me to translate the abstracts in French. I wish them all the best of luck in their future works.

I sincerely acknowledge the financial supports form Natural Science and Engineering Research Council of Canada (NSERC). I would also thank SiliCycle Inc. for their additional funding on this research thesis. I really appreciate the Center in Green Chemistry and Catalysis (CGCC) and the Department of Chemical Engineering at Univeristé Laval for their spare financial support.

Last but foremost, I would like to thank my family and my in-laws for their love and supports during these years of my study. Words cannot express my deep sense of gratitude to my beloved wife and best friend, Marzieh, with her undying love, understanding and support that helped me in each second of this long journey. Sincerely, I couldn’t accomplish this doctorate without her.

To my wonderful wife and best friend,

Marzieh,

A strong and gentle soul who taught me to be strong

Preface

This thesis consists of six chapters. Four of them were written in the form of scientific papers that have been published. The candidate is the primary author of these papers.

Chapter 2 is providing literature reviews, in which some parts are taken from a review paper that has been published as M. R. Gholipour, C. T. Dinh, F. Béland and T. O. Do, Nanocomposite heterojunctions as sunlight-driven photocatalysts for hydrogen production from water splitting, Nanoscale 2015, 7, 8187-8208. In addition, some parts are modified and updated according to the requirement of this thesis.

Chapter 4 has been published as M. R. Gholipour, F. Béland, T. O. Do, Graphitic Carbon Nitride-Titanium Dioxide Nanocomposite for Photocatalytic Hydrogen Production under Visible Light, International Journal of Chemical Reactor Engineering 2016, 14, 851-858.

Chapter 5 has been published as M. Reza Gholipour, F. Beland, T.-O. Do, Post-Calcined Carbon Nitride Nanosheets as an Efficient Photocatalyst for Hydrogen Production under Visible Light Irradiation, ACS Sustainable Chemistry & Engineering 2016, 5, 213-220.

Chapter 6 has been submitted as M. Reza Gholipour, C. C. Nguyen, F. Beland, T.-O. Do, Hollow Microsphere of $Zn_xCd_{1-x}S$ Solid Solution with Noble-metal-free Co-catalyst for Hydrogen Evolution with High Quantum Efficiency in Visible Light, submitted to ChemCatChem, September 2017.

In these works, the candidate synthesized and performed all the experiments under supervision of Prof. Trong On Do and Dr. François Béland, and help from other coauthors. The candidate collected the data and wrote the first drafts of all manuscripts. All the authors revised the manuscripts prior to publication.

Chapter 1. Introduction

This chapter is the introduction of photocatalysts and how this thesis was organized to discuss about nanocomposites. The scope and organization of this thesis is also presented.

1.1 Energy challenges

It has been widely acknowledged that the energy supply shortage and the environmental pollution are the biggest challenges of the 21st century.[1] According to the International Energy Outlook 2016 report, the world energy consumption is expected to increase by 48% from 2012 to 2040 (Figure 1.1). Fossil fuels including oil, natural gas, and coal continue to supply most of the world's energy; so that they are supposed to account for 78% of the world energy consumption in 2040.[2] However, using fossil fuels for providing the world's energy demand has been questioned very strongly due to the limited amount of fossil fuels, the greenhouse gas emissions accompanying fossil fuels combustion, and the high price of fossil fuels. These serious concerns enforce to search for clean, renewable, and cheap energy sources.[1, 2]

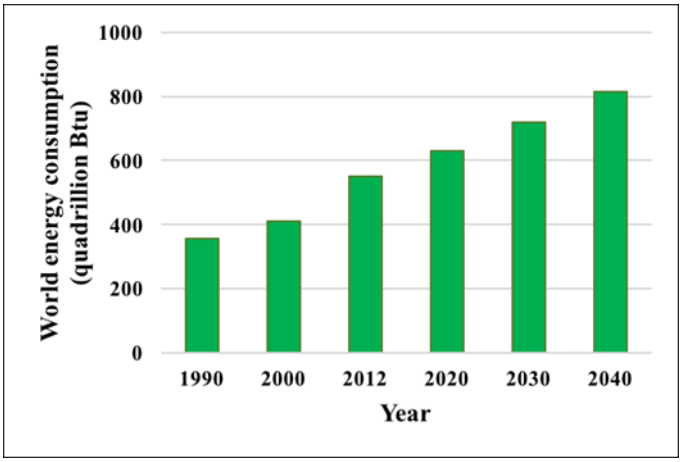

Figure 1.1. World energy consumption, 1990-2040.[2]

Among available renewable energy sources, solar energy is the ultimate renewable source to sustain all lives on earth. Solar energy, which provides the earth with 120000 TW power every year, is the most abundant source of energy on our planet. Less than 0.02% of the total solar energy irradiating on earth is sufficient to provide almost all the worldwide energy demand. However, it has so far been a big challenge to efficiently harvest, convert, and store solar energy. Today, the most popular way to exploit solar energy is photovoltaic cells, which directly convert solar energy into electricity. The generated electricity should be used immediately or stored in a secondary device such as batteries and capacitors. Hence, although the problems of solar energy harvest and conversion are effectively addressed through this method, the problem of energy storage is still

unsolved. An alternative approach to harness solar energy is solar fuel generation through photocatalytic processes. In this technique, a photo-assisted electrochemical process is employed to directly convert abundant raw materials (e.g., water and carbon dioxide) into highly energetic species such as hydrogen and oxygen that can serve as chemical fuels. In this way, all three problems of solar energy harvest, conversion, and storage will effectively be addressed at once.[3, 4]

1.2 Photocatalytic water splitting for hydrogen production

Hydrogen produced from renewable carbon-free resources is regarded as one of the most promising energy carriers to meet the future energy demand of the world. Sunlight and water are abundant and accessible resources that can be utilized to produce hydrogen via photocatalytic water splitting.[5] In 1972, Honda and Fujishima for the first time demonstrated the photocatalytic decomposition of water into hydrogen and oxygen employing a semiconductor TiO_2 based electrochemical cell.[6] Since then, solar water splitting using semiconductor photocatalysts has attracted a great deal of research attention due to its great potential to resolve the energy and environmental issues. In general, an efficient photocatalyst requires close integration of three essential components: a light harvesting antenna for solar energy absorption (semiconductor), a reduction catalyst, and an oxidation catalyst (Figure 1.2). The solar energy absorbed by semiconductor is used to generate excited electrons and holes for subsequent redox reactions. [3, 4] Since a few semiconductors themselves can also demonstrate catalytic function while harvesting light, the catalysts loaded on semiconductors are termed cocatalysts. Therefore, most semiconductor based photocatalysts typically consist of a semiconductor as the light harvesting element and two types of metal (e.g. Pt, Rh) or oxide (e.g. RuO_2) nanoclusters as the cocatalysts.[4, 7] In order to meet the close integration of these components, nanostructured materials have recently attracted considerable attention as novel photocatalysts due to their unique structural, optical, and chemical properties compared to their bulk counterparts.[3, 8-14]

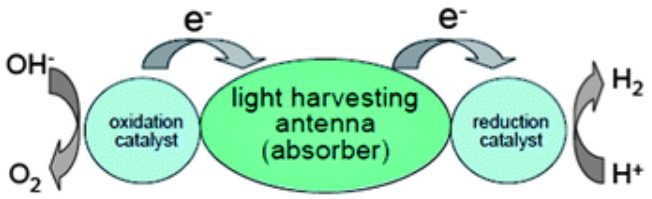

Figure 1.2. Schematic diagram of an efficient photocatalyst.[3]

1.3 Fundamental challenges of semiconductor photocatalysis

Despite considerable efforts to date, significant challenges still remain on developing a photocatalyst that is both efficient and robust enough for practical solar fuel production. Most photocatalysts reported so far are only able to function in the ultraviolet (UV) or near UV regime with limited efficiency because of a number of intertwined limiting factors including mismatch between the solar spectrum and the semiconductor band gap, inefficient charge separation and transportation, and injurious semiconductor degradation side reactions that cause material instability. In general, there is a lack of intrinsic driving force to govern charge separation and transportation in the typical construction of photocatalysts. Therefore, only a small portion of the photo-generated electrons and holes can be separated, and the majority are consumed via non-productive recombination. For the separated free electrons and holes, they may diffuse through the semiconductor to reach the redox catalysts for productive redox reactions. On the other hand, these separated free charge carriers can also diffuse onto the surface of the semiconductor where they reduce or oxidize the semiconductor photocatalyst itself, causing a complete disintegration and deactivation of the photocatalyst.[3, 4]

1.4 Scope of the thesis

Most photocatalysts have large band gaps and high charge recombination rates that lead them to have low quantum efficiencies in visible light region for hydrogen evolution reaction. The scope of this research thesis is to synthesize and develop nanocomposite photocatalysts for hydrogen evolution under visible light irradiation. To achieve this aim, we will work on different strategies to increase hydrogen production in photocatalytic water splitting. They are including reducing band gap of photocatalysts by modifying the structure of semiconductors, improving charge separation

process by making a nanocomposite of two semiconductors as well as introducing some defects in the structure of photocatalyst to provide some charge trapping centers. Furthermore, providing large specific surface area would lead to have higher available active sites for the reduction reaction to take place.

1.5 Organization of the thesis

This short introduction is followed by the next chapter, in which a brief introduction of heterogenous photocatalytic reaction is presented. After that, various methods and techniques on improving the performance of photocatalysts are discussed completely. Furthermore, a review on TiO_2 and its different heterojunctions is given that shows more works in this area needs to be done. Then, graphitic carbon nitride and zinc cadmium sulfide are introduced as promising photocatalysts for hydrogen production under visible light illumination. In addition, various methods and strategies to improve their photocatalytic activity are discussed in detail. In Chapter 3, a review on different characterization techniques, which are used in thesis, are presented and discussed.

In Chapter 4, we report a nanocomposite of g-C_3N_4 nanosheets and TiO_2 nanoparticles. This nanocomposite enhances hydrogen production of g-C_3N_4 nanosheets via improving charge separation procedure, in which photoexcited electrons migrate from g-C_3N_4 conduction band to TiO_2 and over there they react with protons over cocatalyst surface.

In Chapter 5, we propose a novel method to synthesize and develop nanosheets of g-C_3N_4. This new method encompasses two step calcinations that generate nanoholes and some defects as carbon vacancies throughout 2D nanosheet structures. These defects mostly act as highly active sites for hydrogen evolution reaction. In addition, they are considered as charge trapping centers that lead to decline charge recombination process inside the semiconductors. Moreover, this synthesis method enlarges the specific surface area almost 8 times higher than that of bulk g-C_3N_4. Therefore, more active sites are available for the reactants to produce hydrogen and so it shows quantum efficiencies of 29.2 % at 400 nm and 21.3% at 420 nm.

In Chapter 6, we discuss about new approach to synthesize a solid solution of $Zn_xCd_{1-x}S$. In this method, a mixture of metal-glycerate is used to form mixed oxides of ZnO and CdO. Then, during sulfuration step, sulfide ions are replacing with oxygen atoms at high temperature under

flow of H_2S. A series of $Zn_xCd_{1-x}S$ with different ratios of Zn and Cd are generated and tested for photocatalytic hydrogen evolution. It should be noted that $Zn_xCd_{1-x}S$ band gap and crystallinity are directly affected by ratio of Zn/Cd. The optimum ratio for the best hydrogen production and stability is obtained by Zn/Cd=0.3/0.7. Interestingly, it generates 12 mmol h^{-1} g^{-1} hydrogen with quantum efficiencies of 46.6% at 400 nm, 23.4% at 500 nm and 11.3% at 550 nm.

In Chapter 7, we highlight the main conclusions from the work in this thesis. Moreover, new suggestions and approaches for future projects are recommended.

Chapter 2. Nanocomposites photocatalysts for hydrogen production under visible light illumination

This chapter presents an introduction of heterogeneous photocatalysis. Different strategies to improve photocatalytic activity are discussed in detail. In addition, we discuss about the most visible-light active photocatalysts for hydrogen production and their structures are studied completely. We also review their recent development and heterojunction fabrications.

2.1 Fundamentals of heterogeneous photocatalysis

Reactions in chemical industries use catalysts that can be divided into two main group: homogeneous and heterogeneous catalysis. Homogeneous catalysis refers to reactions in which catalysts and reactants are in the same phase. However, heterogeneous catalysis is used where the phase of catalysts and reactants are different from each other. Phase includes solid, liquid and gas as well as immiscible liquids.[15]

Heterogeneous photocatalysis refers to a process where a semiconductor capable of absorbing photon energy of light is used as a catalyst. Generally, a photocatalytic reaction consists of three main steps: (I) a semiconductor absorbs light photons and generates excited electrons and holes; (II) these excited electrons and holes can migrate to the surface of semiconductor or recombine again inside the bulk material; (III) on the surface, holes can oxidize an oxidant (Equation.2.1) and electrons can reduce a reductant (Equation.2.2). Figure 2.1 illustrates schematically the main steps in heterogeneous photocatalysis reaction.

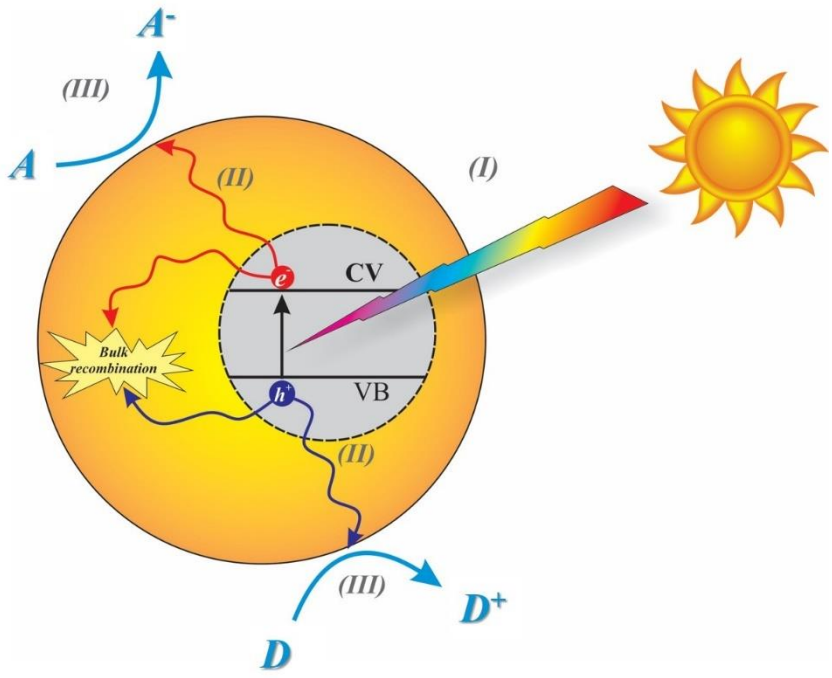

Figure 2.1. Schematic of heterogenous photocatalysis mechanism.

$$D + h^+ \rightarrow D^{\bullet+} \quad (2.1)$$

$$A + e^- \rightarrow A^{\bullet-} \quad (2.2)$$

If protons and oxygen in water are chosen to be reductant and oxidant, the process will become photocatalytic water splitting and half reactions of oxidation and reduction would be as follows:

$$H_2O + 2h^+ \rightarrow \frac{1}{2}O_2 + 2H^+ \quad (2.3)$$

$$2H^+ + 2e^- \rightarrow H_2 \quad (2.4)$$

Semiconductor band gap determines which wavelength of sunlight can be absorbed. The semiconductor with a wide band gap (E_{bg} > 3 eV) can only absorb UV light, which approximately accounts for 5% of solar energy (Figure 2.2).[16-18] In contrast, a narrow band gap semiconductor (E_{bg} < 3 eV) can be activated by visible light irradiation, which constitutes 43% of the sunlight spectrum.[19] Beside band gap, the positions of the valence and conduction bands are also very important in photocatalytic reactions. Figure 2.3 exhibited band structure, valence and conduction band positions of various semiconductors that can be used in various photocatalytic reactions.[20]

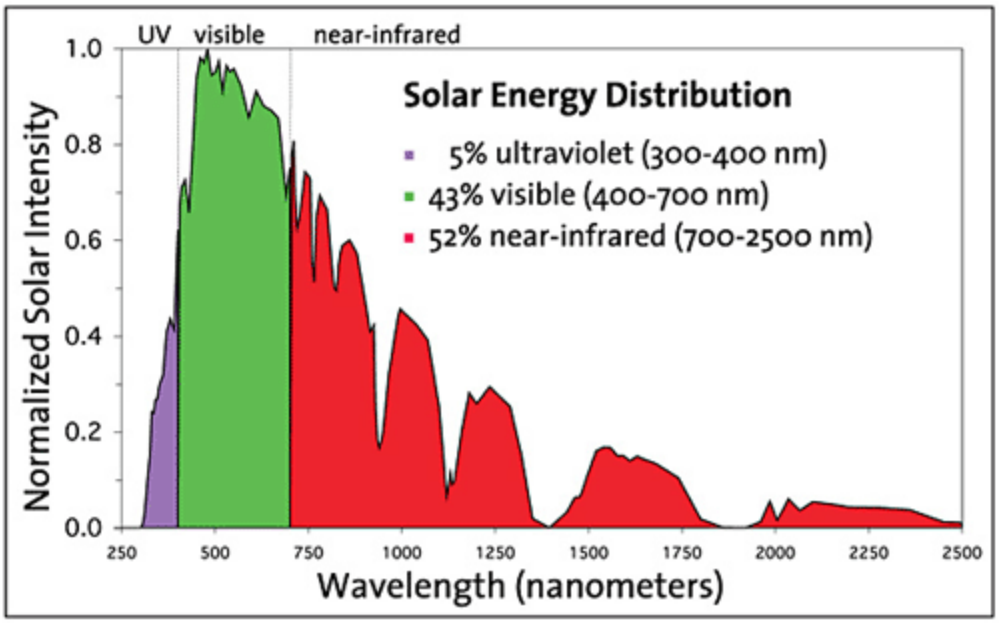

Figure 2.2. Solar energy distribution.[4]

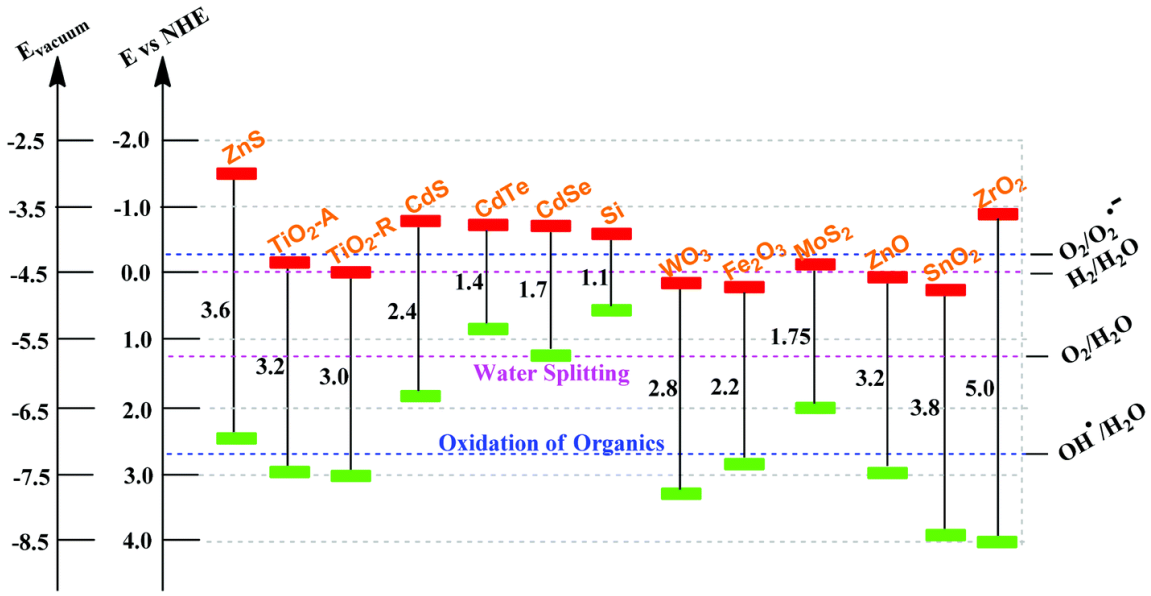

Figure 2.3. Band structure of various semiconductors.[20]

For H_2 evolution, the conduction-band edge should be more negative than the reduction potential of H^+ to H_2 ($E_{H^+/H_2} = 0\ V\ vs\ NHE\ at\ pH = 0$). On the other hand, the valence-band edge should be more positive than the oxidation potential of water ($E_{O_2/H_2O} = 1.23\ V\ vs\ NHE\ at\ pH = 0$) in order to evolve oxygen. Therefore, the band gap of semiconductor should be at least 1.23 eV in order to split the water. The equivalent light wavelength for this band gap energy is 1100 nm, which is in near-infrared region of the sunlight spectrum. By considering other factors such as energy losses during different stages in the photocatalytic process, effective semiconductors should have band gaps larger than 2 eV, which is related to the light with wavelength lower than 620 nm.[21, 22] Although some semiconductors can absorb the infrared light by photon up-conversion mechanism, their applications are usually limited to degradation of organic compounds.[23-26]

2.1.1 Overall water splitting

Fujishima and Honda were pioneers in decomposing water with light illumination.[6] They discovered that TiO_2 and Pt can act as anode and cathode electrodes, respectively, in a

photoelectrochemical cell. This system could split water into hydrogen and oxygen under intense UV irradiation. Some years later, Bard applied the concept of this system to introduce photocatalysis process.[8] Since then, there have been enormous efforts on developing semiconductors that can decompose water into H_2 and O_2 under the light illumination.

To decompose water directly into hydrogen and oxygen under sunlight irradiation is the ultimate goal of photocatalytic hydrogen generation system. In this process, a semiconductor with proper band-edges can absorb photon energy and evolve hydrogen and oxygen simultaneously. However, this reaction is thermodynamically non-spontaneous with the Gibbs free energy of 237 kJ/mol.[27]

$$2H_2O \xrightarrow{photon\ energy} 2H_2 + O_2 \qquad (2.5)$$

Some semiconductors can absorb UV light and split water directly into hydrogen and oxygen, but most of them have an energy conversion efficiency less than 1%.[28-30] Moreover, they cannot produce hydrogen and oxygen in a stoichiometric ratio because one type of charge carriers is accumulated on the surface of photocatalyst.[27] One exceptional example is a GaN-ZnO solid solution photocatalyst that can split water into hydrogen and oxygen stoichiometrically under visible light illumination with a quantum efficiency of about 6%.[31] It is obvious that overall water splitting is very difficult to be proceeded under visible light illumination and becomes one of the greatest challenges for researchers in this field.

2.1.2 Sacrificial reagent systems

It is believed that the overall water splitting is a very hard reaction to be proceeded, and it needs a specific kind of semiconductor with appropriate band edge positions. Nevertheless, some semiconductors can do one of the half reactions of water splitting, i.e. water reduction or oxidation, in the presence of suitable sacrificial reagents (electron donors or acceptors). In principle, sacrificial agents usually react with one type of charge carriers while the other carrier reacts with water to produce hydrogen or oxygen. Electron donors, which consume excited holes on the surface of the semiconductor, are used for water reduction half reaction and electron acceptors (electron scavengers) are usually needed for water oxidation, as illustrated in Figure 2.4. Generally, the

electron donors must be more readily oxidized than water by excited holes, while the electron acceptors must be more readily reduced than water by excited electrons. The most common electron donors are methanol, ethanol, triethanolamine (TEA) and an aqueous solution of Na_2S/Na_2SO_3, whereas metal cations such as Ag^+ and Fe^{3+} are usually utilized as electron acceptors.[27]

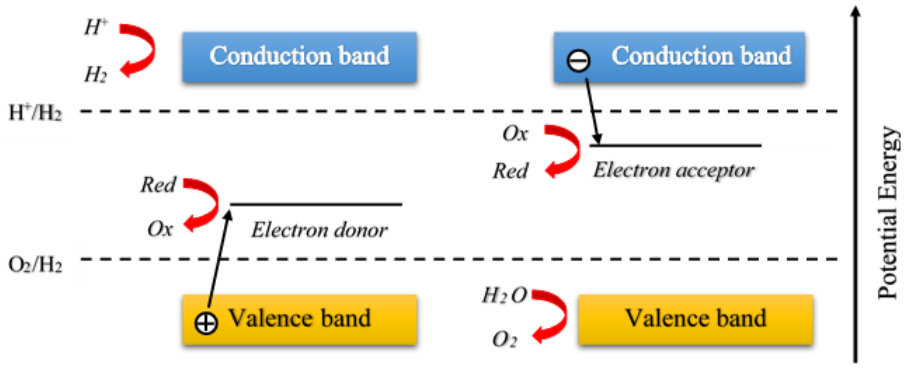

Figure 2.4. Schematic principles of water reduction or oxidation in the presence of sacrificial reagents.[27]

Various mechanisms were proposed to explain the consumption of sacrificial reagents in hydrogen production reactions.[30, 32] These electron donors react more easily with holes than water due to its less positive oxidation potential. This would lead to accelerated holes consumption on the surface of the photocatalyst and so the positive charge accumulation is partially prevented and, as a result, protons and photoexcited electrons can react together more easily. It should be noted that, in the case of using methanol as electron donor, hydrogen is also produced as a result of methanol conversion (Equation.2.6).[33, 34] However, by increasing the carbon chain length, the contribution of H_2 production from alcohol conversions decrease substantially.[34] Moreover, Guzman showed that the direct reaction of methanol with excited holes does not proceed to an appreciable extent in the presence of high concentration of water.[35]

$$CH_3OH + H_2O \rightarrow CO_2 + 3H_2 \qquad (2.6)$$

Semiconductors capable of decomposing water in the presence of sacrificial agents may seem to be useless. Nevertheless, these photocatalysts not only can be used in Z-schematic system but also some of them can be used to produce H_2 using biomass derived sacrificial reagents.[36, 37]

2.1.3 Electron mediator systems

The electron mediator system is also called Z-scheme system or a dual photocatalyst system. The concept of this system is to transfer charge carriers by two different electron mediators in a solution and after participating in redox reactions, they all return to their original chemical states.[38] This procedure for overall water splitting is entirely different than two previous methods. It needs two various photocatalysts: a semiconductor provides photoexcited electrons to participate in half-reaction for H_2 evolution; another one supplies photogenerated holes to take part in half-reaction of water oxidation. Moreover, the two semiconductors should be excited simultaneously and one half of charge carrier will recombine in order to bring electron mediator in their original states (Figure 2.5). Some of the most common electron mediators are Fe^{3+}/Fe^{2+}, IO^{3-}/I^{-} and Ce^{4+}/Ce^{3+}.[39]

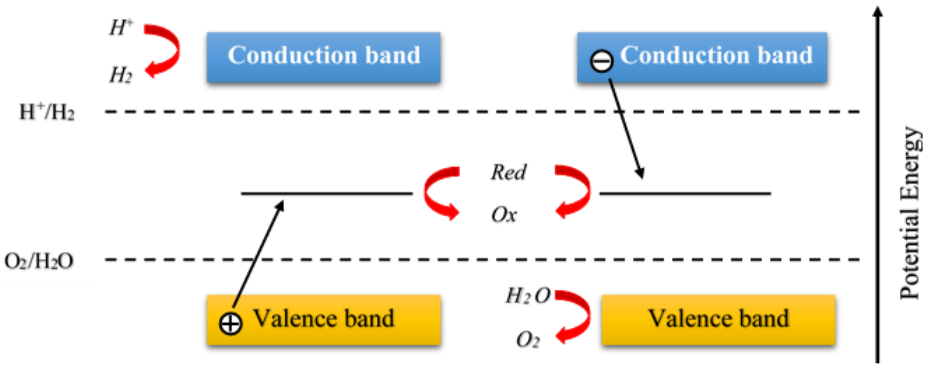

Figure 2.5. Schematic principles of overall water splitting in the Z-scheme system.[38]

There are some review papers discussing different approaches and application of this dual step system, which is similar to plant photosynthesis.[38, 40] Nonetheless, this system has some drawbacks in comparison with the one-step system. For instance, Z-scheme systems are usually more complicated and need more photons to produce the same amount of hydrogen because half of the excited charges are used in order to bring the excited mediator to its ground state for further reactions.[38, 41]

2.1.4 Activity and quantum efficiency

Photocatalytic activity depends on many factors such as light source (Xe or Hg lamps), light intensity, reaction cell, different directions of irradiation (top, inner, or side), reaction media (water or various sacrificial agents), and the quantity of photocatalyst. The simplest way to find semiconductor activity is to measure the amount of evolved gases in a specific period of time and report it in $\mu mol \cdot h^{-1}$ or $\mu mol \cdot h^{-1} \cdot g^{-1}$ units.[39]

Quantum yield (Quantum efficiency) is another way to report photocatalytic activity of a semiconductor. This is independent of effective factors that are mentioned above and it is defined as:[42]

$$Quantum\ yield\ (\%) = \frac{Number\ of\ reacted\ electrons}{Number\ of\ absorbed\ photons} \times 100 \qquad (2.7)$$

Despite this equation can give us accurate quantum yield, it is very hard to measure the real amount of absorbed photons. In order to solve this problem, researchers suggested to use apparent quantum yield, which is declared as follows:[39]

$$\begin{aligned} &Apparent\ quantum\ yield\ (\%) \\ &= \frac{Number\ of\ reacted\ electrons}{Number\ of\ incident\ photons} \times 100\% \\ &= \frac{2\ \times\ Number\ of\ evolved\ H2\ molecules}{Number\ of\ incident\ photons} \\ &\times 100\% \\ &= \frac{4\ \times\ Number\ of\ evolved\ O2\ molecules}{Number\ of\ incident\ photons} \\ &\times 100 \end{aligned} \qquad (2.8)$$

It is obvious that the apparent quantum yield is smaller than the real quantum efficiency because of the difference between the number of absorbed photons and incident light.

Solar energy conversion efficiency is a method to calculate solar cell efficiency, it can also be used to report the photocatalytic activity of a semiconductor.

$$Solar\ energy\ conversion\ efficiency\ (\%) = \frac{Output\ energy\ of\ H2\ evolved}{Energy\ of\ incident\ solar\ light} \times 100\% \quad (2.9)$$

Up to now, semiconductors have extremely low solar energy conversion values and so this indicator is seldom used.[28] It is anticipated that for industrial application of water splitting via sunlight, this efficiency should improve noticeably.

2.1.5 Cocatalysts

A cocatalyst is a compound added to the semiconductors photocatalyst to improve their activity. In photocatalytic water splitting, the cocatalysts can be used to enhance either the water oxidation or reduction reactions. The cocatalyst for water reduction are usually small metal nanoparticles which can form Schottky junction with semiconductors and enhance charge separation in photocatalyst or photoelectrochemical cell.[43, 44] In principle, the contact between metal and semiconductor creates an electric field that separate excited electrons and holes more easily, as demonstrated in Figure 2.6.[45-47] If the work function of the metal matches the conduction band-edge of semiconductor, excited electrons move from the semiconductor to the metal and from there, they can react with water. In addition, the metal provides active sites for hydrogen generation due to its relatively low over-potential for water reduction.

The physical and chemical properties of cocatalyst such as particle size and valence states, which significantly affect their performance, are strongly dependent on the cocatalyst loading methods. Although depositing more cocatalysts provide more active sites for reactions, they reduce the absorption ability of the photocatalyst. Therefore, the concentration of cocatalysts should be optimized to obtain the maximum activity during water splitting under light illumination.

There are two main techniques to deposit cocatalysts on the surface of semiconductors: in situ photodeposition and impregnation. In the first one, cocatalyst is reduced by photoexcited electrons on the surface of a semiconductor under light irradiation in the presence of sacrificial reagents. Therefore, the semiconductor should be mixed with a precursor solution of cocatalyst. If

photo-reduction step is performed with various precursors, a core-shell structure can be achieved easily.[48]

The second one is usually followed by a post-calcination step. First, a semiconductor is impregnated with a solution containing the cocatalyst precursor and then evaporated and dried. After this stage, the dry mixture is calcined in air or other gases such as hydrogen or argon in order to obtain desired states of metal or metal oxide. The final state of cocatalyst depends on gas treatment, temperature and type of precursor.[39]

There have been great efforts to use different types of cocatalysts including transition metals, metal oxides and noble metals for each half reaction of water splitting. The most common cocatalysts for hydrogen evolution are Pt, Rh, Au, NiO and RuO_2. [49-51] [52] [53] [54] Other types such as the core shell configuration of cocatalysts have been recently proposed to improve H_2 evolution in overall water splitting.[48, 55]

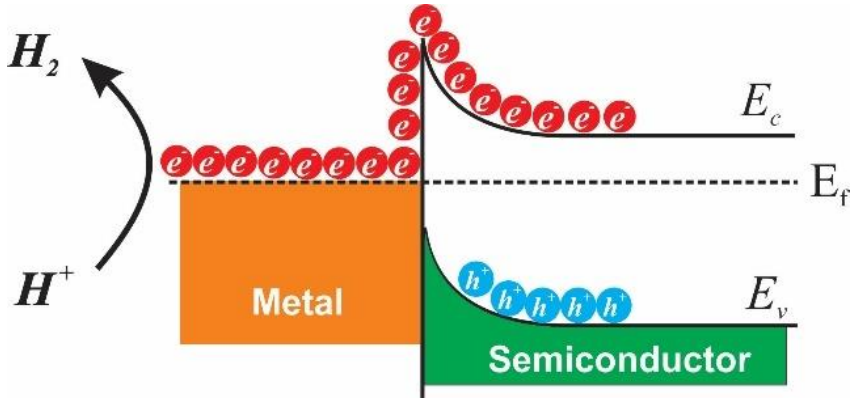

Figure 2.6. A schematic energy band model of Schottky junction.[45-47]

2.1.6 Semiconductor heterojunction structures

Instead of using a single semiconductor, combining a semiconductor with other semiconductors, metals, and molecules would lead to form a heterojunction structure between them. These heterojunctions were found to enhance the performance of various devices such as solar cells, photoluminescence and electro-chromic devices.[13, 56, 57] In addition, the utilization of nanocomposites as photocatalyst instead of a single semiconductor, is another efficient and practicable approach to enhance the photocatalytic performance. In this kind of nanocomposite, excited charges migrate from one semiconductor to another semiconductor (or metal which acts as

a cocatalyst). The second semiconductor should have proper band-edge position or higher efficiency in comparison with the first one. Furthermore, this nanocomposite can improve its efficiency due to the fact that reduction and oxidation reactions happen on two different components.[58]

All of heterojunctions can be categorized into three types based on their conduction and valence band positions, as illustrated in Figure 2.7. In Type 1, both excited electrons and holes move from semiconductor 1 to semiconductor 2 due to their band edge positions. Usually this kind of heterojunction doesn't improve photocatalysts because of accumulation of both charge carriers on one semiconductor.

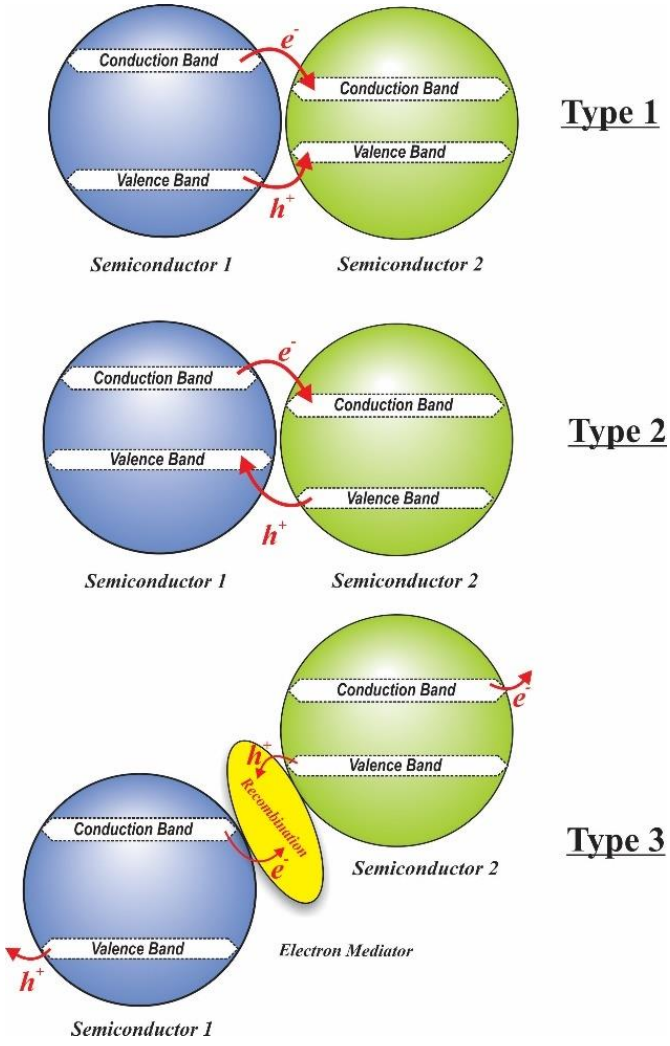

Figure 2.7. Various kinds of heterojunctions.[58]

In the second group of heterojunctions, the conduction band of semiconductor 2 is lower than that of semiconductor 1. However, the valence band of semiconductor 1 has higher value than that of semiconductor 2. As a result, excited electrons can move from semiconductor 1 to 12, although generated holes migrate vice versa. If both semiconductors have sufficient intimate contacts, an efficient charge separation will occur during light illumination. Consequently, charge recombination is decreased and charge carriers have longer lifetime, which results in higher photocatalyst activity. Most of the composites discussed in the literature, are of type 2.

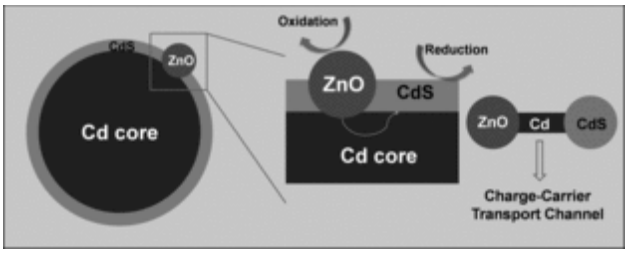

Figure 2.8. Scheme of the improving mechanism of photoexcited charge-carrier transport in the ZnO–CdS@Cd heterostructure.[59]

Type 3 consists of semiconductors with both valence and conduction bands being lower in one than the other, as can be seen from Figure 2.7. This kind can be applied in the Z-scheme system with an appropriate electron mediator or some kind of bridges that attach the two semiconductors. For instance, Wang et al. synthesized a core-shell nanocomposite of ZnO–CdS@Cd in such a way that Cd element acts as the charge-carrier bridge.[59] A schematic of this nanocomposite is demonstrated in Figure 2.8.

2.2 Titanium dioxide photocatalysts

In nature, Titanium dioxide (TiO_2) has three crystal phases including: anatase (tetragonal), rutile (tetragonal), an brookite(orthorhombic).[60-62] Various forms of TiO_2 have slightly different band gaps of around 3 eV (anatase: 3.2 eV, rutile: 3 eV), due to the variety of the crystal structures as demonstrated in Figure 2.9.[63, 64] Both anatase and rutile have the same construction unit of TiO_6, although the distortion of their crystal structure gives them different photocatalytic activities. Rutile is the thermodynamically stable form, and brookite does not usually show appreciable photocatalytic activity, but anatase is often indicated as the most active phase.[65, 66] The redox

potential of TiO_2 valence band is +2.53 V (vs. NHE at pH=0), that can evolve oxygen from water. Moreover, its redox potential of photoexcited electrons is -0.52 V(vs. NHE at pH=0), which is negative enough to produce hydrogen from water.[67, 68]

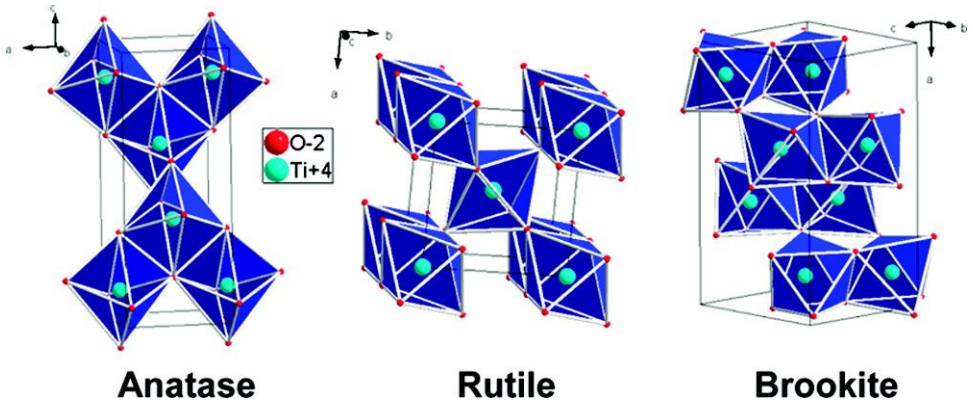

Figure 2.9. Representations of the TiO2 anatase, rutile, and brookite forms.[62]

TiO_2 possesses specific properties that make it almost a perfect photocatalyst for hydrogen production via sunlight energy. These features are: activity in catalyze photocatalytic reaction, ability to activate under sunlight energy, chemically inert and stable under photocatalytic reaction, large specific surface area and low cost. However, its large band gap (> 3 eV) limits its application in visible light region that accounts for a large amount of solar energy. Thus, various methods such as doping with anions and cations have been suggested to decrease its band gap and harvest more visible light energy.[66-70] Moreover, some researchers tried to improve TiO_2 kinetic efficiency by controlling the particle size or increasing its surface area in order to generate more hydrogen under sunlight illumination.[70-73]

After absorbing photon energy, a semiconductor produces excited electrons and holes. The charge carriers are separated or recombined together during their path to the surface of the semiconductor. Clearly, this step plays an important role in determining the light to fuel conversion efficiency.[74] Thus, many efforts has been made to synthesize various junction approach in order to enhance charge separation process. They can be categorized in two main groups as follows: heterojunction with other narrow band gap semiconductors, various phase junction of TiO_2.

2.2.1 Heterojunction of TiO_2 and other semiconductors

Based on discussion in semiconductor heterojunction structures, Type 2 configuration (Figure 2.7) is the best way to increase hydrogen production from TiO_2 and other semiconductors.[75, 76] This structure helps to increase charge separation and enhances carrier's lifetime. Therefore, excited electrons and holes have more time to react with adsorbed radicals on the active sites and as a result, hydrogen production increases significantly compared with pristine semiconductors.

TiO_2 and CdS were the most studied semiconductors during the last decades due to their photocatalytic properties and benefits.[74, 77] However, each of them has some drawbacks that limit their application for hydrogen production from sunlight. For example, TiO_2 has a wide band gap inapplicable for visible light absorption and CdS is instable during photocatalytic reactions. The combination of these semiconductors in nanoscale leads to have more efficient photocatalysts that can generate hydrogen under visible light irradiation with high stability. Under visible light illumination, CdS can absorb photons and produce holes and electrons. Although TiO_2 cannot absorb visible light, due to its wide band gap, excited electrons can move from CdS to TiO_2. This leads to a better charge separation, and results in higher quantum yield. It should be noted that the excited holes remain in the valence band of CdS and from there; they can oxidize any sacrificial agents. [78, 79] Various nanocomposites with different morphologies can be created CdS and TiO_2, which can be generally classified into two groups: CdS nanoparticles on the surface of TiO_2 or TiO_2 nanoparticles deposited on the surface of CdS. Some important morphologies will be discussed here, which resuls in higher light absorption and higher hydrogen evolution in the visible light region.

Generally, two different morphologies for mixing CdS nanoparticles and titanate nanotubes have been proposed in order to improve photocatalytic activity, as illustrated in Figure 2.10.[80-84] CdS/titanate nanotubes (CdS/TNTs) were reported to have higher increase in photocatalytic activity in comparison with traditional nanocomposite CdS@TNTs.[80] The CdS/TNTs nanostructures lead to have a proper dispersion of CdS as well as intimate multipoint contacts between two nanocrystals. It is clear that the ratio of Cd/Ti plays an important role in photocatalyst activity. The optimum value of this proportion was 0.05, which corresponds to 6 wt% of CdS in photocatalysts. With the optimum cocatalyst quantity of Pt (2.0 wt%), the CdS/TNTs could

generate 353.4 μmol h^{-1} hydrogen with 25.5% quantum yield under visible light. Nevertheless, the quantum yield of traditional CdS@TNTs could hardly reach 2.7% and as mentioned before, changing the structure of nanoparticles can have major impacts on their activity. It is noteworthy that this nanocomposite was stable for hydrogen production during 120 h of 6 cycles. Therefore, this nanostructure improved noticeably the stability of photocatalyst during hydrogen evolution.

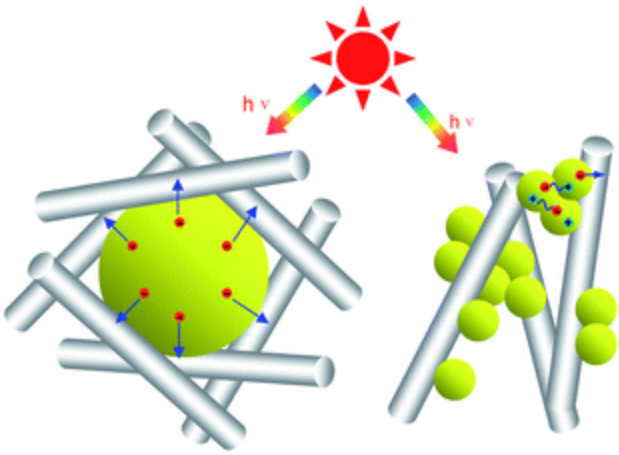

Figure 2.10. Schematic illustration of the two different architectures in CdS/TNTs (left) and CdS@TNTs (right).[80]

Many researchers have investigated the deposition of CdS nanoparticles inside different nanostructure of titanate such as tubular and nanotubes with the aim of obtaining highly efficient nanocomposites.[81, 85] Li et al. deposited homogeneously CdS nanoparticles inside the TiO_2 nanotubes.[81] They examined its photocatalytic water splitting with electron donors containing S^{2-}, SO_3^{2-} at wavelength of 420 nm. They attained 43.4% quantum yield for H_2 evolution. This is due to the quantum size effect of CdS nanoparticles as well as synergetic effects between two nanocomposites. This also means that the potential energy at the interface of CdS and TiO_2 would help electrons to transfer from CdS to TiO2 more easily and consequently enhance photocatalytic activity.

CdS nanoparticles can also be deposited on nanosheets of titanate that leads to increase quantum yield of nanocomposite.[85-88] The powerful interaction between titanate 2D nanostructures and CdS helped to create visible light absorption photocatalysts with high stability towards photocorrosion of CdS. Our group synthesized an ultrathin titanate nanodisks (TNDs) by the solvothermal method.[89] After that, we deposited both CdS nanoparticles as a visible light

semiconductor and Ni nanoparticles as a cocatalyst on the surface of TNDs for hydrogen evolution. This nanocomposite was able to separate photoexcited charges efficiently and as a result it showed a very high activity for water splitting under visible light irradiation. The concept of depositing cocatalysts on the other surface (here on TNDs), would help to enhance photocatalytic activity by increasing charge separation and preventing recombination phenomena. As can be seen in Figure 2.11(a), excited electron can easily transfer from CdS to TNDs and from there to Ni cocatalyst [86]. With an optimum ratio of CdS/TNDs and Ni loading, this nanocomposite can generate H_2 from water-methanol solution under visible light irradiation. The hydrogen evolution rate was 15.326 mmol g^{-1} h^{-1} during 15 h of reaction, which results in having 24% quantum yield at $\lambda \geq$ 420 nm. It is noteworthy that this approach of mixing semiconductors with TND can also be used for other efficient visible light active semiconductor. The intimate contact between TND and CdS plays a crucial role in this kind of nanostructure. In other words, physical mixing of this semiconductors cannot result in high photocatalyst activity. By growing CdS and Ni nanoparticles on the surface of TND by means of ion exchange method we were certain that nanoparticles had intimate contact and so charge carriers can easily transfer between semiconductors, as shown in Figure 2.11(b).[90]

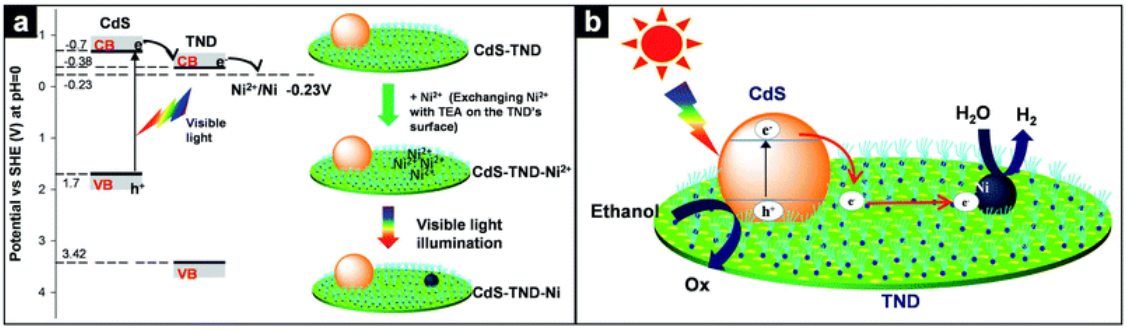

Figure 2.11. Schematic illustration of the electron transfer in the photoreduction of Ni^{2+} adsorbed on the surface of TNDs under visible light illumination and schematic illustration of the formation of Ni clusters on the surface of TND by visible-TND composites by visible light illumination (a). Schematic illustration of the charge transfer in CdS-TND-Ni MPs in the photocatalytic H_2 production from water-ethanol solution under visible light (b).[86]

In another technique, researchers tried to deposit TiO_2 nanoparticles on CdS nanostructures.[78, 79, 91-93] In most of them, a cocatalyst should be utilized in order to have hydrogen production. For instance, Jang et al. made a nanocomposite of CdS nanowires with a high crystallinity, which had TiO_2 nanocrystals on their surfaces, as shown in Figure 2.12.[79] Under

visible light, this nanostructure displayed hydrogen production from an aqueous solution of sulfide and sulfite ions. The optimum ratio of TiO_2 in this nanostructure would be 0.2, which led to having the highest activity under visible light irradiation. The possible role of TiO_2 NP is to provide sites for collecting the photoelectrons generated from CdS NW, enabling thereby an efficient electron-hole separation as depicted in Figure 2.12.

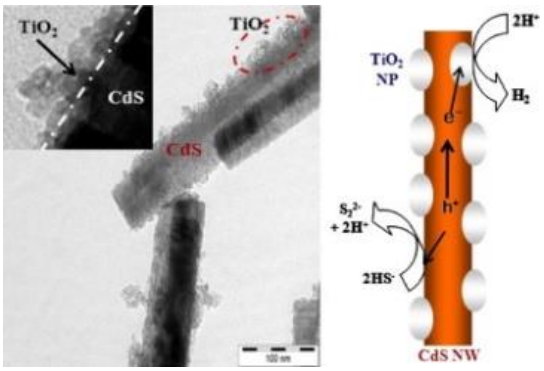

Figure 2.12. A nanocomposite consisting of CdS NW with high crystallinity decorated with nanosized TiO_2 NPs.[79]

Preparing nanocomposite is a very delicate process and each step should be considered precisely, even though the nanostructure and crystallinity may change with the order of adding precursors. Park et al. showed that reversing chemical precipitation order of CdS on TiO_2 nanoparticles caused to have different H_2 evolution rates in H_2 evolution under the same conditions.[94] They prepared CdS_R by adding Cd^{2+} in aqueous solution containing S^{2-} and Pt-loaded TiO_2. Another nanocomposite with an equal molar ratio was prepared by adding sulfide drops into the solution of Cd^{2+} and Pt-TiO_2 (Cd_RS). Surprisingly, CdS_R showed 10 times higher hydrogen evolution than Cd_RS under visible light irradiation (Figure 2.13).

Khatamian et al. prepared a metalosilicate-based (ferrisilicate and aluminosilicate) nanocomposite of CdS/TiO_2 via hydrothermal method.[95] Utilizing metalosilicate support has many advantages such as offering high surface area and providing homogenous dispersion of CdS nanoparticles. Moreover, this support both prevents agglomeration of the semiconductor and facilitates electron transfer and separation. It is noteworthy to consider that applying ferrisilicate, the presence of partially occupied d orbitals of Fe^{3+}, which can interact with TiO_2 orbitals, enhances the photocatalytic activity, while applying aluminosilicate as a support didn't improve its activity

compared to unsupported composite. In the case of CdS phase, hexagonal structure showed around sixfold higher photocatalytic activity than cubic one.

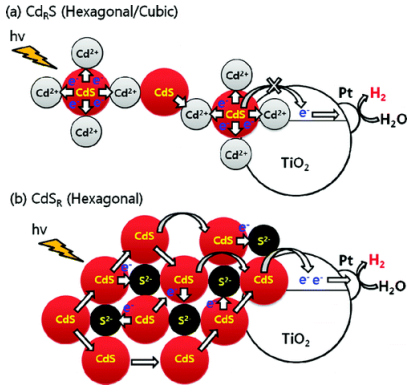

Figure 2.13. Schematic illustration for photocatalytic hydrogen production mechanisms of Cd_RS and CdS_R hybrids.[94]

Vu et al. provided nanocomposite of TiO_2 nanorods and CdS nanoparticles with Ni clusters in order to enhance charge separation and photocatalytic activity.[84] A dominant feature of this nanorod-based materials is that nanoparticles of the second semiconductor could be dispersed uniformly on the nanorod surface. Ni nanoparticles acting as cocatalysts were deposited on the surfaces of these nanorods selectively. This configuration can improve the efficiency of electron transfer from the sensitized CdS nanoparticles to TiO_2 and then to Ni clusters, as depicted in Figure 2.14. The H_2 production rate was 33.36 μmol h^{-1} g^{-1} under visible light in the presence of methanol as a sacrificial reagent, which was about 44 times higher than neat Ni-CdS system. Table 2.1 summarized different nanocomposites of CdS and TiO_2 with their hydrogen production and quantum yields.

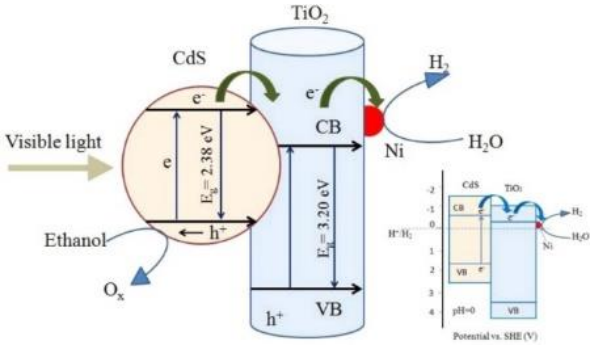

Figure 2.14. Mechanism illustration of the activity of Ni–TiO_2/CdS under visible light for the production of H_2; inset is the potential redox energy corresponding to CdS, TiO_2, and H^+/H_2.[84]

Table 2.1. Different nanocomposites of CdS and TiO2.

Semiconductor 1	Semiconductor 2	Cocatalyst	Sacrificial reagent	Light Source	Hydrogen production ($\mu mol\ h^{-1}\ g^{-1}$)	Quantum yield (%)	Refs
$Na_2Ti_2O_4(OH)_2$ nanotube	CdS	Pt	Na_2S/Na_2SO_3	350 W Xe, $\lambda \geq 430nm$	545	2.7 at λ = 430 nm	[83]
TiO_2 nanotubes	CdS	Pt	Na_2S/Na_2SO_3	300 W Xe, $\lambda \geq 420nm$	2680	43.3 at λ = 420 nm	[81]
Titanate nanotubes	CdS	Pt	Na_2S/Na_2SO_3	500 W Xe, $\lambda \geq 430nm$	1767	25.5 at λ = 420 nm	[80]
Titanate nanodisks	CdS	Ni	Ethanol	300 W Xe, $\lambda \geq 420nm$	11038	21 at λ = 420 nm	[89]
Titanate nanodisks	CdS	Ni	Ethanol	300 W Xe, $\lambda \geq 420nm$	15326	24 at λ = 420 nm	[86]
TiO_2 nanosheet	CdS nanoparticles	---	Na_2S/Na_2SO_3	350 W Xe, $\lambda \geq 400nm$	1651	8.9 at λ = 420 nm	[96]
TiO_2	CdS	Pt	Na_2S/Na_2SO_3	450 W Xe, $\lambda \geq 420nm$	4848	No data	[94]
TiO_2	Hexagonal CdS	---	Na_2S/Na_2SO_3	500 W Osram	8990	No data	[95]
TiO_2 nanorods	CdS nanoparticles	Ni	Ethanol	300 W Xe, $\lambda \geq 420nm$	33.63	No data	[84]
Titanate nanotubes	$Cd_{0.5}Zn_{0.5}S$	---	Na_2S/Na_2SO_3	500 W Xe, $\lambda \geq 430nm$	1738.5	38.1 at λ = 420 nm	[97]
TiO_2 nanosheet	CdS NPs	Pt	Lactic acid	350 W Xe, $\lambda \geq 420nm$	6625	13.9 at λ = 420 nm	[87]
TiO_2	CdS	Pt	Na_2S/Na_2SO_3	350 W Xe, $\lambda \geq 420nm$	6720	4.5 at λ = 420 nm	[98]
Titanate spheres	CdS nanoparticles	---	Na_2S/Na_2SO_3	300 W Xe, $\lambda \geq 420nm$	75	No data	[99]

Table 2.1 Continue.

Semiconductor 1	Semiconductor 2	Cocatalyst	Sacrificial reagent	Light Source	Hydrogen production ($\mu mol\ h^{-1}\ g^{-1}$)	Quantum yield (%)	Refs
nanometer-thick layered titanate nanosheet	CdS quantum dots (QDs)	---	Na_2S/Na_2SO_3	300 W Xe, $\lambda \geq 420nm$	1000	No data	[100]
Bulk CdS	TiO_2 nanoparticles	Pt	Na_2S/Na_2SO_3	350 W Xe, $\lambda \geq 420$ nm	6400	No data	[78]
hex-CdS	TiO_2	Pt	glycerol	300 W Xe, $\lambda \geq 420$ nm	22	No data	[93]
TiO_2	CdS				65		
CdS nanowires	TiO_2 nanoparticles	Pt	Na_2S/Na_2SO_3	500 W Xe, $\lambda \geq 420$ nm	110	No data	[79]
CdS bulk	TiO_2 nanoparticles	Pt	Na_2S/Na_2SO_3	350 W Xe, $\lambda \geq 420$ nm	4224	No data	[91]
Chromosilicate	CdS–TiO_2	---	Na_2S/Na_2SO_3	500 W Osram, , $\lambda \geq 420$ nm	2580	76.27at λ = 450 nm	[101]
TiO_2	CdS	Au	Na_2S/Na_2SO_3	300 W Xe, $\lambda \geq 420$ nm	1970	No data	[92]

Some researchers synthesized nanocomposites of TiO_2 and some of the metal oxides which are activated in the visible light region.[102-110] Interestingly, some of them showed higher hydrogen production in comparison with pristine TiO_2 due to visible light absorption and better charge separation. For instance, Martha et al. tried to increase hydrogen production by combining doped TiO_2 with V_2O_5.[105] Although N, S doped TiO_2 has a very low hydrogen evolution, the combination of the doped-TiO_2 with V_2O_5 exhibited 7 times higher hydrogen production under visible light irradiation (296.6 $\mu mol\ h^{-1}$). Xie et al. showed that nanocomposite of $TiO_2/BiVO_4$ had a much longer lifetime of photoexcited charge carriers and so higher charge separation.[109] The main reason for this phenomenon is related to high movements of photoexcited electrons from

$BiVO_4$ to TiO_2. Due to this reason, this photocatalyst had unexpected visible light activity for water splitting rather than $BiVO_4$ which was almost inactive in this region. They reported that $TiO_2/BiVO_4$ with molar ratio of 5%, could evolve 2.2 mol h^{-1} hydrogen, which was much higher than mixing with reduced graphene oxide nanosheet (0.75 mol h^{-1}) under the similar conditions.[110] Another group deposited Fe-TiO_2 nanoparticles (FTO) on the surface of $CaIn_2O_4$ nanorods (CIO).[107] This nanocomposite revealed hydrogen production in the presence of KI as sacrificial agent and Pt as cocatalyst. The contact of these two nanoparticles facilitated charge separation and to higher hydrogen evolution. This nanocomposite exhibited H_2 production at a rate of 280 μmol h^{-1} g^{-1}, which was 12.3 and 2.2 times higher than $CaIn_2O_4$ and Fe-TiO_2, respectively. Due to the synthesis method (physical mixing of FTO and CIO), there is no control or uniformity of dispersion of FTO on CIO. In addition, cocatalysts should be deposited on FTO in order to be more effective for hydrogen production. It seems that by applying some coating method the activity of this nanocomposite can improve even more than 280 μmol h^{-1} g^{-1}.

It is worth mentioning that iron oxide is capable of using as metal organic framework (MOF) in diverse morphologies with titanium oxide.[111-113] For instance, Lin's group created a nanocomposite of mixed metal oxide (Fe_2O_3 and TiO_2) via MOF templates.[111] They used MIL-101 MOF (Fe source) to deposit on amorphous TiO_2 and after deposition, they calcined the mixture in order to acquire the nanocomposite of Fe_2O_3/TiO_2. As a result, crystalline octahedral nano-shells were obtained which could produce hydrogen under visible light irradiation. Although TiO_2 can only activate under UV light and Fe_2O_3 has a more positive conduction band than reduction potential of H_2, this novel nanocomposite with a help of Pt metal as a cocatalyst produced 30.0 μmol g^{-1} of hydrogen in 48 hours in the presence of TEA as a sacrificial agent. The reason for this activity is that some iron ions from MIL-101 can be doped into TiO_2 crystallinity during the calcination process and the other converted into Fe_2O_3. Fe_2TiO_5 and Ti-doped Fe_2O_3 are both considered as activated photocatalysts under visible light in H_2 formation because of their small band gaps (Fe_2TiO_5 = 2.2 eV and Ti-doped Fe_2O_3 = 2.1 eV) and their edge of conduction bands which are more negative than reduction potential of H^+.[112] Moreover, further characterizations showed that this material was stable during hydrogen evolution and no decreasing in activity was observed. By introducing this kind of hollow nanostructure, the surface area of the photocatalyst increase significantly that results in higher activity owing to more available active sites. Another example of this type was developed in our group. We proposed a new route to prepare a novel type

of photocatalytic hollow Fe2O3-TiO2 nanostructure using MOF-UMCs as a hard template.[113] In this type of MOF-UMCs materials, each trimeric Fe(III) center possesses terminal water molecules that can be removed by vacuum and temperature treatments to generate Lewis acid sites, to which the amine group of titanium precursor can be grafted via the lone electron pair of nitrogen atom for the preparation of core/titania shell nanostructure, as illustrated in Figure 2.15. This achieved hollow nanostructure of Fe_2O_3–TiO_2–PtO_x photocatalyst possesses two distinct cocatalysts which are deposited separately on two sides of its hollow surface. The distance of two cocatalysts (wall thickness of template) was 15-35 nm that strongly facilitated charge separation and so increased photocatalytic activity. One of the cocatalysts was created from metal clusters of the MOF after calcination, located inside the hollow structure and the other was made from metal doping (PtO_x) on the surface of this nanocomposite. Interestingly, the visible light absorption band edge was extended to 610 nm. Under visible light illumination and in the presence of lactic acid, this nanocomposite could produce 22 μmol h^{-1} hydrogen without any reduction in its activity even after 5 cycles. The total amount of H_2 after five cycles was 110 μmol h^{-1} under visible light irradiation. Although this amount of hydrogen production was not so much in comparison with other photocatalysts, but this approach may be used to develop other hollow structures with higher activity for hydrogen evolution in the visible light region.

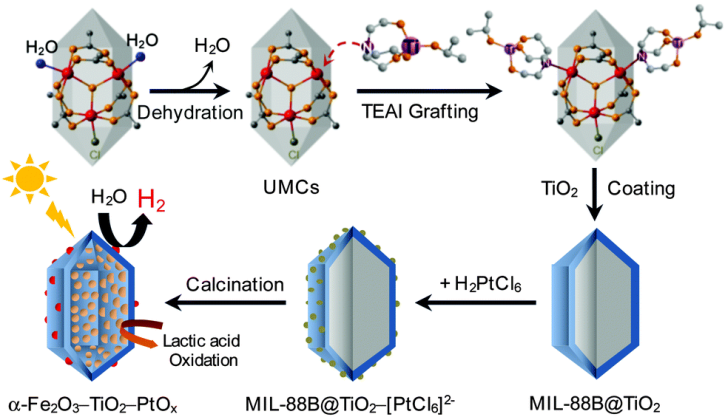

Figure 2.15. Schematic illustration of the formation of the hollow Fe_2O_3–TiO_2–PtO_x nanocomposite.[113]

In addition to metal oxides, scientists tried to mix diverse metal sulfides with titanium oxide due to their higher visible light absorption. CdS is the best metal sulfides to combine with TiO_2 because of its proper conduction band and higher efficiency. Due to the importance of this kind of nanocomposite, different compositions and morphologies will be discussed thoroughly in another

section (Section 2.4). Here, other metal sulfides composites with TiO_2 are explained in detail.[114-118] It was reported that the single nanoparticles of In_2S_3 or Pt/TiO_2 were not active in the H_2 formation under visible light irradiation. However, the combined $In_2S_3/Pt/TiO_2$ nanostructure produced H_2 under visible light at the rate of 135 μmol h^{-1} with the 1% quantum yield at $\lambda \geq 420$ nm.[115] In this nanocomposite, both Pt/TiO_2 and In_2S_3 nanoparticles were in close contact owing to embedding Pt/TiO_2 nanoparticles in the interstices of the In_2S_3. The optimum ratio of $In_2S_3/Pt/TiO_2$ was reported to be 3:2. Furthermore, Jang et al. synthesized a photocatalyst composite of titanium dioxide and $AgGaS_2$ with solid state reaction followed by sol-gel method.[118] In the presence of sulfide and sulfite solution and Pt as a cocatalyst, this composite showed a very good activity for hydrogen under visible light irradiation. Due to the conduction band structure, excited electrons can transfer from $AgGaS_2$ to TiO_2 and from there they can react with protons to produce hydrogen. The maximum quantum yield was 17.5% for the optimum ratio of 1:2 (TiO_2:$AgGaS_2$) and 1% Pt.

Some researchers synthesized nanocomposites of TiO_2 with different carbon based materials such as carbon coated metal, carbon quantum dots, carbon nanotube and graphene.[119-125] For example, Peng's group synthesized a novel nanocomposite of carbon coated Ni (denoted as Ni@C) and TiO_2.[123] This nanocomposite consists of nanorods with 10 nm in diameter and 40-100 nm in length. By using triethanolamine as a sacrificial reagent, this nanostructure could produce hydrogen under visible light irradiation. The highest activity was obtained when 5% of Ni was used in this nanocomposite (300 μmol h^{-1}). Furthermore, the apparent quantum yields are 12% and 7% for $\lambda > 420$ and $\lambda > 520$ nm, respectively. These yields were much higher than for neat Ni@C without TiO_2. Table 2.2 shows some nanocomposites of titanium dioxide as well as their activity under visible light irradiation.

A new ternary nanostructure of three different nanoparticles was synthesized in order to enhance H_2 production under visible light irradiation.[92] Firstly, the authors synthesized nanoparticles of Au with an average size of 40 nm. After this step, they grew TiO_2 nanocrystal as a shell structure on the Au nanoparticles via hydrothermal method according to previous researches.[126] Then, they deposited CdS nanoparticles on the surface of $Au@TiO_2$ core–shell nanostructures. This ternary nanocomposite showed considerable high activity for H_2 evolution rather than both binary

Table 2.2. Different nanocomposites of TiO2 active for hydrogen production (λ>420 nm).

Semiconductor 1	Semiconductor 2	Cocatalyst	Sacrificial reagent	Light Source	Hydrogen production ($\mu mol\ h^{-1}\ g^{-1}$)	Quantum yield (%)	Refs
TiO_2	Carbon coated Ni (Ni@C)	---	Triethanolamine	300 W Xe, $\lambda \geq 420$ nm	2000	12 at λ=420 nm 7 at λ=520 nm	[123]
TiO_2 nanosheet	Graphene	---	Methanol	350 W Xe	736	No data	[119]
TiO_2	In_2S_3	Pt	Na_2S/Na_2SO_3	300 W Xe, $\lambda \geq 420$ nm	1350	1 at λ=420 nm	[115]
TiO_2 mesocrystals	Au nanoparticles	Pt	Propanol	Xe light, λ > 460 nm	0.5	No data	[127]
N,S doped TiO_2	V_2O_5	Pt	Methanol	125 W Hg, $\lambda \geq 400$ nm	2966	No data	[105]
TiO_2	MOF MIL 101	Pt	Triethanolamine	450 W Xe, $\lambda \geq 420$ nm	1250	No data	[111]
TiO_2	MOF MIL 88	PtO_x	Lactic acid	300 W Xe, $\lambda \geq 420$ nm	1100	No data	[128]
TiO_2	$AgIn_5S_8$	Pt	Na_2S/Na_2SO_3	300 W Xe, $\lambda \geq 420$ nm	850	No data	[117]
mesoporous TiO_2	WS_2	Pt	Na_2S	350 W Xe, λ > 430 nm	200	No data	[129]
P25	Carbon quantum dot (CQD)	---	Methanol	500 W Halogen, λ > 450 nm	10	No data	[124]
$AgGaS_2$	TiO_2	Pt	Na_2S/Na_2SO_3	450 W Hg, $\lambda \geq 420$ nm	4200	17.5 at λ=420 nm	[118]
$CaIn_2O_4$	Fe-TiO_2	Pt	KI	300 W Xe, $\lambda \geq 420$ nm	280	No data	[107]
Graphene	Au–TiO_2	---	Methanol	3W LED, λ=420 nm	296	4.1 at λ=420 nm	[120]

nanostructures (CdS−TiO_2 or Au@TiO_2). This ternary design builds up a transfer path for the photoexcited electrons of CdS to the core Au particles via the TiO_2 nanocrystal bridge and thus effectively suppresses the electron-hole recombination on the CdS photocatalyst. However, this nanocomposite is very complicated to obtain and needs precise synthesis method for each step, which is one of its drawbacks in comparison with other binary nanocomposites for hydrogen production.

2.2.2 Various TiO_2 Phase junction

The most common used phase structures of TiO_2 as photocatalyst are anatase and rutile. Although anatase shows higher activity for hydrogen production in comparison with rutile, P25 Degussa TiO_2 (a mixed-phase of anatase and rutile) exhibits higher photocatalytic activity than pristine anatase or rutile.[130-133]

Zhang et al. synthesized TiO_2 particles with phase junction via calcination of anatase TiO_2. [134, 135] The phase transformation happened on the surface of skin of integrated anatase particles. The TiO_2 with mixed phase on the surface showed higher photocatalytic activity and the activity is closely related to the phase junction formed between two phases. Some researchers investigated the charge transportation between the two phases and found that electrons should move from anatase to rutile because of the higher conduction band edge of anatase compared to rutile.[136-138] Although the potential difference between phase junction of anatase and rutile is very small (~ 0.2 eV), it has been proved to be effective in enhancing hydrogen production from TiO_2.[66, 74]

2.3 Graphitic carbon nitride photocatalysts

Graphitic carbon nitride (g-C_3N_4) is a metal-free semiconductor that consists of s-triazine or tri-s-triazine units, as can be seen in Figure 2.16.[139, 140] These units are connected in two-dimensional graphite-like framework by amino groups in each layer and weak van der Waals forces between layers.[141] As a result, this polymeric semiconductor shows very high thermal and chemical stability. It can be synthesized by thermal condensation at high temperature (450-650ºC) form nitrogen-rich compounds such as: cyanamide, dicyanamide, melamine, thiourea and urea (Figure 2.17).[142-147] It should be mentioned that carbon nitride has several phase structures

such as α-C_3N_4, β-C_3N_4, cubic-C_3N_4, etc. with different band gaps. .[148] g-C_3N_4 possesses the lowest band gap of 2.7-2.8 eV among all of other carbon nitride crystal structures, which leads to absorb visible light energy of 450-460 nm.[149]

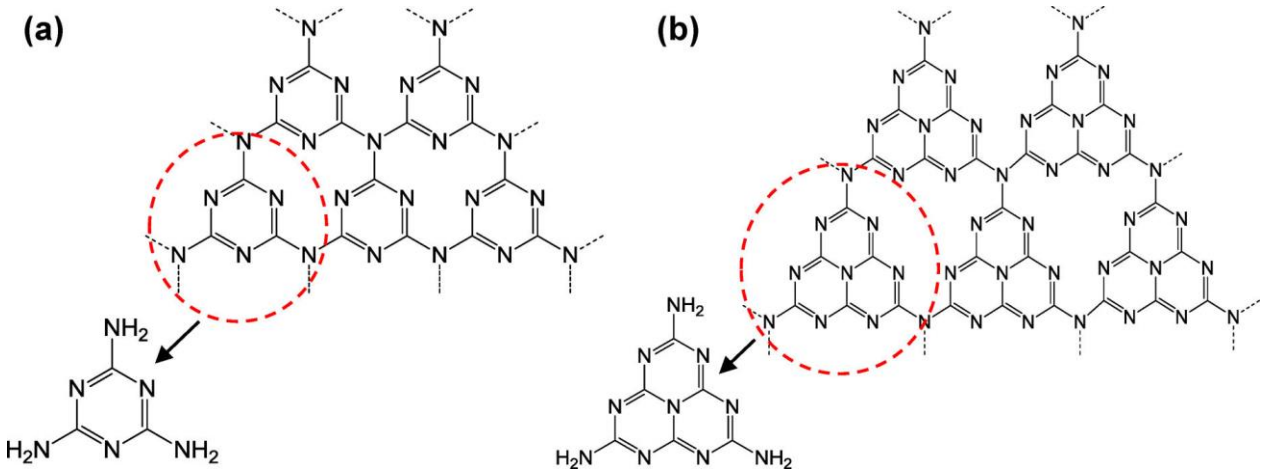

Figure 2.16. (a) Triazine and (b) tri-s-triazine (heptazine) structures of g-C_3N_4.[150]

In 2009, Wang et al. synthesized g-C_3N_4 from cyanamide by pyrolysis at high temperature (400-600 ºC).[151] They showed that this photocatalyst not only produces hydrogen under visible light irradiation from aqueous solution of triethanolamine (TEA), but also it had steady hydrogen production rate over 75 hr. In addition, with a help of TGA and XRD analyses of intermediate compound, they suggested a synthesis procedure, displays in Figure 2.18.[150] Briefly, the cyanamide molecules were converted to dicyandiamide and melamine at the temperature between 200-235 ºC. Simultaneously, ammonia was generated as a by-product of the reaction until all the melamine-based compounds were formed (T~335 ºC). Further increasing in temperature to 390 ºC, rearranged the melamine in order to generate tri-s-triazine units. Finally, between 500-520 ºC polymerization of building units produced g-C_3N_4. It remained perfectly stable until 600 ºC and above that it became unstable and vanished completely above 650 ºC.[150, 152]

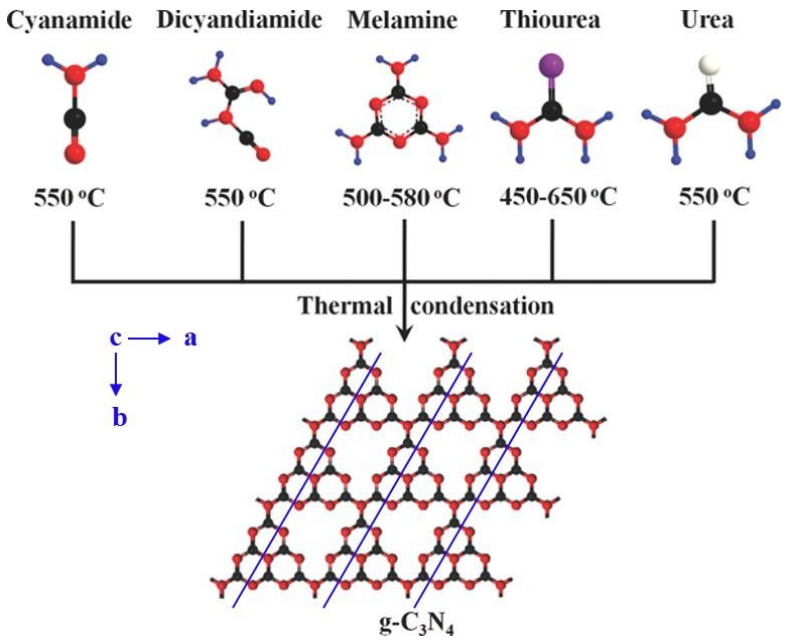

Figure 2.17. Various precursors of g-C_3N_4.[153]

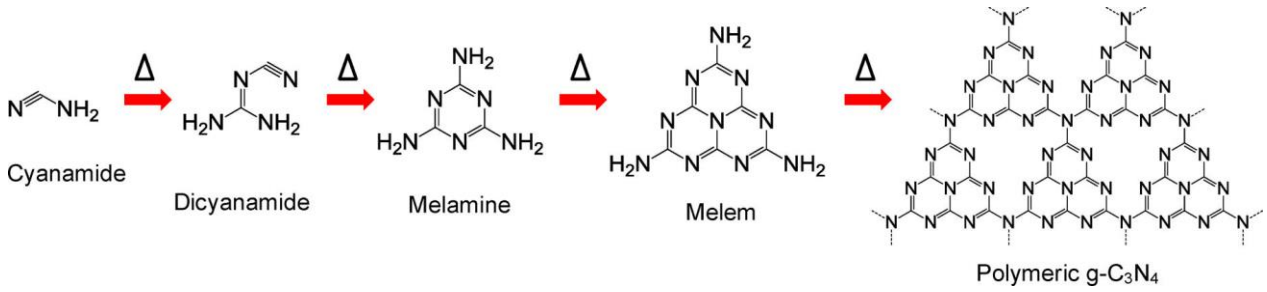

Figure 2.18. Synthesis procedure of g-C3N4 from cyanamide confirmed via TGA and XRD.[150]

Figure 2.19 displays various characterizations of bulk g-C_3N_4 synthesized from cyanamide at 550 ºC. It is clear from UV-visible spectrum that it has a capability of absorbing visible light up to 460 nm. The X-ray diffraction (XRD) curve for analysing the crystal structure of the g-C_3N_4 is shown in Figure 2.19-b. Obviously, it has two distinct peaks at about 13.0º and 27.4º. The former one corresponds to the (100) plane (d=0.681 nm) that is due to the in-plane structural packing motif of g-C_3N_4 (the lattice plane parallel to the c-axis as exhibited by solid line in Figure 2.17). The other peaks can be attributed to interlayer stacking of the long-range aromatic system, which is presented as (002) plane with a d-spacing of 0.326 nm.[154-156] It should be noted that within the

g-C_3N_4 layer, the carbon and nitrogen atoms are connected with covalent bonds, whereas weak van der Waals forces stack its layers together.[157]

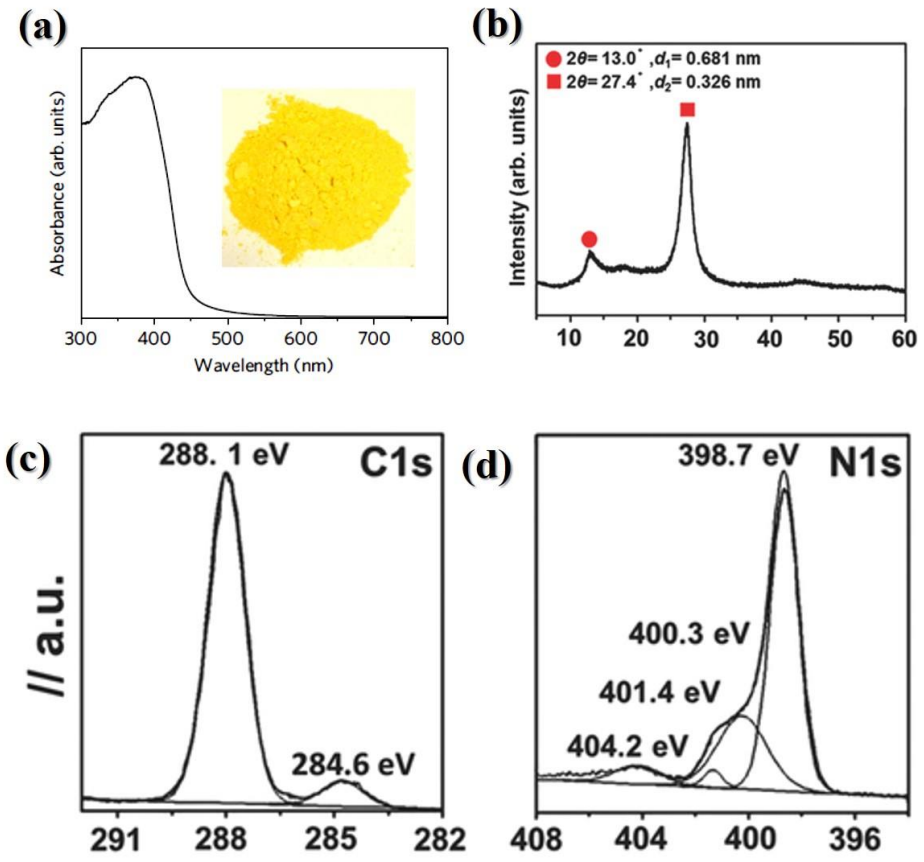

Figure 2.19. a) UV-visible diffuse reflectance spectrum, b) XRD pattern, High-resolution XPS spectra of c) C1s and d) N1s of bulk g-C_3N_4.[151, 153]

The elements status in g-C_3N_4 are examined by X-ray photoelectron spectroscopy (XPS) and are displayed in Figure 2.19-c,d. The C1s curve showed two main peaks at 284.6 and 288.1 eV, that can be related to sp^2-bonded carbon in C−C and N−C=N, respectively. The N1s spectrum can be deconvoluted into four main peaks corresponding to nitrogen status in various bond structures including: the sp^2-bonded in C−N=C (ca. 398.7 eV), tertiary in N− C_3 (ca. 400.3 eV), amino groups with hydrogen atom C−NH (ca. 401.4 eV) and a positive charge localisation in heptazine rings (ca. 404.2 eV). [153, 158, 159] The Bulk g-C_3N_4 has a potential to be one of the best photocatalyst for hydrogen production in visible light region. Nevertheless, it showed very little hydrogen production mainly due to its low specific surface area and high electron-holes recombination process. As a result, many researchers and scientists tried to enhance its hydrogen production by

various methods such as providing large surface area, making nanosheets of g-C_3N_4, utilizing various cocatalysts and creating heterojunctions with other semiconductors.

Due to the structure similarity of carbon bonds in carbon based nanostructures (nanotubes and graphene) with graphite carbon nitride, it is believed that these materials can mix together and as a result photocatalytic efficiency will increase substantially. [145, 147] For instance, g-C_3N_4 nanosheet was mixed with graphene in order to increase visible light photocatalytic activity for H_2 generation.[145] This metal-free nanocomposite could generate hydrogen from an aqueous solution of methanol under light illumination ($\lambda > 400$ nm). By using 1 wt% of graphene with Pt-loaded g-C_3N_4, the H_2 evolution rate was noticeably enhanced from 147 μmol h^{-1} g^{-1} to 451 μmol h^{-1} g^{-1}. Another group tried to modify g-C_3N_4 by introducing carbon nanotubes into its structure.[147] Despite the fact that the new composite and pure g-C_3N_4 are very similar in their properties, the new photocatalyst possessed higher activity (around 2.5 times) than the other one. With optimal amount of carbon nanotubes (2 wt%), it produced 394 μmol h^{-1} g^{-1} hydrogen under visible light illumination because of increasing the lifetime of excited electron and holes and prevent them to recombine together.

Furthermore, other semiconductors can be combined with g-C_3N_4 in order to prevent charge recombination. [143, 144, 160-165] For example, Chai et al. generated a nanocomposite consisting of porous g-C_3N_4 with TiO_2 nanoparticles.[143] According to the close interaction between these nanomaterials, when this nanocomposite was improved by Pt metal as a cocatalyst, it showed hydrogen evolution under visible light illumination ($\lambda > 420$ nm). The maximum hydrogen evolution (178 μmol h^{-1}) was achieved when the mass ratio of g-C_3N_4 and TiO_2 was 70 to 30. Kang et al. synthesized a composite of graphitic carbon nitride and Rh-doped $SrTiO_3$.[144] With help of Pt as a cocatalyst, this photocatalyst could produce hydrogen from aqueous solution of methanol at 410 nm with a quantum yield of 5.5%. Doping Rh into the structure of $SrTiO_3$ provides the donor level in band gap region of $SrTiO_3$:Rh. As a result, the excited holes can easily transfer from $SrTiO_3$:Rh semiconductor to carbon nitride and the excited electrons move from the conduction band of g-C_3N_4 to $SrTiO_3$:Rh. This leads to have high charge separation and higher hydrogen production (2223 μmol h^{-1} g^{-1}) in comparison with each of the semiconductors alone. Table 2.3 shows various heterojunctions of g-C_3N_4 and semiconductors that could improve hydrogen production under visible light.

Another effective method to enhance g-C_3N_4 photoactivity is to increase its specific surface area, which is less than 10 m^2 g^{-1} for the bulk material.[166] Due to its graphite-like layered structure, various methods were suggested to synthesize multilayer and monolayer nanosheets of g-C_3N_4.[154, 167-169] Reducing the thickness of nanosheets causes its band gap to increase due to quantum confinement effect.[154] In thermal exfoliation technique, increasing the time of synthesis up to 4-6 h or recalcining the bulk material again in controlled conditions (low ramping rate, static air or inert gas), led to have nanosheets of g-C_3N_4. As shown in Figure 2.20, the reaction time considerably affects the thickness of g-C_3N_4.[168, 170] Other groups used liquid exfoliation methods to obtain the nanosheets.[154, 169, 171] They usually used a mixture of water and another solvent with appropriate surface energy such as ethanol, isopropanol or dimethyl formamide. Then, ultrasonic bath was used more than 10 hr, in order to transmit require energy for breaking the van der Waals forces between the layers. After this step was completed, a highly uniform and stable suspension of nanosheets of g-C_3N_4 was obtained, as depicted in Figure 2.21. This method was widely utilized for fabricating nanosheets of g-C_3N_4 because of its facile and convenient process.

Some researchers using hard and soft templates in order to produce mesoporous g-C_3N_4 with high specific surface area. For instance, He et al. synthesized mesoporous sucrose-mediated g-C_3N_4 by using thermal condensation of sucrose and melamine.[172] Firstly, they dissolved sucrose in an ethanol aqueous solution, then under continuous stirring, melamine was added. After drying in water bath, the obtained mixture was heated to 600 ºC for 2 hr. During calcination step, oxidation and decomposition of sucrose formed mesoporous g-C_3N_4, as demonstrated in Figure 2.22. As a result, the specific surface area was enhanced to 128 m^2 g^{-1} from 18.6 m^2 g^{-1} of bulk g-C_3N_4.

Table 2.3. Different nanocomposite of graphitic carbon nitride.

Semiconductor 1	Semiconductor 2	Cocatalyst	Sacrificial reagent	Light Source	Hydrogen production ($\mu mol\ h^{-1}\ g^{-1}$)	Quantum yield (%)	Refs
layered g-C_3N_4 sheets	graphitized polyacrylonitrile	Pt	Triethanolamine	150 W Halogen, $\lambda \geq 420$ nm	370	No data	[173]
g-C_3N_4	Nickel sulfide (NiS)	---	Triethanolamine	300 W Xe, $\lambda \geq 420$ nm	447.7	No data	[160]
g-C_3N_4	zinc phthalocyanine	Pt	Ascorbic acid	350 W Xe, $\lambda \geq 420$ nm	12500	1.85 at $\lambda = 700$ nm	[174]
g-C_3N_4	C/N co-doped TiO2	Ag	Methanol	300 W Xe, $\lambda \geq 420$ nm	96	No data	[161]
g-C_3N_4	PEDOT	Pt	Triethanolamine	300 W Xe, $\lambda \geq 420$ nm	327	No data	[146]
g-C_3N_4	WO_3	Pt	Triethanolamine	300 W Xe, $\lambda \geq 420$ nm	110	0.9 at $\lambda = 420$ nm	[162]
g-C_3N_4	carbon nanotubes	Pt	Triethanolamine	350 W Xe, $\lambda \geq 420$nm	394	No data	[147]
g-C_3N_4	$ZnFe_2O_4$	Pt	Triethanolamine	300 W Xe, $\lambda \geq 420$ nm	200.77	No data	[163]
g-C_3N_4	Ag_2S	---	Methanol	300 W Xe, $\lambda \geq 420$ nm	200	No data	[164]

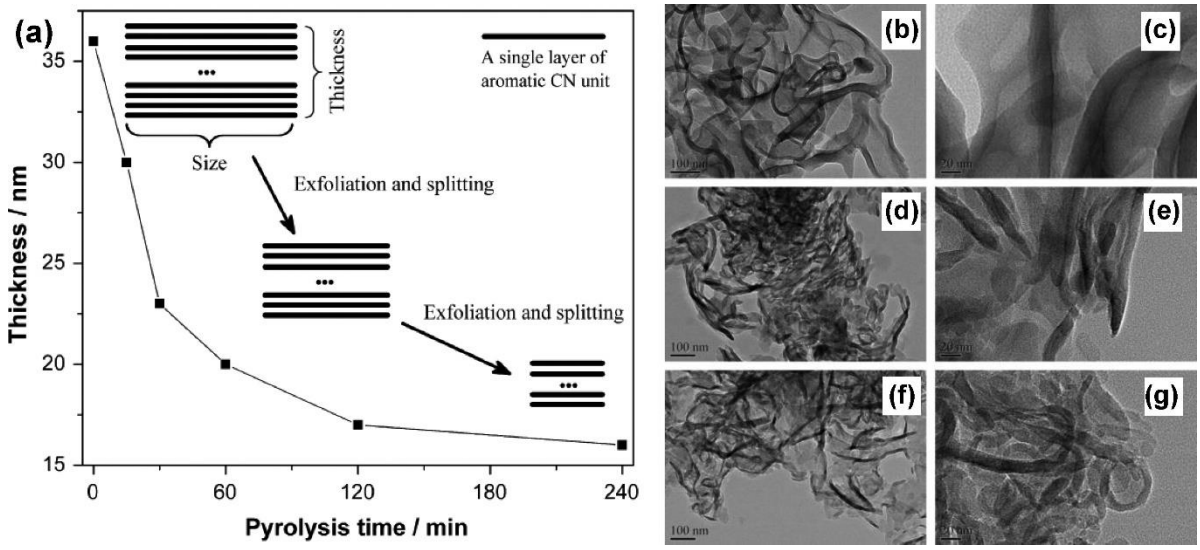

Figure 2.20. (a) Relationship between the pyrolysis duration and layer thickness of g-C_3N_4 and the diagram for the layer-by-layer exfoliation and splitting mechanism of g-C_3N_4 with decreased thickness and size. (b–g) TEM images of g-C_3N_4synthesized at 550 °C for (b–c) 0 min, (d–e) 60 min, and (f–g) 240 min, excluding the heating-up time.[150, 170]

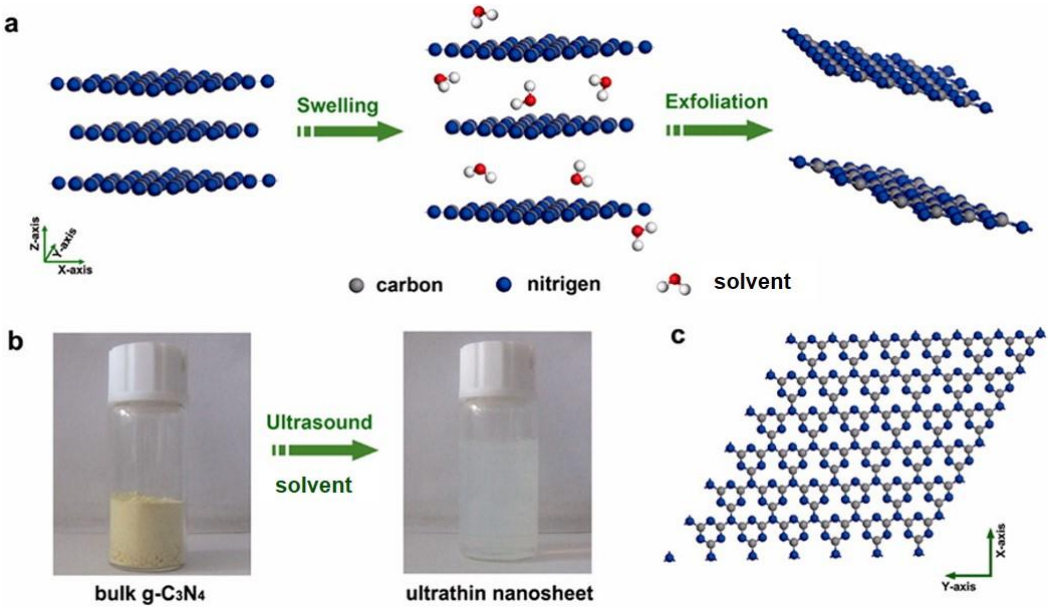

Figure 2.21. (a) Schematic illustration of liquid-exfoliation process from bulk g-C_3N_4 to ultrathin nanosheets. (b) Photograph of bulk g-C_3N_4 and suspension of ultrathin g-C_3N_4 nanosheets. (c) A theoretically perfect crystal structure of the g-C_3N_4 projected along the z-axis.[175]

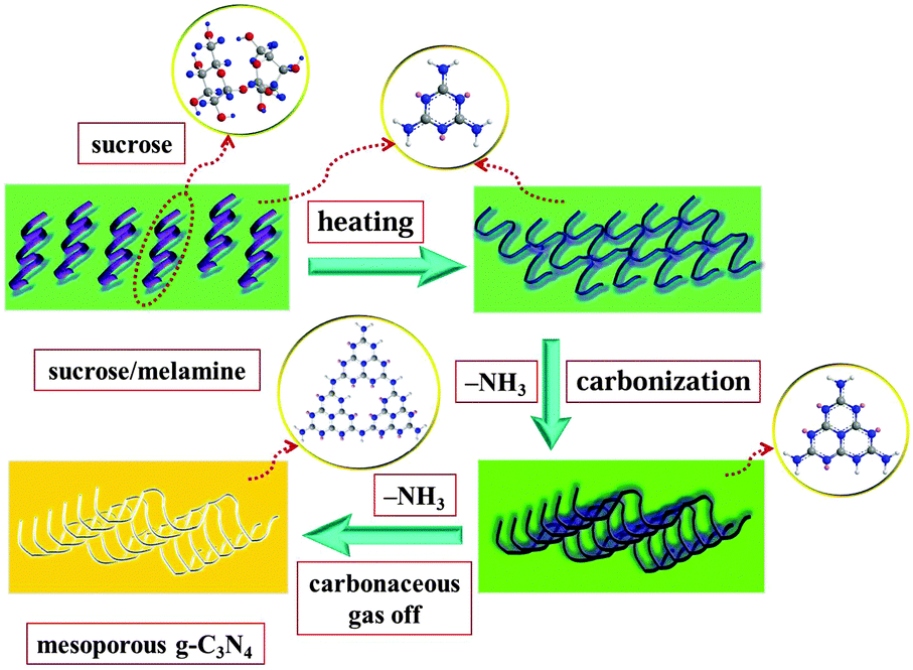

Figure 2.22. Schematic illustration for the formation of mesoporous sucrose-mediated g-C_3N_4.[172]

Another group created honeycomb-like g-C_3N_4 with one-step thermal polymerization of urea in the presence of water at 450 ºC.[176] As illustrated in Figure 2.23, during g-C_3N_4 synthesis procedure, large numbers of soft bubbles from the NH_3 and CO_2 gases were formed, which resulted in having bubble-like structure of g-C_3N_4. Later, these bubbles burst, leaving behind honeycomb nanosheets of g-C_3N_4. This nanostructure not only increases specific surface area, but also helps having multiple light reflections in the porous material as well as increasing reactant diffusion throughout the nanosheets (as demonstrated in Figure 2.23-Right).

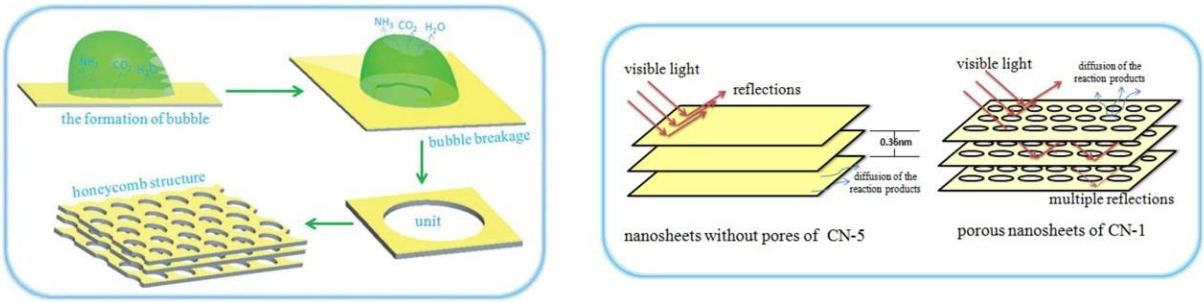

Figure 2.23. (Left) Formation mechanism of the honeycomb-like morphology of g-C_3N_4. (Right) Schematic illustration of the differences between g-C_3N_4 nanosheets with and without pores.[176]

The reaction atmosphere significantly affected the photocatalytic activity of g-C_3N_4 through generating structural defects, carbon and nitrogen vacancies as well as inducing disordered structures. The structural defects are crucial for heterogeneous catalysis because they provide active sites for reactant molecules. In addition, the defects have impacts on electronic band structures and they can introduce additional energy levels between the valence band and the conduction band.[177-179] The defects and lattice disorders can provide band tail states, which are midgap states for excited electron-hole pairs.[180] Thus, the obtained semiconductor can absorb more visible light energy and so it can produce more hydrogen.[181, 182] Furthermore, these defects generate more trapping sites on the surface of semiconductors, which enhance lifetime of excited charges by slowing down the recombination procedure.[183]

Niu et al. synthesized g-C_3N_4 with nitrogen vacancies via modulating the synthesis temperature in static air.[156] These defects left extra electrons in the structure of carbon nitride resulting having nitrogen vancancy-related C^{3+} state in the band gap. Thus, the band gap of the obtained material decreases from 2.74 to 2.66 eV. Nitrogen vacancies can also be obtained by changing the reaction atmosphere to H_2 gas.[184] They observed that H_2 diffusion through the surface to the bulk of g-C_3N_4 in the space originated from the periodic layer stacking along the c-axis of melon (Figure 2.17), can make homogeneous self-modification in layered structure (Figure 2.24)

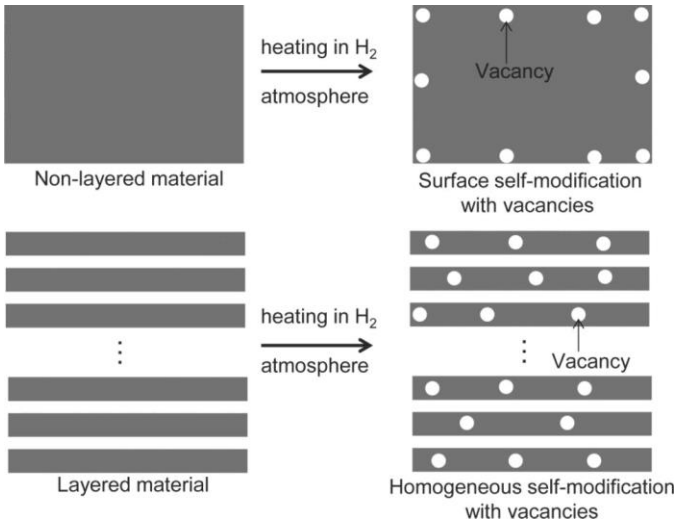

Figure 2.24. Schematic illustration of surface self-modification with vacancies in a nonlayered material and homogeneous self-modification with vacancies in a layered material upon thermal treatment under H_2 environment.[184]

2.4 Zinc cadmium sulfide photocatalyst

Cadmium sulfide (CdS) is one of the best semiconductors for photocatalytic hydrogen production because of its narrow band gap and conduction edge-band position. In other words, it can absorb visible light with long wavelength and also it can reduce protons to hydrogen. However, this photocatalyst has two main disadvantages which are: (1) due to its small band gap, the recombination process of photoexcited electrons and holes is very easy; (2) this semiconductor is unstable under light irradiation and it is effortlessly corroded by excited holes.[185] For these reasons, CdS needs to be combined with other semiconductors in order to overcome its drawbacks.

It has two crystal forms: the hexagonal Wurtzite (found in the mineral Greenokite) and the cubic blend structure (found in the mineral Hawleyite).[186] Although in both forms cadmium and sulfur atoms are in four coordination, the hexagonal crystal structure is more stable than the cubic one.[187] This semiconductor is a n-type 2.42 eV that can be excited via visible light irradiation. It should be noted that its photocatalytic properties and activity are affected by the particle size and the morphology.[185, 188, 189]

Due to a highly visible light absorption of CdS (2.42 eV), scientists tried to enhance photocatalytic efficiencies of CdS with modifying nanostructures of this semiconductor. Nanostructure of CdS provided more active sites for water splitting reaction and so increase its photocatalytic activity.[190] Another technique is preparing CdS in nano-porous structures that can raise the quantum yield up to 60% in the presence of Na_2SO_3 and Na_2S as sacrificial agents ($\lambda \geq 420$ nm).[191] The main reasons for this development in quantum yield are effective charge separation, fast movements of charge carriers, and quick chemical reaction at the interface of CdS nanostructure. Combing CdS nanoparticles with another semiconductor is another way to enhance its photocatalytic efficiency.[192]

Although metal oxides are usually possessing wide band gap and cannot absorb long wavelength of sunlight spectrum, they are very stable during photocatalytic processes. Therefore, some studies were done in order to mix these semiconductors together and obtained more efficient photocatalysts.[59, 193-203] For instance, Wang and co-workers prepared core-shell nanostructures from ZnO and CdS.[193] This nanocomposite was able to split water to produce H_2 with sacrificial reagents. Interestingly, loading RuO_2 cocatalyst showed more activity rather than Pt metal. In addition, the ratio of ZnO to CdS in $(ZnO)_{1-x}(CdS)_x$, strongly affected its photocatalytic

efficiency and it slightly dropped by raising CdS molar ratio. The highest H_2 evolution is 2.96 mmol h^{-1} g^{-1} by x = 0.2, which is 34.4 times and 7.8 times higher than that of ZnO nanorods (prepared by the hydrothermal route) and CdS (prepared by the solid-state route), respectively. As mentioned before, RuO_2 has a great impact on photocatalytic activity resulted in a sudden increase by around 200%. This nanocomposite could constantly produce H_2 for more than 30 h. Hou et al. synthesized a nanocomposite of CdS (2.45 eV) and TaON (2.5 eV) in a core-shell structure.[195] They deposited TaON on the core of CdS and used Pt as a cocatalyst. Due to the band edge positions of these semiconductors, electrons migrate from CdS to TaON and holes can move from TaON to CdS. Although hydrogen evolution rates for pure CdS and TaON were 13.5 and 9 µmol h^{-1}, respectively, this nanocomposite could evolve 306 µmol h^{-1} hydrogen using a sacrificial reagent. Moreover, combining this nanostructure with 1wt% graphene oxide led to produce more than two times higher hydrogens than the previous one with a 31% quantum yield under visible light irradiation. Nonetheless, they didn't examine the stability of this nanocomposite for multiple cycles in longer runtime. Because one of the purpose of combining CdS with other materials is to enhance its stability during reaction time. Usually the photocatalyst should run 3-4 cycles of 3-5 hr of hydrogen production in order to observe its stability under light illumination.

In addition to binary metal oxides, some researchers made a nanocomposite of CdS and ternary metal oxides.[204-207],[110,111] In these nanostructures, generated holes can transfer from CdS to metal oxides, due to their valence band positions, and photoexcited electrons remain in the conduction band of CdS and reduce protons to hydrogen. These charge carriers' movements are completely different than in other nanocomposites. Usually electrons transfer to other semiconductors from CdS but in this case holes transfer and so both charge recombination and photocorrosion are avoided. However, it should be noted that the synthesis procedure of these ternary nanocomposites is usually complicated and needs careful attention in order to obtain desire nanostructure.

Furthermore, CdS can be combined with other metal sulfides in various morphologies such as nanocrystals[208], nanowires[209], nano-layers[210] in order to enhance its efficiency. Among all metal sulfides, ZnS attracts more attention due to its high ability to form solid solution with CdS which results in higher charge separation and more quantum efficiency.[211-218] For example, a solid solution of $(Zn_{0.95}Cu_{0.05})_{1-x}Cd_xS$ was examined with various ratios of Cd for H_2 production

under visible light and in the presence of SO_3^{2-} and S_2^{2-}.[211] This solid solution consisted of nanocrystals of about 2-5 nm and had a band gap of 2.0 eV. This nanostructure showed 508 μmol h^{-1} without any cocatalyst and possesses a quantum yield of 15.7% under visible light when x equal to 0.33. However, by depositing 0.75% Pt, its activity enhanced significantly and hydrogen production and quantum yield reached to 1.09 mmol h^{-1} and 31.8%, respectively. Moreover, this nanocomposite was stable after 3 cycles 12 h. Zhang and al. synthesized a nanocrystal of solid solution ZnS-CdS that was involved in H_2 evolution at 420 nm.[213] They used MoS_2 compound as a cocatalysts and reported that with 0.2 wt% of this cocatalysts, the hydrogen formation was 36 times higher than CdS with noble metals as cocatalysts.[219, 220] Moreover, Liu et al. showed that nano-twin structures of $Cd_{1-x}Zn_xS$ solid solution could produce hydrogen from water without noble metals. Its apparent quantum yield was reported to be 43% at 425 nm in the presence of sacrificial reagents.[214] Another type of nanocomposites of ZnS and CdS is the physical mixture of their nanoparticles without making a solid solution phase. Shen et al. improved nanocrystals of ZnS/CdS (5-10 nm) with In_2S_3 without any surfactant or supports at room temperature and normal pressure.[208] These microspheres could produce hydrogen from aqueous solution of sulfide and sulfite ions with no cocatalysts and it was reported that the quantum yield achieved to 40.9 % at $\lambda \geq 420$nm. The optimum ratio of CdS is 75%, which can produce 8.1 mmol h^{-1} g^{-1} hydrogen. Despite the fact that this nanocomposite showed a very high hydrogen evolution, no detailed observation was done to examine its stability during hydrogen production, which should be considered in further studies.

In addition to solid solution, CdS can mix with other metal sulfides in order to increase hydrogen production under visible light irradiation.[209, 221-223] For instance, TiS_2 and TaS_2 are both semiconductors with small band gap less than 1 eV. A nano-layer combination of one of these two semiconductors with nanoparticles of CdS resulted in high efficient photocatalysts for H_2 evolution from an aqueous solution of benzyl alcohol.[210] The nanocomposite of TiS_2 and CdS could generate 1000 μmol $h^{-1}g^{-1}$ hydrogen, whereas the other one (TaS_2 and CdS) showed 2.3 times higher hydrogen evolution (2320 μmol $h^{-1}g^{-1}$) under visible light irradiation. The reason for this phenomenon was explained by the metallic nature of few-layer TaS_2. In another study, Zhang et al. deposited NiS nanoparticles on the CdS surface with the help of hydrothermal route.[221] They reported that the nanocomposite with 1.2% of NiS had the highest activity and quantum yield. Its quantum efficiency under visible light irradiation ($\lambda > 420$nm) was 51.3 %, which was the highest

photocatalyst activity without noble metal cocatalyst. In addition, its H_2 evolution rate was 2.18 mmol h^{-1} which was 35 times higher than that of alone CdS. Hou et al. decoreated $CdLa_2S_4$ microspheres with CdS nanocrystals by a hydrothermal procedure in order to enhance hydrogen generation.[218] Due to the intimate contact of these nanoparticles and also high dispersion of CdS nanocrystals, this nanocomposite exhibited a significant quantum yield of 54% under visible light region corresponding to 2250 μmol h^{-1} g^{-1}, which was 9 times higher than the pristine $CdLa_2S_4$.

Carbon nanotubes is one of the most famous building block for synthesizing nanostructures that can be combine with diverse semiconductors particularly CdS in order to enhance charge separation step, as demonstrated in Figure 2.25.[224-229] Furthermore, graphene nanosheet has some special properties such as high surface area, high charge carrier mobility (due to its two-dimensional sp^2-hybridized), and good mechanical stability.[230] The intimate contact between CdS and graphene can enhance the migration of photoexcited electrons and surpass the recombination process more efficiently. In principle, photoexcited electrons move from the conduction band of the CdS to graphene and according to great mobility of electrons on the graphene sheets, the recombination process is partially prevented.[227, 229, 231-237] For instance, Li et al. synthesized CdS nanoparticles of about 3 nm in autoclave and they dispersed them on graphene nanosheet completely.[237] This nanocomposite, which had 1 wt% graphene and 0.5 wt% Pt, showed 1.12 mmol h^{-1} hydrogen evolution from a solution of lactic acid. This rate of hydrogen production was around 5 times higher than pristine CdS and the apparent quantum efficiency was reported 22.5% at $\lambda \geq 420$ nm.

There have been different methods to synthesize graphene-based photocatalysts, but the simplest and most direct technique is to mix graphene with target semiconductors.[238-240] The other popular method to provide nanocomposites of various semiconductors with graphene is in situ growth method in which graphene oxide (GO)[195, 237, 241] or reduced graphene oxide (RGO)[242-250] is chosen as starting materials.[251] Nanocrystals of CdS or other semiconductors can grow on the surface of graphene nanosheet via oxygen-containing functional groups which act as nucleation sites.[252] The structure and electrical properties of RGO as well as the location of the conduction band of CdS and RGO lead the photoexcited electrons transfer from CdS to RGO and from there, they can reduce hydrogen atoms (Figure 2.26). Table 2.4 summarized hydrogen

production of different nanocomposite of CdS under visible light irradiation with their quantum yields.

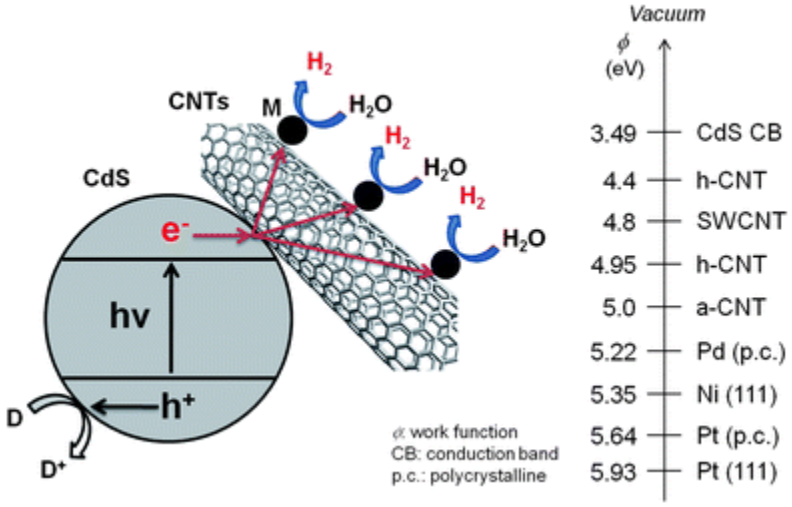

Figure 2.25. Illustration of photocatalytic hydrogen production in CdS/CNT/M suspensions under light irradiation. M and D refer to metal catalyst and electron donor, respectively. On the right-hand side, the reported work functions of selected materials are given. [225]

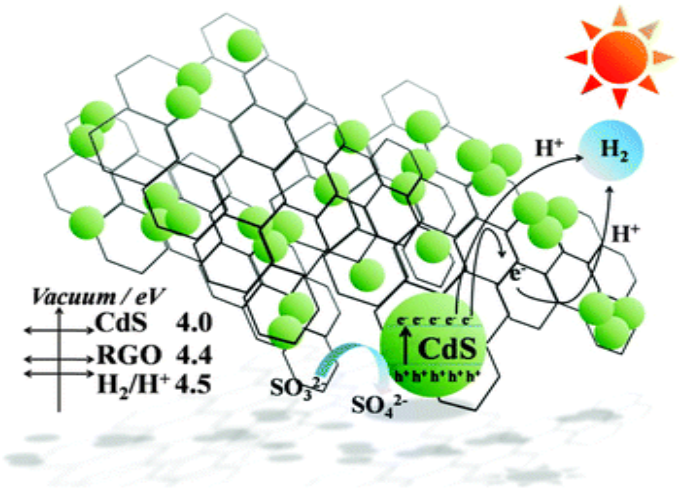

Figure 2.26. Schematic diagram of the proposed mechanism for photocatalytic H_2 production over RGO–CdS.[250]

Table 2.4. Various nanocomposites of CdS active under visible light illumination.

Semiconductor 1	Semiconductor 2	Cocatalyst	Sacrificial reagent	Light Source	Hydrogen production ($\mu mol\ h^{-1}\ g^{-1}$)	Quantum yield (%)	Refs
CdS	SrS	---	Na_2S/Na_2SO_3	300 W Xe, $\lambda > 400$ nm	246	10 at $\lambda = 420$ nm	[209]
CdS	ZnCu	---	Na_2S/Na_2SO_3	300 W Halogen, $\lambda \geq 420$ nm	1693	15.7 at $\lambda =$ 420 nm	[213]
CdS	ZnCu	Pt	Na_2S/Na_2SO_3		3633	31.8 at $\lambda =$ 420 nm	[213]
CdS	CuIn	---	Na_2S/Na_2SO_3	300 W Xe, $\lambda \geq 420$ nm	649.9	2.14 at $\lambda =$ 420 nm	[212]
CdS	CuIn	Pt	Na_2S/Na_2SO_3		2456	26.5 at $\lambda =$ 420 nm	[212]
CdS	ZnO	Pt	Na_2S/Na_2SO_3	300 W Xe	2960	No data	[193]
CdS nanorods	CdSe	Pt	2-propanol	300 W Xe	40500	20 at $\lambda = 450$ nm	[253]
CdS	Ni/NiO/$KNbO_3$	---	Isopropanol	500 W Hg−Xe, $\lambda > 400$ nm	203.5	8.8 at $\lambda >$ 400 nm	[207]
CdS	Ni/NiO/$KNbO_3$	---	Isopropanol	500 W Hg−Xe, $\lambda > 400$ nm	150	4.4 at $\lambda >$ 400 nm	[206]
CdS	$LaMnO_3$	---	Na_2S/Na_2SO_3	300 W Xe, $\lambda \geq 420$ nm	595	No data	[205], [254]
$Cd_{0.8}Zn_{0.2}S$	ZnO	Pt	benzyl alcohol	450 W Xe,	36500	50.4 at $\lambda =$ 400 nm	[217]
CdS nanorods	NiS	---	Na_2S/Na_2SO_3	300 W Xe, $\lambda \geq 420$ nm	1131	6.1 at $\lambda =$ 420 nm	[255]

Table 2.4 Continue.

Semiconductor 1	Semiconductor 2	Cocatalyst	Sacrificial reagent	Light Source	Hydrogen production ($\mu mol\ h^{-1}\ g^{-1}$)	Quantum yield (%)	Refs
$Cd_{0.1}Zn_{0.9}S$	Multi-walled carbon nanotube	---	Na_2S/Na_2SO_3	300 W Xe, $\lambda \geq 420$ nm	1563.2	7.9 at λ = 420 nm	[226]
CdS	CeO_2	---	Na_2S/Na_2SO_3	300 W Xe	223	No data	[197]
CdS	Multi-walled carbon nanotubes	Pt	Na_2S/Na_2SO_3	300 W Halogen, $\lambda > 400$ nm	825	No data	[225]
CdS	MWCNTs	---	Na_2S/Na_2SO_3	300 W Xe, $\lambda \geq 420$nm	4977	2.16 at λ = 420 nm	[224]
CdS	ZnS	Ru	Formic acid	300 W Xe, $\lambda \geq 420$nm	6000	20 at λ = 400 nm	[256]
In_2S_3	CdS-ZnS	---	Na_2S/Na_2SO_3	300 W Xe, $\lambda > 400$nm	8100	40.9 at λ = 420 nm	[208]
$CdLa_2S_4$ microspheres	CdS nanocrystal	Pt	Na_2S/Na_2SO_3	300 W Xe, $\lambda \geq 420$nm	2250	54 at λ = 420 nm	[218]
ZnS	CdS	---	Na_2S/Na_2SO_3	500 W Halogen	46	No data	[216]
TaON	CdS	Pt	Na_2S/Na_2SO_3	300 W Xe, $\lambda \geq 420$nm	1530	15 at λ = 400 nm	[195]
Graphene oxide	CdS@TaON				3165	31 at λ = 420 nm	
ZnO	CdS	---	Na_2S/Na_2SO_3	500 W Xe, $\lambda > 400$nm	851	3 at λ = 420 nm	[198]
$CdOW_4$	CdS	---	Na_2S/Na_2SO_3	500 W Xe	90.25	No data	[204]
reduced graphene oxide	CdS	MoS_2	lactic acid	350 W Xe, $\lambda \geq 420$nm	1980	9.8 at λ = 420 nm	[246]

Table 2.4 Continue.

Semiconductor 1	Semiconductor 2	Cocatalyst	Sacrificial reagent	Light Source	Hydrogen production ($\mu mol\ h^{-1}\ g^{-1}$)	Quantum yield (%)	Refs
nanosized MoS_2/graphene hybrid	CdS	MoS_2	lactic acid	300 W Xe, $\lambda \geq 420nm$	9000	28.1 at λ = 420 nm	[235]
reduced graphene oxide	UiO-66 and CdS	Pt	Na_2S/Na_2SO_3	300 W Xe, λ >400 nm	2100	No data	[245]
vermiculite	CdS quantum dot		Na_2S/Na_2SO_3	300 W Xe, $\lambda \geq 420nm$	920	17.7 at λ = 420 nm	[257]
SiC	CdS particles	Pt	Na_2S/Na_2SO_3	300 W Xe, $\lambda \geq 420nm$	555	0.2 at λ = 420 nm	[258]
framework of structured WO3	orderly depositing Au and CdS	---	Na_2S/Na_2SO_3	300 W Xe, $\lambda \geq 420nm$	1730	No data	[199]
ZSM-5 type metalosilicates	CdS nanoparticles	---	Na_2S/Na_2SO_3	500 W Osram, $\lambda \geq 420nm$	11000	65.62 at λ = 420 nm	[259]
γ-TaON hollow spheres	CdS nanoparticles	MoS_2	Na_2S/Na_2SO_3	300 W Xe, $\lambda \geq 420nm$	3142.5	No data	[200]
ZnO core/shell nanofibers	CdS	---	Na_2S/Na_2SO_3	500 W Xe, $\lambda \geq 420nm$	354	No data	[201]
$ZnIn_2S_4$ heterostructures coupled with graphene	CdS quantum dots	Pt	Na_2S/Na_2SO_3	300 W Xe, $\lambda \geq 420nm$	27000	56 at λ = 420 nm	[236]
Carbon nanotube	$Zn_xCd_{1-x}S$	---	Na_2S/Na_2SO_3	500 W Xe	6030	No data	[227]
Carbon nanotube	CdS	NiS	Na_2S/Na_2SO_3	350 W Xe, $\lambda \geq 420nm$	12130	No data	[228]

Table 2.4. Continue.

Semiconductor 1	Semiconductor 2	Cocatalyst	Sacrificial reagent	Light Source	Hydrogen production ($\mu mol\ h^{-1}\ g^{-1}$)	Quantum yield (%)	Refs
reduced graphene oxide	$Cu_{0.02}In_{0.3}ZnS_{1.47}$	Pt	Na_2S/Na_2SO_3	800 W Xe–Hg, $\lambda \geq 420$ nm	3800	No data	[244]
Ti-MCM-48 mesoporous	CdS	RuO_2	Ethanol	300 W Xe, $\lambda >$ 400nm	2730	36.3 at $\lambda =$ 400 nm	[260]
MoO_3	CdS	---	Na_2S/Na_2SO_3	300 W Xe, $\lambda \geq$ 420nm	5250	28.86 at $\lambda =$ 420 nm	[202]
cubic MCM-48 mesoporous	CdS	Pt	Ethanol	300 W Xe, $\lambda >$ 400nm	1810	16.6 at $\lambda =$ 400 nm	[261]
Reduced graphene oxide Ga_2O_3	CdS quantum dots	---	Na_2S/Na_2SO_3 Lactic acid	300 W Xe, $\lambda \geq$ 420nm 300 W Xe, $\lambda \geq$ 420nm	4200	10.4 at $\lambda =$ 420 nm	[243]
Reduced graphene oxide Ga_2O_3	CdS quantum dots	Pt	Na_2S/Na_2SO_3 Lactic acid		9052	43.6 at $\lambda =$ 460 nm	[203]
In_2O_3 TiS2	CdS	---	Benzyl alcohol	450 W Xe, $\lambda >$ 400nm	9382	45.3 at $\lambda =$ 460 nm	[210]

Table 2.4. Continue.

Semiconductor 1	Semiconductor 2	Cocatalyst	Sacrificial reagent	Light Source	Hydrogen production ($\mu mol\ h^{-1}\ g^{-1}$)	Quantum yield (%)	Refs
MCM-41	CdS	---	Triethanolamine	300 W Xe, $\lambda \geq$ 430nm	47.1	No data	[262]
$AgGaS_2$	CdS	Pt	Na_2S/Na_2SO_3	450 W Hg, $\lambda \geq$ 420 nm	4730	19.7at λ = 420 nm	[263]
reduced graphene oxide	CdS	$Ni(OH)_2$	Na_2S/Na_2SO_3	300 W Xe, $\lambda \geq$ 420nm	4731	No data	[242]
graphene oxide	CdS	---	Na_2S/Na_2SO_3	300 W Xe, $\lambda \geq$ 420nm	3410	4.8at λ = 420 nm	[241]
graphene oxide	CdS clusters	Pt	lactic acid	350 W Xe, $\lambda \geq$ 420nm	5600	22.5at λ = 420 nm	[237]
N-graphene	CdS	---	Na_2S/Na_2SO_3	300 W Xe, $\lambda \geq$ 420nm	1050	No data	[234]
g-C_3N_4	CdS quantum dots	Pt	Methanol	300 W Xe, $\lambda \geq$ 420nm	348	No data	[264]

Zinc sulfide (ZnS) is a semiconductor with a direct band gap of 3.12-3.70 eV that can be found in nature as the mineral sphalerite[265, 266] Generally, Zn and S atoms are located in tetrahedral coordination in order to create two crystal structures for ZnS. The more stable cubic form is known as sphalerite or zinc blende and another one has hexagonal structure and is called as mineral Wurtzite.[187] It is evident that this semiconductor cannot generate hydrogen under visible light illumination due to its large band gap.

Recently, a group of researchers created a nanocomposite of ZnO/CdS in a core/shell structure.[267] They used a simple solvothermal method to synthesized CdS nanorods after a shell of ZnO was deposited on their surface via a solution deposition technique. They observed that it showed a very high activity for hydrogen evolution under visible light irradiation and they reported to obtain 44% quantum yield at 420nm. The reasons to have such a high photocatalytic activity are as follow: (1) the transparency of ZnO thin shell allowed CdS to absorb all visible light energy; (2) the photoexcited electrons can transfer to ZnO conduction band from CdS because of the favorable energy band structure; (3) the in-situ ZnS formation prevents CdS from photocorrosion process and also enhances charge separation.

Jiang et al. created a core shell nanocomposite of ZnS and CdS, in which CdS nanorods are decorated by ZnS nanoparticles.[268] As a result, an intimate contact was formed between two semiconductors, which led the electronic structures to be coupled together. Thus, the photogenerated charge carriers could easily move between them which caused an improvement in both hydrogen evolution and photostability of the synthesized nanocomposite. The apparent quantum efficiency was reported to be around 17% at 420 nm.

It is proved that a solid solution of ZnS and CdS not only can produce hydrogen in the visible light region, but also it resolves the photocorrosion issue of CdS.[269-271] Therefore, considerable efforts have been done to synthesize zinc cadmium sulfide ($Zn_xCd_{1-x}S$) solid solution in various sizes (bulk and nanoscale), morphologies, and crystal structures. Interestingly, most of them were successful and could generate hydrogen under visible light with high quantum efficiencies.

Dai et al. deposited CoP semiconductor as a cocatalyst on the surface of $Zn_{0.5}Cd_{0.5}S$ nanorods with two-step in-situ chemical deposition.[272] The nanoparticles of CoP are uniformly deposited on the surface of the solid solution and made intimate contact with nanorods, as demonstrated in Figure 2.27. Obviously, the excited electrons transfer from $Zn_{0.5}Cd_{0.5}S$ to conduction band of CoP and there they react with protons. The CoP not only provides active sites and plays as a cocatalyst in this configuration, but also it increases charge separation process due to its lower conduction band edge than $Zn_{0.5}Cd_{0.5}S$. As a result, with the optimum amount of CoP (5%) this heterojunction generated 20 times more hydrogen compared with pure $Zn_{0.5}Cd_{0.5}S$. Interestingly, this noble-metal-free cocatalyst could produce more than twice hydrogen as Pt-loaded $Zn_{0.5}Cd_{0.5}S$. Another group deposited novel AuPd bimetallic as cocatalyst on the surface of $Cd_{0.5}Zn_{0.5}S$ by an in-situ chemical

deposition technique.[273] It produced 12 times higher hydrogen than pure $Cd_{0.5}Zn_{0.5}S$ due to its significant photogenerated charge separation efficiency.

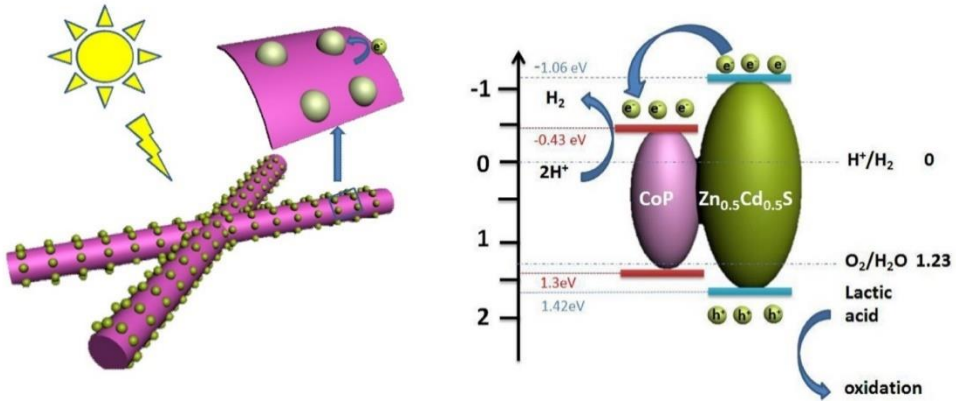

Figure 2.27. Schematic illustration for the charge transfer and separation in $CoP/Zn_{0.5}Cd_{0.5}S$ system and proposed mechanism for photocatalytic H_2 production under visible light irradiation.[272]

Another group synthesized a solid solution of $Zn_xCd_{1-x}S$ by solvothermal methods using ethylenediamine as the solvent and thioacetamide as the source of sulfur.[269] They obtained homogeneous solid solution of $Zn_xCd_{1-x}S$ ($0.3 \leq x \leq 0.5$) in the forms of nanorods and nanoparticles. Interestingly, $Zn_{0.5}Cd_{0.5}S$ exhibited an excellent hydrogen production without using any kind of cocatalyst. It generated hydrogen under visible light irradiation at a rate of 1097 μmol h^{-1} ($\lambda \geq 420$ nm) corresponding to the quantum efficiency of 30% at 420 nm. Nevertheless, the stability of this photocatalyst declined over time and over various cycles because of the Zn^{2+} leaching process during photocatalytic reaction which reduced its crystallinity and generated some lattice defects in the structure of the solid solution.

2.5 Other nanocomposites photocatalysts

In spite of above nanocomposites and nanostructures, scientists have tried to synthesize and combined other nanoscale semiconductors in order to achieve high efficient photocatalysts for hydrogen evolution under visible light illumination. 1D and 2D nanoparticles and nanostructures such as nanowires, nanotubes, nanorods, nanobelts, nanosheets, and nanoflates, have been interested among researchers in the last decade for water splitting via sunlight.[274-287] The combination of these kinds of nanostructures can enhance charge separation effectively and prevent the recombination process and so increase photocatalyst efficiency as summarized in Table 2.5.

Andrew Frame et al. found that CdSe nanoribbons were active in photocatalytic H_2 evolution from S^{2-}/SO_3^{2-} solution under visible light, whereas bulk CdSe was not.[282] By linking these nanoparticles with MoS_2 nanoplates, they activity enhanced about four times and so their quantum yields reached to 9.2% at 440 nm. Interestingly, in this nanocomposite Pt cannot be used as a cocatalyst due to sulfide poisoning of surface sites.

Jing et al. synthesized Cu-doped core/shell tubular nanocomposite of ZnO/ZnS.[283] They tried to deposit Cu-doped ZnS nanoparticles on the outside of ZnO nanotubes. As a result, this nanocomposite showed higher hydrogen evolution than undoped ZnO/ZnS nanocomposite. Copper ions act as donor level to induce visible light response of ZnS and thus excited electrons can migrate from ZnS to ZnO and from there they reduce protons.

Two ferrites chemical of calcium (CFO) and magnesium (MFO), i.e. $CaFe_2O_4$ and $MgFe_2O_4$ were used to synthesize nanocomposites for H_2 evolution reaction.[285] Due to the difference band position of these semiconductors, photoexcited electrons transfer from $CaFe_2O_4$ to $MgFe_2O_4$, whereas the holes can move vice versa. Both of CFO and MFO are active for hydrogen production under visible light irradiation when promoting with cocatalysts (Pt and RuO_2 for CFO and MFO, respectively). However, the nanocomposite of CFO and MFO produced 82.8 mmol h^{-1} g^{-1} with quantum yield of 10.1% which was an order of magnitude higher than RuO_2/MFO or Pt/CFO.

Pradhan et al. synthesized mesoporous nanocomposite of Fe/Al_2O_3–MCM-41 with size of 50 nm. They reported that this photocatalysts with 5 wt% of Fe had the hydrogen production activity under visible light (146 µmol h^{-1}) with the quantum yield of 6.1%. The main reason for such activity is due to the properties of mesoporous materials which are high pore volume, narrow pore size distribution and high surface area. Furthermore, iron doping on the surface helped to absorb visible light, although the mesoporous nanocomposite by itself didn't show any activity for $\lambda > 400$ nm.[286]

Table 2.5. Other nanocomposites for hydrogen production under visible light irradiation.

Semiconductor 1	Semiconductor 2	Cocatalyst	Sacrificial reagent	Light Source	Hydrogen production ($\mu mol\ h^{-1}\ g^{-1}$)	Quantum yield (%)	Refs
ZnS	ZnO core/shell nanotube	Pt	Na_2S/Na_2SO_3	300 W Xe, $\lambda \geq 420nm$	18	No data	[283]
$NaNbO_3$ nanorods	In_2O_3 nanoparticles	Pt	Methanol	300 W Xe, $\lambda \geq 420nm$	16.4	1.45 at λ = 420 nm	[284]
$MgFe_2O_4$	$CaFe_2O_4$	RuO2 on guest and Pt on host	Methanol	450 W W-Arc, $\lambda \geq 420$ nm	82.1	10.1 at λ = 420 nm	[285]
Al_2O_3–MCM-41	Fe	---	Methanol	150 W Hg, $\lambda \geq 400nm$	1460	6.1 at λ = 400 nm	[286]
Fe_2O_3	Fe_4N	---	---	300 W Xe, $\lambda \geq 420nm$	25	1.7 at λ = 400 nm	[287]
WO_3	Au	Pt	Glycerol	300 W Xe, $\lambda \geq 420nm$	132	0.2 at λ = 420 nm	[288]
Ta_2O_5	Au	Pt	Methanol	350 W Xe, $\lambda \geq 420nm$	55	No data	[289]
ZnS–Bi_2S_3 nanorods	ZnO	---	Glycerol	300 W Xe, $\lambda \geq 420nm$	310	No data	[290]
Rh-doped $SrTiO_3$	$BiVO_4$	Ru	---	350 W Xe, $\lambda \geq 420$ nm	200	1.6 at λ = 400 nm	[291]
ZnO	In_2O_3	---	Methanol	300 W Xe, $\lambda \geq 420$ nm	1784	No data	[292]
$SrTiO_3$ (La,Cr)	Sr_2TiO_4	Pt	Methanol	300 W Xe, $\lambda \geq 420$ nm	24	No data	[293]
Bi–$NaTaO_3$	Bi_2O_3	---	Methanol	300 W Xe, $\lambda \geq 420$ nm	102.5	No data	[294]
$GdCrO_3$	$Gd_2Ti_2O_7$	---	Methanol	350 W Hg, $\lambda \geq 400$ nm	1231.5	4.1 at λ = 400 nm	[295]

Table 2.5. Continue.

Semiconductor 1	Semiconductor 2	Cocatalyst	Sacrificial reagent	Light Source	Hydrogen production ($\mu mol\ h^{-1}\ g^{-1}$)	Quantum yield (%)	Refs
$Ag_3PW_{12}O_{40}$	Carbon quantum dots	Ag	---	300 W Xe, $\lambda \geq 420$ nm	3.8	4.9 at $\lambda = 480$ nm	[296]
$Cu_{1.8}S$	ZnS	---	Na_2S/Na_2SO_3	300 W Xe, $\lambda \geq 420$ nm	467	No data	[297]
2D ultrathin curled $ZnIn_2S_4$ nanosheet	MoS_2	---	Na_2S/Na_2SO_3	300 W Xe, $\lambda \geq 420$ nm	975	No data	[298]
In_2O_3	$Gd_2Ti_2O_7$	---	Methanol	300 W Xe, $\lambda \geq 420$ nm	5789	No data	[299]
$K_2La_2Ti_3O_{10}$	$ZnIn_2S_4$	---	Na_2S/Na_2SO_3	300 W Xe, $\lambda \geq 420$ nm	2096	No data	[300]
Ta_2O_5	In_2O_3	Pt	Methanol	300 W Xe, $\lambda \geq 420$ nm	10	No data	[301]

2.6 Conclusion and future developments

In this chapter, firstly we presented an introduction about the fundamentals of photocatalysis process and how it can be used to generate hydrogen from solar energy and water. After that, the overall water splitting procedure and using sacrificial chemicals to facilitate this process for hydrogen production was discussed completely. In addition, we talked about how the photocatalytic activity of a photocatalyst was calculated via the quantum efficiency formula (Equation 2.7). Then, a brief introduction about cocatalysts, helped us to understand their important roles in photocatalysis application specially in hydrogen evolution form water splitting. Moreover, a discussion about various configurations of heterojunctions in semiconductors based on their conduction and valence bands positions were presented completely.

TiO_2 as the first and the most well-known photocatalyst was discussed thoroughly and its challenge to evolve hydrogen in visible light region was mentioned. Then, we talked about various nanocomposites structures between TiO_2 and other visible light active photocatalysts. In addition, the improvement in hydrogen production before and after applying heterojunctions was discussed together. The heterojunctions mostly increased hydrogen evolution due to enhancement of charge separation process. In other words, one kind of photogenerated charge carriers (electrons) migrate from one semiconductor to another, and from there they reduced protons. However, the other photoexcited charge carriers (holes) stayed in the first photocatalyst. Therefore, charge recombination process declined significantly and so hydrogen generation was improved.

After that, graphitic carbon nitride (g-C_3N_4) and its physical and chemical properties were completely explained. Furthermore, its potentials such as a narrow band gap and challenges such as low specific surface area and high rate of charge recombination, to generate large amount of hydrogen were discussed. Then, different approaches to improve its photocatalytic activity were reviewed. They are including creating heterojunctions with other semiconductors, using templates to increase its specific surface area, synthesizing nanosheets of g-C_3N_4 and generating elements vacancies such as carbon vacancies throughout the nanosheets. Although most of the methods displayed significant improvement in hydrogen generation, more works need to be done owing to g-C_3N_4 special physical and chemical characteristics.

Finally, the zinc cadmium sulfide ($Zn_xCd_{1-x}S$) photocatalyst was introduced and its features as a solid solution of two semiconductors (ZnS and CdS) were discussed. As a result, a solid solution of $Zn_xCd_{1-x}S$ possesses a controllable narrow band gap (via ratio of Zn/Cd) as well as high stability to produce hydrogen under visible light illumination. Its crystal morphologies between hexagonal and cubic, affected directly on its activity. Moreover, creating some defects in its structure helped to have more active sites for reducing protons. Even though this photocatalyst showed a good hydrogen production without any cocatalysts, many works were investigated the application of noble metals as well as noble-metal-free cocatalysts on its hydrogen production. They observed that utilizing cocatalysts enhanced its photocatalytic activity considerably and so more researches require for investigate this photocatalyst with other cocatalysts.

Chapter 3. Materials Characterization Techniques

This chapter explains the fundamental and operations of different characterization techniques that have been utilized in order to characterize the physical and chemical features of the synthesized and developed materials in this thesis.

3.1 Electron microscopy

Electron microscopy provides an excellent opportunity for studying the microstructure of materials with much higher magnification and resolution than optical microscopy. While the detection of features smaller than about 1 μm is not possible by optical microscopy, electron microscopy reveals details with a resolution of ~ 0.1 nm. This is simply because the wavelengths of electron beams are about 10000 times shorter than that of visible light (a few hundred nanometers). In an electron microscope, the interaction between the focused beam of high-energy electrons (100-400 keV) and the sample leads to many detectable signals including: transmitted electrons, diffracted electrons, secondary electrons, back-scattered electrons, auger electrons, and X-rays (). Therefore, the electron microscopy can provide a wealth of information on morphology, crystallography, and chemical composition of materials. The most commonly used electron microscopy techniques are transmission electron microscopy (TEM) and scanning electron microscopy (SEM).

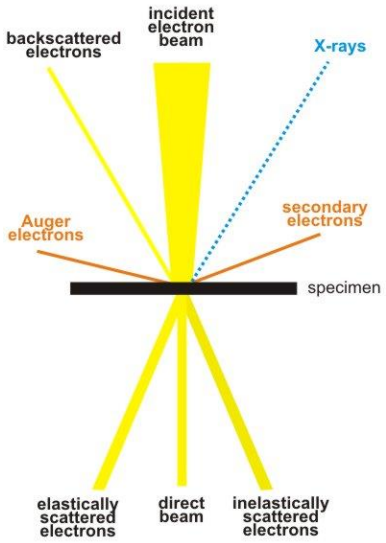

Figure 3.1. Interaction between the electron beam and the sample.

3.1.1 Transmission electron microscopy

The schematic diagram of a typical transmission electron microscope is shown in Figure 3.2. This instrument, which is in a sense similar to an optical microscope, consists of three main parts: electron gun, electromagnetic lenses, and specimen stage. The electron gun generates a primary

electron beam of high energy and high intensity, which hits the sample after passing through condenser lenses. It is worth reminding that the condenser lenses control the diameter and the convergence angle of the beams. The intensity of the electron beam decreases as it is transmitted through the specimen. The decrease in the intensity of a beam, or attenuation, strongly depends on the density and the thickness of sample. Therefore, the transmitted electrons create a two-dimensional projection of the sample mass, which is afterward magnified by the electromagnetic lenses to produce a so-called bright-field image. At the same time, the diffracted electron beams that are marginally off-angle from the transmitted electron beam form a so-called dark-field image.

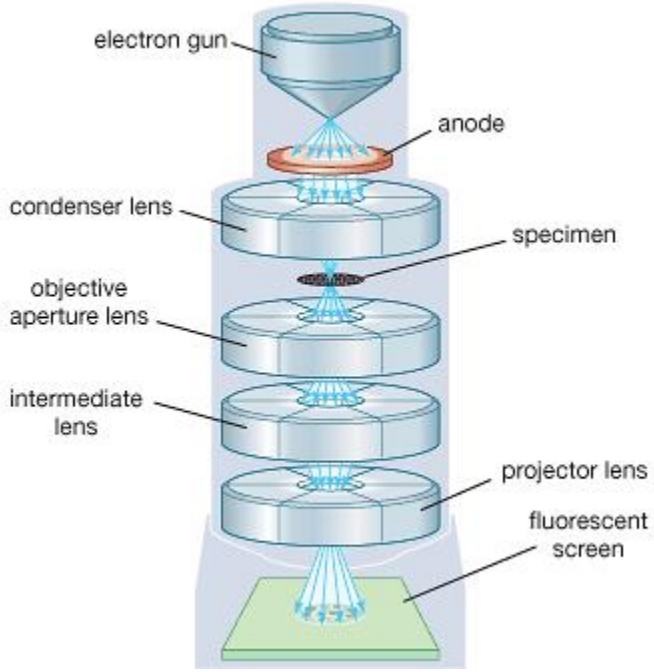

Figure 3.2. Structure of a transmission electron microscope and the optical path.

TEM, with a high resolution of 0.3 nm, is the most commonly applied form of electron microscopy for studying supported catalysts. Usually if the contrast between the particles and support are sufficient, their detections are possible. This may impede applications of TEM on well-dispersed supported oxides. Contrast in the transmission mode is caused not only by the attenuation of electrons due to intensity and thickness variations over the sample, but also by diffraction and interference.

3.1.2 Scanning electron microscopy

The scanning electron microscope (SEM) is an electron microscope that examines microscopic structure of the sample via scanning its surface with high resolution and great depth. An image is generated by a focused electron beam that scans over the surface area of the sample. It should be mentioned that the most important feature of SEM images is the three-dimensional appearance of the sample. Moreover, SEM system could provide chemical information of a sample via X-ray energy dispersive spectrometer (EDS). Similar to TEM system, SEM possesses an electron gun and a series of electromagnetic lenses and apertures. Nevertheless, the electron beam is condensed to a fine probe for surface scanning. Its brightness has more important role in imaging quality in SEM rather than TEM. The acceleration voltage for generating an electron beam is in the range 1‑40 kV, which is about one order of magnitude less than that for a TEM.

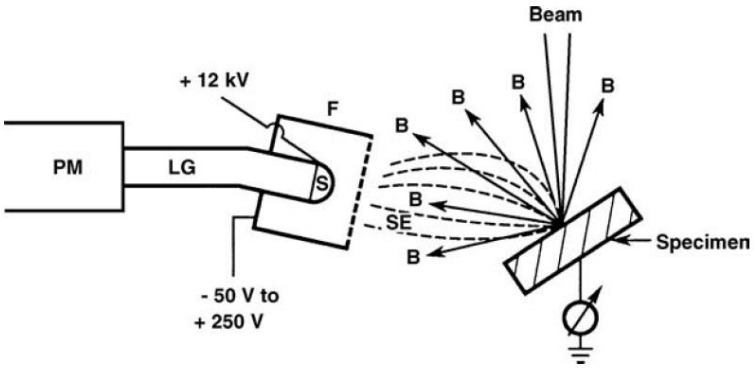

Figure 3.3. Signal collection by the Everhart‑Thornley detector. B, backscattered electron trajectory; SE, secondary electron trajectory; F, Faraday cage; S, scintillator; LG, light guide; PM, photomultiplier tube.[302]

SEM functionality depends on two kinds of scattering: elastic and inelastic. Incident electrons scatter by atoms in the sample are elastic scattering or the backscattered electrons. They are usually deflected at large angles and with little energy losses (20-40% energy loss). Electrons ejected from atoms in the material create secondary electrons which is called inelastic scattering. These ones are normally deflected at small angles and possess significantly lower energy in comparison with incident electrons. During inelastic scattering, an incident electron transfers kinetic energy to an electron in a specimen atom. Any electron in atoms in the specimen with sufficient kinetic energy will leave its orbital to become a secondary electron (Figure 3.3).

Secondary electrons are responsible for obtaining topographic contrast, while backscattered electrons are used to gain information of elemental composition contrast.

3.2 Nitrogen physisorption

Surface area and pore size distribution of porous materials can be determined through physisorption isotherm analysis. The physisorption isotherm is defined as a plot of the amount of adsorbed gas against the equilibrium relative pressure (P/P_0) at a constant temperature.

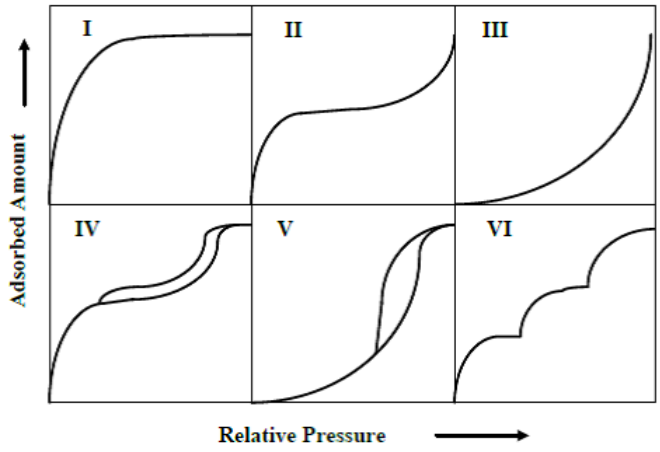

Figure 3.4. Different kinds of physisorption isotherms.

As it can be seen in Figure 3.4, there are different kinds of physisorption isotherm. Microporous materials show the Type I isotherm that is reversible. In this kind of isotherm, there is a rapid rise at low pressures related to monolayer adsorption and a plateau at higher pressures because of micropores filling. Non-porous or macroporous materials represent the reversible Type II and III isotherms. In the Type II isotherm, monolayer adsorption completes at point B and multilayer adsorption begins. In the Type III isotherm, which is an uncommon form of isotherm for non-porous or macroporous materials, the role of adsorbate-adsorbate interactions is significant. Mesoporous materials exhibit the Type IV and V isotherms with the main characteristic of hysteresis loop due to capillary condensation. In the uncommon Type V isotherm, which is related to Type III isotherm, the adsorbent-adsorbate interaction is weak. Uniform non-porous materials display the Type VI isotherm, which is typical of stepwise multilayer adsorption.[303]

Hysteresis loop, the main feature of the Type IV isotherm, is related to capillary condensation in mesoporous materials and happens when the adsorption and desorption graphs do not coincide. Different types of hysteresis loops are illustrated in Figure 3.5. Type H1 hysteresis, which in that there are almost vertical and nearly parallel adsorption/desorption curves over a wide range of P/P_0, is given by cylindrical pores with a narrow pore size distribution. Type H2 hysteresis, including of a desorption curve far sharper than the adsorption curve, is displayed by 'ink-bottle' pores with narrow necks and wide bodies. Type H3 and H4 hysteresis loops are related to slit-shaped pores and narrow slit-like pores, respectively.[304]

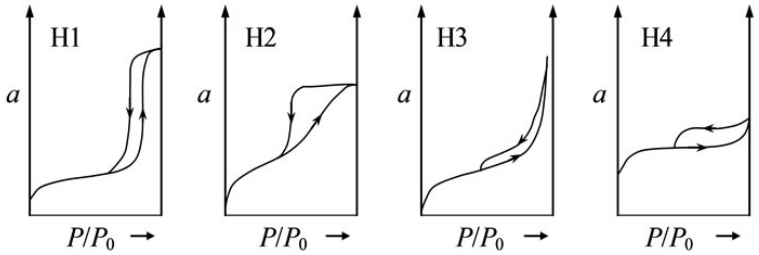

Figure 3.5. Different kinds of hysteresis loops.

To date, various theories are introduced to specify the surface area of porous materials among them the Brunauer-Emmett-Teller (BET) theory is the most widespread method. The BET equation is usually given in the following form

$$\frac{P/P_0}{n(1-P/P_0)} = \frac{1}{n_m c} + \frac{c-1}{n_m c} \times \frac{P}{P_0} \qquad (3.1)$$

A linear relationship between $\frac{P/P_0}{n\,(1-P/P_0)}$ and P/P_0 is obtained by the BET equation. The intercept $\frac{1}{n_m c}$ and slope $\frac{c-1}{n_m c}$ can be used to calculate the values of n_m and c. Therefore, the surface area can be computed from the monolayer capacity on the assumption of close packing:

$$A = n_m \alpha_m L \qquad (3.2)$$

where α_m is the molecular cross-sectional area; n_m is the monolayer capacity and L is the Avogadro constant. It is indeed supposed that nitrogen is the most appropriate gas for surface area

determination. If it is assumed that the BET monolayer is close-packed, α_m will be 0.162 nm^2 at 77 K.

3.3 Photoluminescence spectroscopy

Luminescence is a photon emission process that differs from refraction, reflection and scattering of light in which it happens through electron excitation stages. They include excitonic transition, intrinsic electron transitions between energy bands, and extrinsic electronic transitions at impurities and defects of semiconductors, insulators, and organic molecular solids. Photoexcitation via optical photon absorption is called photoluminescence (PL). PL is spontaneous emission of photons, whereas stimulated photon emission plays an important role in solid-state and semiconductor lasers. This method is zero-background test and so it is a sensitive optical technique for analysing the structure of different materials including organic and inorganic materials, semiconductors and insulators. In this characterization, an energy from absorbing a photon can excite an electron from its ground state within femtosecond timescale. If there are multiple excited states as in organic molecules, then electrons excited to higher excited states rapidly relax to the lowest excited states by exciting molecular vibrations in molecules or emitting phonons in solids in picosecond order. After that, the excited electrons recombine radiatively to the ground state by emitting photons. As a result, the emitted photons are usually lower in energy than the adsorbed photons.

PL consists of two individual one-photon steps, that is, photon absorption is succeeded by photon emission with a transition time of more than 0.1 ns. The HOMO (highest occupied molecular orbital) state and the LUMO (lowest unoccupied molecular orbital) state correspond to the valence band (VB) edge and the conduction band (CB) edge, respectively. PL of semiconductors and ionic crystals is classified into two categories, intrinsic PL and extrinsic PL. Intrinsic PL happens with the band-to-band radiative transition in a highly pure semiconductor at a relatively high temperature, where an electron and a hole are excited in CB and VB, respectively, via photon adsorption. Then, they radiatively recombine to give rise to intrinsic PL. It should be noted that donors and acceptors are intentionally generated in the semiconductor via impurities. The other PL occurs between an electron trapped by a neutral donor state D^0 and a hole at the top

of VB and between an electron at the bottom of CB and a hole of the neutral acceptor state A^0. Bound excitons are generated by the capture of a free exciton by a neutral impurity state (neutral donor D^0 or acceptor A^0), ionized impurity state (ionized donor D^+ or acceptor A^-), or by a defect. Bound excitons recombination dominates over free exciton recombination for a less pure material and shows a sharp line in the highly-resolved PL spectrum at a low temperature. Excitonic recombination procedures become more important in semiconductor quantum wells, quantum wires, and QDs, where the excitonic PL can be observed even at much higher temperatures due to the increased exciton binding energy by quantum confinement. When both types of impurities are present as compensated semiconductors, donor to acceptor pair (DAP) recombination occurs through radiative tunneling. Figure 3.6 demonstrates various radiative recombination processes with impurities.

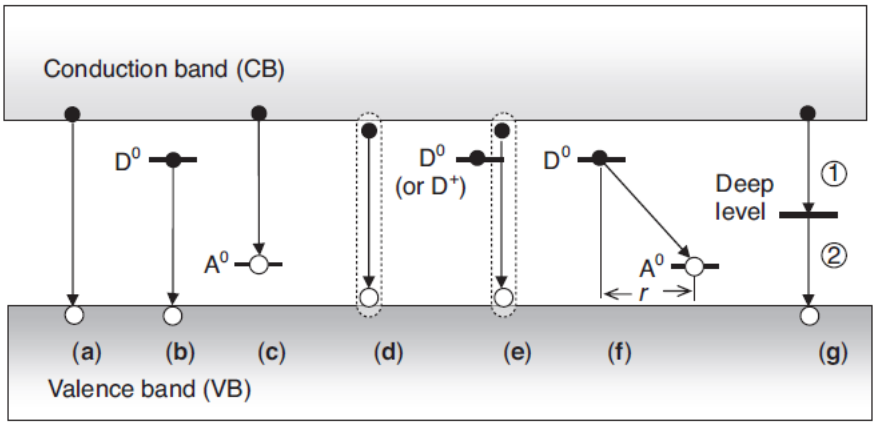

Figure 3.6. Schema of radiative recombination processes in semiconductors. (a) Band-to-band recombination, (b) neutral donor (D^0) to VB transition, (c) CB to neutral acceptor (A^0) transition, (d) radiative recombination of FE, (e) radiative recombination of BE, which is bound to D^0 (recombination of BE bound to ionized donor D^+ is also possible), (f) DAP recombination with separation r, and (g) deep-level defect luminescence (either one of the two transitions (1) and (2) is radiative).[305]

A schematic of steady-state PL spectroscopy instrument is shown in Figure 3.7. Its light excitation source can be any laser with emission energy larger or close to the sample bandgap. Using band-pass filter (BPF) is essential to eliminate the plasma line of the gaseous laser or unwanted laser lines like harmonic generation. After producing emission and illuminating on the sample, the emission from it is collected with monochromator to acquire the PL spectrum, which

is PL intensity versus wavelength or photon energy. PL can be detected via different detectors such as a photomultiplier tube, which is the most sensitive detector with high-speed response.

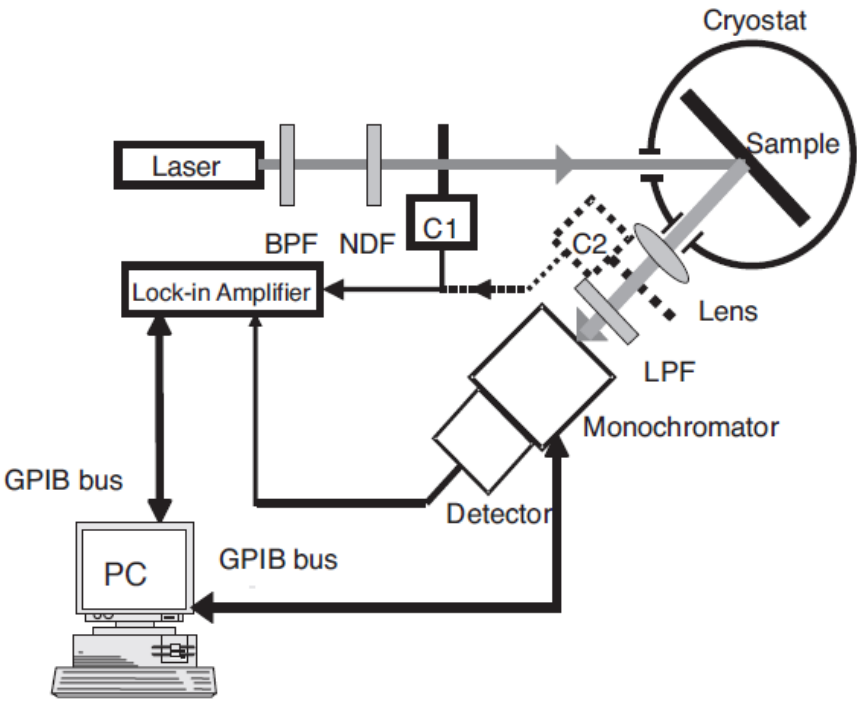

Figure 3.7. Experimental setup of static PL spectroscopy. C1,optical chopper at normal position; C2, optical chopper for long-lived PL decay measurement; BPF, band-pass filter; NDF, neutral density filter; LPF, long-pass filter; PC, personal computer.

3.4 UV-visible spectroscopy

Ultraviolet–visible spectroscopy or ultraviolet-visible spectrophotometry (UV-Vis or UV/Vis) analyazes the wavelength dependent interaction of photons with a material. It measures the attenuation of a beam light after it passes through a sample or after reflection from a sample surface. Absorption measurements can be at a single wavelength or over an extended spectral range. The UV-vis absorbance can be classified into two group: transmission and diffuse reflectance spectroscopies.

Transmission UV-vis spectroscopy is usually utilized with a sample transparent enough to allow photons pass through it. As it can be seen in Figure 3.8, the UV-vis light is pass through a solution (or thin film), and the transmitted light is collected by a detector. The difference between a transmitted light from a reference and a target sample is displayed in the figure. This technique

is generally used to analyze the organic dyes, metal or semiconductor nanoparticles highly dispersed in a solution. In an ideal solution, there is a linear relation between the absorbance wavelength and concentration. A calibration curve is prepared by plotting the absorbance of a series of standard samples as a function of their concentration and so the concentration of an unknown sample can be determined via measuring its absorbance.

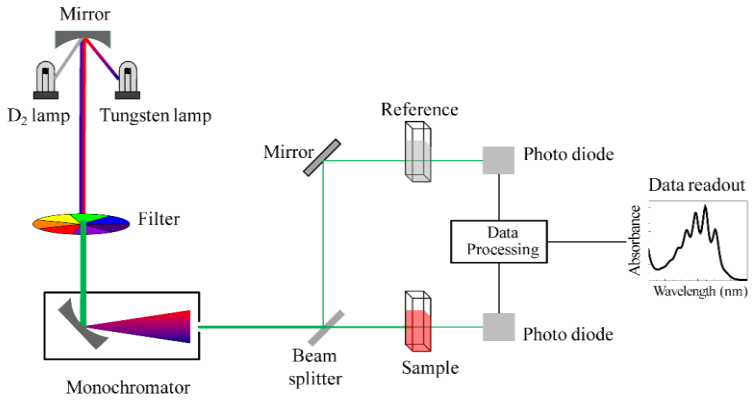

Figure 3.8. Schematic of transmission UV- visible spectrophotometer.

When the sample is not transparent and so it absorbs 100% across the entire wavelength, diffuse reflectance UV-vis spectroscopy is utilized. In general, the light beam is irradiated on the sample resulting to have light reflection in all directions. This reflected light is collected by an integrating sphere and then analyzed with a detector (Figure 3.9). This method is used to characterize the optical properties of semiconductors and metal samples in the powder form.

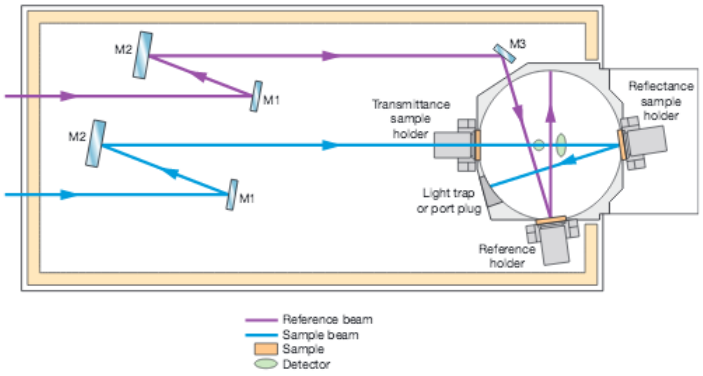

Figure 3.9. Schematic of Diffuse reflectance UV- visible spectrophotometer

3.5 Fourier Transform Infrared Spectroscopy

Generally, vibrational spectroscopy is a method to determine the molecules structures by measuring the interaction between electromagnetic radiation and nuclear vibrations in molecules. This technique employs electromagnetic waves with longer wavelength (in order of 10^{-7}), which are typically related to infrared light. Vibrational spectroscopy detects the molecular vibrations by the absorption of infrared light or by the inelastic scattering of light by a molecule. This technique can be utilized to examine the molecules structures of inorganic and organic materials in gas, liquid or solid phases. Nonetheless, it cannot analyze metallic materials due to their strong electromagnetic reflections. When a molecule is irradiated by infrared electromagnetic waves, one frequency may match the vibrational frequency of the molecule. Therefore, the molecular vibration will be excited by waves with the frequency. The excitation means that the energy of molecular vibration will increase. In the meantime, the electromagnetic radiations with the specific frequency will be absorbed by the molecule because the photon energy is transferred to excite molecular vibrations.

Fourier transform infrared spectroscopy (FTIR) is the most widely used vibrational spectroscopic technique that the Fourier transform method is utilized to obtain an infrared spectrum in a whole range of wavenumbers simultaneously. It differs from the dispersive method, which entails creating a spectrum by collecting signals at each wavenumber separately. The most important part of FTIR is the Michelson interferometer (Figure 3.10). It consists of two mirrors and a beam-splitter. The beam-splitter transmits half of the infrared beam from the source and reflects the other half. These two beams hit two mirrors and then they combine again to illuminate on the sample before reaching to a detector. The moving mirror act as a changer for the optical path lengths to create light interference between two split beams. If its distance is the same as the fixed mirror, the optical paths for both are the same. The difference in optical paths has the same affect of diffraction in crystallographic planes. The two split beams exhibit constructive and destructive interference periodically. A figure of light interference intensity as function of optical path difference is interferogram, as can be seen in Figure 3.11. The sharp center burst related to the position of the moving mirror considering as zero path difference with the maximum intensity of the interferogram. Then, by applying Fourier transform formula, the interferogram converts to the infrared spectrum, as demonstrated in Figure 3.11.

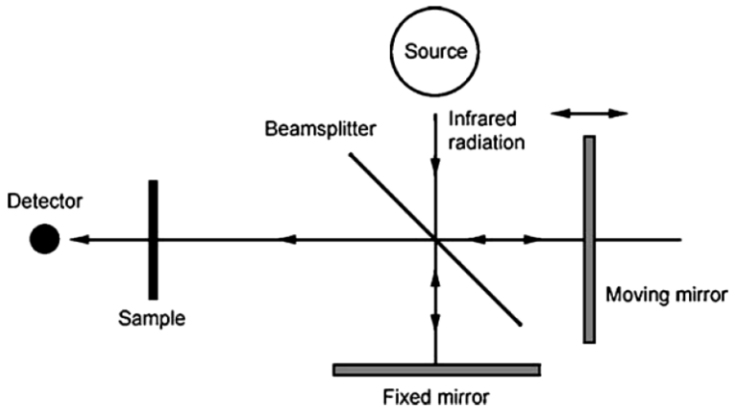

Figure 3.10. Optical diagram of a Michelson interferometer in FTIR.

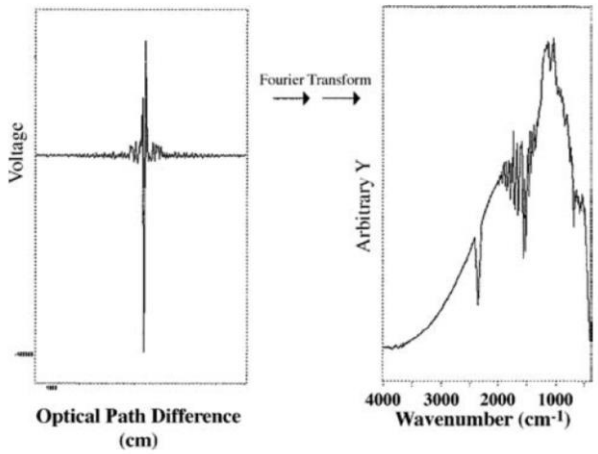

Figure 3.11. Plots of: (left) an interferogram; and (right) a Fourier transform from an interferogram to an IR spectrum.[306]

3.6 Atomic Force Microscopy

Atomic force microscope (AFM) is a technique to map sample topography. It detects near-field forces between its very sharp tip and the sample surface. There are several kinds of near-field forces including short-range, Van der Walls, electrostatic and capillary forces. The short-range forces refer to atomic forces between atoms when their distance is close to atomic spacing. The van der Waals forces are the interactive forces between dipoles of molecules. Electrostatic forces are the interactive forces between the electric charges of tip and sample. Finally, capillary forces are forces resulting from water vapor condensation between tip and sample. The key element in this characterization is the microscopic force sensor and the most widely used one is a cantilever.

The tip is loaded at the end of a cantilever and the force detection is based on a beam reflection technique as shown in Figure 3.12. The cantilever bends elastically when there is a force between the tip and sample. The amount of bending is monitored and recorded by position-sensitive photodiodes which are arranged in four quadrants. Any small deflection of the cantilever will tilt the laser beam and change its striking position on the photodiodes. The difference between the two photodiode signals indicates the amount of cantilever deflection. The amount of deflection, in turn, can be mathematically converted into the force on the tip, according to the elastic properties of the cantilever.

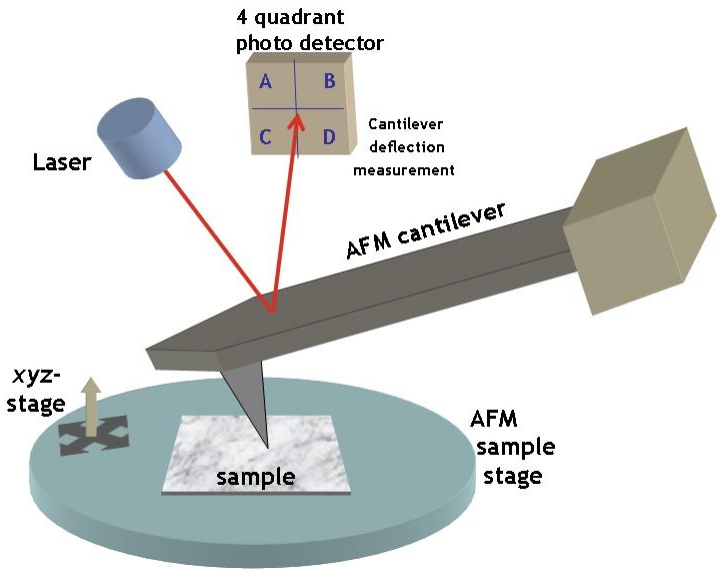

Figure 3.12. Atomic force microscope block diagram.

3.7 X-ray Diffractometry

X-ray diffractometry (XRD), one of the most widely used techniques in materials characterization, is applied to identify crystalline phases and to obtain an indication of crystallite size. X-ray diffraction is the elastic scattering of X-ray photons by atoms in a periodic network. The scattered monochromatic X-rays that are in phase produce constructive interference, which leads to a new wave that has a higher amplitude (diffraction peak). It is worth reminding that the waves are said to be in phase when their crests and troughs occur simultaneously. Figure 1.1 shows how the wavelength of the X-rays (λ), the distance between two network planes (d), the angle

between the incoming X-rays and the reflecting lattice plane (θ), and the order of interference (n) are related by the Bragg equation[307]:

$$n\lambda = 2d \sin\theta \qquad (3.3)$$

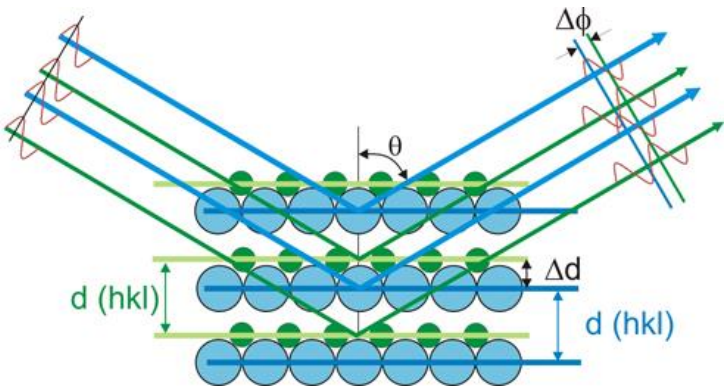

Figure 3.13. Schematic illustration of the Bragg's law.

A typical XRD instrument consists of three main parts: X-ray tube, specimen stage, and X-ray detector. The X-ray beam generated by the X-ray tube passes through special slits, which collimate the X-ray beam and prevent beam divergence. After passing through the slits, the X-ray beam strikes the specimen that is supported by the plane of specimen. The X-rays diffracted by the specimen interfere constructively when they are in phase and produce a convergent beam at receiving slits before entering the detector. By continuously changing the incident angle of the X-ray beam, diffraction intensity is recorded in a range of 2θ. The obtained spectrum is compared with a database consisting of over 60,000 diffraction spectra of known crystalline materials to identify the crystalline phases.

The XRD technique has one important limitation; the sample must possess sufficient long-range order in order to observe clear diffraction peaks. This limitation, however, has an advantage, which is that the width of diffraction peaks provides information on the dimensions of the reflecting planes. While diffraction lines from perfect crystals are very narrow, line broadening occurs for crystallite sizes below 100 nm because of incomplete destructive interference in scattering directions. The Scherrer equation relates crystallite size to line width:

$$\langle L \rangle = \frac{K\lambda}{\beta \cos\theta} \qquad (3.3)$$

where <L> is the dimension of the particle; λ is the X-ray wavelength; β is the peak width; θ is the angle between the incoming X-rays and the reflecting lattice plane; K is a constant.

3.8 X-ray photoemission spectroscopy

X-ray photoemission spectroscopy (XPS) is a technique that utilizes characteristic electron emitted from a solid for analyzing surface chemicals. The features of emitted electron not only quantitively identify the chemical composition of the target sample, but also the chemical states of its elements can be detected.

It works based on the fact that if an atom absorbs an X-ray photon with energy of hν, an electron with binding energy of E_b is ejected out of atom with a kinetic energy of:

$$E_k = h\nu - E_b - \varphi \qquad (3.4)$$

where E_k is the kinetic energy of the photoelectron; h is Planck's constant, ν is the frequency of the exciting radiation; E_b is the binding energy of the photoelectron with respect to the Fermi level of the sample and φ is the work function of the spectrometer.

In XPS analysis, the intensity of photoelectrons as a function of their kinetic energy is measured and with this equation, the kinetic energy can be converted to binding energy (usually placed on x-axis of spectrum). Binding energy of an electron exhibits the characteristic of the element from which the photoelectron originates. In addition, it can be used to identify the chemical state of the element because the energy levels of core an electron rely slightly on the chemical state of the atom. Therefore, small shifts in binding energy (less than 3 eV) shows various chemical states in atom. Generally, the binding energy of an atom, increases with increasing oxidation state and with the electronegativity of the ligands for a fixed oxidation state.

3.9 Photocatalytic test

The main goal of this thesis is to synthesize or develop a photocatalyst for generating hydrogen under visible light. The performance of original (for comparison) and developed photocatalysts are measured with photocatalytic testing system, as shown in Figure 3.14. The reactor is made of stainless steel with a Pyrex glass window on its top. Above it, there is a solar

simulator with capability of loading various light filters. Moreover, a magnetic stirrer is used to have a good mixing in the liquid phase, which is normally consists of water and a sacrificial agent with a concentration of 10-15% (volume%). An external gas pump helps to have homogenous concentration of hydrogen throughout the system. After deposition of cocatalysts via photodeposition technique, the reactor is purged with nitrogen for 10 min and then the mixture is illuminated with light beam from solar simulator with full spectrum or other light filters. After several hours, a small sample of gas phase is taken and injected to GC for analyzing its H_2 concentrations.

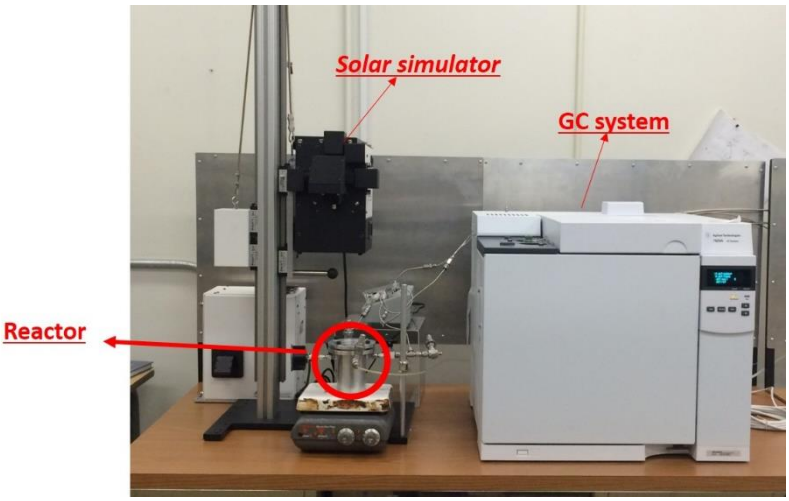

Figure 3.14. A picture of photocatalytic test for hydrogen production under solar simulator.

3.10 Synthesis methods of developed materials

3.10.1 Titanate nanodisks

To synthesize titanate nanodisks with diameter of around 20 nm, 2g of titanium butoxide, 12g of oleylamine, 12g of benzyl alcohol (oleylamine:benzyl alcohol weight ratio of 1:1) and 30g of benzyl ether were added to a 100-mL round-bottom flask.[308] The reaction mixture was heated to 190 ºC at the heating rate of 5 ºC/min under nitrogen flow. After 20 h, the reaction was stopped and cooled down to room temperature. After addition of excess absolute ethanol, the titanate nanodisks were obtained by centrifugation and redispersed in toluene and re-precipitated by ethanol for three times in order to remove the unreacted reagents.

Then, 5 mmol of as-synthesized titanate nanodisks (according to Ti atom) were dispersed in a mixture of tetraethyl ammonium hydroxide (15 mmol), ethanol (15 ml) and water (15 ml). The mixture was stirred overnight at room temperature. To the clear solution obtained was added access acetone to precipitate titanate nanodisks. The precipitate was then washed several times with acetone and finally dispersed in 10 ml of water.

3.10.2 Bulk graphitic carbon nitride

Bulk material of graphitic carbon nitride (g-C_3N_4) was synthesized from two different precursors.[309, 310] In the chapter 4, the bulk material was produced from melamine. Typically, 10 g melamine was heated in a crucible to 550 ºC and kept at this temperature for 3 h. Then, the obtained yellow powder was grounded and washed with water and ethanol several times. After that it was dried completely in an oven at 70 ºC overnight. In chapter 5, the bulk material of g-C_3N_4 was created from dicyandiamide. The precursor was calcined in a muffle furnace at 550 ºC in air for 4 h. Then, the obtained material was washed with distilled water to remove unreacted chemicals and then it was dried in an oven overnight at 70 ºC.

3.10.3 Carbon nitride nanosheets by liquid exfoliation

After synthesizing bulk g-C_3N_4, nanosheets of carbon nitride via liquid exfoliation method was synthesized as follows [154, 169]: 1 g of bulk g-C_3N_4 was added to a mixture of 100 ml isopropanol and 100 ml water, Then, the mixture was put in ultrasonication bath for 12 h. After this step, dispersed nanosheets of g-C_3N_4 were separated from residual bulk material (aggregates) with centrifugation at 3,000 rpm for 10 min. Then, the obtained nanosheets were centrifuged at 10,000 rpm for 15 min and dried at 70 ºC.

3.10.4 Carbon nitride nanosheets by gas template method

In this method, nanosheets of g-C_3N_4 were synthesized by one step calcination method.[167] First, 15 g of ammonium chloride was dissolved in 300 ml of water and then 3 g melamine was added to the mixture. Later, it was heated to 60 ºC in order to remove water and then, it was dried completely overnight. After this step is completed, the white powder was heated to 550 ºC in a semi-closed system and was kept for 4 h. After cooling down, the nanosheets were washed several times with ethanol and water and dried in oven.

3.10.5 Post-calcined graphitic carbon nitride

In chapter 5, after synthesizing bulk g-C_3N_4, it was heated again up to 650 ºC under argon gas flow of 200 mL/min for 2 h. Then, the obtained material was re-calcined in air in a muffle furnace at 500 ºC for 2 h. Later, the developed material was washed several times with water to remove contaminants and dried in an oven at 70 ºC.

3.10.6 Zinc cadmium sulfide solid solution

Zinc Cadmium sulfide solid solutions were synthesized as follow: First, 50 mL of glycerol was dissolved in 200 mL isopropanol. Typically, 1.5 mmol of zinc nitrate and 1.5 mmol of cadmium nitrate were dissolved in the mixture in order to have Zn/Cd ratio of 50%/50% (for all other samples the total mole of 3 mmol was considered constant and only the ratios of Zn/Cd were changed). Then, the mixture was transferred to an autoclave and was heated to 180 ºC for 6h. Later, the synthesized material was collected via centrifugation at 5,000 rpm and dried at 70ºC overnight. The obtained sample was calcined in air at 500ºC for 4 h to acquire zinc and cadmium mixed oxide. Subsequently, the mixed oxide was exposed to a flowing gas mixture of H_2S (10%)/Ar at 450ºC for 2 h. Therefore, sulfide (S^{-2}) ions could substitute with oxygen and so the mixed oxide was converted to a mixed sulfide.

Chapter 4. Graphitic carbon nitride-titanium dioxide nanocomposite for photocatalytic hydrogen production under visible light

Mohammad Reza Gholipour,[a] François Béland[b] and Trong-On Do[a,*]

[a] Department of Chemical Engineering, Université Laval, Québec, G1V 0A6, Canada

[b] SiliCycle Inc., 2500, Boul. du Parc-Technologique

Québec (QC) G1P 4S6, Canada.

International Journal of Chemical Reactor Engineering, **2016**, **14**, 851–858

Special Issue in honor of Dr. Serge Kaliaguine

Résumé

La production d'hydrogène à partir de la décomposition de l'eau par des réactions photocatalytiques peut être une énergie propre, alternative aux combustibles fossiles dans le futur. Le nitrure graphitique de carbone (g-C_3N_4) est l'un des photocatalyseurs actifs dans la région visible du spectre lumineux qui peut être combiné avec d'autres semi-conducteurs afin d'augmenter son efficacité photocatalytique. Le TiO_2 est l'un des choix les plus appropriés à combiner avec g-C_3N_4 en raison de l'intervalle entre ses bandes de valence et de conduction et de ses diverses formes de nanostructures existantes. Dans ce travail, des nano feuilles de g-C_3N_4 ont été mélangés avec des nanoparticules d'oxyde de titanate afin d'améliorer la séparation des charges et l'efficacité photocatalytique de la structure. En conséquence, le rendement de ce nouveau nanocomposite vis-à-vis de la production de dihydrogène est presque deux fois celui du g-C_3N_4 pure.

Abstract

Hydrogen production from water splitting via photocatalytic reactions can be an alternative clean energy of fossil fuels in the future. Graphitic carbon nitride (g-C_3N_4) is one of the photocatalysts active in the visible light region that can be combined with other semiconductors in order to increase its photocatalytic efficiency. TiO_2 is one of the most appropriate choices to combine with g-C_3N_4 because of its conduction band edge and variety forms of nanostructures. In this work, nanosheets of g-C_3N_4 were mixed with nanoparticles of titanate in order to enhance charge separation and photocatalytic efficiency. Consequently, the hydrogen evolution of this novel nanocomposite produced almost twice as much hydrogen in comparison with g-C_3N_4.

4.1 Introduction

Fossil fuels provide the cheapest source of energy for human beings, in spite of their environmental issues such as: air pollution and CO_2 emissions, which causes to global warming and climate change. As a matter of fact, energy demands are increasing annually and so fossil fuels are used more quickly than before. However, the resources of this kind of energy are limited and we may face an energy crisis in the near future.

Scientists believe that solar energy is one of the best alternatives to substitute for fossil fuels because it is abundant, renewable and environmentally friendly. It is estimated that the worldwide energy consumption of one year can be produced by only 0.01% of sunlight irradiation during one second.[17, 58, 77] However, the most important concern of this energy resources is how to utilize it into practical applications. It has been suggested that utilizing hydrogen as an energy carriers not only solves these problems, but can also reduce air pollution. [30, 311] Moreover, water is the only product from hydrogen combustion and so there are no CO_2 emissions during hydrogen consumption.

In 1972, Fujishima and Honda made the discovery that TiO_2 and Pt could split water into hydrogen and oxygen under UV light illumination.[6] Since then, researchers have tried to synthesize photocatalysts that can produce hydrogen from water under sunlight irradiation. However, the majority of sunlight illumination is in the visible light region and so efficient photocatalysts should be activated under visible light irradiation (400-700 nm).[27]

Graphitic carbon nitride (g-C_3N_4) is one of the best visible light active photocatalyst that has attracted much of interest, recently.[142, 312, 313] Wang et al. showed that g-C_3N_4 can be excited under visible light irradiation and produce hydrogen from a mixture of water and a sacrificial reagent.[151] They used triethanolamine as an electron scavenger and Pt as a cocatalyst. Later many researchers have tried to improve its efficiency by introducing various methods such as doping with other elements, applying different cocatalysts, making nanosheets of g-C_3N_4 and creating carbon nitride based nanocomposites.[314] In this work, a nanocomposite of g-C_3N_4 nanosheets and titanate nanodisks (TNDs) is proposed in order to increase charge separation and so enhance hydrogen production under visible light illumination. Titanate nanodisks were synthesized according to previous reports. [89, 308] These nanoparticles of TiO_2 have lower conduction band in comparison with g-C_3N_4 and so excited electron can transfer from g-C_3N_4 to

TiO_2.[315] Meanwhile, excited holes remain in g-C_3N_4 valence band and as a result charge recombination phenomenon is partially prohibited and the photocatalyst efficiency for hydrogen production increases.

4.2 Experimental

4.2.1 Carbon nitride bulk material

Graphitic carbon nitride was produced from melamine as reported previously. [309, 310] Briefly, 10 g melamine was heated in a crucible to 550 °C and kept at this temperature for 3 h. Then, the obtained yellow powder was ground and washed with water and ethanol several times. It was, then, dried thoroughly in an oven at 70 °C.

4.2.2 Carbon nitride nanosheet by liquid exfoliation

After synthesizing bulk g-C_3N_4, nanosheets of carbon nitride were made by liquid exfoliation (denoted as g-C_3N_4-LE).[154, 169] Typically, 1 g of bulk material was added to a mixture of 100 ml isopropanol and 100 ml water. Then, the mixture was sonicated for 12 h. Nanosheets were, then, separated from residual bulk material (aggregates) by centrifugation at 3000 rpm for 10 min. Then, the obtained nanosheets were centrifuged at 10000 rpm for 15 min and dried at 70 °C.

4.2.3 Carbon nitride nanosheets by gas template

Nanosheets of g-C_3N_4 were synthesized by one step method called gas template (denoted as g-C_3N_4-GT) according to the method reported in ref. [167]. First, 15 g of ammonium chloride was dissolve in 200 ml of water and then 3 g melamine was added to the mixture. Later, it was heated to 60 °C in order to remove water and then, it was dried in an oven at 70 °C. Once this step is completed, the white powder was heated at 550 °C for 4 h in a semi-closed system. During the calcination process, ammonium chloride acts as a dynamic gas template, helping to synthesize ultrathin g-C_3N_4.[167] After this stage, the resultant nanosheets were washed several times with ethanol and water and dried in an over.

4.2.4 Titanate nanodisks

TNDs were prepared by a solvothermal method described in our previous work.[308] Briefly, 3.4g of titanium butoxide was added to a mixture of 20g oleylamine and 20g benzyl alcohol. Then, 90g benzyl ether was added to the mixture and all of them were transfer to a round-bottom flask. The flask was kept in an oven at 180 °C for 24 h. After cooling down, the obtained TNDs were washed completely with toluene and ethanol and were treated with tetraethylammonium hydroxide in order to obtain water-soluble TEA-TNDs. As a result, TNDs with ability to disperse in water were obtained (Figure 4.1). These highly uniform nanoparticles with an average diameter of 35 nm can be utilized on the surface of g-C_3N_4 nanosheets. Therefore, charge separation between TND and nanosheets of g-C_3N_4 become more effective because of their very small size and high g-C_3N_4/TNDs interface.

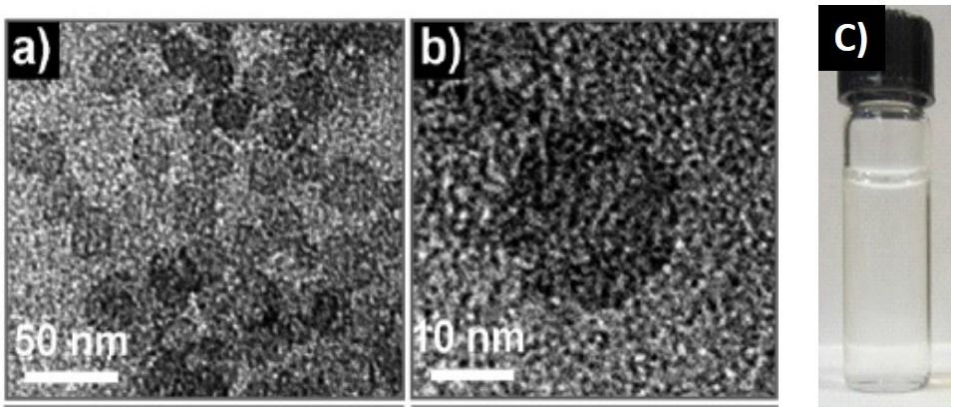

Figure 4.1. TEM pictures of TNDs (a), (b) and photograph of highly dispersed TNDs in water (c)

4.2.5 Nanocomposite of g-C_3N_4 nanosheets and TNDs

After synthesizing TNDs and g-C_3N_4 nanosheets, both nanomaterials were mixed together with the ratio of 30 wt% TNDs as follows. The pH of nanosheets was decreased in order to make the surface positive charges.[310] Due to the negative charge surface of TNDs, both nanoparticles can make better contact at lower pH. The mixture was heated under agitation until it dried. After that, the obtained powder was calcined at 400 °C for 3 h to obtain a g-C_3N_4/TiO_2 nanocomposite. Owing to the particle size of TNDs (20 nm), they deposited on the surface of g-C_3N_4 nanosheets.[316] Then, Pt metal nanoparticles were deposited on the surface of the nanocomposite

via photodeposition technique under visible light irradiation.[317] Although Pt nanoparticles are partially deposited on both surfaces of semiconductors, those that deposited on the TiO_2 nanoparticles have more ability to enhance charge separation and so hydrogen generation would be increased.

4.2.6 Characterization

Transmission electron microscopy (TEM) images of the samples were obtained on a JOEL JEM 1230 operated at 120kV. Powder X-ray diffraction (XRD) patterns of the samples were obtained on a Bruker SMART APEXII X-ray diffractometer equipped with a Cu Kα radiation source (λ=1.5418 Å). The UV-vis spectra were recorded on a Cary 300 Bio UV-visible spectrophotometer. Fourier transform infrared (FTIR) absorption spectra were measured with a FTS 45 infrared spectrophotometer with the KBr pellet technique.

4.2.7 Photocatalytic test

The photocatalytic reactions were performed in a gas-tight 10 ml Pyrex reaction cell as follows: 5 mg of the typical synthesized nanocomposite photocatalysts were dispersed in 5 ml aqueous solution of 10 wt% of triethanolamine. An adequate amount of chloroplatinic acid (H_2PtCl_6) was, then, dissolved directly in the above mixture in order to get 2 wt% of Pt, which acts as a cocatalyst and deposited by an in-situ photodeposition technique. After this stage is completed, the cell was evacuated and then purged with nitrogen for 10 min in order to eliminate dissolved oxygen. Then, the mixture was illuminated with a 300W Xe arc lamp equipped under stirring condition to prevent particles from settling at the bottom of the cell. A 0.5 mL of gas was sampled intermittently through septum, and hydrogen was analyzed by gas chromatography equipped with TCD detector and carboxen-1010 capillary column.

4.3 Results and discussions

4.3.1 Sample characterizations

The crystal structure of bulk carbon nitride and the obtained nanosheets from liquid exfoliation and gas template were characterized by XRD (Figure 4.2). According to the XRD results, the peaks in our samples can be indexed to g-C_3N_4. The strongest peak around 27.5° is characterized as (002) peak and related to the interlayer stacking peak of aromatic system.[151] It should be noted that this peak noticeably decrease, showing that g-C_3N_4 nanosheets were obtained. [154, 318] The other peak around 13° is indexed as (100) plane and is attributed to inter-planar structure of tri-s-triazine with a distance of about 0.675 nm. It is not surprising that after calcination a nanocomposite of g-C_3N_4 nanosheets and TNDs, the TNDs being converted to TiO_2 nanoparticles that cannot be detected by XRD, due to their small particle sizes, good dispersion and weak crystallinity.[319] The optical absorption spectra for graphitic carbon nitride and nanosheets are shown in Figure 4.3. The results showed that all the samples are semiconductors with the strong visible light absorption ability in the range of 400 to 550 nm. As can be seen in Figure 4.3, nanosheets of g-C_3N, due to the quantum confinement effect, their band gaps increased and the UV-visible curve shifted to shorter wavelengths and so they could absorb less visible light. The differences between UV-visible spectra of nanosheets from liquid exfoliation (LE) and gas template (GT) methods, indicated that the nanosheets of g-C_3N_4-GT were thinner than g-C_3N_4-LE. Furthermore, the band gap energies of all samples, which were estimated from the intercept of the tangents to the plot of $(Ah\nu)^{1/2}$ vs. photon energy, proved the same results.[320, 321] As it is calculated the band gap of bulk graphitic carbon nitride is 2.70 eV, which is in good agreement with the literature (Figure 4.4-a).[151] As it is demonstrated in Figure 4.4-b,c, the band gap energies of nanosheets synthesized from liquid exfoliation technique and gas template approach, are 2.74 and 2.76 eV, respectively. In other words, by obtaining nanosheet structure of g-C_3N_4 due to the quantum confinement effect, the band gap increased and it could absorb less visible light.

The molecular structure of the synthesized sample is investigated by FT-IR spectra, as shown in Figure 4.5. The broad band between 3000 and 3500 cm^{-1} can be related to N-H stretching and

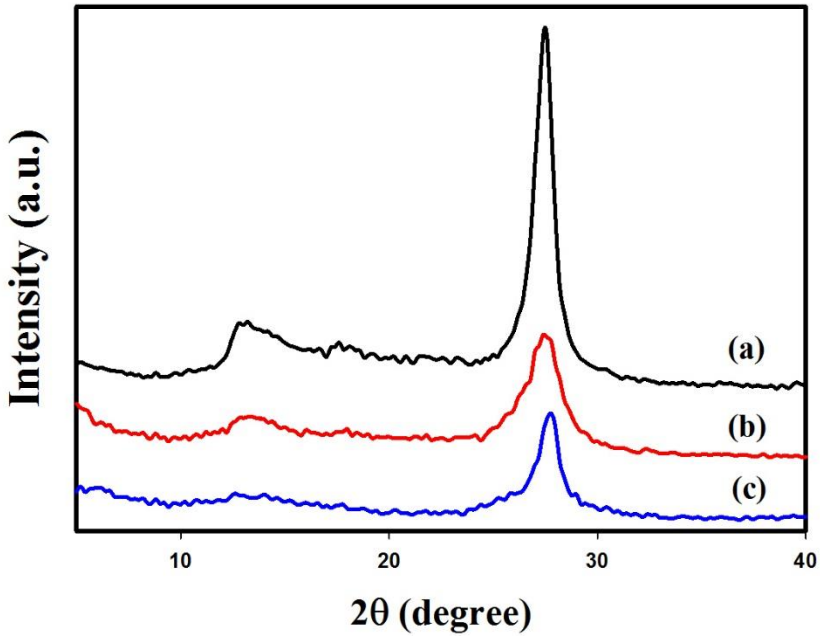

Figure 4.2. XRD pattern of (a) g-C_3N_4 in bulk; (b) and (c) g-C_3N_4 nanosheets prepared by gas template and liquid exfoliation, respectively.

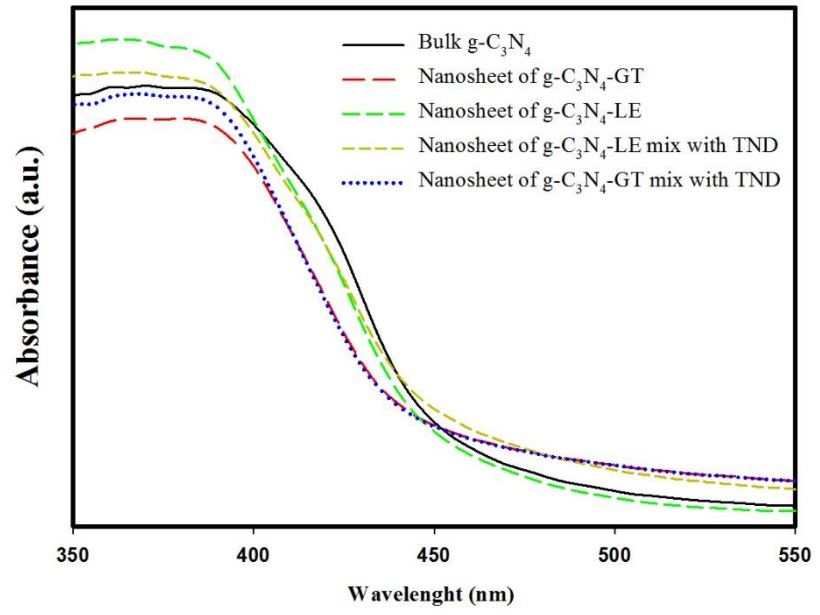

Figure 4.3. UV-visible absorption spectra of g-C_3N_4 bulk, g-C_3N_4 nanosheets prepared by gas template and liquid exfoliation, and nanosheets with TND before calcination

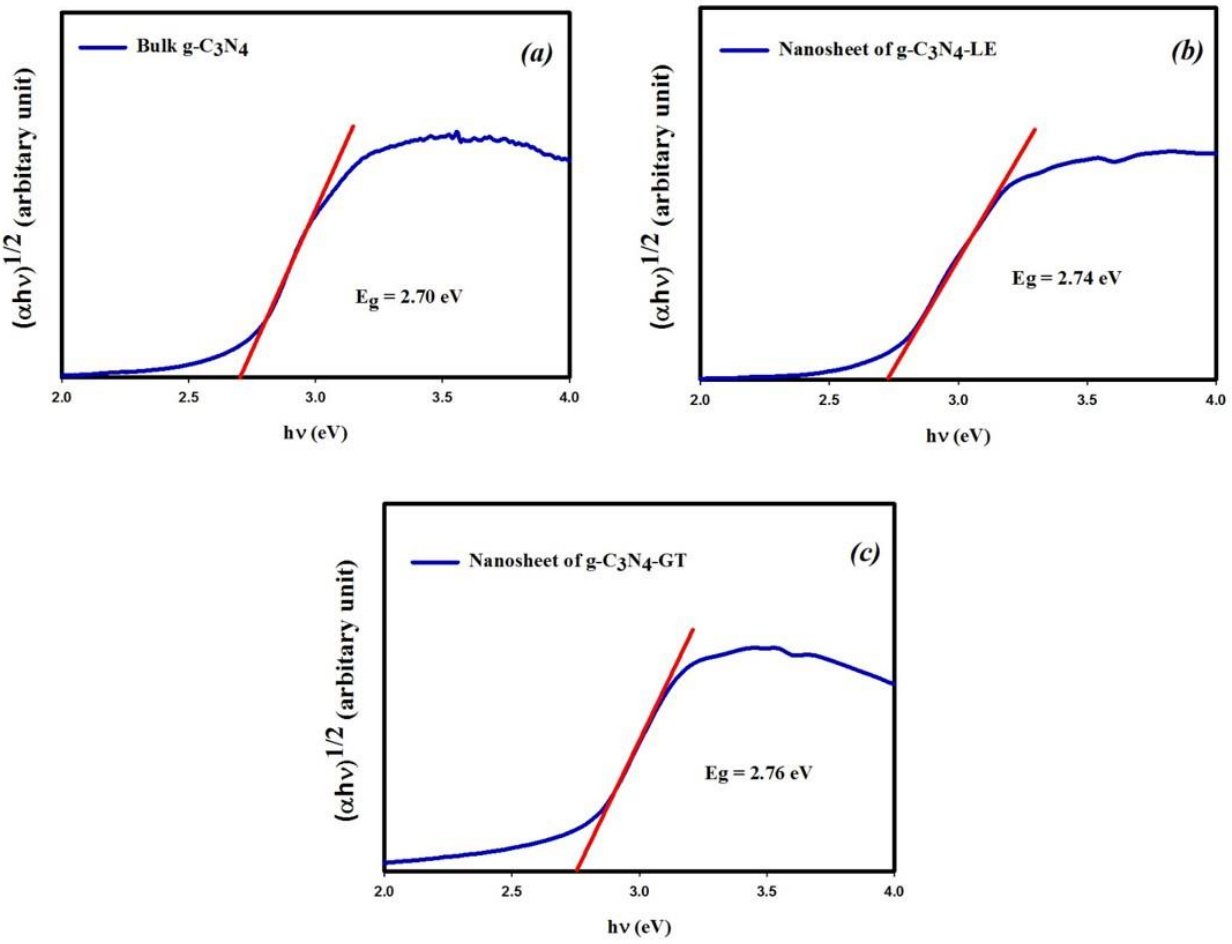

Figure 4.4. The estimated band gap energy of (a) bulk g-C_3N_4 (b) g-C_3N_4 nanosheet via liquid exfoliation method (c) g-C_3N_4 nanosheet via gas template method

and some absorbed water molecules. [229, 322] Some strong bands were observed at 1570-1634 cm^{-1} is owing to the presence of C=N and the peaks showed in the range of 1258-1480 cm^{-1} can be attributed to stretching modes of C-N heterocycles.[322] Some strong bands were observed at 1570-1634 cm^{-1} is owing to the presence of C=N and the peaks showed in the range of 1258-1480 cm^{-1} can be attributed to stretching modes of C-N heterocycles.[322] Moreover, the vibration in the region of 810-880 cm^{-1} corresponds to triazine unit characteristic of the chemical g-C_3N_4 structure [145, 323]

The nitrogen adsorption-desorption isotherms of the different samples are presented in Figure 4.6. As can be seen, they all are type IV, according to IUPAC classification, showing mesopores materials. [310, 316] The hysteresis loop of nanocomposite of g-C_3N_4 and TiO_2 becomes larger

and shifts to the lower pressure region in comparison to g-C_3N_4 nanosheets. This reveals that relatively larger mesopores are created during synthesis of the nanocomposite. Based on BET analysis the specific surface area of the nanocomposite is 75 m^2/g, which is higher than that of bulk g-C_3N_4 material (21 m^2/g) and g-C_3N_4 nanosheets (63 m^2/g).

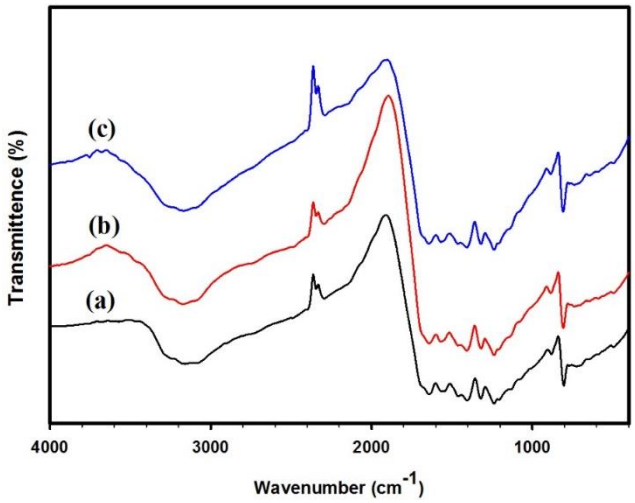

Figure 4.5. FTIR spectra of (a) bulk g-C_3N_4 and (b) and (c) g-C_3N_4 nanosheets obtained by liquid exfoliation and gas template, respectively.

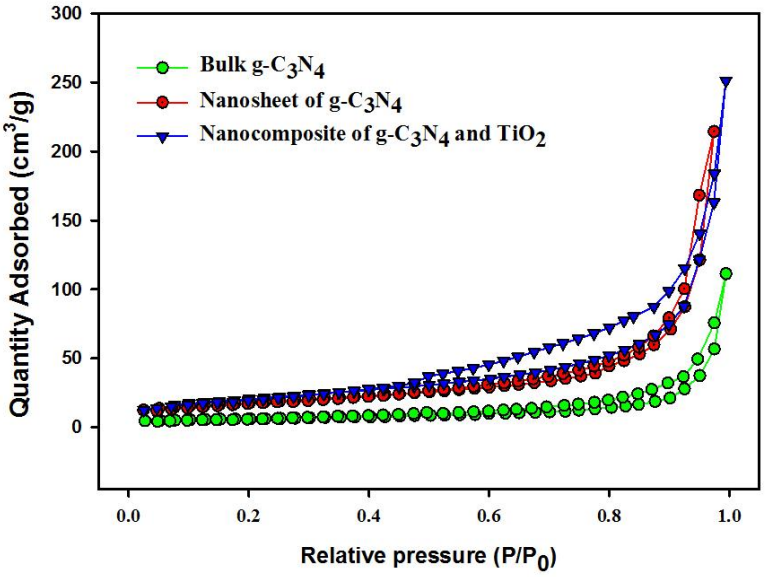

Figure 4.6. Nitrogen adsorption-desorption isotherms for the g-C_3N_4 bulk, g-C_3N_4 nanosheets, and g-C_3N_4/TiO_2 nanocomposite.

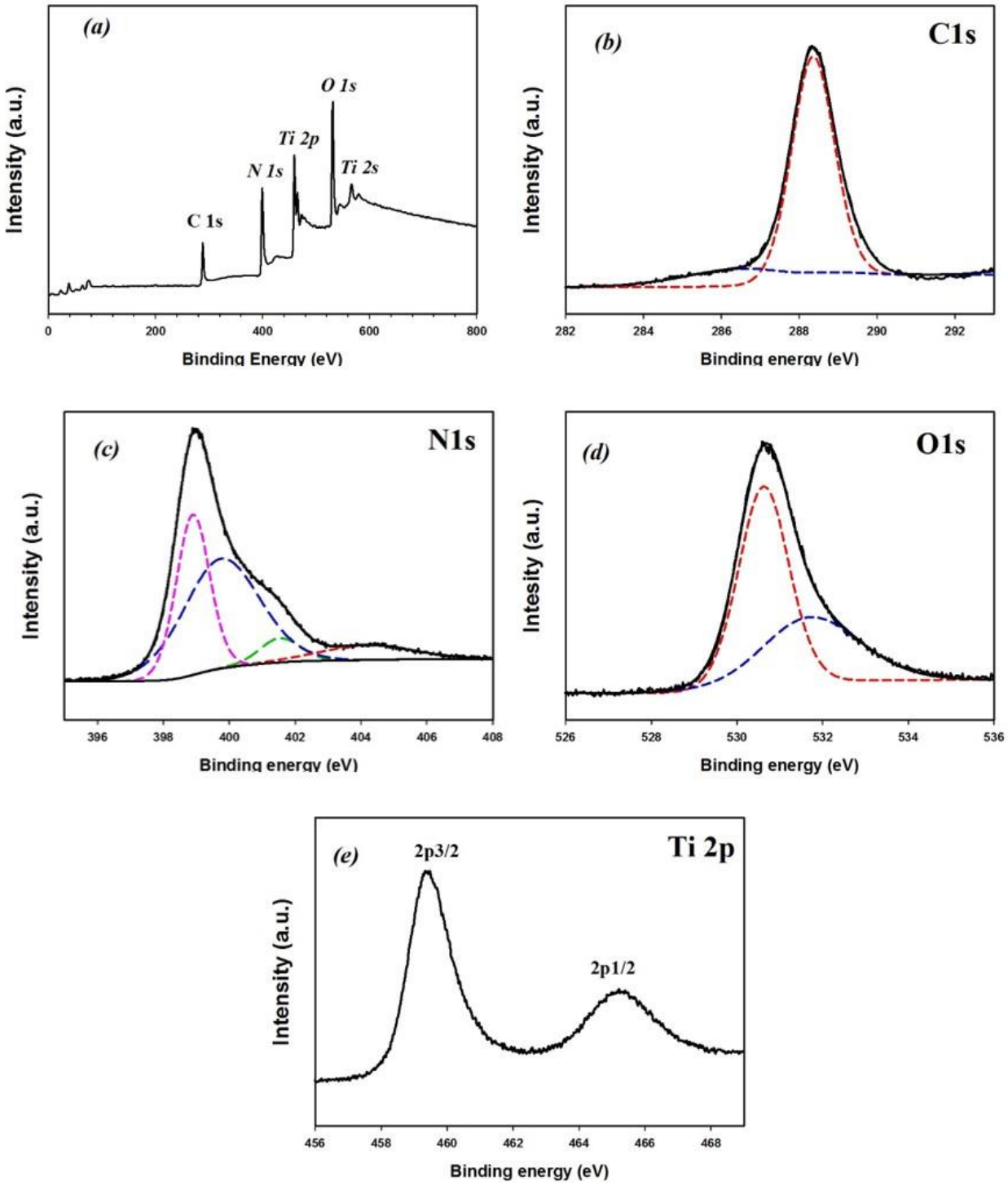

Figure 4.7. XPS survey spectrum of (a) the g-C_3N_4-TiO_2 nanocomposite. High resolution XPS spectra of (b) C 1s, (c) N 1s, (d) O 1s and (e) Ti 2p of the g-C_3N_4-TiO_2 nanocomposite.

Figure 4.7 displays XPS analysis of the g-C_3N_4/TiO_2 nanocomposites. As shown in Figure 4.7-a, the obtained nanocomposite consists of C, N, O and Ti which are located at binding energies of 288, 399, 530 and 459 eV, respectively. The high-resolution XPS spectrum of C 1s shown in Figure 4.7-b, can be fitted into two peaks at 286.1 and 288.4 eV, that are related to the C–N–C and the C–$(N)_3$ group of graphitic carbon nitride.[143, 324] The XPS spectrum of N 1s (Figure 4.7-c) can be ascribed to four different kinds of bonds as follows: C=N–C at 398.8 eV, tertiary nitrogen $(C)_3$–N at 399.7, N–H at 401.4 and π–excitation at 404.4.[310, 324] As illustrated in Figure 4.7-d, the O1s XPS spectrum can be deconvoluted into two main energy values of 530.6 and 531.8.[143] The first peak is associated with the O^{2-} in the TiO_2 and the other one is attributed of –OH bands on the nanocomposite surface. [315, 319, 325] The XPS Ti 2p high-resolution analysis (Figure 4.7-e) displays two main peaks at 459.4 and 465.1 related to binding energy of Ti $2p_{3/2}$ and $2p_{1/2}$, respectively, and are characteristic of Ti^{4+}.[316, 325]

4.3.2 Photocatalytic activity of nanocomposite for hydrogen production

Figure 4.8 displays hydrogen production under visible light illumination after 3 h. As it can be seen, the nanocomposites showed higher hydrogen evolution in comparison with pristine nanosheets of g-C_3N_4 prepared by two different methods (all samples containing 2 wt% Pt as a cocatalyst). Although both nanosheets of g-C_3N_4-LE and g-C_3N_4-GT produced about the same amount of hydrogen (734 and 726 μmol h^{-1} g^{-1}cat, respectively) after 3 h under visible light irradiation, their nanocomposites showed slightly different behaviours. As it is shown, the nanocomposite of g-C_3N_4-LE/TiO_2(70:30 wt%) could generate 1633 μmol h^{-1} g^{-1}cat of hydrogen, while the nanocomposite of g-C_3N_4-GT/TiO_2(70:30 wt%)produced 1886 μmol h^{-1} g^{-1}cat. This can be attributed to the higher surface area of g-C_3N_4-GT nanosheets and closer contact with TiO_2 nanoparticles. [167] According to the results of photocatalytic tests (Figure 4.8), the optimum amount of TiO_2 should be 30 wt%. Although 10 wt% loading of TiO_2 in the nanocomposite can improve charge separation as described in the next section, this amount is not sufficient to acquire the maximum hydrogen generation. Furthermore, by depositing 50 wt% of TiO_2 on the surface of g-C_3N_4 nanosheets, more surface of g-C_3N_4 is covered by TiO2 nanoparticle and so the visible light absorption of g-C_3N_4 is declined and as a result the hydrogen production is reduced significantly.[143]

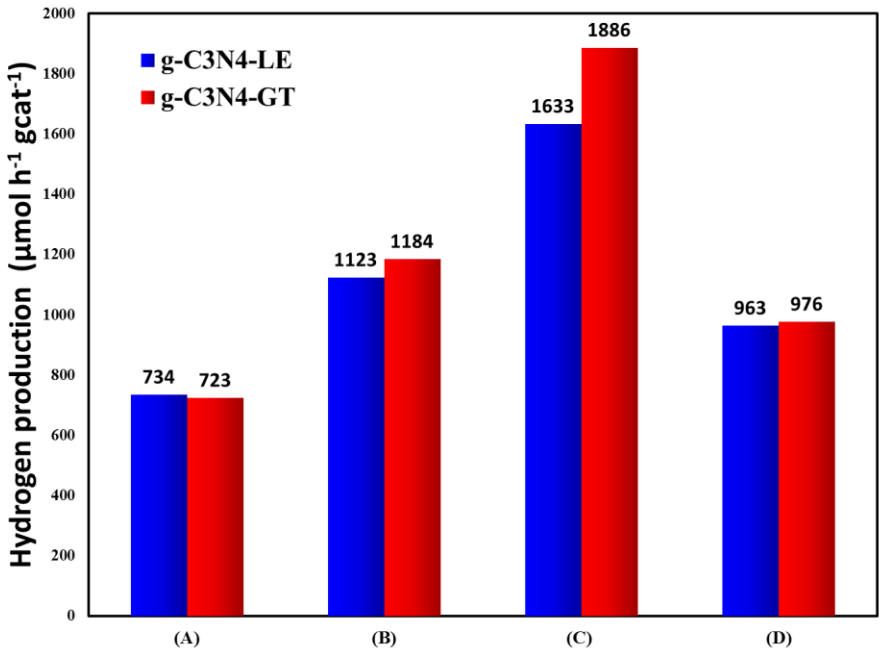

Figure 4.8. Hydrogen production of different nanocomposite under visible light irradiation after 3 h: (A) g-C_3N_4 nanosheets without TiO_2, (B) g-C_3N_4 nanosheets with 10wt% TiO_2, (C) g-C_3N_4 nanosheets with 30wt% TiO_2 and (D) g-C_3N_4 nanosheets with 50wt% TiO_2.

The mechanism of hydrogen production improvement of this nanocomposite is demonstrated in Figure 4.9.First, g-C_3N_4 nanosheet absorbs the photon energy of visible light and produces excited electrons and holes, which are generated in the conduction and valence bands, respectively. Because of ultrathin g-C_3N_4 nanosheets (thickness ~ 1-3 nm), photoexcited charge carriers can easily transfer to the surface of g-C_3N_4. Although excited holes remain on the g-C_3N_4 nanosheet valence band, photogenerated electrons can transfer from conduction band of g-C_3N_4 to TiO_2 nanoparticles because of lower conduction band edge of TiO_2 (as displayed in Figure 4.9). These electrons can move to Pt nanoparticles and reduce protons to hydrogen. As a result, photogenerated electrons and holes separate from each other and the probability of charge recombination declines significantly. Therefore, charge carriers in the proposed nanocomposite have longer lifetime than pristine g-C_3N_4 and so this nanocomposite could produce more hydrogen compared to g-C_3N_4 nanosheets.

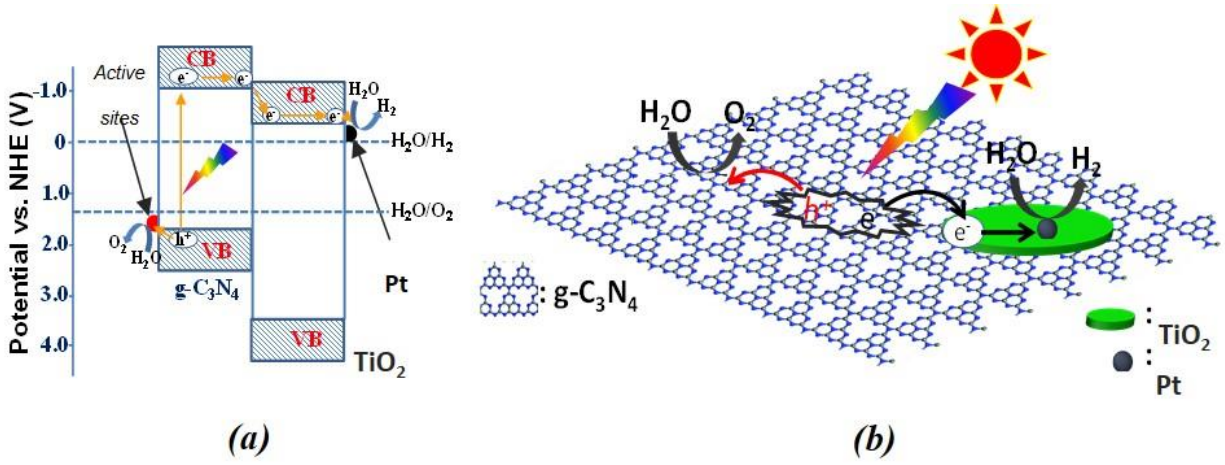

Figure 4.9. Schematic illustration of (a) potential energy diagram, (b) charge transfer in the nanocomposite of Pt-g-C_3N_4-TiO_2

4.4 Conclusion

Graphitic carbon nitride is a semiconductor that is activated under visible light illumination for hydrogen evolution from water. Many scientists have tried to improve its performance in order to obtain more hydrogen in the same conditions. One of the ways to gain more hydrogen is creation of novel nanocomposites of g-C_3N_4 with other semiconductors such as TiO_2. In this research, a nanocomposite of g-C_3N_4 nanosheets and titanate nanodisks (TNDs) has been proposed with the aim of raising hydrogen evolution efficiency. After synthesizing various nanosheets of g-C_3N_4 from different methods, TNDs were introduced by the impregnation technique. After drying and calcination, this nanocomposite showed almost doubled hydrogen production under visible light illumination which resulted from a better charge separation between g-C_3N_4 and TNDs. Therefore, charge recombination is partially prevented and so more excited electrons can react with protons and generate hydrogen molecules.

Chapter 5. Post-Calcined Carbon Nitride Nanosheets as an Efficient Photocatalyst for Hydrogen Production under Visible Light Irradiation

Mohammad Reza Gholipour,[a] François Béland[b] and Trong-On Do[a,*]

[a] Department of Chemical Engineering, Université Laval, Québec, G1V 0A6, Canada

[b] SiliCycle Inc., 2500, Boul. du Parc-Technologique

Québec (QC) G1P 4S6, Canada.

ACS Sustainable Chemistry & Engineering, **2017**, **5 (1)**, 213 – 220

Résumé

La production d'hydrogène par décomposition photocatalytique de l'eau en utilisant la lumière du soleil a un énorme potentiel pour résoudre la crise mondiale de l'énergie et de l'environnement. Le défi majeur dans ce processus est de développer des photocatalyseurs efficaces qui doivent satisfaire plusieurs critères tels qu'une forte absorption du rayonnement solaire, une séparation efficace des charges et une forte stabilité photochimique. Le nitrure de carbone graphitique est l'un des meilleurs semiconducteurs pour la production de l'hydrogène en raison de la position de ses bandes de valences et de conduction ainsi que de leur gap mais aussi en raison de sa haute stabilité chimique. Cependant, il produit une petite quantité d'hydrogène sous irradiation de la lumière visible en raison de sa petite surface et de son taux de recombinaison élevés. Dans ce travail, des feuilles nanométriques de nitrure de carbone graphitique avec des lacunes en carbone ainsi que des pores ont été synthétisés par un double traitement (traitement à l'argon suivi d'une calcination à l'air). Ces feuilles de nitrure de carbone post-calcinés présentaient une activité photocatalytique beaucoup plus élevée par rapport au nitrure de carbone graphitique brut. En déposant du platine en tant que cocatalyseur via un procédé de photodéposition, ce semi-conducteur a montré une amélioration notable de son taux de production d'hydrogène, dix fois plus que le nitrure de carbone graphitique brut. Sa vitesse de production de l'hydrogène était de 5261 $\mu mol.h^{-1}.g^{-1}$ sous éclairage lumineux visible avec une efficacité quantique de 29,2% à 400 nm et 21,3% à 420 nm. Ce rendement élevé pour la production d'hydrogène pourrait être due à une plus grande surface spécifique, à une extension de l'absorption de lumière visible et à des centres de recombinaison de charge plus faibles dans tout le semi-conducteur. En outre, par étape de récurrence dans l'air, certains défauts sont introduits dans la structure des feuilles de nitrure de carbone en raison de postes vacants au carbone. Ces défauts sont considérés comme des sites photocatalytiques très actifs pour la production d'hydrogène.

Abstract

Hydrogen production via photocatalytic water splitting using sunlight has an enormous potential to solve the worldwide energy and environmental crisis. The key challenge in this process is to develop efficient photocatalysts which must satisfy several criteria such as strong sunlight absorption, effective charge separation, and high photochemical stability. Graphitic carbon nitride is one of the best semiconductors for hydrogen evolution because of its conduction band edge, narrow band gap, and high chemical stability. However, it produces a little amount of hydrogen under visible light irradiation due to its small surface area and high recombination rates. In this work, nanosheets of graphitic carbon nitride with carbon vacancies and nanoholes were synthesized by two-step treatment process (argon treatment followed by air calcination). These post-calcined carbon nitride nanosheets exhibited much higher photocatalytic activity compared to common graphitic carbon nitride. By depositing platinum as a cocatalyst via photodeposition method, this semiconductor showed noticeable improvement in hydrogen production rate by ten times as much as graphitic carbon nitride. Its hydrogen evolution rate was 5261 μmol h^{-1} g^{-1} under visible light illumination with a quantum efficiency of 29.2% at 400 nm and 21.3% at 420 nm. This high amount of hydrogen production rate could be due to large specific surface area, an extension of visible light absorption tail-end and lower charge recombination centers throughout the semiconductor. In addition, by recalcination step in air, some defects are introduced into the structure of carbon nitride nanosheets owing to carbon vacancies. These defects are considered as highly active photocatalytic sites for hydrogen production.

5.1 Introduction

Development of technology requires a cheap and accessible source of energy. Although fossil fuels are the most well-known sources of energy for their low cost and availability, they have some important issues for human mankind such as emitting a high amount of carbon dioxide into the atmosphere which is believed to be the main reason of the greenhouse effect and climate change. Others claim that fossil fuel resources are limited and cannot be recovered once they are used. Therefore, researchers have tried to find other alternatives for fossil fuels and the best option is solar energy.

Solar energy is abundant and only a very small amount of it can provide all the energy demands of humanity around the world for one year.[16, 77] Moreover, this source of energy is renewable and sustainable, which means there is no way to over-consume it in present or future. Interestingly, sunlight energy is environmentally friendly and it doesn't produce any harmful gases as a result we won't have any climate crisis in the future.[16] However, using this source of energy is quite expensive and so it is very difficult to utilize it in large scale applications.

Hydrogen molecules can act as an energy carrier in order to store solar energy and use it later. One of the best promising ways to produce hydrogen energy is splitting water into hydrogen and oxygen with the photocatalytic process. A photocatalyst is a semiconductor that can absorb sunlight energy and generate excited electrons and holes. These charge carriers can perform redox reactions with water molecules and so generate hydrogen and oxygen.[326] One of the best photocatalysts for using solar energy is graphitic carbon nitride (g-C_3N_4), because of its low band gap energy that can utilize visible light to produce hydrogen from water.[312, 327]

Graphitic carbon nitride (g-C_3N_4) is a semiconductor consisting of tri-s-triazine units positioned in a two-dimensional graphitic-like polymer structure.[152] Due to its proper conduction band-edge position and narrow band gap, which is between 2.7-2.9 eV corresponding to wavelengths of 460-430 nm, it can generate hydrogen from water splitting under visible light irradiation.[153, 328] However, its quantum efficiency is very low mainly due to its small specific surface area and rapid charge recombination rate.[151, 329] The main synthesis method of g-C_3N_4 is a thermal condensation (at 500-550°C for 2-4 h) of nitrogen-rich precursors such as cyanamide, dicyandiamide, urea, and melamine.[77, 153, 330] Thermogravimetric analysis (TGA) exhibits that

g-C_3N_4 is stable up to 600°C even in the air, but becomes slightly unstable above this temperature, and at 700°C, it completely disappears even under an inert gas condition.[328, 331, 332]

Various methods and techniques were proposed in order to enhance the photocatalytic activity of g-C_3N_4 and they can be classified into four main groups as electronic structure modulation, nanostructure design, crystal structure engineering and heterostructure construction.[153, 329]Some of them such as synthesizing nanosheets of g-C_3N_4 can enhance hydrogen evolution significantly due to high specific surface area, enhancing charge carriers mobility and providing less charge recombination centers.[167, 169, 333, 334] In this work, a facile two-step synthesizing method for the synthesis of g-C_3N_4 nanosheets with some carbon vacancies and micropores is proposed that can considerably increase hydrogen production under visible light illumination. This photocatalyst showed a quantum efficiency of 29.20% at 400 nm, which is among the highest quantum efficiencies that have been reported, previously.

5.2 Experimental section

5.2.1 Sample Preparation

Bulk g-C_3N_4 was synthesized from dicyandiamide as reported in other literature.[156, 168, 335] Briefly, the precursors were calcined in a muffle furnace at 550°C in air for 4 h. Then, the obtained bulk g-C_3N_4 (GCN) was washed with distilled water several times. After this step, the photocatalyst was heated to 650°C under argon gas flow of 200 ml/min for 2h (argon treatment of g-C_3N_4, noted as AGCN). After this stage is completed, the obtained material was calcined again in the air, in a muffle furnace at 500°C for 2hr (recalcination of AGCN of g-C_3N_4 in air, noted as SGCN). Then, the material was washed several times with water to remove contaminants and dried in an oven overnight at 70°C.

5.2.2 Characterization

Transmission electron microscopy (TEM) images of the samples were obtained on a JOEL JEM 1230 operated at 120kV. Powder X-ray diffraction (XRD) patterns of the samples were

obtained on a Bruker SMART APEXII X-ray diffractometer equipped with a Cu Kα radiation source (λ=1.5418 Å). X-ray photoelectron spectroscopy (XPS) measurements carried out in an ion-pumped chamber (evacuated to 10^{-9} Torr) of a photoelectron spectrometer (Kratos Axis-Ultra) equipped with a focused X-ray source (Al Kα, hν = 1486.6 eV). The UV-vis spectra were recorded on a Cary 300 Bio UV-visible spectrophotometer. Fourier transform infrared (FTIR) absorption spectra were measured with an FTS 45 infrared spectrophotometer with the KBr pellet technique. The photoluminescence (PL) spectra were measured with the Horiba Jobin Yvon Nanolog spectrofluorimeter equipped with a 450W Xenon lamp as a source, a double monochromator for both excitation and detection, and a photomultiplier tube (PMT) detector sensitive from 250 to 850 nm. Nitrogen adsorption-desorption isotherms of the samples were measured at -196°C using Micromeretics ASAP 2010 instrument. Before the measurements, the samples were outgassed under vacuum for 6 h at 150 °C. The total pore volume (V_{pore}) was calculated from the amount of nitrogen adsorbed at $P/P_0 = 0.95$.

5.2.3 Photocatalytic test

The certain amount of photocatalysts (the optimum amount was 50 mg) was added to the 100 ml of aqueous solution of 10% triethanolamine as a sacrificial reagent. After that, the mixture was purged with nitrogen for 10 min and then under the solar simulator light, 2 wt% Pt as the co-catalyst was deposited via photodeposition technique for 2 hr. Then, the cell was purged again with nitrogen for 30 min and after the sample was ready for hydrogen production test during 3-hour cycles.

The quantum efficiency of the prepared sample was calculated according to follow equations [30, 336]:

$$\text{Quantum Efficiency (QE)} = \frac{\text{Number of reacted electrons}}{\text{Number of incident photons}} \times 100 \qquad \text{(Eq. 5.1)}$$

$$= \frac{2 \times \text{Number of evolved hydrogen molecules}}{\text{Number of incident photons}}$$

5.3 Result and discussions

5.3.1 Material characterization

Figure 5.1 demonstrates a 2D nanosheet of SGCN sample after recalcination in air in different scales. Although the nanosheet length and width are more than several hundred nanometers (Figure 5.1-A,B), AFM analysis shows that the thickness of the nanosheet hardly reaches to 10 nm (Figure 5.1-G,H).[154, 155, 337] Furthermore, as can be seen in Figure 5.1-E, there are some uniform small white dots all over the nanosheets that can be described as nanoholes and carbon vacancies generated during the second calcination step in air.[337] Due to the layered structure of graphitic carbon nitride, these vacancies were created homogeneously inside of the nanosheet planes. These vacancies with a size of less than 10 nm not only can act as active sites but also they can change the bandgap of the photocatalyst by introducing additional energy levels.[63, 178, 183] It should be noted that these in-plane nanoholes can noticeably enhance mass and charge transfer across the nanosheets of SGCN during photocatalytic process.[184, 337] Moreover, ultrathin nanosheets provide shorter pathways for photoexcited charges to migrate significantly shorter distances from the bulk material to the reaction sites located on its surfaces.[23, 27, 77] In addition, carbon vacancies can act as new active edges and cross-plane diffusion channels that can greatly speed up mass transfer and the diffusion of photogenerated charge carrier.[184, 337] Therefore, charge carriers can travel shorter distances between the inside of the nanosheets and their surfaces in order to reach the active sites and so the chance of their recombination reduced dramatically. Figure 5.1-F displays an TEM image of SGCN with photodeposited platinum nanoparticles after photocatalysis reaction. It is obvious the cocatalyst particles are uniformly deposited on the surface of nanosheets of SGCN.

Figure 5.2 displays the N_2 adsorption/desorption isotherms of three samples: GCN, AGCN, and SACN at 77K. All of the samples showed a type IV isotherm and their adsorption capacity enhanced significantly with increasing the relative pressure (P/P_0: 0.9~1), The specific surface area measured by the BET technique increased considerably and reached to 160 $m^2\ g^{-1}$ for SGCN (Table 5.1). This specific surface area is much higher than those of AGCN and GCN, which were 46 and 28 $m^2\ g^{-1}$, respectively. It should be noted that the total pore volume of SGCN (1.47 $cm^3\ g^{-1}$) is around 13 times higher than that of GCN (0.12 $cm^3\ g^{-1}$). This increase in specific surface area and

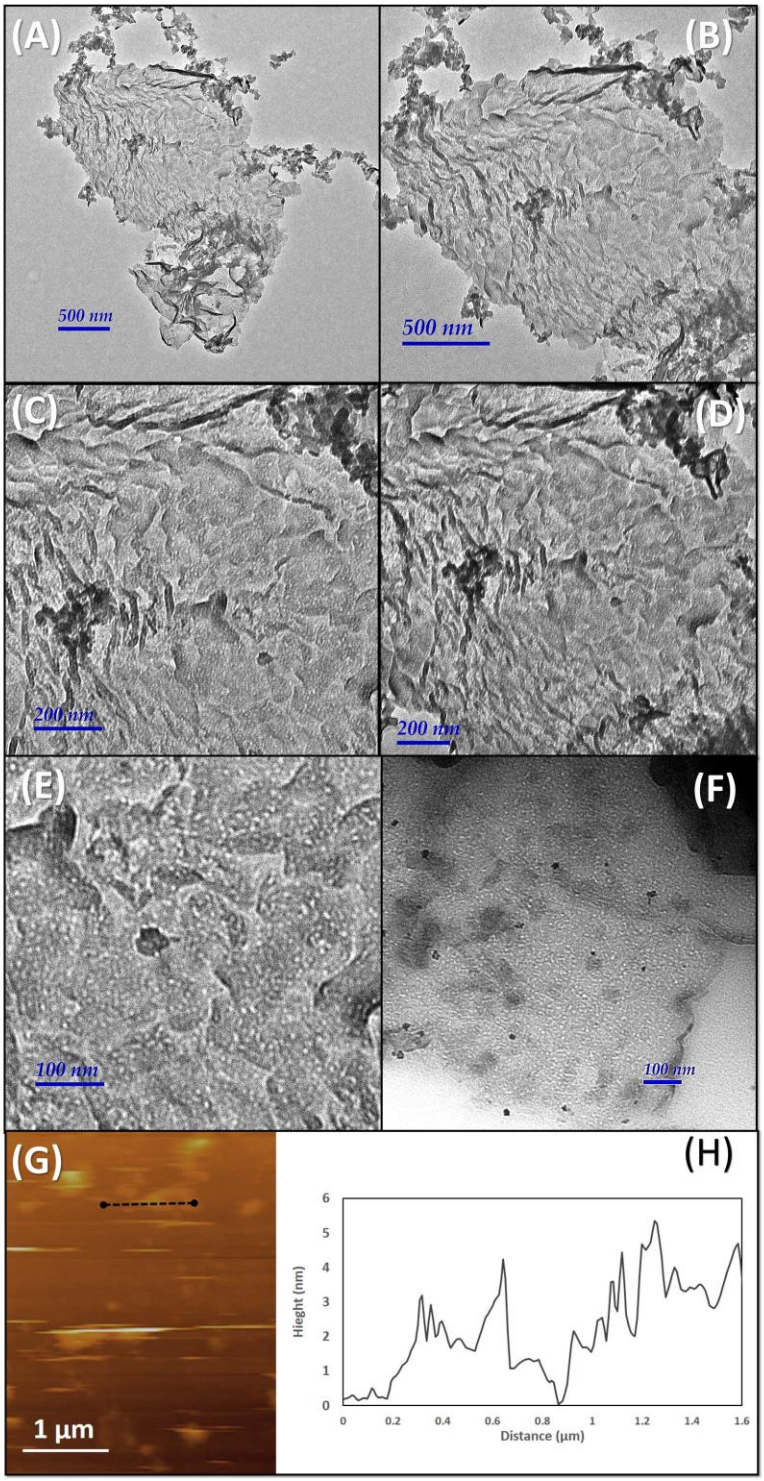

Figure 5.1. TEM images of 2-dimensional SGCN nanosheets after recalcination in air in different scales (small white dots show nanoholes inside of the nanosheet of SGCN). F) Nanosheets of SGCN with 2% Pt after photodeposition. G) Representative AFM image of SGCN and H) corresponding cross-sectional profile of typical SGCN.

total pore volume is due to a large number of in-plane holes and the crumpled structure. Furthermore, the BJH pore size distribution curves were also demonstrated in Figure 5.2-inset. Although it seems that the pore size distribution of GCN and AGCN argon-treated at 650 °C were almost similar, treatment in argon at high temperature led to having more uniform pore sizes distribution. Nevertheless, the SGCN showed a wide range of pore sizes between 1 nm and 5 nm that demonstrated the SGCN is the mixture of micropores and mesopores. These pores were mainly related to inter-particle distances and carbon vacancies throughout the SGCN nanosheets that were made during second calcination in air as described in TEM images (Figure 5.1). [158, 184, 337]

Samples	***Total pore volume*** ***(cm^{-3} gr^{-1})***	***BET surface area*** ***(m^2 gr^{-1})***	***Bandgap (eV)***	***Hydrogen Production*** ***(μmol h^{-1} g^{-1})***
GCN	0.12	28.0	2.75	647.5
AGCN	0.52	45.0	2.56	771.5
SGCN	1.47	160.0	2.79	5262.0

Table 5.1. Total pore volume, specific surface area, band gap values, and hydrogen generation rate of GCN, AGCN and SGCN

Figure 5.3 shows the XPS spectra of the bulk sample (GCN) after different treatments; argon treatment (AGCN), followed by calcination in air (SGCN). As seen in Figure 5.3, the C 1s and N 1s XPS spectra of GCN, AGCN, and SGCN are almost similar to each other. Nonetheless, an increase in the intensities of AGCN and SGCN illustrated that C and N atoms neighboring carbon vacancies get fewer electrons than those ones on the normal sites.[337] As seen in Figure 5.3-A, the C 1s XPS spectrum of GCN can be deconvoluted into two main peaks at 285.0 and 288.1 eV, which are attributed to C−C and N−C=N, respectively.[153] Moreover, the C 1s XPS spectra of AGCN and SGCN can be resolved into two additional peaks. The peak observed at 289.6 eV can be corresponding to the sp^2 carbon of tri-s-triazine units attached to the NH group (sp^2 C−NH). The other peak at 286.5 eV is related to sp^3 C atoms in the structure of carbon nitride. Furthermore, the absorptions detected around 294 eV have been assigned to the charge effect of electronic delocalization associated with the presence of conjugation.[158]

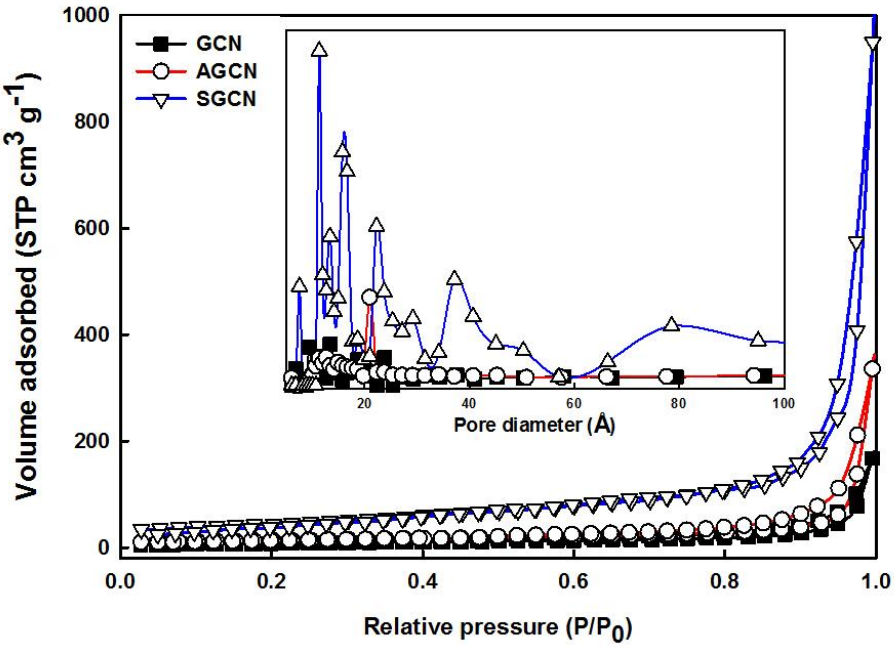

Figure 5.2. Nitrogen adsorption-desorption isotherms at 77 K and relating pore size distribution curves of GCN, AGCN, and SGCN (inset)

In the N 1s XPS spectra (Figure 5.3-B), the main curve can be divided into four peaks. The peaks located at 398.7 eV is related to the sp^2-bonded nitrogen in C−N=C and the peaks corresponding to the nitrogen in the tertiary group (N− $(C)_3$) are located at 400.1 eV. Moreover, the amino-functional groups with a hydrogen atom C−NH can be attributed to 401.5 eV and the absorption at 404.0 eV is due to a positive charge localization in heptazine rings.[158, 159] According to these XPS analyses, during argon treatment at high temperature some carbon atoms in the structure of GCN became loose and as a result a few of them were able to leave the bulk material and left some carbon vacancies behind in the SGCN. Following by further calcination in air, more loose carbons were able to leave carbon nitride. As a result, not only the number of carbon vacancies increased, but also some uniform nanoholes were produced.

In order to investigate the valence state of platinum as a cocatalyst, XPS analysis of Pt4f after photocatalysis reaction was conducted. The main peak of Pt 4f can be deconvoluted into two peaks at 70.4 and 73.9 eV, which are ascribed to metallic Pt 4f7/2 and Pt 4f5/2, respectively.[338-340]

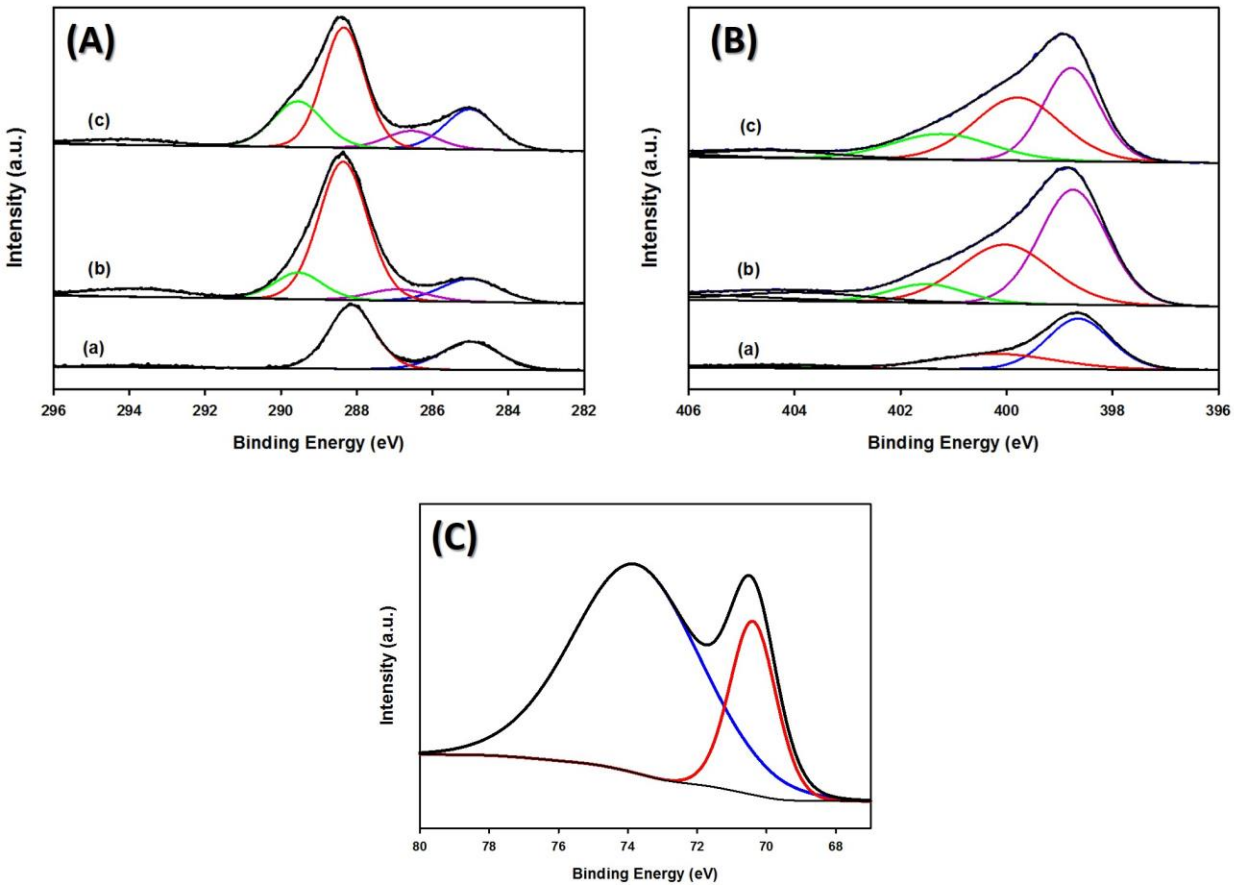

Figure 5.3. High-resolution XPS survey spectra of A) C 1s and B) N 1s for a) GCN, b) AGCN and c) SGCN. C) High-resolution XPS of the Pt4f region for Pt-SGCN photodeposited after photocatalysis

Figure 5.4 presents the X-ray diffraction (XRD) results of the synthesized bulk g-C_3N_4 material after different treatments. The crystal structure of bulk g-C_3N_4 (e.g., GCN) is shown by two main peaks of (100) and (002), which are located at 13.1° and 27.4°, respectively. The former peak ascribed to the in-plane trigonal nitrogen linkage of tri-s-triazine units and the latter one related to the periodic stacking of layers of conjugated aromatic systems. [153] The disappearance of 13.1° peak of AGCN shows that the long-range order of atomic arrangements in graphitic layers of AGCN were destroyed and as a result, AGCN can be considered as an amorphous phase of carbon nitride.[155, 158, 337, 341] In addition, the other peak with very low intensity at 27.4° indicates that we have g-C_3N_4 nanosheets, as displayed in TEM images. In other words, the distance between different layers of g-C_3N_4 increased significantly and so nanosheets of g-C_3N_4 were obtained.[154, 159]

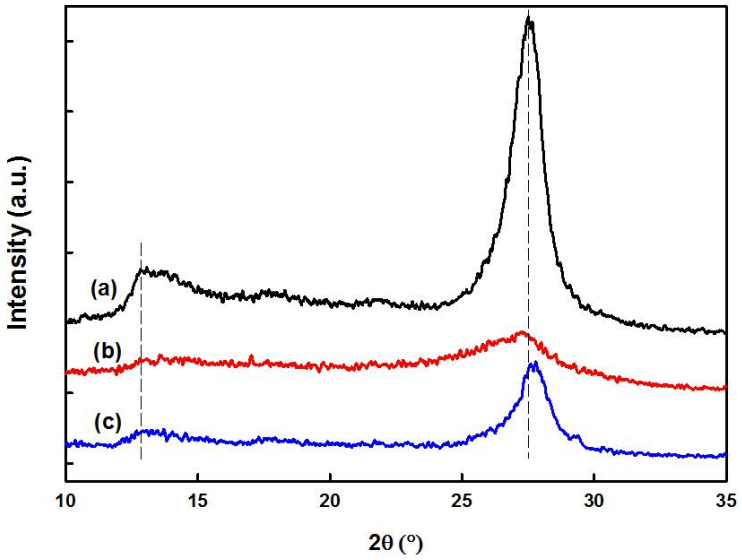

Figure 5.4. X-ray diffraction analyses of a) GCN, b) AGCN and c) SGCN

After recalcination in air (e.g., SGCN sample), the crystal structure of carbon nitride nanosheets improve moderately, and as a result, the two peaks appeared again. However, because of obtaining nanosheets and some vacancies inside of the planes of graphitic carbon nitride, the restructuring could not be completed and so the intensity of (002) peak wasn't as high as GCN. It is worth mentioning that during recalcination, most of the weak-bonded carbon and nitrogen atoms left from the bulk material in forms of various gases. These generated gases acted as a soft template in order to produce ultrathin nanosheets of graphitic carbon nitride.[167] In addition, this leaving of weak-bonded atoms generated much more vacancies and nanoholes throughout the nanosheets, which improved hydrogen generation in various ways as mentioned earlier.[156, 342]

Figure 5.5 illustrates the FTIR spectra of the GCN, AGCN, and SGCN samples to investigate their graphitic structures. The strong peak at 810 cm^{-1} is attributed to the typical breathing mode of tri-s-triazine units.[145] The absorption bands between 1200 and 1700 cm^{-1} region related to different stretching vibrations of heptazine-derived repeating units.[310, 343] In addition, broad peaks from 3000 to 3400 cm^{-1} corresponding to N-H band, which is caused by uncondensed amino functional groups in the products.[344] There is no difference between FTIR spectra of the three materials suggesting that the nature of carbon nitride was preserved during argon treatment and recalcination in air.

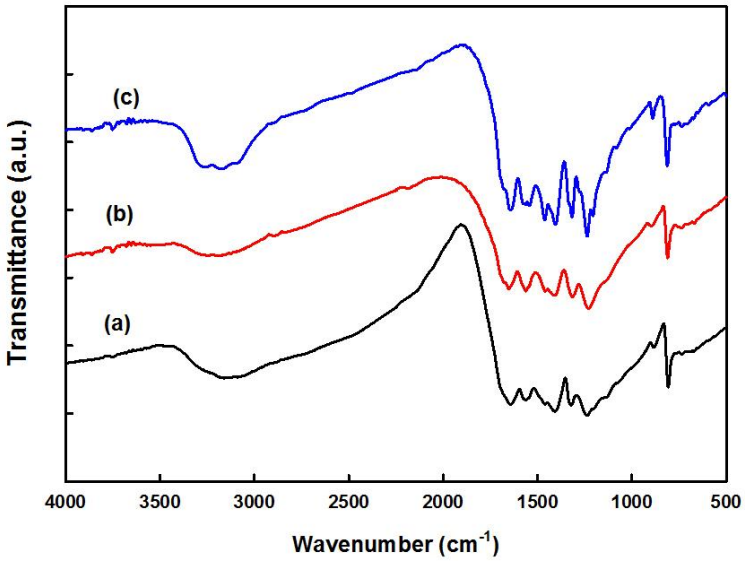

Figure 5.5. FTIR spectra of a) GCN, b) AGCN and c) SGCN

UV-visible spectroscopy is usually used in order to measure the light absorption capacity of the semiconductors and also its data can be used to calculate band structure and band gap of a photocatalyst. UV-visible spectra of GCN, AGCN and SGCN were presented in Figure 5.6. GCN can absorb visible light with a wavelength of 420 nm, because of its low band gap (2.75 eV). After argon treatment at 650°C, the UV-vis spectrum of AGCN shifted to the red region and its band gap reduced to 2.56 eV (Figure 5.6-B). Even though it could absorb visible light with a longer wavelength, it couldn't produce more hydrogen than GCN. This is due to its low crystallinity (essentially amorphous phase) and a high number of recombination centers. In addition, the band structure of AGCN seemed to not develop completely because of observing two stages in its UV-visible spectrum (the curve is different below and above 450 nm). Nonetheless, the SGCN spectrum showed that by recalcination in air, its curve shifted to blue region and so the band gap increased (to 2.79 eV). Moreover, this recalcination step helped to improve crystal structure and as a result, more charge carriers can transfer more easily across the nanosheets with limit recombination together. In addition, another absorption tail started at 430 nm to around 600 nm exhibited that the SGCN can absorb more visible light energy in comparison with GCN. It is worth mentioning that this crystallinity changes between amorphous and graphitic layer structure of nanosheets may introduce some different band energy inside the band gap structure as shown by Chen et al.[179]

These intermediate band energies can promote charge excitation as well as charge lifetime. In other words, not only charge excitation step become easier, but also photo-excited charge carriers have different stages which could help them to have less recombination process.

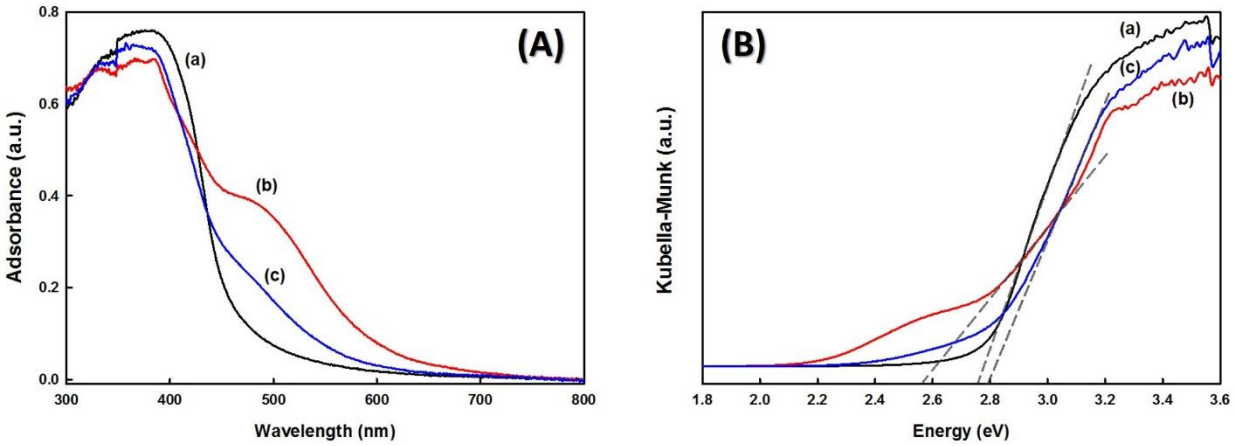

Figure 5.6. A) UV-visible absorption spectra and B) Kubelka-Munk function curves of a) GCN, b) AGCN and c) SGCN

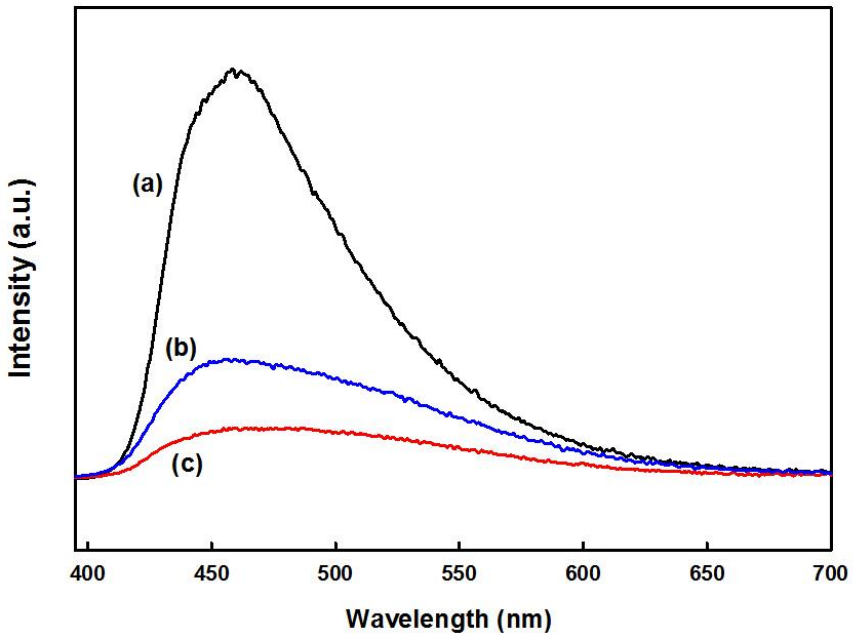

Figure 5.7. Photoluminescence spectra (390 nm excitation) of a) GCN, b) AGCN and c) SGCN (Steady state emission spectra were recorded on powdered sample under excitation wavelength of 380 nm.)

Figure 5.7 displays the steady-state photoluminescence spectra of all three samples. The prepared bulk GCN showed the highest peak intensity with respect to AGCN and SGCN relating to high radiative recombination of photoexcited electrons and holes.[155, 179, 345] In contrast, SGCN exhibited the lowest peak intensity, suggesting much lower charge recombination process during photocatalytic activity.

5.3.2 Photocatalytic hydrogen production

Figure 5.8-A demonstrated the hydrogen production of the three samples: GCN, AGCN and SGCN via solar simulator system with full spectrum. As seen in Figure 7-A, AGCN could only improve slightly hydrogen generation compared to that of GNC. However, SGCN could enhance hydrogen evolution more than eight times higher than GCN (5261 μmol h^{-1} g^{-1} for SGCN and 647 μmol h^{-1} g^{-1} for GCN). This considerable increase in hydrogen generation is mainly due to the presence of carbon vacancies, the high surface area and the extension tail of light absorption. The carbon vacancies not only can act like trapping spot for excited charge carriers, but also they promote mass transfer between nanosheets that help to have a higher hydrogen generation. Furthermore, these nanoholes inside of SGCN nanosheets could act as active sites for reactants. Moreover, the improvement in the structure of SGCN after the second calcination as shown in Figure 5.4, enhance the charge mobility inside of the nanosheet of graphitic carbon nitride.

For further investigation, hydrogen generation under visible light with the same system was studied with applying a light filter that surpasses wavelengths of lower than 420 nm (Figure 5.8-B). Due to a decrease in the band gap of AGCN and the fact that it can absorb more visible light, it could produce more hydrogen than GCN under visible light irradiation. The hydrogen evolution rates were 104 and 85 μmol h^{-1} g^{-1} for AGCN and GCN, respectively. However, SGCN showed significantly higher hydrogen production in the same conditions in comparison with the other two samples. Interestingly, it generated 387 μmol h^{-1} g^{-1} hydrogen, which was about 4.5 times higher than that of GCN.

Furthermore, the quantum efficiency of SGCN was also calculated with different band-pass filters (band-pass filters at 400, 420, 460, 500 and 550 nm). As it exhibited in Figure 5.8-C, the highest quantum efficiency was 29.2% which was obtained at 400 nm. This amount is among the

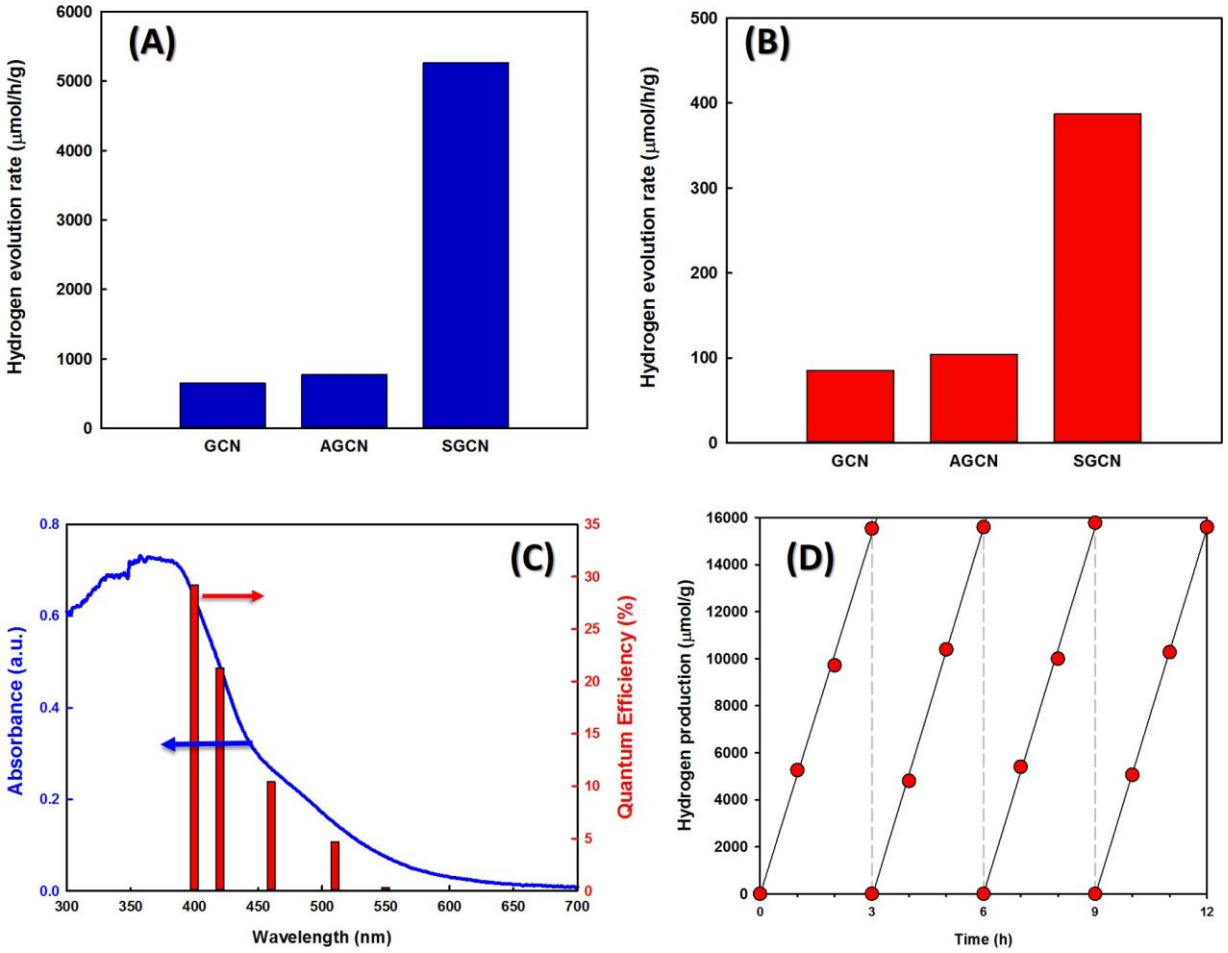

Figure 5.8. A) Hydrogen evolution rate under full spectrum via solar simulator system. B) Hydrogen generation rate under visible light irradiation with a solar simulator ($\lambda > 420$ nm).C) UV-visible spectrum and quantum efficiency of the SGCN sample. D) Hydrogen production of the SGCN for 4 cycles. Reaction conditions: 50 mg of photocatalyst loaded with 2 wt% of Pt cocatalyst; 100 ml of H_2O containing 10 vol.% triethanolamine under simulator solar light 1.5 AM (ABET), equipped with 150 W Xe lamp.

highest quantum efficiency which was reported for graphitic carbon nitride under visible light illumination. In addition, the quantum efficiency calculated at 420 nm was 21.3% that shows very high hydrogen evolution in the visible light region. Because of the large band gap of SGCN nanosheets, the quantum efficiency decreased for longer light wavelengths and reached to almost 0.34% for 550 nm (Figure 5.8-C). Furthermore, the SGCN generated hydrogen over 12 h without any reduction in its activity for hydrogen production (Figure 5.8-D). It is worth mentioning that the SGCN has a great potential in order to combine with other semiconductors (nanocomposite

systems) and metals (as cocatalysts), because of its special properties such as large surface area and having enormous active sites all over the nanosheets of SGCN.

5.4 Conclusion

Photocatalytic hydrogen evolution from sunlight energy is one of the best options to replace with fossil fuels. Graphitic carbon nitride is one of the best photocatalysts for hydrogen production under the visible light because of its low band gap that can absorb the energy of light in a visible region. By synthesizing post-calcined nanosheets of graphitic carbon nitride with facile two-step calcination (argon treatment followed by air recalcination), ultrathin nanosheets of carbon nitride with carbon vacancies and nanoholes were obtained. This photocatalyst showed considerably high specific surface area (160 m^2/g) and better crystallinity compared to the amorphous phase of carbon nitride. Existing of nanoholes and carbon vacancies throughout the nanosheets caused to have more active sites for reactants as well as more charge trapping centers that can reduce charge recombination process. By applying platinum as a cocatalyst, this new photocatalyst could generate hydrogen at a rate of 5261 $\mu mol\ h^{-1}\ g^{-1}$ under sunlight irradiation. Moreover, the hydrogen evolution rate under visible light ($\lambda \geq 420$ nm) was around 387 $\mu mol\ h^{-1}\ g^{-1}$. In order to compare this novel photocatalyst with graphitic carbon nitride the quantum efficiency (Q.E.) of the band-pass filter was calculated. The Q.E. at 400 nm was 29.2% and at 420 nm was 21.3%. These values are among the highest quantum efficiencies that were reported for graphitic carbon nitride under visible light illumination.

Chapter 6. Hollow Microspheres of $Zn_xCd_{1-x}S$ Solid Solution with Noble-metal-free Co-catalysts for Hydrogen Evolution with High Quantum Efficiency in Visible Light

Mohammad Reza Gholipour,[a] Chinh Chien Nguyen,[a] François Béland[b] and Trong-On Do[a,*]

[a] Department of Chemical Engineering, Université Laval, Québec, G1V 0A6, Canada

[b] SiliCycle Inc., 2500, Boul. du Parc-Technologique

Québec (QC) G1P 4S6, Canada.

Revised to Journal of Photochemistry and Photobiology A: Chemistry, December 2017

Résumé

L'utilisation de l'énergie solaire pour produire de l'hydrogène à partir de l'eau est l'une des technologies clés qui traitent des problèmes d'énergie et d'environnement. Un photocatalyseur à petit gap avec une bonne séparation des charges et une grande stabilité peux jouer un rôle important dans ce processus. Récemment, le sulfate de zinc et de cadmium ($Zn_xCd_{1-x}S$) a attiré l'attention des chercheurs en raison de ses propriétés photocatalytiques uniques telles que sa large absorption du spectre lumineux visible et une forte stabilité lors de la production de dihydrogène. En outre, la caractéristique unique de ce semi-conducteur est sa capacité à modifier la distance entre ses bandes de conduction et de valence en modifiant le rapport Zn / Cd. Dans ce projet, une série de solution solide $Zn_xCd_{1-x}S$ a été synthétisée en utilisant du glycérol métallique suivi d'une calcination dans l'air et de la sulfuration dans un flux de H_2S. Cette nouvelle méthode a abouti à la création d'une solution solide homogène de wurtzite hexagonale qui pourrait produire une quantité massive d'hydrogène par absorption d'une grande partie de la lumière visible. En outre, l'application de MoS_2 en tant que cocatalyseur par la technique de la photo-dépôt, a généré la même quantité d'hydrogène que l'utilisation de Pt comme cocatalyseur. Les meilleurs résultats ont été obtenus par une solution solide $Zn_{30}Cd_{70}S$ qui pourrait générer plus de 12 $mmol.h^{-1}.g^{-1}$ sous la lumière d'un simulateur solaire. Il convient de mentionner qu'il existait des rendements quantiques très élevés ; 46,6% à 400 nm à 23,4% à 500 nm ainsi que 11,3% à 550 nm. Ils sont parmi les rendements quantiques les plus élevés qui ont déjà été signalés pour ce type de matériaux dans la région de la lumière visible.

Abstract

Utilizing solar energy in order to produce hydrogen from water is one of the key technologies to deal with energy and environment issues. A photocatalyst with a small band gap, good charge separation, and high stability plays an important role in this process. Recently, zinc cadmium sulfide ($Zn_xCd_{1-x}S$) has caught researchers' attention due to its unique photocatalytic properties such as the wide range of visible light energy absorption and strong stability during water splitting. Moreover, a unique feature of this semiconductor is the capability of modifying its band gap structure by changing the Zn/Cd ratio. Herein, a series of $Zn_xCd_{1-x}S$ solid solutions was synthesized by utilizing metal-glycerate followed by calcination in air and sulfuration under flowing H_2S. This new method resulted in a homogeneous hexagonal wurtzite solid solution that could produce a massive amount of hydrogen in a large range of visible light illumination. Moreover, applying MoS_2 as a cocatalyst via photo-deposition, generated the same amount of hydrogen as using Pt as a cocatalyst. The best results were obtained for the $Zn_{30}Cd_{70}S$ solid solution that could generate more than 12 mmol h^{-1} g^{-1} under solar simulator light. It exhibited very high quantum efficiencies; 46.6 % at 400 nm to 23.4% at 500 nm as well as 11.3% at 550 nm. There are among the highest QE that have been ever reported for this kind of material under visible light.

6.1 Introduction

No one can deny that the climate changes are happening due to global warming effects of greenhouse gases. One of the main reason for this crucial issue is the use of an immense amount of fossil fuels resulting in the massive emission of carbon dioxide into the atmosphere. One of the promising solutions for this problem is converting solar energy into hydrogen molecules via the photocatalytic process of water splitting. Honda and Fujishima were pioneers of splitting water into hydrogen and oxygen using TiO_2 under UV light.[6] However, the low efficiency of hydrogen production, which originates from absorption limited to the UV region, resulting in a limitation on its practical applications. This motivate many scientists to explore other efficient photocatalysts that can absorb the energy of visible light, which accounts for about 50% of sunlight energy.[77, 346, 347]

It has been established that CdS can act as a photocatalyst in hydrogen production reaction from water under visible light irradiation because of its narrow band gap and a proper conduction band position.[30, 348] The valence band of this metal sulfide is composed by S 3p orbitals located at higher energy levels, resulting in a narrow band gap with a strong visible light response.[269, 349] Nonetheless, its high photo-corrosion affects considerably its stability during photocatalysis reactions.[350] Various approaches have been investigated in order to improve the photocatalytic performance such as utilizing either a metal as co-catalyst or synthesizing composite materials with different elements.[23, 77, 351] Among these strategies, making solid solutions with other semiconductors is an interesting method to improve the photoactivity of CdS because of the ability to control the potentials of the conduction and valence bands of a solid solution by changing their compositions.[352]

$Zn_xCd_{1-x}S$ solid solution possesses an adjustable band gap width and a good resistance towards photo-corrosion.[353, 354] Moreover, this solid solution can produce hydrogen more efficiently than CdS alone, because its potential of conduction band edge is more negative than CdS.[352] Therefore, scientists and researchers have tried to synthesize it in various ways and enhanced its photocatalytic activities via different techniques.[19, 30, 77, 355, 356] Xing et al. synthesized $Zn_xCd_{1-x}S$ solid solution via a co-precipitation technique followed by thermal treatment.[357] They found that its band gap could be varied between 2.2 eV and 3.1 eV based on the value of x and the best hydrogen evolution was found with x = 0.2 that led to having a band

gap of 2.35 eV. Another group used thermal sulfuration method to enhance the activity of $Zn_xCd_{1-x}S$ solid solution for hydrogen production.[358] Furthermore, other methods such as doping or synthesizing nanoparticles of $Zn_xCd_{1-x}S$ solid solution have been used in order to improve its photocatalytic efficiency under visible light.[359-362] It should be mentioned that even the different crystal structures of $Zn_xCd_{1-x}S$ solid solution might affect its hydrogen evolution performance. For instance, hexagonal wurtzite $Zn_xCd_{1-x}S$ photocatalysts and cubic zinc-blend phase of this solid solution had various photocatalytic activities.[269, 270, 363] According to the literature, a photocatalyst with cubic zinc-blend phase showed significantly higher hydrogen production in comparison with hexagonal phase.[348, 352, 363] Interestingly, Liu et al. reported that $Zn_xCd_{1-x}S$ with nano-twinned structures could prevent the recombination of photoexcited carriers, resulting in considerably higher hydrogen evolution under visible light illumination.[270] Based on their observation, the photocatalyst with the help of Pt as a cocatalyst could generate 1.79 mmol of hydrogen with a QE of 43% at 425 nm. It is proved that defects in the structure of $Zn_xCd_{1-x}S$, could act as electron pools and so promote hydrogen production during photocatalytic water splitting.[270] However, the defect states in semiconductors should be controlled in order to obtain the maximum hydrogen evolution.

In this study, a series of $Zn_xCd_{1-x}S$ solid solutions were synthesized. By forming metal-glycerate of cadmium and zinc that were later converted to mixed oxides. The fact that the mixture consisted of two metal oxides which were homogeneously mixed together at atomic scale, made the mixture a good precursor for synthesizing a solid solution. This aim was achieved by further sulfuration by reaction with H_2S gas at high temperature. As a result, a highly activated solid solution of $Zn_xCd_{1-x}S$ was obtained that was surprisingly active under a large range of visible light illumination with a high quantum efficiency. This was one further step towards industrial application of this kind of photocatalysts. Moreover, depositing MoS_2 as a cocatalyst on the surface of this solid solution could allow producing as much hydrogen as using Pt. It is proved that platinum is one of the most efficient cocatalysts for photocatalytic hydrogen evolution reaction. However, its high cost and scarcity place some limitations on its usage especially for its large-scale applications. This usage of MoS_2 can lead to having a noble-metal-free photocatalyst with considerable quantum efficiency under visible light illumination.

6.2 Experimental section

6.2.1 Sample preparation

Zinc Cadmium sulfide solid solutions were synthesized as follows: First, glycerol and zinc nitrate and cadmium nitrate were dissolved in isopropanol and transferred into an autoclave. The autoclave was heated up to 180ºC for 6 h. During solvothermal treatment, microspheres of carbons were made from glycerol.[364] The microspheres contained numerous -OH^- ions that provided a good capacity to absorb various cations specially Zn^{2+} and Cd^{2+}.[365] Later, the microspheres with adsorbed cations were collected via centrifugation and dried at 70ºC overnight. The obtained samples were calcined at 500ºC for 4 h yielding zinc and cadmium mixed oxide. Subsequently, the mixed oxide was exposed to a flowing gas mixture of H_2S (10%)/Ar at 450ºC for 2 h. Therefore, sulfide (S^{2-}) ions could substitute with oxygen and so the mixed oxide was converted to a mixed sulfide. Different atomic Cd/Zn ratios were used to synthesize of various compositions solid solutions which are noted as $Zn_xCd_{1-x}S$.

6.2.2 Characterization

TEM images of the samples were obtained with a JEOL JEM 1230 instrument operated at 120 kV. High-resolution TEM (HR-TEM) images were obtained by using JEOL JEM-2100F instrument operated at 300 kV. SEM images were obtained on a JEOL 6360 instrument operated at 15 kV. Powder XRD patterns were obtained on a Bruker SMART APEXII X-ray diffractometer equipped with a Cu Kα radiation source (λ = 1.5418 Å). XPS measurements were carried out in an ion-pumped chamber (evacuated to 10−9 Torr) of a photoelectron spectrometer (Kratos Axis-Ultra) equipped with a focused X-ray source (Al Kα, hν = 1486.6 eV). The UV-Vis spectra were recorded on a Cary 300 Bio UV-visible spectrophotometer.

6.2.3 Photocatalytic test

The certain amount of photocatalysts (the optimum amount was 50 mg) was added to the 100 ml of an aqueous solution of 0.5M Na_2S and Na_2SO_3 as a sacrificial reagent. After that, the mixture was purged with nitrogen for 10 min and then under the solar simulator light (used for a deposition), co-catalyst was deposited via photo-deposition technique for 2 h. Then, the cell was purged again

with nitrogen for 30 min and the sample was ready for hydrogen production test during 3-hour cycles.

The quantum efficiency of the prepared sample was calculated according to follow equations[336]:

$$\text{Quantum Efficiency (QE)} = \frac{\text{Number of reacted electrons}}{\text{Number of incident photons}} \times 100$$

$$= \frac{2 \times \text{Number of evolved hydrogen molecules}}{\text{Number of incident photons}}$$

6.3 Results and Discussions

6.3.1 Material Characterizations

Figure 6.1 exhibited XRD analysis of samples after specific stages. It is clear that air calcination after sample synthesis provides a mixed oxide of CdO and ZnO that coexist together in two separate phases. According to the references, ZnO has a hexagonal crystal structure, whereas CdO crystal structure is a cubic one. After H_2S treatment, oxygen was replaced by sulfur and thus solid solutions of $Zn_xCd_{1-x}S$ were obtained (Figure 6.1-B). The XRD peaks of $Zn_{0.9}Cd_{0.1}S$ were very close to index peaks of hexagonal wurtzite phase of ZnS (JCPDS No. 00-003-1093).[270] It seems that in this concentration, cadmium cations were incorporated into the hexagonal structure of ZnS and simultaneously oxygen atoms were replaced by sulfur atoms. Obviously, the diffraction peaks shifted toward the lower angle because of the enhancement in fringe lattice distance of the ZnS crystal structure due to the larger radius of Cd^{2+} than Zn^{2+} (0.97 and 0.74 Å, respectively). By further increase in Cd content, the peaks shifted to even lower angle and its crystal structure transferred from hexagonal ZnS to hexagonal wurtzite CdS (JCPDS No. 00-041-1049).

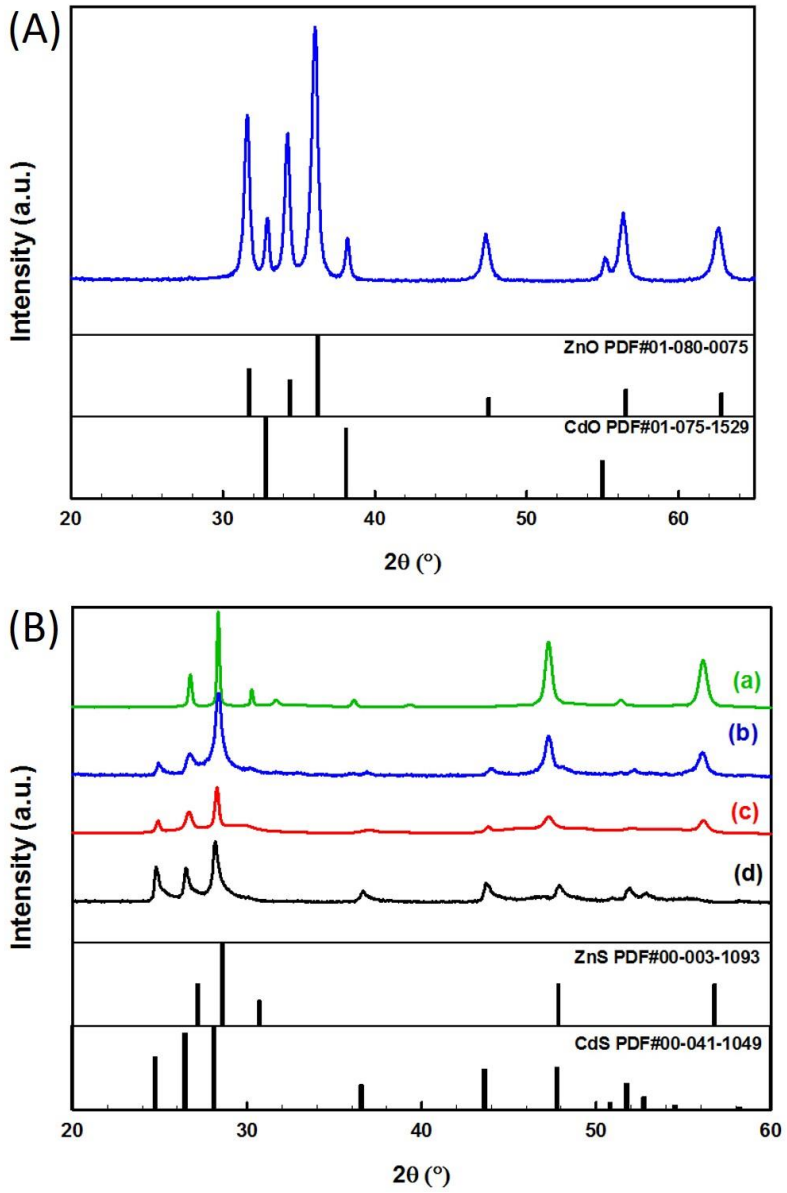

Figure 6.1. XRD patterns of (A) $Zn_{0.5}Cd_{0.5}O$ mixed oxide after calcination in air (B) solid solutions of (a) $Zn_{0.9}Cd_{0.1}S$ (b) $Zn_{0.7}Cd_{0.30}S$ (c) $Zn_{0.5}Cd_{0.5}S$ (d) $Zn_{0.3}Cd_{0.7}S$

According to XRD results, the two phases of ZnO and CdO were observed in $Zn_{0.5}Cd_{0.5}O$ after calcination (Figure 6.2-right). This mixed oxide doesn't have a clear band gap structure in visible region (Figure 6.2-left) and so it cannot generate excited charge carriers. Nevertheless, all solid solutions of $Zn_{1-x}Cd_xS$ exhibited clear band gap structure that can be excited in the visible region. It should be mentioned that ZnS can only be activated under UV light illumination because

of its large band gap (3.4 eV). Furthermore, by increasing the amount of Cd, the band gap decreases relatively and so the solid solutions could absorb more visible light energy. The lowest bandgap energy was related to CdS with 2.37 eV as it can be seen in Figure 6.2.

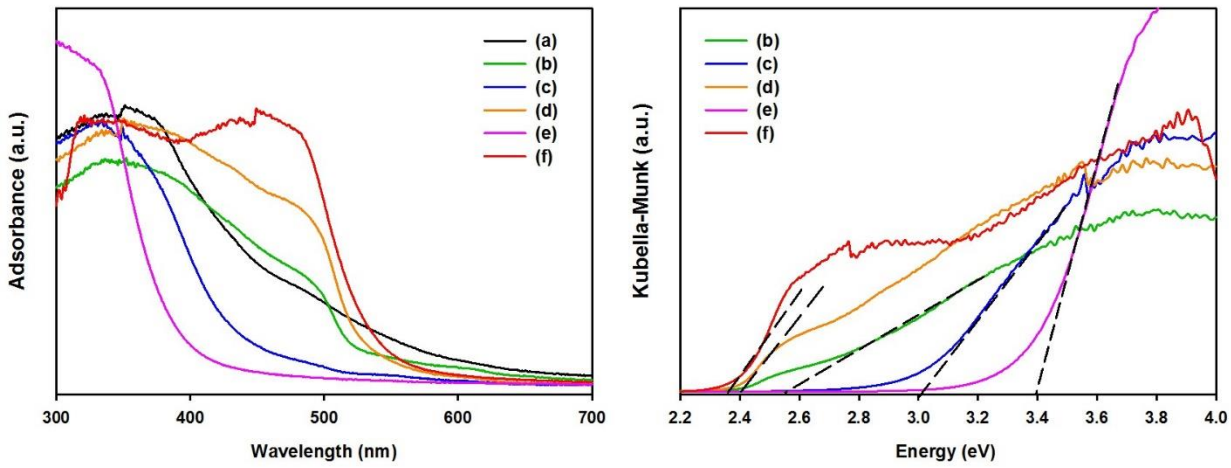

Figure 6.2. UV-Visible spectra and bandgap calculations of (a) $Zn_{0.50}Cd_{0.5}O$ (b) $Zn_{0.5}Cd_{0.5}S$ (c) $Zn_{0.7}Cd_{0.3}O$ (d) $Zn_{0.3}Cd_{0.7}O$ (e) ZnS (f) CdS

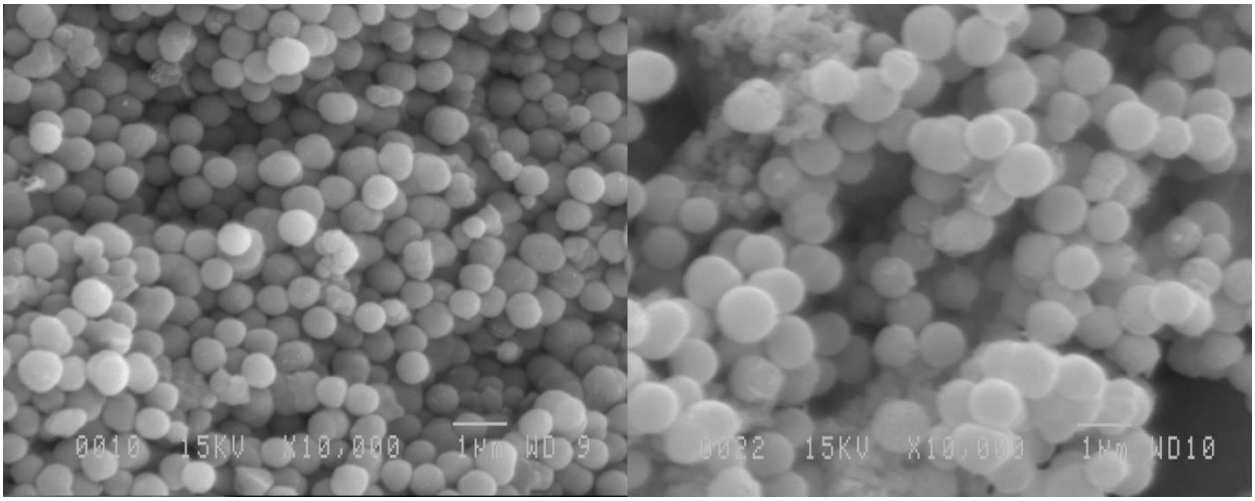

Figure 6.3. SEM images of ZnCd-glycerate after synthesized in an autoclave.

During the solvothermal step, metal-glycerate microspheres (ZnCd-glycerate) were formed in the autoclaves with a help of glycerol and metal cations.[364, 365] These microspheres were uniform with an average diameter of 500 nm, as shown in Figure 6.3. The metal-glycerate spheres were easily reacted with oxygen in air during calcination step and converted into a mixture of zinc

and cadmium oxides. Interestingly, some carbon atoms remained in the mixture that will be discussed in detail in XPS section.

The morphology and 2D microstructure of $Zn_{0.5}Cd_{0.5}S$ solid solution are exhibited via TEM images in Figure 6.4. It is obvious that even after calcination and sulfuration steps, most of the microsphere structures were still preserved resulting from burning off carbon templates during calcination step (Figure 6.4-A, B). Clearly, these hollow spheres were mainly composed of well-defined nanoparticles in the range of 20 nm to 100 nm (Figure 6.4-C, D, E). Figure 6.4-F reveals the selected area election diffraction (SAED) pattern of an individual particle shown in Figure 6.4-G. The ring patterns can be attributed to (111), (220) and (311) planes of $Zn_{0.5}Cd_{0.5}Z$ with d-spacing of 0.32 nm, 0.19 nm, and 0.16 nm, respectively. Furthermore, high-resolution transmission electron microscope (HRTEM) perfectly shows the lattice structure of a typical nanoparticle. As it can be seen from Figure 6.4-H, the measurement shows that the interplanar spacing is 0.32 nm that corresponding to the interplanar distance of the (111) plane of $Zn_{0.5}Cd_{0.5}Z$.[363]

According to XPS characterizations that are illustrated in Figure 6.5, Zn 2p showed two different peaks at 1044.9 and 1021.7 (eV) which are related to Zn $2p_{1/2}$ and Zn $2P_{2/3}$, respectively. These binding energies confirmed that the valence state of zinc in the solid solution of $Zn_xCd_{1-x}S$ and ZnS were the same. Furthermore, there are two various peaks of Cd which can be attributed to Cd $3d_{3/2}$ at 412.0 (eV) and Cd $3d_{5/2}$ at 405.2 (eV). In addition, the whole S 2p spectrum can be deconvoluted into two main peaks for S $2P_{1/2}$ and S $2p_{3/2}$ at 163.1 and 161.9 (eV), respectively. These binding energies of Zn, Cd and S are in good agreement with CdS and ZnS which are reported in the literature.[87, 353, 354, 366] Interestingly, some carbon peaks were found in the XPS spectra of all samples. Although the samples were calcined at 500ºC for 4 hr, some carbon residues were not able to react with oxygen and left the sample. The spectrum of C 1s can be deconvoluted into 3 main peaks of 285, 286.7 and 289 (eV), that can be related to C-C, C-O and C=O chemical bonds, respectively (Figure 6.5-D).

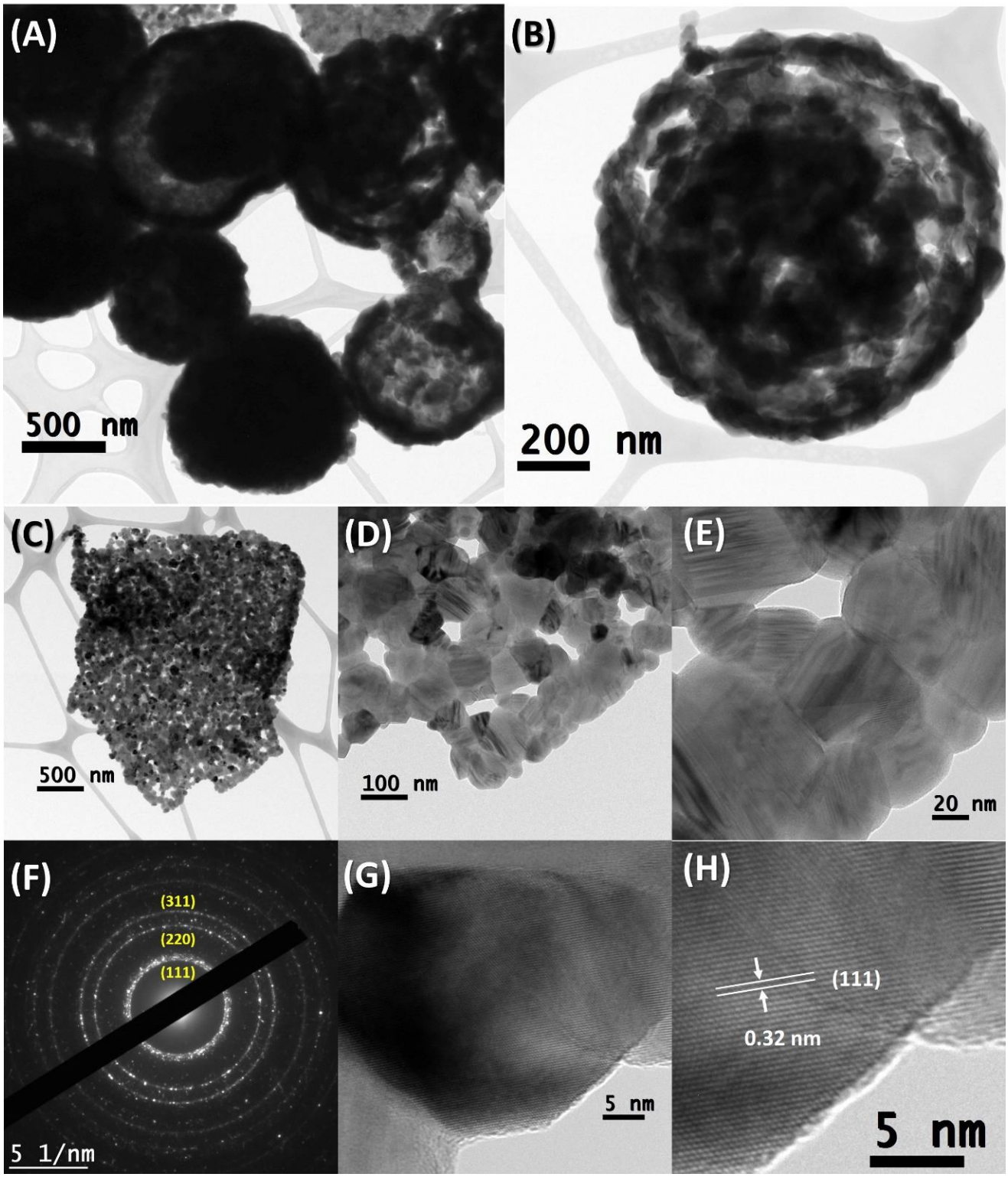

Figure 6.4. (A-E) TEM images, (F) SAED pattern and (G,H) HRTEM of $Zn_{0.5}Cd_{0.5}S$ after H_2S treatment.

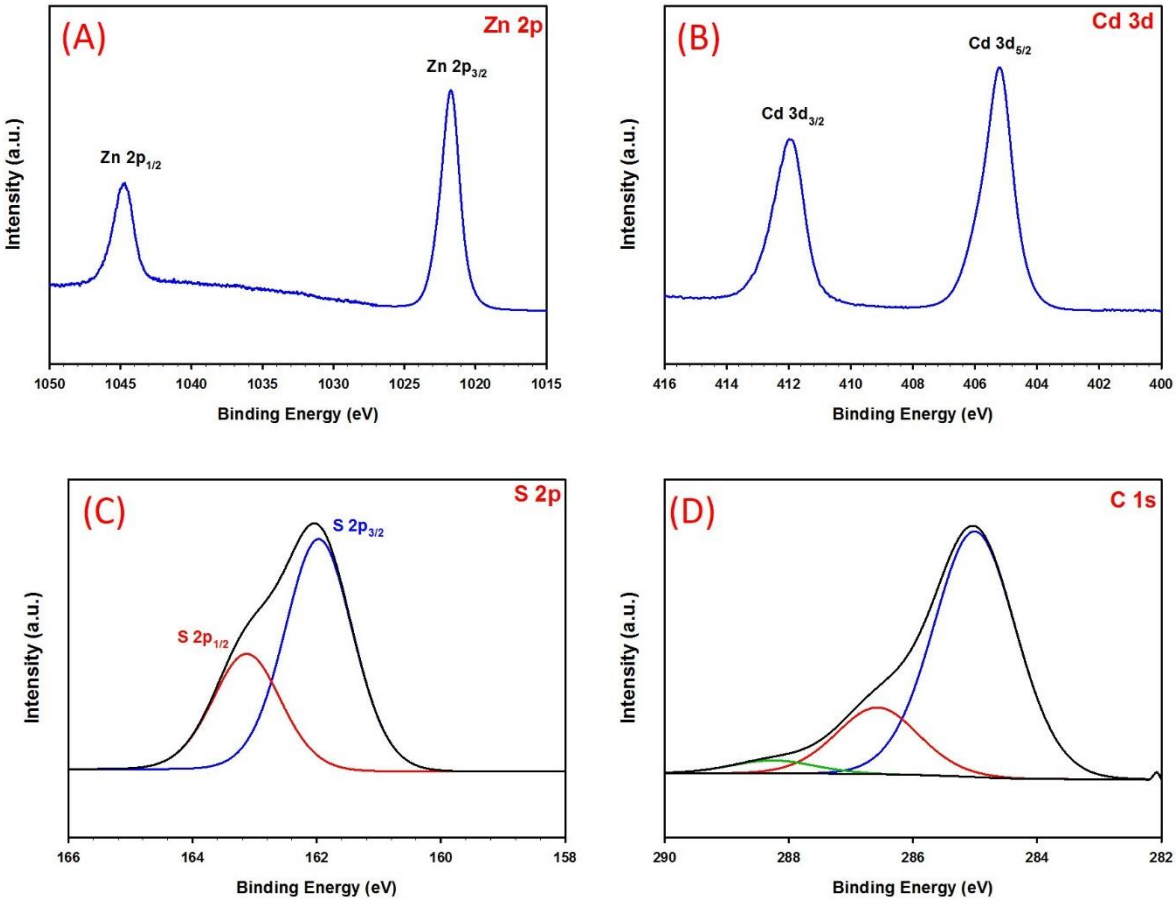

Figure 6.5. XPS spectra of (A) Zn 2p, (B) Cd 3d, (C) S 2p and (D) C 1s of $Zn_{0.3}Cd_{0.7}S$

6.3.2 Photocatalytic hydrogen production

Hydrogen production of $Zn_xCd_{1-x}S$ in various conditions and different cocatalysts under solar simulator are displayed in Figure 6.6. It should be mentioned that in order to be able to compare results to each other most of the parameters including the amount of photocatalyst, sacrificial reagent and water were kept the same in all reactions. One of the most important parts of photocatalysis process is an optimum amount of cocatalyst because little amount of cocatalyst cannot produce enough active sites for reduction reactions and too much of it can cause to reduce light absorption on the photocatalyst surface which results in lower hydrogen generation. The best hydrogen production of the solid solution of $Zn_xCd_{1-x}S$ was achieved with using 2 wt% of Pt. This optimum amount of cocatalyst is the same in various concentration of Zn and Cd. Interestingly, MoS_2 also could be deposited on the surface of $Zn_xCd_{1-x}S$ via photo-deposition method and the

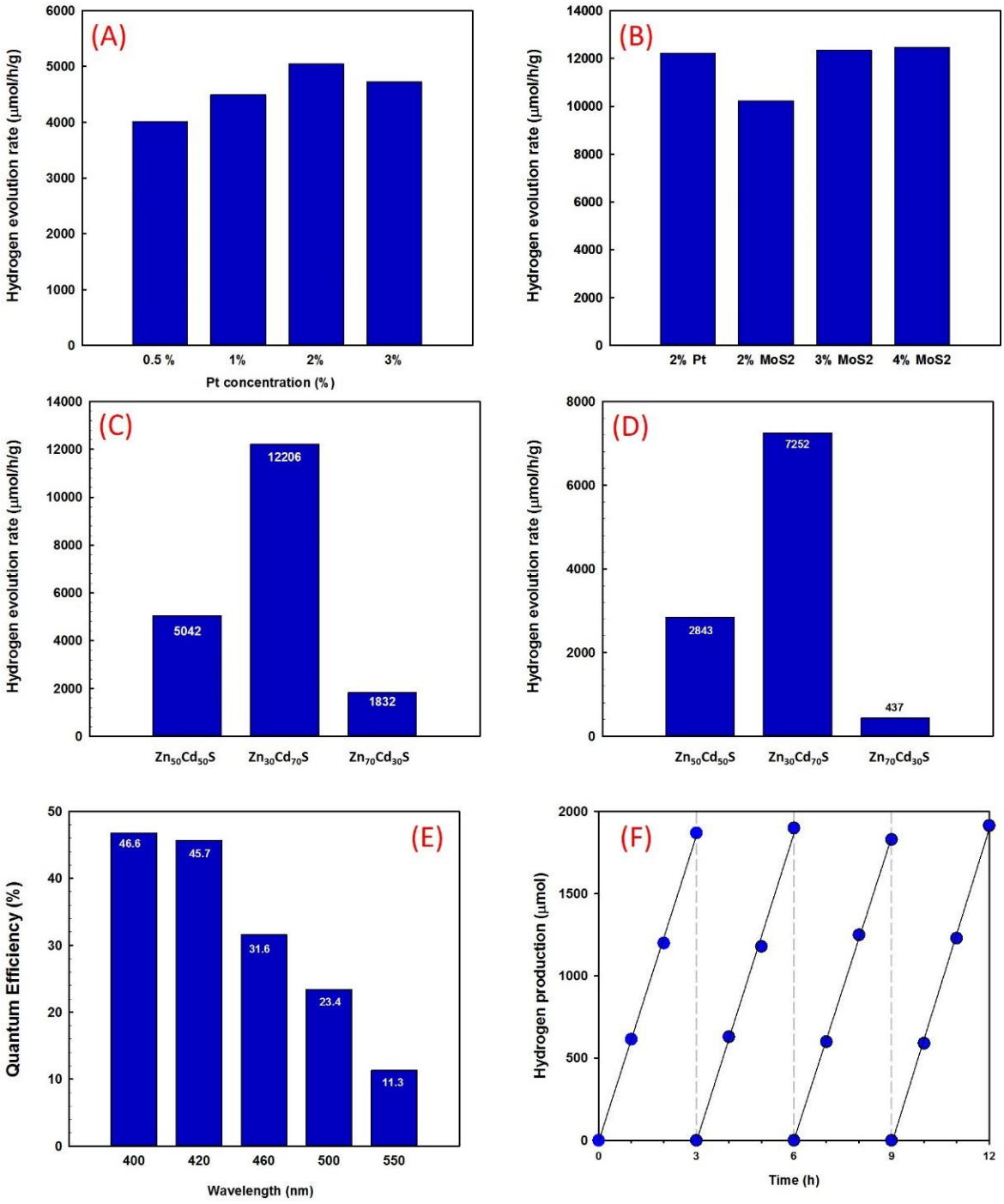

Figure 6.6. Hydrogen production of (A) $Zn_xCd_{1-x}S$ with various concentration of Pt as a cocatalyst under visible light (λ>420 nm), (B) 2% of Pt and different concentration of MoS_2 as cocatalysts deposited via photodeposited on $Zn_{0.3}Cd_{0.7}S$ (full spectrum), (C) various concentration of Zn and Cd in a solid solution of $Zn_xCd_{1-x}S$ under solar simulator full spectrum and (D) under visible light (λ>420 nm) with 3% MoS_2 as a cocatalyst. (E) Quantum efficiency of $Zn_{0.3}Cd_{0.7}S$ in various wavelengths under solar simulator irradiations via 3% MoS_2 as a cocatalyst. (F) Hydrogen production of $Zn_{0.3}Cd_{0.7}S$ for 4 cycles. Reaction Conditions: 50 mg of photocatalyst was dispersed in 100 ml aqueous solution of 0.5M Na_2S and Na_2SO_3.

optimum amount of this cocatalyst was 3 wt% that could produce as much hydrogen as platinum in the same photocatalytic reaction conditions (Figure 6.6-B). It should be mentioned that using MoS_2 as a cocatalyst has some privileges in comparison with platinum because of its low cost and wide availability compared to platinum. Moreover, MoS_2 can be synthesized and deposited on various semiconductors via different approaches that would lead to developing more practical and efficient photocatalysts.

The observed high activity of MoS_2 can be attributed to physical and electrochemical properties of molybdenum and MoS_2. Firstly, Mo has smaller electronegativity than Pt (Pauling scale: 2.16 and 2.28, respectively).[367-369] Moreover, MoS_2 is a semiconductor with a direct band gap of 1.68 eV, which consists of the conduction band of Mo metal and valence band of S species.[370] The small band gap of MoS_2 helps that the excited charge carriers have a longer lifetime before recombination with together. In addition, the similarity of valence bands of MoS_2 and $Zn_xCd_{1-x}S$ leads to having the better-excited charge flow between the cocatalyst and the support. Furthermore, the work function of MoS_2 (5.15-5.39 eV) is slightly lower than Pt (5.22-5.60 eV) and so both cocatalysts showed similar performance for hydrogen generation.[370, 371]

Figure 6.6-C exhibits hydrogen generation of various concentration of $Zn_xCd_{1-x}S$ solid solutions under full spectrum illumination of solar simulator after 3 hr. Clearly, the highest amount of hydrogen produced with the $Zn_{0.3}Cd_{0.7}S$ solid solution which was around 12.206 mmol $h^{-1}gr^{-1}$. Moreover, this photocatalyst could produce more than 7.2 mmol h^{-1} gr^{-1} of hydrogen when a light filter ($\lambda \geq 420$ nm) of visible light was used. This amount of hydrogen generation was significantly higher than other concentrations of Zn and Cd. The reason could be attributed to the good development of crystal structure of Zn and Cd in this solid solution and also narrower band gap of $Zn_{0.3}Cd_{0.7}S$ in comparison with other concentrations. Furthermore, the quantum efficiencies of the $Zn_{0.3}Cd_{0.7}S$ solid solution was calculated via the various bandpass filters. Quantum efficiency at 400 and 420 nm are almost the same due to the fact that this semiconductor can mostly excited in visible light region (46.6% and 45.7%, respectively). Interestingly, this solid solution is active at much longer wavelengths as can be seen in Figure 6.6-E. The longest wavelength that $Zn_{0.3}Cd_{0.7}S$ can produce hydrogen was 550 nm with a quantum efficiency of 11.3%. In comparison with literatures, all of the QEs in various wavelengths of $Zn_{0.3}Cd_{0.7}S$ with MoS_2, are among the highest QE that has been reported for this kind of material.

This such high activity of $Zn_{0.3}Cd_{0.7}S$ with MoS_2 as a cocatalyst in a wide range of visible light spectrum can be explained by the uniform creation of hexagonal solid solution of ZnS and CdS. In addition, oxygen replacement by S_2^{-2} during sulfuration led to having some defects on the surface of the solid photocatalyst, which could be acted as excited charges pools.[270, 372] These pools can help to deposit cocatalyst much easier and they can also help to produce hydrogen more efficiently.

6.4 Conclusion

The zinc cadmium sulfide ($Zn_xCd_{1-x}S$) solid solution is one of the best semiconductors can act as a photocatalyst to generate hydrogen from water under sunlight illumination. Its crystal structure as a solid solution can be controlled by varying different amount of Zn/Cd ratio. Therefore, this solid solution possesses an adjustable conduction and valence bands positions as well as controllable band gap. In addition, its considerably stronger stability in comparison with CdS alone during photocatalytic reactions, make it a good candidate for the further industrial application. In this work, metal-glycerate from zinc and cadmium was synthesized via the solvothermal method. Then, the mixture of mixed oxides of ZnO and CdO was created from the metal-glycerate. After this step, sulfide ions (S^{-2}) was used in order to convert mixed oxides into solid solution of $Zn_xCd_{1-x}S$. The obtained semiconductor can absorb a wide range of visible light energy because of its narrow band gap. The best results for hydrogen production from water splitting reaction were obtained by utilizing Zn/Cd = 0.3/0.7. Interestingly, utilizing MoS_2 as a cocatalyst could generate almost the same amount of hydrogen as Pt which was around 12 mmol h^{-1} g^{-1} hydrogen under solar simulator illumination. Moreover, the calculated quantum efficiencies were 46.6% at 400 nm, 23.4% at 500 nm and 11.3% at 550 nm, which were among the highest quantum efficiencies have ever reported for this semiconductor.

Chapter 7. Conclusion and Future Outlook

In this chapter, we summarize the main conclusions of the research presented in this thesis and outline future research directions.

7.1 General conclusion

The main purpose of this research thesis was to improve hydrogen production of active visible-light photocatalysts for water splitting reaction. To reach this, three main strategies were chosen to follow including: reducing charge recombination process of semiconductors via fabricating nanocomposites, enhancing specific surface area of photocatalysts by reducing their particle size to nanoscale and improving visible light absorption capacities. After reviewing recent studies, graphitic carbon nitride (g-C_3N_4) and zinc cadmium sulfide ($Zn_xCd_{1-x}S$) were selected as base photocatalysts for further development on their hydrogen evolution. Both have narrow band gaps of less than 3 eV, which make them sensitive in the visible light region. In addition, their conduction band edges are more negative than the reduction potential of H^+ to H_2. They also exhibited good stability during the photocatalytic water splitting process.

We started by synthesizing a nanocomposite of g-C_3N_4 and another semiconductor in order to increase charge separation. TiO_2 is a good candidate to combine with g-C_3N_4 because of its conduction band edge position, which is lower than that of g-C_3N_4, and the high crystallinity of its nanoparticles. Previously, our group synthesized and developed titanate nanodisks (TNDs) with an average diameter of 12 to 35 nm. First, bulk material of g-C_3N_4 was synthesized from melamine precursors. Then, nanosheets of g-C_3N_4 were created with two techniques: liquid exfoliation and gas template. Then, the nanosheets obtained from each method, were mixed with TNDs. Further calcination, converted TNDs to TiO_2 nanoparticles dispersed on the surface of g-C_3N_4 nanosheets and so the g-C_3N_4/TiO_2 was synthesized. This nanocomposite reduced charge recombination by transferring photoexcited electrons from the g-C_3N_4 to TiO_2, whereas photogenerated holes remained in g-C_3N_4 nanosheets. As a result, using Pt as a cocatalyst, the photocatalyst could generate more than twice hydrogen as pristine g-C_3N_4 nanosheets under visible light illumination.

Since g-C_3N_4 is one of the hottest topics in photocatalytic field, our next aim was to develop its capacity for hydrogen evolution under visible light illumination. However, its low specific surface area and high charge recombination rates, are the biggest issues. Nanosheets of g-C_3N_4 possess large specific surface area, but their band gaps are even larger than the bulk material because of the quantum confinement effect and so it cannot absorb more energy from sunlight in the visible light region. The amorphous phase of g-C_3N_4 showed a narrower band gap in comparison with bulk g-C_3N_4 and so it could absorb more photons energy form visible light and

generate more photoexcited charge carriers. However, its low crystallinity leads the charge recombination rates to increase significantly. We synthesized nanosheets of g-C_3N_4 by a two step thermal treatment (argon heat treatment followed by air recalcination) that could address both issues simultaneously. Therefore, we obtained nanosheets of g-C_3N_4 with large specific surface area and good crystallinity. Moreover, during the synthesis procedure, nanoholes and carbon vacancies were introduced throughout the nanosheets planes. These defects are not only considered as highly active sites for reactants but also, they provide charge trapping centers that can decrease charge recombination considerably. As a result, this photocatalyst showed hydrogen evolution in the visible light region with quantum efficiencies of 29.2% at 400 nm and 21.3% at 420 nm, which are among the highest activity reported so far for g-C_3N_4.

Finally, we developed a novel method to synthesize a $Zn_xCd_{1-x}S$ solid solution as highly active visible light photocatalyst for hydrogen production. Due to its solid solution nature, both its crystallinity and band gap are strongly affected by varying the atomic ratio of zinc to cadmium. Moreover, its good stability towards photocorrosion during photocatalytic reactions, makes it a very good candidate for industrial applications. First, a mixture of metal-glycerate was made from cadmium and zinc precursors in an autoclave. Then, it was converted to a mixed metal oxide by calcination in air at 500 ºC. After that, sulfide ions (S^{2-}) were replaced with oxygen atoms by treating the material at high temperature under flowing H_2S gas. As a result, we obtained a solid solution of $Zn_xCd_{1-x}S$ with homogenous hexagonal wurtzite crystal structure. This photocatalyst exhibited massive hydrogen generation under visible light by applying Pt as cocatalyst. Interestingly, utilizing MoS_2 as cocatalyst could produce hydrogen as much as Pt, which is more practical due to its lower cost compared with Pt. Under visible light illumination ($\lambda \geq 420$ nm), it could produce hydrogen at a rate of 12 mmol h^{-1} g^{-1}. Furthermore, the quantum efficiencies at various wavelengths were calculated as: 46.6% at 400 nm, 23.4% at 500 nm and 11.3% at 550 nm.

7.2 Future works and suggestions

In this thesis, we synthesized and developed various photocatalysts for hydrogen production under visible light illumination. Despite the fact that some promising results in hydrogen evolution were obtained with these photocatalysts, the studies in this field are still in preliminary states and further works need to be done. The suggestions may lighten future paths for developing commercial photocatalysts for industrial application.

Although massive works have been done on achieving effective cocatalysts, our scientific knowledge about them is still scarce and more investigations in this field are required, which completely affect the quantum efficiency and solar energy to fuel conversion of photocatalysts. As discussed in chapter 3, TiO_2 helped to increase charge separation in the nanocomposite of g-C_3N_4. It would be a good idea to investigate various combinations of g-C_3N_4 and other visible-light sensitive semiconductors. Thus, both semiconductors could generate photoexcited charge carriers and simultaneously participate in the charge separation process. Moreover, applying two different cocatalysts for reduction and oxidation half-reactions would enhance the quantum efficiency.

According to the new g-C_3N_4 nanosheets developed in chapter 4, further studies could be done to increase its light harvesting ability up to 550 nm by various methods such as doping with other anions and cations in the structure of nanosheets. Another recommendation is to use carbon vacancies as anchoring sites for the decoration of nanoparticles to create hybrid systems. Moreover, surface functionalization of g-C_3N_4 would help to selectively deposit semiconductors or nanoparticles of cocatalysts on its surface. Using some noble-metal-free cocatalysts with 2D nanostructures such as MoS_2 could result in increasing its quantum efficiency. In all cases, we exclusively focused on hydrogen production and so sacrificial reagents were used in order to accelerate photocatalytic hydrogen production. However, g-C_3N_4 could also oxidize water and produce oxygen under solar energy that would be very interesting to study as overall water splitting reaction.

Finally, based on the results of $Zn_xCd_{1-x}S$ solid solution, further suggestions to developed this photocatalyst are as follow: fabricating doped solid solution of $Zn_xCd_{1-x}S$ and investigating the different effects of various dopants; depositing two different cocatalysts for reduction and oxidation reactions. Furthermore, generating nanocomposites of this material and other photocatalysts to increase charge separation process and consequently enhance its quantum efficiency.

References

1. Sharma, S. and S.K. Ghoshal, *Hydrogen the future transportation fuel: from production to applications.* Renewable and sustainable energy reviews, 2015. **43**: p. 1151-1158.
2. Administration, E.I., *International Energy Outlook 2016*. 2016, US Department of Energy.
3. Zhou, H., Y. Qu, T. Zeid, and X. Duan, *Towards highly efficient photocatalysts using semiconductor nanoarchitectures.* Energy & Environmental Science, 2012. **5**(5): p. 6732-6743.
4. Qu, Y. and X. Duan, *Progress, challenge and perspective of heterogeneous photocatalysts.* Chemical Society Reviews, 2013. **42**(7): p. 2568-2580.
5. Xu, Y., M. Kraft, and R. Xu, *Metal-free carbonaceous electrocatalysts and photocatalysts for water splitting.* Chemical Society Reviews, 2016. **45**(11): p. 3039-3052.
6. Fujishima, A. and K. Honda, *Electrochemical Photolysis of Water at a Semiconductor Electrode.* Nature, 1972. **238**: p. 37-38.
7. Yang, J., H. Yan, X. Zong, F. Wen, M. Liu, and C. Li, *Roles of cocatalysts in semiconductor-based photocatalytic hydrogen production.* Phil. Trans. R. Soc. A, 2013. **371**(1996): p. 20110430.
8. Bard, A.J., *Photoelectrochemistry and heterogeneous photo-catalysis at semiconductors.* Journal of Photochemistry, 1979. **10**(1): p. 59-75.
9. Hagfeldt, A. and M. Grätzel, *Molecular photovoltaics.* Accounts of Chemical Research, 2000. **33**(5): p. 269-277.
10. Law, M., L.E. Greene, J.C. Johnson, R. Saykally, and P. Yang, *Nanowire dye-sensitized solar cells.* Nature materials, 2005. **4**(6): p. 455-459.
11. Hayden, O., R. Agarwal, and C.M. Lieber, *Nanoscale avalanche photodiodes for highly sensitive and spatially resolved photon detection.* Nature materials, 2006. **5**(5): p. 352.
12. Lewis, N.S., *Toward cost-effective solar energy use.* science, 2007. **315**(5813): p. 798-801.
13. Gur, I., N.A. Fromer, M.L. Geier, and A.P. Alivisatos, *Air-stable all-inorganic nanocrystal solar cells processed from solution.* Science, 2005. **310**(5747): p. 462-465.
14. Dukovic, G., M.G. Merkle, J.H. Nelson, S.M. Hughes, and A.P. Alivisatos, *Photodeposition of Pt on colloidal CdS and CdSe/CdS semiconductor nanostructures.* Advanced Materials, 2008. **20**(22): p. 4306-4311.
15. Farrauto, R.J., L. Dorazio, and C.H. Bartholomew, *Introduction to catalysis and industrial catalytic processes.* 2016: p. 310.
16. Lewis, N.S., G. Crabtree, A.J. Nozik, M.R. Wasielewski, and P. Alivisatos, *Basic Research Needs for Solar Energy Utilization.* Basic Energy Sciences Workshop on Solar Energy Utilization, 2005: p. 276.

17. Lewis, N.S. and D.G. Nocera, *Powering the planet: Chemical challenges in solar energy utilization.* Proceedings of the National Academy of Sciences, 2006. **103**(43): p. 15729-15735.

18. Judd, D.B., D.L. MacAdam, G. Wyszecki, H.W. Budde, H.R. Condit, S.T. Henderson, and J.L. Simonds, *Spectral Distribution of Typical Daylight as a Function of Correlated Color Temperature.* Journal of the Optical Society of America, 1964. **54**(8): p. 1031-1040.

19. Maeda, K. and K. Domen, *Photocatalytic Water Splitting: Recent Progress and Future Challenges.* The Journal of Physical Chemistry Letters, 2010. **1**: p. 2655-2661.

20. Kitano, M. and M. Hara, *Heterogeneous photocatalytic cleavage of water.* Journal of Materials Chemistry, 2010. **20**(4): p. 627-641.

21. Alexander, B.D., P.J. Kulesza, I. Rutkowska, R. Solarska, and J. Augustynski, *Metal oxide photoanodes for solar hydrogen production.* Journal of Materials Chemistry, 2008. **18**(20): p. 2298-2303.

22. Bak, T., J. Nowotny, M. Rekas, and C. Sorrell, *Photo-electrochemical hydrogen generation from water using solar energy. Materials-related aspects.* International journal of hydrogen energy, 2002. **27**(10): p. 991-1022.

23. Kudo, A. and Y. Miseki, *Heterogeneous photocatalyst materials for water splitting.* Chemical Society Reviews, 2009. **38**(1): p. 253-278.

24. Zhang, D., G. Li, H. Li, and Y. Lu, *The Development of Better Photocatalysts Through Composition-and Structure-Engineering.* Chemistry–An Asian Journal, 2013. **8**(1): p. 26-40.

25. Sang, Y., H. Liu, and A. Umar, *Photocatalysis from UV/Vis to Near-Infrared Light: Towards Full Solar-Light Spectrum Activity.* ChemCatChem, 2015. **7**(4): p. 559-573.

26. Tang, Y., W. Di, X. Zhai, R. Yang, and W. Qin, *NIR-Responsive Photocatalytic Activity and Mechanism of $NaYF_4$:Yb,Tm@TiO_2 Core–Shell Nanoparticles.* ACS Catalysis, 2013. **3**(3): p. 405-412.

27. Shen, S., J. Shi, P. Guo, and L. Guo, *Visible-light-driven photocatalytic water splitting on nanostructured semiconducting materials.* International Journal of Nanotechnology, 2011. **8**(6): p. 523-591.

28. Nowotny, J., C. Sorrell, T. Bak, and L. Sheppard, *Solar-hydrogen: Unresolved problems in solid-state science.* Solar Energy, 2005. **78**(5): p. 593-602.

29. Zou, Z., J. Ye, K. Sayama, and H. Arakawa, *Direct splitting of water under visible light irradiation with an oxide semiconductor photocatalyst.* Nature, 2001. **414**(6864): p. 625-627.

30. Chen, X., S. Shen, L. Guo, and S.S. Mao, *Semiconductor-based photocatalytic hydrogen generation.* Chemical Reviews, 2010. **110**(11): p. 6503-6570.

31. Maeda, K., K. Teramura, and K. Domen, *Effect of post-calcination on photocatalytic activity of ($Ga_{1-x}Zn_x$)($N_{1-x}O_x$) solid solution for overall water splitting under visible light.* Journal of catalysis, 2008. **254**(2): p. 198-204.

32. Esswein, A.J. and D.G. Nocera, *Hydrogen Production by Molecular Photocatalysis.* Chemical Reviews, 2007. **107**(10): p. 4022-4047.

33. Galińska, A. and J. Walendziewski, *Photocatalytic Water Splitting over Pt−TiO_2 in the Presence of Sacrificial Reagents.* Energy & Fuels, 2005. **19**(3): p. 1143-1147.

34. Wang, J., P. Yang, B. Cao, J. Zhao, and Z. Zhu, *Photocatalytic carbon–carbon bond formation with concurrent hydrogen evolution on the Pt/TiO_2 nanotube.* Applied Surface Science, 2015. **325**(0): p. 86-90.

35. Guzman, F., S.S.C. Chuang, and C. Yang, *Role of Methanol Sacrificing Reagent in the Photocatalytic Evolution of Hydrogen.* Industrial & Engineering Chemistry Research, 2012. **52**(1): p. 61-65.

36. Kawai, T. and T. Sakata, *Production of H_2 and CO from liquid water and carbon using solar energy.* Journal of the Chemical Society, Chemical Communications, 1979(23): p. 1047-1048.

37. Kawai, T. and T. Sakata, *Photocatalytic hydrogen production from liquid methanol and water.* Journal of the Chemical Society, Chemical Communications, 1980(15): p. 694-695.

38. Zhou, P., J. Yu, and M. Jaroniec, *All-Solid-State Z-Scheme Photocatalytic Systems.* Advanced Materials, 2014. **26**(29): p. 4920-4935.

39. Zong, X., G. Lu, and L. Wang, *Nanocatalysts for Water Splitting.* Nanocatalysis Synthesis and Applications, 2013: p. 495-559.

40. Maeda, K., *Z-Scheme Water Splitting Using Two Different Semiconductor Photocatalysts.* ACS Catalysis, 2013. **3**(7): p. 1486-1503.

41. Sayama, K., K. Mukasa, R. Abe, Y. Abe, and H. Arakawa, *A new photocatalytic water splitting system under visible light irradiation mimicking a Z-scheme mechanism in photosynthesis.* Journal of Photochemistry and Photobiology A: Chemistry, 2002. **148**(1): p. 71-77.

42. Serpone, N., D. Lawless, R. Khairutdinov, and E. Pelizzetti, *Subnanosecond relaxation dynamics in TiO_2 colloidal Sols (particle sizes Rp= 1.0-13.4 nm). relevance to heterogeneous photocatalysis.* The Journal of Physical Chemistry, 1995. **99**(45): p. 16655-16661.

43. Khan, S. and S. Majumder, *Optimization of p-silicon surface by etching and electrodeposition of Pt and Ni for photosplitting of water.* International journal of hydrogen energy, 1989. **14**(9): p. 653-660.

44. Akikusa, J. and S.U. Khan, *Photoelectrolysis of water to hydrogen in p-SiC/Pt and p-SiC/n-TiO_2 cells.* International journal of hydrogen energy, 2002. **27**(9): p. 863-870.

45. Gurunathan, K., *Photocatalytic hydrogen production using transition metal ions-doped γ-Bi_2O_3 semiconductor particles.* International Journal of Hydrogen Energy, 2004. **29**(9): p. 933-940.

46. Jang, J.S., K.Y. Yoon, X. Xiao, F.-R.F. Fan, and A.J. Bard, *Development of a Potential Fe_2O_3-Based Photocatalyst Thin Film for Water Oxidation by Scanning Electrochemical*

Microscopy: Effects of Ag− Fe_2O_3 Nanocomposite and Sn Doping. Chemistry of Materials, 2009. **21**(20): p. 4803-4810.

47. Jang, J.S., S.H. Choi, H.G. Kim, and J.S. Lee, *Location and state of Pt in platinized CdS/TiO_2 photocatalysts for hydrogen production from water under visible light.* The Journal of Physical Chemistry C, 2008. **112**(44): p. 17200-17205.

48. Maeda, K., K. Teramura, D. Lu, N. Saito, Y. Inoue, and K. Domen, *Noble-Metal/Cr_2O_3 Core/Shell Nanoparticles as a Cocatalyst for Photocatalytic Overall Water Splitting.* Angewandte Chemie, 2006. **118**(46): p. 7970-7973.

49. Sato, S. and J. White, *Photodecomposition of water over Pt/TiO_2 catalysts.* Chemical Physics Letters, 1980. **72**(1): p. 83-86.

50. Lehn, J., J. Sauvage, R. Zlessel, and L. Hilaire, *Water Photolysis by UV Irradiation of Rhodium Loaded Strontium Titanate Catalysts. Relation between Catalytic Activity and Nature of the Deposit from Combined Photolysis and ESCA Studies.* Israel Journal of Chemistry, 1982. **22**(2): p. 168-172.

51. Yamaguti, K. and S. Sato, *Photolysis of water over metallized powdered titanium dioxide.* Journal of the Chemical Society, Faraday Transactions 1: Physical Chemistry in Condensed Phases, 1985. **81**(5): p. 1237-1246.

52. Iwase, A., H. Kato, and A. Kudo, *Nanosized Au particles as an efficient cocatalyst for photocatalytic overall water splitting.* Catalysis letters, 2006. **108**(1-2): p. 7-10.

53. Domen, K., S. Naito, T. Onishi, and K. Tamaru, *Photocatalytic decomposition of liquid water on a NiO. $SrTiO_3$ catalyst.* Chemical Physics Letters, 1982. **92**(4): p. 433-434.

54. Inoue, Y., O. Hayashi, and K. Sato, *Photocatalytic activities of potassium-doped lead niobates and the effect of poling.* J. Chem. Soc., Faraday Trans., 1990. **86**(12): p. 2277-2282.

55. Maeda, K., K. Teramura, N. Saito, Y. Inoue, and K. Domen, *Improvement of photocatalytic activity of ($Ga_{1-x}Zn_x$)($N_{1-x}O_x$) solid solution for overall water splitting by co-loading Cr and another transition metal.* Journal of Catalysis, 2006. **243**(2): p. 303-308.

56. Steckel, J.S., J.P. Zimmer, S. Coe-Sullivan, N.E. Stott, V. Bulović, and M.G. Bawendi, *Blue luminescence from (CdS) ZnS core–shell nanocrystals.* Angewandte Chemie International Edition, 2004. **43**(16): p. 2154-2158.

57. Ohko, Y., T. Tatsuma, T. Fujii, K. Naoi, C. Niwa, Y. Kubota, and A. Fujishima, *Multicolour photochromism of TiO_2 films loaded with silver nanoparticles.* Nature Materials, 2003. **2**(1): p. 29-31.

58. Fan, W., Q. Zhang, and Y. Wang, *Semiconductor-based nanocomposites for photocatalytic H_2 production and CO_2 conversion.* Physical Chemistry Chemical Physics, 2013. **15**(8): p. 2632-2649.

59. Wang, X., G. Liu, L. Wang, Z.G. Chen, G.Q.M. Lu, and H.M. Cheng, *ZnO–CdS@ Cd heterostructure for effective photocatalytic hydrogen generation.* Advanced Energy Materials, 2012. **2**(1): p. 42-46.

60. Zhu, J. and M. Zäch, *Nanostructured materials for photocatalytic hydrogen production.* Current Opinion in Colloid & Interface Science, 2009. **14**(4): p. 260-269.

61. Mo, S.-D. and W. Ching, *Electronic and optical properties of three phases of titanium dioxide: rutile, anatase, and brookite.* Physical Review B, 1995. **51**(19): p. 13023.

62. Dambournet, D., I. Belharouak, and K. Amine, *Tailored Preparation Methods of TiO_2 Anatase, Rutile, Brookite: Mechanism of Formation and Electrochemical Properties.* Chemistry of Materials, 2010. **22**(3): p. 1173-1179.

63. Liu, L. and X. Chen, *Titanium dioxide nanomaterials: self-structural modifications.* Chemical reviews, 2014. **114**: p. 9890-9918.

64. Chen, X. and S.S. Mao, *Titanium dioxide nanomaterials: synthesis, properties, modifications, and applications.* Chem. Rev, 2007. **107**(7): p. 2891-2959.

65. Chen, H., C.E. Nanayakkara, and V.H. Grassian, *Titanium dioxide photocatalysis in atmospheric chemistry.* Chemical Reviews, 2012. **112**(11): p. 5919-5948.

66. Fujishima, A., X. Zhang, and D.A. Tryk, *TiO_2 photocatalysis and related surface phenomena.* Surface Science Reports, 2008. **63**(12): p. 515-582.

67. Linsebigler, A.L., G. Lu, and J.T. Yates Jr, *Photocatalysis on TiO_2 surfaces: principles, mechanisms, and selected results.* Chemical reviews, 1995. **95**(3): p. 735-758.

68. Hashimoto, K., H. Irie, and A. Fujishima, *TiO_2 photocatalysis: a historical overview and future prospects.* Japanese journal of applied physics, 2005. **44**(12R): p. 8269.

69. Zaleska, A., *Doped-TiO_2: a review.* Recent Patents on Engineering, 2008. **2**(3): p. 157-164.

70. Kapilashrami, M., Y. Zhang, Y.-S. Liu, A. Hagfeldt, and J. Guo, *Probing the Optical Property and Electronic Structure of TiO_2 Nanomaterials for Renewable Energy Applications.* Chemical Reviews, 2014. **114**(19): p. 9662-9707.

71. Gupta, S.M. and M. Tripathi, *A review of TiO_2 nanoparticles.* Chinese Science Bulletin, 2011. **56**(16): p. 1639.

72. Sang, L., Y. Zhao, and C. Burda, *TiO_2 Nanoparticles as Functional Building Blocks.* Chemical Reviews, 2014. **114**(19): p. 9283-9318.

73. Cargnello, M., T.R. Gordon, and C.B. Murray, *Solution-Phase Synthesis of Titanium Dioxide Nanoparticles and Nanocrystals.* Chemical Reviews, 2014. **114**(19): p. 9319-9345.

74. Ma, Y., X. Wang, Y. Jia, X. Chen, H. Han, and C. Li, *Titanium Dioxide-Based Nanomaterials for Photocatalytic Fuel Generations.* Chemical Reviews, 2014. **114**(19): p. 9987-10043.

75. Marschall, R., *Semiconductor Composites: Strategies for Enhancing Charge Carrier Separation to Improve Photocatalytic Activity.* Advanced Functional Materials, 2014. **24**(17): p. 2421-2440.

76. Dahl, M., Y. Liu, and Y. Yin, *Composite Titanium Dioxide Nanomaterials.* Chemical Reviews, 2014. **114**(19): p. 9853-9889.

77. Gholipour, M.R., C.-T. Dinh, F. Béland, and T.-O. Do, *Nanocomposite heterojunctions as sunlight-driven photocatalysts for hydrogen production from water splitting.* Nanoscale, 2015. **7**(18): p. 8187-8208.

78. Jang, J.S., S.M. Ji, S.W. Bae, H.C. Son, and J.S. Lee, *Optimization of CdS/TiO_2 nano-bulk composite photocatalysts for hydrogen production from Na_2S/Na_2SO_3 aqueous electrolyte solution under visible light ($\lambda \geq 420$ nm).* Journal of photochemistry and photobiology. A, Chemistry, 2007. **188**(1): p. 112-119.

79. Jang, J.S., H.G. Kim, U.A. Joshi, J.W. Jang, and J.S. Lee, *Fabrication of CdS nanowires decorated with TiO_2 nanoparticles for photocatalytic hydrogen production under visible light irradiation.* International Journal of Hydrogen Energy, 2008. **33**(21): p. 5975-5980.

80. Chen, Y., L. Wang, G.M. Lu, X. Yao, and L. Guo, *Nanoparticles enwrapped with nanotubes: a unique architecture of CdS/titanate nanotubes for efficient photocatalytic hydrogen production from water.* Journal of Materials Chemistry, 2011. **21**(13): p. 5134-5141.

81. Li, C., J. Yuan, B. Han, L. Jiang, and W. Shangguan, *TiO_2 nanotubes incorporated with CdS for photocatalytic hydrogen production from splitting water under visible light irradiation.* International journal of hydrogen energy, 2010. **35**(13): p. 7073-7079.

82. Zhang, Y.J., Y.C. Wang, W. Yan, T. Li, S. Li, and Y.R. Hu, *Synthesis of Cr_2O_3/TNTs nanocomposite and its photocatalytic hydrogen generation under visible light irradiation.* Applied Surface Science, 2009. **255**(23): p. 9508-9511.

83. Xing, C., D. Jing, M. Liu, and L. Guo, *Photocatalytic hydrogen production over $Na_2Ti_2O_4(OH)_2$ nanotube sensitized by CdS nanoparticles.* Materials Research Bulletin, 2009. **44**(2): p. 442-445.

84. Vu, T.T.D., F. Mighri, A. Ajji, and T.-O. Do, *Synthesis of Titanium Dioxide/Cadmium Sulfide nanosphere particles for photocatalyst applications.* Industrial & Engineering Chemistry Research, 2014. **53**(10): p. 3888-3897.

85. Kim, H.N., T.W. Kim, I.Y. Kim, and S.J. Hwang, *Cocatalyst-Free Photocatalysts for Efficient Visible-Light-Induced H_2 Production: Porous Assemblies of CdS Quantum Dots and Layered Titanate Nanosheets.* Advanced Functional Materials, 2011. **21**(16): p. 3111-3118.

86. Dinh, T.C., M.-H. Pham, Y. Seo, F. Kleitz, and T.-O. Do, *Design of multicomponent photocatalysts for hydrogen production under visible light using water-soluble titanate nanodisks.* Nanoscale, 2014.

87. Qi, L., J. Yu, and M. Jaroniec, *Preparation and enhanced visible-light photocatalytic H_2-production activity of CdS-sensitized Pt/TiO_2 nanosheets with exposed (001) facets.* Physical Chemistry Chemical Physics, 2011. **13**(19): p. 8915-8923.

88. He, D., M. Chen, F. Teng, G. Li, H. Shi, J. Wang, M. Xu, T. Lu, X. Ji, Y. Lv, and Y. Zhu, *Enhanced cyclability of CdS/TiO2 photocatalyst by stable interface structure.* Superlattices and Microstructures, 2012. **51**(6): p. 799-808.

89. Dinh, C.-T., M.-H. Pham, F. Kleitz, and T.-O. Do, *Design of water-soluble CdS–titanate–nickel nanocomposites for photocatalytic hydrogen production under sunlight.* Journal of Materials Chemistry A, 2013. **1**(42): p. 13308-13313.

90. Nguyen, T.D., C.T. Dinh, and T.O. Do, *Tailoring the assembly, interfaces, and porosity of nanostructures toward enhanced catalytic activity.* Chem Commun (Camb), 2014.

91. Jang, J.S., W. Li, S.H. Oh, and J.S. Lee, *Fabrication of CdS/TiO_2 nano-bulk composite photocatalysts for hydrogen production from aqueous H_2S solution under visible light.* Chemical Physics Letters, 2006. **425**(4–6): p. 278-282.

92. Fang, J., L. Xu, Z. Zhang, Y. Yuan, S. Cao, Z. Wang, L. Yin, Y. Liao, and C. Xue, *Au@ TiO_2–CdS Ternary Nanostructures for Efficient Visible-Light-Driven Hydrogen Generation.* ACS applied materials & interfaces, 2013. **5**(16): p. 8088-8092.

93. de Oliveira Melo, M. and L.A. Silva, *Visible light-induced hydrogen production from glycerol aqueous solution on hybrid Pt–CdS–TiO_2 photocatalysts.* Journal of Photochemistry and Photobiology A: Chemistry, 2011. **226**(1): p. 36-41.

94. Park, H., Y.K. Kim, and W. Choi, *Reversing CdS preparation order and its effects on photocatalytic hydrogen production of CdS/Pt-TiO_2 hybrids under visible light.* The Journal of Physical Chemistry C, 2011. **115**(13): p. 6141-6148.

95. Khatamian, M., M. Saket Oskoui, M. Haghighi, and M. Darbandi, *Visible-light response photocatalytic water splitting over CdS/TiO2 and CdS–TiO2/metalosilicate composites.* International Journal of Energy Research, 2014.

96. He, D., M. Chen, F. Teng, G. Li, H. Shi, J. Wang, M. Xu, T. Lu, X. Ji, and Y. Lv, *Enhanced cyclability of CdS/TiO_2 photocatalyst by stable interface structure.* Superlattices and Microstructures, 2012. **51**(6): p. 799-808.

97. Chen, Y. and L. Guo, *Highly efficient visible-light-driven photocatalytic hydrogen production from water using Cd0.5Zn0.5S/TNTs (titanate nanotubes) nanocomposites without noble metals.* Journal of Materials Chemistry, 2012. **22**(15): p. 7507-7514.

98. Park, H., W. Choi, and M.R. Hoffmann, *Effects of the preparation method of the ternary CdS/TiO2/Pt hybrid photocatalysts on visible light-induced hydrogen production.* Journal of Materials Chemistry, 2008. **18**(20): p. 2379-2385.

99. Zhang, Y., Y. Tang, X. Liu, Z. Dong, H.H. Hng, Z. Chen, T.C. Sum, and X. Chen, *Three-Dimensional CdS–Titanate Composite Nanomaterials for Enhanced Visible-Light-Driven Hydrogen Evolution.* Small, 2013. **9**(7): p. 996-1002.

100. Kim, H.N., T.W. Kim, I.Y. Kim, and S.-J. Hwang, *Cocatalyst-Free Photocatalysts for Efficient Visible-Light-Induced H2 Production: Porous Assemblies of CdS Quantum Dots and Layered Titanate Nanosheets.* Advanced Functional Materials, 2011. **21**(16): p. 3111-3118.

101. Oskoui, M.S., M. Khatamian, M. Haghighi, and A. Yavari, *Photocatalytic hydrogen evolution from water over chromosilicate-based catalysts.* RSC Advances, 2014. **4**(38): p. 19569-19577.

102. Liu, Y., L. Guo, W. Yan, and H. Liu, *A composite visible-light photocatalyst for hydrogen production.* Journal of Power Sources, 2006. **159**(2): p. 1300-1304.

103. Yang, H., L. Guo, W. Yan, and H. Liu, *A novel composite photocatalyst for water splitting hydrogen production.* Journal of Power Sources, 2006. **159**(2): p. 1305-1309.

104. Naik, B., S. Martha, and K. Parida, *Facile fabrication of $Bi_2O_3/TiO_{2-x}N_x$ nanocomposites for excellent visible light driven photocatalytic hydrogen evolution.* International journal of hydrogen energy, 2011. **36**(4): p. 2794-2802.

105. Martha, S., D.P. Das, N. Biswal, and K.M. Parida, *Facile synthesis of visible light responsive $V_2O_5/N,S$-TiO_2 composite photocatalyst: enhanced hydrogen production and phenol degradation.* Journal of Materials Chemistry, 2012. **22**(21): p. 10695-10703.

106. Xie, M., X. Fu, L. Jing, P. Luan, Y. Feng, and H. Fu, *Long-Lived, Visible-Light-Excited Charge Carriers of $TiO_2/BiVO_4$ Nanocomposites and their Unexpected Photoactivity for Water Splitting.* Advanced Energy Materials, 2014. **4**(5): p. 1-6.

107. Yan, W., Y. Zhang, W. Xie, S. Sun, J. Ding, J. Bao, and C. Gao, *$CaIn_2O_4/Fe$-TiO_2 Composite Photocatalysts with Enhanced Visible Light Performance for Hydrogen Production.* The Journal of Physical Chemistry C, 2014. **118**(12): p. 6077-6083.

108. Zhu, S., F. Yao, C. Yin, Y. Li, W. Peng, J. Ma, and D. Zhang, *Fe_2O_3/TiO_2 photocatalyst of hierarchical structure for H_2 production from water under visible light irradiation.* Microporous and Mesoporous Materials, 2014. **190**(0): p. 10-16.

109. Xie, M., X. Fu, L. Jing, P. Luan, Y. Feng, and H. Fu, *Long-Lived, Visible-Light-Excited Charge Carriers of $TiO_2/BiVO_4$ Nanocomposites and their Unexpected Photoactivity for Water Splitting.* Advanced Energy Materials, 2013.

110. Ng, Y.H., A. Iwase, A. Kudo, and R. Amal, *Reducing graphene oxide on a visible-light $BiVO_4$ photocatalyst for an enhanced photoelectrochemical water splitting.* J. Phys. Chem. Lett, 2010. **1**(17): p. 2607-2612.

111. deKrafft, K.E., C. Wang, and W. Lin, *Metal-Organic Framework Templated Synthesis of Fe_2O_3/TiO_2 Nanocomposite for Hydrogen Production.* Advanced Materials, 2012. **24**(15): p. 2014-2018.

112. Thimsen, E., S. Biswas, C.S. Lo, and P. Biswas, *Predicting the band structure of mixed transition metal oxides: theory and experiment.* The Journal of Physical Chemistry C, 2009. **113**(5): p. 2014-2021.

113. Pham, M.-H., T.C. Dinh, G.-T. Vuong, N.-D. Ta, and T.-O. Do, *Visible Light Induced Hydrogen Generation using a Hollow Photocatalyst with Two Cocatalysts Separated on Two Surface Sides.* Physical Chemistry Chemical Physics, 2014.

114. Sarkar, S.K., J.Y. Kim, D.N. Goldstein, N.R. Neale, K. Zhu, C.M. Elliott, A.J. Frank, and S.M. George, *In_2S_3 atomic layer deposition and its application as a sensitizer on TiO_2 nanotube arrays for solar energy conversion.* The Journal of Physical Chemistry C, 2010. **114**(17): p. 8032-8039.

115. Chai, B., T. Peng, P. Zeng, and J. Mao, *Synthesis of floriated In_2S_3 decorated with TiO_2 nanoparticles for efficient photocatalytic hydrogen production under visible light.* Journal of Materials Chemistry, 2011. **21**(38): p. 14587-14593.

116. Shen, S. and L. Guo, *Structural, textural and photocatalytic properties of quantum-sized In_2S_3-sensitized Ti-MCM-41 prepared by ion-exchange and sulfidation methods.* Journal of Solid State Chemistry, 2006. **179**(8): p. 2629-2635.

117. Li, K., B. Chai, T. Peng, J. Mao, and L. Zan, *Preparation of $AgIn_5S_8/TiO_2$ Heterojunction Nanocomposite and Its Enhanced Photocatalytic H_2 Production Property under Visible Light.* ACS Catalysis, 2013. **3**(2): p. 170-177.

118. Jang, J.S., S.J. Hong, J.Y. Kim, and J.S. Lee, *Heterojunction photocatalyst $TiO_2/AgGaS_2$ for hydrogen production from water under visible light.* Chemical Physics Letters, 2009. **475**(1–3): p. 78-81.

119. Xiang, Q., J. Yu, and M. Jaroniec, *Enhanced photocatalytic H_2-production activity of graphene-modified titania nanosheets.* Nanoscale, 2011. **3**(9): p. 3670-3678.

120. Wang, Y., J. Yu, W. Xiao, and Q. Li, *Microwave-assisted hydrothermal synthesis of graphene based Au-TiO_2 photocatalysts for efficient visible-light hydrogen production.* Journal of Materials Chemistry A, 2014. **2**(11): p. 3847-3855.

121. Brown, P. and P.V. Kamat, *Quantum Dot Solar Cells. Electrophoretic Deposition of CdSe−C_{60} Composite Films and Capture of Photogenerated Electrons with n-C_{60} Cluster Shell.* Journal of the American Chemical Society, 2008. **130**(28): p. 8890-8891.

122. Zhang, X.-Y., H.-P. Li, X.-L. Cui, and Y. Lin, *Graphene/TiO_2 nanocomposites: synthesis, characterization and application in hydrogen evolution from water photocatalytic splitting.* Journal of Materials Chemistry, 2010. **20**(14): p. 2801-2806.

123. Zeng, P., X. Zhang, X. Zhang, B. Chai, and T. Peng, *Efficient photocatalytic hydrogen production over Ni@ C/TiO_2 nanocomposite under visible light irradiation.* Chemical Physics Letters, 2011. **503**(4): p. 262-265.

124. Yu, H., Y. Zhao, C. Zhou, L. Shang, Y. Peng, Y. Cao, L.-Z. Wu, C.-H. Tung, and T. Zhang, *Carbon quantum dots/TiO_2 composites for efficient photocatalytic hydrogen evolution.* J. Mater. Chem. A, 2014. **2**(10): p. 3344-3351.

125. Ou, Y., J. Lin, S. Fang, and D. Liao, *MWNT–TiO_2:Ni composite catalyst: A new class of catalyst for photocatalytic H_2 evolution from water under visible light illumination.* Chemical Physics Letters, 2006. **429**(1–3): p. 199-203.

126. Wu, X.-F., H.-Y. Song, J.-M. Yoon, Y.-T. Yu, and Y.-F. Chen, *Synthesis of core− shell Au@ TiO_2 nanoparticles with truncated wedge-shaped morphology and their photocatalytic properties.* Langmuir, 2009. **25**(11): p. 6438-6447.

127. Bian, Z., T. Tachikawa, P. Zhang, M. Fujitsuka, and T. Majima, *Au/TiO2 Superstructure-Based Plasmonic Photocatalysts Exhibiting Efficient Charge Separation and Unprecedented Activity.* Journal of the American Chemical Society, 2013. **136**(1): p. 458-465.

128. Pham, M.-H., C.-T. Dinh, G.-T. Vuong, N.-D. Ta, and T.-O. Do, *Visible light induced hydrogen generation using a hollow photocatalyst with two cocatalysts separated on two surface sides.* Physical Chemistry Chemical Physics, 2014. **16**(13): p. 5937-5941.

129. Jing, D. and L. Guo, *WS2 sensitized mesoporous TiO2 for efficient photocatalytic hydrogen production from water under visible light irradiation.* Catalysis Communications, 2007. **8**(5): p. 795-799.

130. Yu, J., C.Y. Jimmy, W. Ho, and Z. Jiang, *Effects of calcination temperature on the photocatalytic activity and photo-induced super-hydrophilicity of mesoporous TiO_2 thin films.* New Journal of Chemistry, 2002. **26**(5): p. 607-613.

131. Sung, Y.-M., J.-K. Lee, and W.-S. Chae, *Controlled crystallization of nanoporous and core/shell structure titania photocatalyst particles.* Crystal growth & design, 2006. **6**(4): p. 805-808.

132. Schulte, K.L., P.A. DeSario, and K.A. Gray, *Effect of crystal phase composition on the reductive and oxidative abilities of TiO_2 nanotubes under UV and visible light.* Applied Catalysis B: Environmental, 2010. **97**(3): p. 354-360.

133. Su, C., B.-Y. Hong, and C.-M. Tseng, *Sol–gel preparation and photocatalysis of titanium dioxide.* Catalysis Today, 2004. **96**(3): p. 119-126.

134. Zhang, J., Q. Xu, Z. Feng, M. Li, and C. Li, *Importance of the relationship between surface phases and photocatalytic activity of TiO_2.* Angewandte Chemie International Edition, 2008. **47**(9): p. 1766-1769.

135. Zhang, J., S. Yan, S. Zhao, Q. Xu, and C. Li, *Photocatalytic activity for H_2 evolution of TiO_2 with tuned surface crystalline phase.* Applied Surface Science, 2013. **280**: p. 304-311.

136. Nakajima, H., T. Mori, Q. Shen, and T. Toyoda, *Photoluminescence study of mixtures of anatase and rutile TiO_2 nanoparticles: influence of charge transfer between the nanoparticles on their photoluminescence excitation bands.* Chemical Physics Letters, 2005. **409**(1): p. 81-84.

137. Kawahara, T., Y. Konishi, H. Tada, N. Tohge, J. Nishii, and S. Ito, *A Patterned TiO_2 (Anatase)/TiO_2 (Rutile) Bilayer-Type Photocatalyst: Effect of the Anatase/Rutile Junction on the Photocatalytic Activity.* Angewandte Chemie, 2002. **114**(15): p. 2935-2937.

138. Miyagi, T., M. Kamei, T. Mitsuhashi, T. Ishigaki, and A. Yamazaki, *Charge separation at the rutile/anatase interface: a dominant factor of photocatalytic activity.* Chemical Physics Letters, 2004. **390**(4): p. 399-402.

139. Zhao, Y., J. Zhang, and L. Qu, *Graphitic carbon nitride/graphene hybrids as new active materials for energy conversion and storage.* ChemNanoMat, 2015. **1**(5): p. 298-318.

140. Zambon, A., J.M. Mouesca, C. Gheorghiu, P.A. Bayle, J. Pecaut, M. Claeys-Bruno, S. Gambarelli, and L. Dubois, *s-Heptazine oligomers: promising structural models for graphitic carbon nitride.* Chemical Science, 2016. **7**(2): p. 945-950.

141. Wang, Y., X. Wang, and M. Antonietti, *Polymeric Graphitic Carbon Nitride as a Heterogeneous Organocatalyst: From Photochemistry to Multipurpose Catalysis to Sustainable Chemistry.* Angewandte Chemie International Edition, 2012. **51**(1): p. 68-89.

142. Cao, S. and J. Yu, *g-C_3N_4-Based Photocatalysts for Hydrogen Generation.* The Journal of Physical Chemistry Letters, 2014. **5**(12): p. 2101-2107.

143. Chai, B., T. Peng, J. Mao, K. Li, and L. Zan, *Graphitic carbon nitride (gC_3N_4)–Pt-TiO_2 nanocomposite as an efficient photocatalyst for hydrogen production under visible light irradiation.* Physical Chemistry Chemical Physics, 2012. **14**(48): p. 16745-16752.

144. Kang, H.W., S.N. Lim, D. Song, and S.B. Park, *Organic-inorganic composite of g-C_3N_4–$SrTiO_3$:Rh photocatalyst for improved H_2 evolution under visible light irradiation.* International Journal of Hydrogen Energy, 2012. **37**(16): p. 11602-11610.

145. Xiang, Q., J. Yu, and M. Jaroniec, *Preparation and enhanced visible-light photocatalytic H_2-production activity of graphene/C_3N_4 composites.* The Journal of Physical Chemistry C, 2011. **115**(15): p. 7355-7363.

146. Xing, Z., Z. Chen, X. Zong, and L. Wang, *A new type of carbon nitride-based polymer composite for enhanced photocatalytic hydrogen production.* Chemical Communications, 2014. **50**(51): p. 6762-6764.

147. Chen, Y., J. Li, Z. Hong, B. Shen, B. Lin, and B. Gao, *Origin of the enhanced visible-light photocatalytic activity of CNT modified g-C_3N_4 for H_2 production.* Physical Chemistry Chemical Physics, 2014. **16**(17): p. 8106-8113.

148. Teter, D.M. and R.J. Hemley, *Low-compressibility carbon nitrides.* Science, 1996. **271**(5245): p. 53.

149. Dong, F., Z. Zhao, T. Xiong, Z. Ni, W. Zhang, Y. Sun, and W.-K. Ho, *In situ construction of g-C_3N_4/g-C_3N_4 metal-free heterojunction for enhanced visible-light photocatalysis.* ACS applied materials & interfaces, 2013. **5**(21): p. 11392-11401.

150. Ong, W.-J., L.-L. Tan, Y.H. Ng, S.-T. Yong, and S.-P. Chai, *Graphitic Carbon Nitride (g-C_3N_4)-Based Photocatalysts for Artificial Photosynthesis and Environmental Remediation: Are We a Step Closer To Achieving Sustainability?* Chemical Reviews, 2016. **116**(12): p. 7159-7329.

151. Wang, X., K. Maeda, A. Thomas, K. Takanabe, G. Xin, J.M. Carlsson, K. Domen, and M. Antonietti, *A metal-free polymeric photocatalyst for hydrogen production from water under visible light.* Nat Mater, 2009. **8**(1): p. 76-80.

152. Thomas, A., A. Fischer, F. Goettmann, M. Antonietti, J.-O. Muller, R. Schlogl, and J.M. Carlsson, *Graphitic carbon nitride materials: variation of structure and morphology and their use as metal-free catalysts.* Journal of Materials Chemistry, 2008. **18**(41): p. 4893-4908.

153. Cao, S., J. Low, J. Yu, and M. Jaroniec, *Polymeric Photocatalysts Based on Graphitic Carbon Nitride.* Advanced Materials, 2015. **27**: p. 2150-2176.

154. Yang, S., Y. Gong, J. Zhang, L. Zhan, L. Ma, Z. Fang, R. Vajtai, X. Wang, and P.M. Ajayan, *Exfoliated Graphitic Carbon Nitride Nanosheets as Efficient Catalysts for Hydrogen Evolution Under Visible Light.* Advanced Materials, 2013. **25**(17): p. 2452-2456.

155. Kang, Y., Y. Yang, L.-C. Yin, X. Kang, G. Liu, and H.-M. Cheng, *An Amorphous Carbon Nitride Photocatalyst with Greatly Extended Visible-Light-Responsive Range for Photocatalytic Hydrogen Generation.* Advanced Materials, 2015. **27**: p. 4572-4577.

156. Niu, P., G. Liu, and H.-M. Cheng, *N Vacancy Nitrogen Vacancy-Promoted Photocatalytic Activity of Graphitic Carbon Nitride.* The Journal of Physical Chemistry C, 2012. **116**: p. 11013-11018.

157. Zhang, X., Z. Meng, D. Rao, Y. Wang, Q. Shi, Y. Liu, H. Wu, K. Deng, H. Liu, and R. Lu, *Efficient band structure tuning, charge separation, and visible-light response in ZrS_2-based van der Waals heterostructures.* Energy & Environmental Science, 2016. **9**(3): p. 841-849.

158. Li, X., G. Hartley, A.J. Ward, P.A. Young, A.F. Masters, and T. Maschmeyer, *Hydrogenated Defects in Graphitic Carbon Nitride Nanosheets for Improved Photocatalytic Hydrogen Evolution.* The Journal of Physical Chemistry C, 2015. **119**: p. 14938-14946.

159. Han, Q., B. Wang, J. Gao, Z. Cheng, Y. Zhao, Z. Zhang, and L. Qu, *Atomically Thin Mesoporous Nanomesh of Graphitic C_3N_4 for High-Efficiency Photocatalytic Hydrogen Evolution.* ACS nano, 2016. **10**: p. 2745-51.

160. Chen, Z., P. Sun, B. Fan, Z. Zhang, and X. Fang, *In Situ Template-Free Ion-Exchange Process to Prepare Visible-Light-Active g-C_3N_4/NiS Hybrid Photocatalysts with Enhanced Hydrogen Evolution Activity.* The Journal of Physical Chemistry C, 2014. **118**(15): p. 7801-7807.

161. Jiang, Z., D. Liu, D. Jiang, W. Wei, K. Qian, M. Chen, and J. Xie, *Bamboo leaf-assisted formation of carbon/nitrogen co-doped anatase TiO_2 modified with silver and graphitic carbon nitride: novel and green synthesis and cooperative photocatalytic activity.* Dalton Transactions, 2014. **43**(36): p. 13792-13802.

162. Katsumata, H., Y. Tachi, T. Suzuki, and S. Kaneco, *Z-scheme photocatalytic hydrogen production over WO_3/g-C_3N_4 composite photocatalysts.* RSC Advances, 2014. **4**(41): p. 21405-21409.

163. Chen, J., S. Shen, P. Guo, P. Wu, and L. Guo, *Spatial engineering of photo-active sites on g-C_3N_4 for efficient solar hydrogen generation.* Journal of Materials Chemistry A, 2014. **2**(13): p. 4605-4612.

164. Jiang, D., L. Chen, J. Xie, and M. Chen, *Ag_2S/g-C_3N_4 composite photocatalysts for efficient Pt-free hydrogen production. The co-catalyst function of Ag/Ag_2S formed by simultaneous photodeposition.* Dalton Transactions, 2014. **43**(12): p. 4878-4885.

165. Ge, L. and C. Han, *Synthesis of MWNTs/g-C_3N_4 composite photocatalysts with efficient visible light photocatalytic hydrogen evolution activity.* Applied Catalysis B: Environmental, 2012. **117–118**(0): p. 268-274.

166. Chen, D., K. Wang, D. Xiang, R. Zong, W. Yao, and Y. Zhu, *Significantly enhancement of photocatalytic performances via core–shell structure of ZnO@mpg-C_3N_4.* Applied Catalysis B: Environmental, 2014. **147**(Supplement C): p. 554-561.

167. Lu, X., K. Xu, P. Chen, K. Jia, S. Liu, and C. Wu, *Facile one step method realizing scalable production of g-C_3N_4 nanosheets and study of their photocatalytic H_2 evolution activity.* Journal of Materials Chemistry A, 2014. **2**(44): p. 18924-18928.

168. Niu, P., L. Zhang, G. Liu, and H.-M. Cheng, *Graphene-Like Carbon Nitride Nanosheets for Improved Photocatalytic Activities.* Advanced Functional Materials, 2012. **22**(22): p. 4763-4770.

169. Lin, Q., L. Li, S. Liang, M. Liu, J. Bi, and L. Wu, *Efficient synthesis of monolayer carbon nitride 2D nanosheet with tunable concentration and enhanced visible-light photocatalytic activities.* Applied Catalysis B: Environmental, 2015. **163**(0): p. 135-142.

170. Dong, F., Z. Wang, Y. Sun, W.-K. Ho, and H. Zhang, *Engineering the nanoarchitecture and texture of polymeric carbon nitride semiconductor for enhanced visible light photocatalytic activity.* Journal of Colloid and Interface Science, 2013. **401**(Supplement C): p. 70-79.

171. She, X., H. Xu, Y. Xu, J. Yan, J. Xia, L. Xu, Y. Song, Y. Jiang, Q. Zhang, and H. Li, *Exfoliated graphene-like carbon nitride in organic solvents: enhanced photocatalytic activity and highly selective and sensitive sensor for the detection of trace amounts of Cu^{2+}.* Journal of Materials Chemistry A, 2014. **2**(8): p. 2563-2570.

172. He, F., G. Chen, Y. Zhou, Y. Yu, Y. Zheng, and S. Hao, *The facile synthesis of mesoporous g-C_3N_4 with highly enhanced photocatalytic H_2 evolution performance.* Chemical Communications, 2015. **51**(90): p. 16244-16246.

173. He, F., G. Chen, Y. Yu, S. Hao, Y. Zhou, and Y. Zheng, *Facile Approach to Synthesize g-PAN/g-C3N4 Composites with Enhanced Photocatalytic H2 Evolution Activity.* ACS Applied Materials & Interfaces, 2014. **6**(10): p. 7171-7179.

174. Zhang, X., L. Yu, C. Zhuang, T. Peng, R. Li, and X. Li, *Highly Asymmetric Phthalocyanine as a Sensitizer of Graphitic Carbon Nitride for Extremely Efficient Photocatalytic H2 Production under Near-Infrared Light.* ACS Catalysis, 2013. **4**(1): p. 162-170.

175. Zhang, X., X. Xie, H. Wang, J. Zhang, B. Pan, and Y. Xie, *Enhanced photoresponsive ultrathin graphitic-phase C_3N_4 nanosheets for bioimaging.* J. Am. Chem. Soc, 2013. **135**(1): p. 18-21.

176. Wang, Z., W. Guan, Y. Sun, F. Dong, Y. Zhou, and W.-K. Ho, *Water-assisted production of honeycomb-like g-C_3N_4 with ultralong carrier lifetime and outstanding photocatalytic activity.* Nanoscale, 2015. **7**(6): p. 2471-2479.

177. Gong, X.-Q., A. Selloni, M. Batzill, and U. Diebold, *Steps on anatase TiO_2 (101).* Nature Materials, 2006. **5**(8): p. 665.

178. Nowotny, M.K., L.R. Sheppard, T. Bak, and J. Nowotny, *Defect chemistry of titanium dioxide. Application of defect engineering in processing of TiO_2-based photocatalysts.* The Journal of Physical Chemistry C, 2008. **112**(14): p. 5275-5300.

179. Chen, Y., B. Wang, S. Lin, Y. Zhang, and X. Wang, *Activation of $n \rightarrow \pi^*$ Transitions in Two-Dimensional Conjugated Polymers for Visible Light Photocatalysis.* The Journal of Physical Chemistry C, 2014. **118**: p. 29981-29989.

180. Thompson, T.L. and J.T. Yates, *Surface science studies of the photoactivation of TiO_2 new photochemical processes.* Chemical Reviews, 2006. **106**(10): p. 4428-4453.

181. Hong, Z., B. Shen, Y. Chen, B. Lin, and B. Gao, *Enhancement of photocatalytic H_2 evolution over nitrogen-deficient graphitic carbon nitride.* Journal of Materials Chemistry A, 2013. **1**(38): p. 11754-11761.

182. Lau, V.W.-h., M.B. Mesch, V. Duppel, V. Blum, J.r. Senker, and B.V. Lotsch, *Low-molecular-weight carbon nitrides for solar hydrogen evolution.* Journal of the American Chemical Society, 2015. **137**(3): p. 1064-1072.

183. Chen, X., L. Liu, P.Y. Yu, and S.S. Mao, *Increasing solar absorption for photocatalysis with black hydrogenated titanium dioxide nanocrystals.* Science (New York, N.Y.), 2011. **331**: p. 746-750.

184. Niu, P., L.C. Yin, Y.Q. Yang, G. Liu, and H.M. Cheng, *Increasing the visible light absorption of graphitic carbon nitride (Melon) photocatalysts by homogeneous self-modifi cation with nitrogen vacancies.* Advanced Materials, 2014. **26**: p. 8046-8052.

185. Chen, X. and W. Shangguan, *Hydrogen production from water splitting on CdS-based photocatalysts using solar light.* Frontiers in Energy, 2013. **7**(1): p. 111.

186. Wiberg, E. and N. Wiberg, *Arnold Frederick Holleman.* Inorganic chemistry. Academic Press, 2001.

187. Wells, A.F., *Structural inorganic chemistry*. 2012: Oxford University Press.

188. Sathish, M., B. Viswanathan, and R. Viswanath, *Alternate synthetic strategy for the preparation of CdS nanoparticles and its exploitation for water splitting.* International Journal of Hydrogen Energy, 2006. **31**(7): p. 891-898.

189. Agarwal, R., C.J. Barrelet, and C.M. Lieber, *Lasing in single cadmium sulfide nanowire optical cavities.* Nano letters, 2005. **5**(5): p. 917-920.

190. Jing, D. and L. Guo, *A novel method for the preparation of a highly stable and active CdS photocatalyst with a special surface nanostructure.* The Journal of Physical Chemistry B, 2006. **110**(23): p. 11139-11145.

191. Bao, N., L. Shen, T. Takata, and K. Domen, *Self-templated synthesis of nanoporous CdS nanostructures for highly efficient photocatalytic hydrogen production under visible light.* Chemistry of Materials, 2007. **20**(1): p. 110-117.

192. Cao, J., J.Z. Sun, J. Hong, H.Y. Li, H.Z. Chen, and M. Wang, *Carbon Nanotube/CdS Core–Shell Nanowires Prepared by a Simple Room-Temperature Chemical Reduction Method.* Advanced Materials, 2004. **16**(1): p. 84-87.

193. Wang, X., G. Liu, G.Q. Lu, and H.-M. Cheng, *Stable photocatalytic hydrogen evolution from water over ZnO–CdS core–shell nanorods.* international journal of hydrogen energy, 2010. **35**(15): p. 8199-8205.

194. QingáLu, G., *Enhanced photocatalytic hydrogen evolution by prolonging the lifetime of carriers in ZnO/CdS heterostructures.* Chemical Communications, 2009(23): p. 3452-3454.

195. Hou, J., Z. Wang, W. Kan, S. Jiao, H. Zhu, and R. Kumar, *Efficient visible-light-driven photocatalytic hydrogen production using CdS@ TaON core–shell composites coupled*

with graphene oxide nanosheets. Journal of Materials Chemistry, 2012. **22**(15): p. 7291-7299.

196. Zou, X., P.-P. Wang, C. Li, J. Zhao, D. Wang, T. Asefa, and G.-D. Li, *One-pot cation exchange synthesis of 1D porous CdS/ZnO heterostructures for visible-light-driven H2 evolution.* Journal of Materials Chemistry A, 2014.

197. Lu, X.-H., S.-L. Xie, T. Zhai, Y.-F. Zhao, P. Zhang, Y.-L. Zhang, and Y.-X. Tong, *Monodisperse CeO2/CdS heterostructured spheres: one-pot synthesis and enhanced photocatalytic hydrogen activity.* RSC Advances, 2011. **1**(7): p. 1207-1210.

198. Zou, X., P.-P. Wang, C. Li, J. Zhao, D. Wang, T. Asefa, and G.-D. Li, *One-pot cation exchange synthesis of 1D porous CdS/ZnO heterostructures for visible-light-driven H2 evolution.* J. Mater. Chem. A, 2014. **2**(13): p. 4682-4689.

199. Cui, X., Y. Wang, G. Jiang, Z. Zhao, C. Xu, Y. Wei, A. Duan, J. Liu, and J. Gao, *A photonic crystal-based CdS-Au-WO3 heterostructure for efficient visible-light photocatalytic hydrogen and oxygen evolution.* RSC Advances, 2014. **4**(30): p. 15689-15694.

200. Wang, Z., J. Hou, C. Yang, S. Jiao, and H. Zhu, *Three-dimensional MoS2-CdS-[gamma]-TaON hollow composites for enhanced visible-light-driven hydrogen evolution.* Chemical Communications, 2014. **50**(14): p. 1731-1734.

201. Yang, G., W. Yan, Q. Zhang, S. Shen, and S. Ding, *One-dimensional CdS/ZnO core/shell nanofibers via single-spinneret electrospinning: tunable morphology and efficient photocatalytic hydrogen production.* Nanoscale, 2013. **5**(24): p. 12432-12439.

202. Shen, Z., G. Chen, Y. Yu, Q. Wang, C. Zhou, L. Hao, Y. Li, L. He, and R. Mu, *Sonochemistry synthesis of nanocrystals embedded in a MoO3-CdS core-shell photocatalyst with enhanced hydrogen production and photodegradation.* Journal of Materials Chemistry, 2012. **22**(37): p. 19646-19651.

203. Pan, Y.-x., H. Zhuang, J. Hong, Z. Fang, H. Liu, B. Liu, Y. Huang, and R. Xu, *Cadmium Sulfide Quantum Dots Supported on Gallium and Indium Oxide for Visible-Light-Driven Hydrogen Evolution from Water.* ChemSusChem, 2014. **7**(9): p. 2537-2544.

204. Wang, L. and W. Wang, *In situ synthesis of CdS modified CdWO4 nanorods and their application in photocatalytic H2 evolution.* CrystEngComm, 2012. **14**(9): p. 3315-3320.

205. Kida, T., G. Guan, and A. Yoshida, *LaMnO3/CdS nanocomposite: a new photocatalyst for hydrogen production from water under visible light irradiation.* Chemical physics letters, 2003. **371**(5): p. 563-567.

206. Choi, J., S.Y. Ryu, W. Balcerski, T. Lee, and M.R. Hoffmann, *Photocatalytic production of hydrogen on Ni/NiO/KNbO3/CdS nanocomposites using visible light.* Journal of Materials Chemistry, 2008. **18**(20): p. 2371-2378.

207. Ryu, S.Y., J. Choi, W. Balcerski, T.K. Lee, and M.R. Hoffmann, *Photocatalytic production of H2 on nanocomposite catalysts.* Industrial & Engineering Chemistry Research, 2007. **46**(23): p. 7476-7488.

208. Shen, Z., G. Chen, Q. Wang, Y. Yu, C. Zhou, and Y. Wang, *Sonochemistry synthesis and enhanced photocatalytic H2-production activity of nanocrystals embedded in CdS/ZnS/In2S3 microspheres.* Nanoscale, 2012. **4**(6): p. 2010-2017.

209. Khan, Z., T.R. Chetia, and M. Qureshi, *Rational design of hyperbranched 3D heteroarrays of SrS/CdS: synthesis, characterization and evaluation of photocatalytic properties for efficient hydrogen generation and organic dye degradation.* Nanoscale, 2012. **4**(11): p. 3543-3550.

210. Gupta, U., B.G. Rao, U. Maitra, B.E. Prasad, and C.N.R. Rao, *Visible-Light-Induced Generation of H2 by Nanocomposites of Few-Layer TiS2 and TaS2 with CdS Nanoparticles.* Chemistry – An Asian Journal, 2014. **9**(5): p. 1311-1315.

211. Zhang, W., Z. Zhong, Y. Wang, and R. Xu, *Doped Solid Solution:(Zn0. 95Cu0. 05) 1− x Cd x S Nanocrystals with High Activity for H2 Evolution from Aqueous Solutions under Visible Light.* The Journal of Physical Chemistry C, 2008. **112**(45): p. 17635-17642.

212. Ren, L., F. Yang, Y.-R. Deng, N.-N. Yan, S. Huang, D. Lei, Q. Sun, and Y. Yu, *Synthesis of (CuIn) xCd2 (1-x) S2 photocatalysts for H2 evolution under visible light by using a low-temperature hydrothermal method.* International journal of hydrogen energy, 2010. **35**(8): p. 3297-3305.

213. Zhang, W., Z. Zhong, Y. Wang, and R. Xu, *Doped solid solution: (Zn0.95Cu0.05) 1-xCdxS nanocrystals with high activity for H2 evolution from aqueous solutions under visible light.* Journal of Physical Chemistry C, 2008. **112**(45): p. 17635-17642.

214. Liu, M., L. Wang, G.M. Lu, X. Yao, and L. Guo, *Twins in Cd1− xZnxS solid solution: Highly efficient photocatalyst for hydrogen generation from water.* Energy & Environmental Science, 2011. **4**(4): p. 1372-1378.

215. Reber, J.F. and M. Rusek, *Photochemical hydrogen production with platinized suspensions of cadmium sulfide and cadmium zinc sulfide modified by silver sulfide.* The Journal of Physical Chemistry, 1986. **90**(5): p. 824-834.

216. Deshpande, A., P. Shah, R. Gholap, and N.M. Gupta, *Interfacial and physico-chemical properties of polymer-supported CdS· ZnS nanocomposites and their role in the visible-light mediated photocatalytic splitting of water.* Journal of colloid and interface science, 2009. **333**(1): p. 263-268.

217. Lingampalli, S.R., U.K. Gautam, and C.N.R. Rao, *Highly efficient photocatalytic hydrogen generation by solution-processed ZnO/Pt/CdS, ZnO/Pt/Cd1-xZnxS and ZnO/Pt/CdS1-xSex hybrid nanostructures.* Energy & Environmental Science, 2013. **6**(12): p. 3589-3594.

218. Hou, J., C. Yang, Z. Wang, S. Jiao, and H. Zhu, *Hydrothermal synthesis of CdS/CdLa2S4 heterostructures for efficient visible-light-driven photocatalytic hydrogen production.* RSC Advances, 2012. **2**(27): p. 10330-10336.

219. Zong, X., H. Yan, G. Wu, G. Ma, F. Wen, L. Wang, and C. Li, *Enhancement of photocatalytic H2 evolution on CdS by loading MoS2 as cocatalyst under visible light irradiation.* Journal of the American Chemical Society, 2008. **130**(23): p. 7176-7177.

220. Jang, J.S., D.J. Ham, N. Lakshminarasimhan, and J.S. Lee, *Role of platinum-like tungsten carbide as cocatalyst of CdS photocatalyst for hydrogen production under visible light irradiation.* Applied Catalysis A: General, 2008. **346**(1): p. 149-154.

221. Zhang, W., Y. Wang, Z. Wang, Z. Zhong, and R. Xu, *Highly efficient and noble metal-free NiS/CdS photocatalysts for H_2 evolution from lactic acid sacrificial solution under visible light.* Chemical Communications, 2010. **46**(40): p. 7631-7633.

222. Yan, H., J. Yang, G. Ma, G. Wu, X. Zong, Z. Lei, J. Shi, and C. Li, *Visible-light-driven hydrogen production with extremely high quantum efficiency on Pt–PdS/CdS photocatalyst.* Journal of Catalysis, 2009. **266**(2): p. 165-168.

223. Yuliati, L., M. Kimi, and M. Shamsuddin, *High activity of Ag-doped Cd0. 1Zn0. 9S photocatalyst prepared by the hydrothermal method for hydrogen production under visible-light irradiation.* Beilstein Journal of Nanotechnology, 2014. **5**(1): p. 587-595.

224. Peng, T., P. Zeng, D. Ke, X. Liu, and X. Zhang, *Hydrothermal preparation of multiwalled carbon nanotubes (MWCNTs)/CdS nanocomposite and its efficient photocatalytic hydrogen production under visible light irradiation.* Energy & Fuels, 2011. **25**(5): p. 2203-2210.

225. Kim, Y.K. and H. Park, *Light-harvesting multi-walled carbon nanotubes and CdS hybrids: Application to photocatalytic hydrogen production from water.* Energy & Environmental Science, 2011. **4**(3): p. 685-694.

226. Yu, J., B. Yang, and B. Cheng, *Noble-metal-free carbon nanotube-Cd0.1Zn0.9S composites for high visible-light photocatalytic H2-production performance.* Nanoscale, 2012. **4**(8): p. 2670-2677.

227. Wang, L., Z. Yao, F. Jia, B. Chen, and Z. Jiang, *A facile synthesis of ZnxCd1-xS/CNTs nanocomposite photocatalyst for H2 production.* Dalton Transactions, 2013. **42**(27): p. 9976-9981.

228. Wang, X., M. Liu, Q. Chen, K. Zhang, J. Chen, M. Wang, P. Guo, and L. Guo, *Synthesis of CdS/CNTs photocatalysts and study of hydrogen production by photocatalytic water splitting.* International Journal of Hydrogen Energy, 2013. **38**(29): p. 13091-13096.

229. Ye, A., W. Fan, Q. Zhang, W. Deng, and Y. Wang, *CdS–graphene and CdS–CNT nanocomposites as visible-light photocatalysts for hydrogen evolution and organic dye degradation.* Catalysis Science & Technology, 2012. **2**(5): p. 969-978.

230. Novoselov, K.S., *Graphene: materials in the flatland (Nobel Lecture).* Angewandte Chemie International Edition, 2011. **50**(31): p. 6986-7002.

231. Lv, X.-J., W.-F. Fu, H.-X. Chang, H. Zhang, J.-S. Cheng, G.-J. Zhang, Y. Song, C.-Y. Hu, and J.-H. Li, *Hydrogen evolution from water using semiconductor nanoparticle/graphene composite photocatalysts without noble metals.* Journal of Materials Chemistry, 2012. **22**(4): p. 1539-1546.

232. Wang, J., P. Yang, J. Zhao, and Z. Zhu, *Photoactivity enhancement of the CdxZn1− xS nanoparticles by immobilizing on the graphene under visible light irradiation.* Applied Surface Science, 2013. **282**: p. 930-936.

233. Li, Q., H. Meng, J. Yu, W. Xiao, Y. Zheng, and J. Wang, *Enhanced Photocatalytic Hydrogen-Production Performance of Graphene–ZnxCd1− xS Composites by Using an Organic S Source.* Chemistry-A European Journal, 2014. **20**(4): p. 1176-1185.

234. Jia, L., D.-H. Wang, Y.-X. Huang, A.-W. Xu, and H.-Q. Yu, *Highly Durable N-Doped Graphene/CdS Nanocomposites with Enhanced Photocatalytic Hydrogen Evolution from Water under Visible Light Irradiation.* The Journal of Physical Chemistry C, 2011. **115**(23): p. 11466-11473.

235. Chang, K., Z. Mei, T. Wang, Q. Kang, S. Ouyang, and J. Ye, *MoS2/Graphene Cocatalyst for Efficient Photocatalytic H2 Evolution under Visible Light Irradiation.* ACS Nano, 2014. **8**(7): p. 7078-7087.

236. Hou, J., C. Yang, H. Cheng, Z. Wang, S. Jiao, and H. Zhu, *Ternary 3D architectures of CdS QDs/graphene/ZnIn2S4 heterostructures for efficient photocatalytic H2 production.* Physical Chemistry Chemical Physics, 2013. **15**(37): p. 15660-15668.

237. Li, Q., B. Guo, J. Yu, J. Ran, B. Zhang, H. Yan, and J.R. Gong, *Highly Efficient Visible-Light-Driven Photocatalytic Hydrogen Production of CdS-Cluster-Decorated Graphene Nanosheets.* Journal of the American Chemical Society, 2011. **133**(28): p. 10878-10884.

238. Liu, J., H. Bai, Y. Wang, Z. Liu, X. Zhang, and D.D. Sun, *Self-Assembling TiO2 Nanorods on Large Graphene Oxide Sheets at a Two-Phase Interface and Their Anti-Recombination in Photocatalytic Applications.* Advanced Functional Materials, 2010. **20**(23): p. 4175-4181.

239. Nguyen-Phan, T.-D., V.H. Pham, E.W. Shin, H.-D. Pham, S. Kim, J.S. Chung, E.J. Kim, and S.H. Hur, *The role of graphene oxide content on the adsorption-enhanced photocatalysis of titanium dioxide/graphene oxide composites.* Chemical Engineering Journal, 2011. **170**(1): p. 226-232.

240. Xiang, Q., J. Yu, and M. Jaroniec, *Graphene-based semiconductor photocatalysts.* Chemical Society Reviews, 2012. **41**(2): p. 782-796.

241. Peng, T., K. Li, P. Zeng, Q. Zhang, and X. Zhang, *Enhanced Photocatalytic Hydrogen Production over Graphene Oxide–Cadmium Sulfide Nanocomposite under Visible Light Irradiation.* The Journal of Physical Chemistry C, 2012. **116**(43): p. 22720-22726.

242. Yan, Z., X. Yu, A. Han, P. Xu, and P. Du, *Noble-Metal-Free Ni(OH)2-Modified CdS/Reduced Graphene Oxide Nanocomposite with Enhanced Photocatalytic Activity for Hydrogen Production under Visible Light Irradiation.* The Journal of Physical Chemistry C, 2014.

243. Zeng, P., Q. Zhang, T. Peng, and X. Zhang, *One-pot synthesis of reduced graphene oxide-cadmium sulfide nanocomposite and its photocatalytic hydrogen production.* Physical Chemistry Chemical Physics, 2011. **13**(48): p. 21496-21502.

244. Tang, X., Q. Tay, Z. Chen, Y. Chen, G.K.L. Goh, and J. Xue, *CuInZnS-decorated graphene nanosheets for highly efficient visible-light-driven photocatalytic hydrogen production.* Journal of Materials Chemistry A, 2013. **1**(21): p. 6359-6365.

245. Lin, R., L. Shen, Z. Ren, W. Wu, Y. Tan, H. Fu, J. Zhang, and L. Wu, *Enhanced photocatalytic hydrogen production activity via dual modification of MOF and reduced graphene oxide on CdS.* Chemical Communications, 2014. **50**(62): p. 8533-8535.

246. Li, Y., H. Wang, and S. Peng, *Tunable Photodeposition of MoS2 onto a Composite of Reduced Graphene Oxide and CdS for Synergic Photocatalytic Hydrogen Generation.* The Journal of Physical Chemistry C, 2014. **118**(34): p. 19842-19848.

247. Zhang, J., J. Yu, M. Jaroniec, and J.R. Gong, *Noble Metal-Free Reduced Graphene Oxide-$Zn_xCd_{1-x}S$ Nanocomposite with Enhanced Solar Photocatalytic H_2-Production Performance.* Nano letters, 2012. **12**(9): p. 4584-4589.

248. Schedin, F., A. Geim, S. Morozov, E. Hill, P. Blake, M. Katsnelson, and K. Novoselov, *Detection of individual gas molecules adsorbed on graphene.* Nature materials, 2007. **6**(9): p. 652-655.

249. Wang, X., L. Yin, and G. Liu, *Light irradiation-assisted synthesis of ZnO–CdS/reduced graphene oxide heterostructured sheets for efficient photocatalytic H 2 evolution.* Chemical Communications, 2014. **50**(26): p. 3460-3463.

250. Zeng, P., Q. Zhang, T. Peng, and X. Zhang, *One-pot synthesis of reduced graphene oxide–cadmium sulfide nanocomposite and its photocatalytic hydrogen production.* Physical Chemistry Chemical Physics, 2011. **13**(48): p. 21496-21502.

251. Tu, W., Y. Zhou, and Z. Zou, *Versatile Graphene-Promoting Photocatalytic Performance of Semiconductors: Basic Principles, Synthesis, Solar Energy Conversion, and Environmental Applications.* Advanced Functional Materials, 2013. **23**(40): p. 4996-5008.

252. Bai, S. and X. Shen, *Graphene–inorganic nanocomposites.* Rsc Advances, 2012. **2**(1): p. 64-98.

253. Amirav, L. and A.P. Alivisatos, *Photocatalytic hydrogen production with tunable nanorod heterostructures.* The Journal of Physical Chemistry Letters, 2010. **1**(7): p. 1051-1054.

254. Kida, T., G. Guan, Y. Minami, T. Ma, and A. Yoshida, *Photocatalytic hydrogen production from water over a LaMnO3/CdS nanocomposite prepared by the reverse micelle method.* Journal of Materials Chemistry, 2003. **13**(5): p. 1186-1191.

255. Zhang, J., S.Z. Qiao, L. Qi, and J. Yu, *Fabrication of NiS modified CdS nanorod p-n junction photocatalysts with enhanced visible-light photocatalytic H2-production activity.* Physical Chemistry Chemical Physics, 2013. **15**(29): p. 12088-12094.

256. Wang, X., W.-c. Peng, and X.-y. Li, *Photocatalytic hydrogen generation with simultaneous organic degradation by composite CdS–ZnS nanoparticles under visible light.* International Journal of Hydrogen Energy, 2014. **39**(25): p. 13454-13461.

257. Zhang, J., W. Zhu, and X. Liu, *Stable hydrogen generation from vermiculite sensitized by CdS quantum dot photocatalytic splitting of water under visible-light irradiation.* Dalton Transactions, 2014. **43**(24): p. 9296-9302.

258. Peng, Y., Z. Guo, J. Yang, D. Wang, and W. Yuan, *Enhanced photocatalytic H2 evolution over micro-SiC by coupling with CdS under visible light irradiation.* Journal of Materials Chemistry A, 2014. **2**(18): p. 6296-6300.

259. Khatamian, M., M. Saket Oskoui, and M. Haghighi, *Photocatalytic hydrogen generation over CdS-metalosilicate composites under visible light irradiation.* New Journal of Chemistry, 2014. **38**(4): p. 1684-1693.

260. Peng, R., C.-M. Wu, J. Baltrusaitis, N.M. Dimitrijevic, T. Rajh, and R.T. Koodali, *Ultra-stable CdS incorporated Ti-MCM-48 mesoporous materials for efficient photocatalytic decomposition of water under visible light illumination.* Chemical Communications, 2013. **49**(31): p. 3221-3223.

261. Peng, R., D. Zhao, J. Baltrusaitis, C.-M. Wu, and R.T. Koodali, *Visible light driven photocatalytic evolution of hydrogen from water over CdS encapsulated MCM-48 materials.* RSC Advances, 2012. **2**(13): p. 5754-5767.

262. Liu, Z., S. Shen, and L. Guo, *Study on photocatalytic performance for hydrogen evolution over CdS/M-MCM-41 (M = Zr, Ti) composite photocatalysts under visible light illumination.* International Journal of Hydrogen Energy, 2012. **37**(1): p. 816-821.

263. Jang, J.S., D.W. Hwang, and J.S. Lee, *CdS–AgGaS2 photocatalytic diodes for hydrogen production from aqueous Na2S/Na2SO3 electrolyte solution under visible light (λ ≥ 420 nm).* Catalysis Today, 2007. **120**(2): p. 174-181.

264. Ge, L., F. Zuo, J. Liu, Q. Ma, C. Wang, D. Sun, L. Bartels, and P. Feng, *Synthesis and Efficient Visible Light Photocatalytic Hydrogen Evolution of Polymeric g-C3N4 Coupled with CdS Quantum Dots.* The Journal of Physical Chemistry C, 2012. **116**(25): p. 13708-13714.

265. Zhang, J., Y. Wang, J. Zhang, Z. Lin, F. Huang, and J. Yu, *Enhanced photocatalytic hydrogen production activities of Au-loaded ZnS flowers.* 2013.

266. Tian, Y., G.-F. Huang, L.-J. Tang, M.-G. Xia, W.-Q. Huang, and Z.-L. Ma, *Size-controllable synthesis and enhanced photocatalytic activity of porous ZnS nanospheres.* Materials Letters, 2012. **83**: p. 104-107.

267. Irfan, R.M., D. Jiang, Z. Sun, L. Zhang, S. Cui, and P. Du, *Incorporating a molecular co-catalyst with a heterogeneous semiconductor heterojunction photocatalyst: Novel mechanism with two electron-transfer pathways for enhanced solar hydrogen production.* Journal of Catalysis, 2017. **353**: p. 274-285.

268. Jiang, D., Z. Sun, H. Jia, D. Lu, and P. Du, *A cocatalyst-free CdS nanorod/ZnS nanoparticle composite for high-performance visible-light-driven hydrogen production from water.* Journal of Materials Chemistry A, 2016. **4**(2): p. 675-683.

269. Wang, Y., J. Wu, J. Zheng, and R. Xu, *Highly active $Zn_xCd_{1-x}S$ photocatalysts containing earth abundant elements only for H_2 production from water under visible light.* Catalysis Science & Technology, 2011. **1**(6): p. 940-947.

270. Shi, J., H.n. Cui, Z. Liang, X. Lu, Y. Tong, C. Su, and H. Liu, *The roles of defect states in photoelectric and photocatalytic processes for ZnxCd1-xS.* Energy & Environmental Science, 2011. **4**(2): p. 466-470.

271. Shen, C.-C., Y.-N. Liu, X. Zhou, H.-L. Guo, Z.-W. Zhao, K. Liang, and A.-W. Xu, *Large improvement of visible-light photocatalytic H_2-evolution based on cocatalyst-free $Zn_{0.5}Cd_{0.5}S$ synthesized through a two-step process.* Catalysis Science & Technology, 2017. **7**(4): p. 961-967.

272. Dai, D., H. Xu, L. Ge, C. Han, Y. Gao, S. Li, and Y. Lu, *In-situ synthesis of CoP co-catalyst decorated $Zn_{0.5}Cd_{0.5}S$ photocatalysts with enhanced photocatalytic hydrogen production*

activity under visible light irradiation. Applied Catalysis B: Environmental, 2017. **217**: p. 429-436.

273. Wu, L., J. Gong, L. Ge, C. Han, S. Fang, Y. Xin, Y. Li, and Y. Lu, *AuPd bimetallic nanoparticles decorated $Cd_{0.5}Zn_{0.5}S$ photocatalysts with enhanced visible-light photocatalytic H_2 production activity.* International Journal of Hydrogen Energy, 2016. **41**(33): p. 14704-14712.

274. Bao, N., L. Shen, T. Takata, D. Lu, and K. Domen, *Highly ordered Pt-loaded CdS nanowire arrays for photocatalytic hydrogen production under visible light.* Chem Lett, 2006. **35**(3).

275. Liu, H., J. Yang, J. Liang, Y. Huang, and C. Tang, *ZnO nanofiber and nanoparticle synthesized through electrospinning and their photocatalytic activity under visible light.* Journal of the American Ceramic Society, 2008. **91**(4): p. 1287-1291.

276. Jiang, Z., F. Yang, N. Luo, B.T. Chu, D. Sun, H. Shi, T. Xiao, and P.P. Edwards, *Solvothermal synthesis of N-doped TiO2 nanotubes for visible-light-responsive photocatalysis.* Chemical Communications, 2008(47): p. 6372-6374.

277. Jitputti, J., S. Pavasupree, Y. Suzuki, and S. Yoshikawa, *Synthesis of TiO2 nanotubes and its photocatalytic activity for H2 evolution.* Japanese Journal of Applied Physics, 2008. **47**(1S): p. 751.

278. Li, Y., T. Sasaki, Y. Shimizu, and N. Koshizaki, *Hexagonal-close-packed, hierarchical amorphous TiO2 nanocolumn arrays: transferability, enhanced photocatalytic activity, and superamphiphilicity without UV irradiation.* Journal of the American Chemical Society, 2008. **130**(44): p. 14755-14762.

279. Wang, W.W., Y.J. Zhu, and L.X. Yang, *ZnO–SnO2 hollow spheres and hierarchical nanosheets: hydrothermal preparation, formation mechanism, and photocatalytic properties.* Advanced Functional Materials, 2007. **17**(1): p. 59-64.

280. Carroll, E.C., O.C. Compton, D. Madsen, F.E. Osterloh, and D.S. Larsen, *Ultrafast carrier dynamics in exfoliated and functionalized calcium niobate nanosheets in water and methanol.* The Journal of Physical Chemistry C, 2008. **112**(7): p. 2394-2403.

281. Ye, C., Y. Bando, G. Shen, and D. Golberg, *Thickness-dependent photocatalytic performance of ZnO nanoplatelets.* The Journal of Physical Chemistry B, 2006. **110**(31): p. 15146-15151.

282. Andrew Frame, F., E.C. Carroll, D.S. Larsen, M. Sarahan, N.D. Browning, and F.E. Osterloh, *First demonstration of CdSe as a photocatalyst for hydrogen evolution from water under UV and visible light.* Chemical Communications, 2008(19): p. 2206-2208.

283. Jing, D., R. Li, M. Liu, and L. Guo, *Copper-doped ZnO/ZnS core/shell nanotube as a novel photocatalyst system for photocatalytic hydrogen production under visible light.* International Journal of Nanotechnology, 2011. **8**(6): p. 446-457.

284. Lv, J., T. Kako, Z. Li, Z. Zou, and J. Ye, *Synthesis and photocatalytic activities of NaNbO3 rods modified by In2O3 nanoparticles.* The Journal of Physical Chemistry C, 2010. **114**(13): p. 6157-6162.

285. Gyu Kim, H., J. Suk Jang, E. Duck Jeong, Y. Jae Suh, and J. Sung Lee, *Fabrication of CaFe2O4/MgFe2O4 bulk heterojunction for enhanced visible light photocatalysis.* Chemical Communications, 2009(39): p. 5889-5891.

286. Pradhan, A.C., S. Martha, S. Mahanta, and K. Parida, *Mesoporous nanocomposite Fe/Al2O3–MCM-41: An efficient photocatalyst for hydrogen production under visible light.* International Journal of Hydrogen Energy, 2011. **36**(20): p. 12753-12760.

287. Dhanasekaran, P., H.G. Salunke, and N.M. Gupta, *Visible-Light-Induced Photosplitting of Water over γ′-Fe4N and γ′-Fe4N/α-Fe2O3 Nanocatalysts.* The Journal of Physical Chemistry C, 2012. **116**(22): p. 12156-12164.

288. Tanaka, A., K. Hashimoto, and H. Kominami, *Visible-Light-Induced Hydrogen and Oxygen Formation over Pt/Au/WO3 Photocatalyst Utilizing Two Types of Photoabsorption Due to Surface Plasmon Resonance and Band-Gap Excitation.* Journal of the American Chemical Society, 2013. **136**(2): p. 586-589.

289. Luo, Y., X. Liu, X. Tang, Y. Luo, Q. Zeng, X. Deng, S. Ding, and Y. Sun, *Gold nanoparticles embedded in Ta2O5/Ta3N5 as active visible-light plasmonic photocatalysts for solar hydrogen evolution.* Journal of Materials Chemistry A, 2014. **2**(36): p. 14927-14939.

290. Xitao, W., L. Rong, and W. Kang, *Synthesis of ZnO@ZnS-Bi2S3 core-shell nanorod grown on reduced graphene oxide sheets and its enhanced photocatalytic performance.* Journal of Materials Chemistry A, 2014. **2**(22): p. 8304-8313.

291. Jia, Q., A. Iwase, and A. Kudo, *BiVO4-Ru/SrTiO3:Rh composite Z-scheme photocatalyst for solar water splitting.* Chemical Science, 2014. **5**(4): p. 1513-1519.

292. Martha, S., K.H. Reddy, and K.M. Parida, *Fabrication of In2O3 modified ZnO for enhancing stability, optical behaviour, electronic properties and photocatalytic activity for hydrogen production under visible light.* Journal of Materials Chemistry A, 2014. **2**(10): p. 3621-3631.

293. Jia, Y., S. Shen, D. Wang, X. Wang, J. Shi, F. Zhang, H. Han, and C. Li, *Composite Sr2TiO4/SrTiO3(La,Cr) heterojunction based photocatalyst for hydrogen production under visible light irradiation.* Journal of Materials Chemistry A, 2013. **1**(27): p. 7905-7912.

294. Reddy, K.H., S. Martha, and K.M. Parida, *Facile fabrication of Bi_2O_3/Bi-$NaTaO_3$ photocatalysts for hydrogen generation under visible light irradiation.* RSC Advances, 2012. **2**(25): p. 9423-9436.

295. Parida, K.M., A. Nashim, and S.K. Mahanta, *Visible-light driven Gd2Ti2O7/GdCrO3 composite for hydrogen evolution.* Dalton Transactions, 2011. **40**(48): p. 12839-12845.

296. Liu, J., H. Zhang, D. Tang, X. Zhang, L. Yan, Y. Han, H. Huang, Y. Liu, and Z. Kang, *Carbon Quantum Dot/Silver Nanoparticle/Polyoxometalate Composites as Photocatalysts for Overall Water Splitting in Visible Light.* ChemCatChem, 2014. **6**(9): p. 2634-2641.

297. Zhu, T., C.K. Nuo Peh, M. Hong, and G.W. Ho, *Outside-In Recrystallization of ZnS–Cu1.8S Hollow Spheres with Interdispersed Lattices for Enhanced Visible Light Solar Hydrogen Generation.* Chemistry – A European Journal, 2014. **20**(36): p. 11505-11510.

298. Tian, G., Y. Chen, Z. Ren, C. Tian, K. Pan, W. Zhou, J. Wang, and H. Fu, *Enhanced Photocatalytic Hydrogen Evolution over Hierarchical Composites of ZnIn2S4 Nanosheets Grown on MoS2 Slices.* Chemistry – An Asian Journal, 2014. **9**(5): p. 1291-1297.

299. Nashim , A., S. Martha, and K.M. Parida *Gd2Ti2O7/In2O3: Efficient Visible-Light-Driven Heterojunction-Based Composite Photocatalysts for Hydrogen Production.* ChemCatChem, 2013. **5**(8): p. 2352-2359.

300. Cui, W., D. Guo, L. Liu, J. Hu, D. Rana, and Y. Liang, *Preparation of ZnIn2S4/K2La2Ti3O10 composites and their photocatalytic H2 evolution from aqueous Na2S/Na2SO3 under visible light irradiation.* Catalysis Communications, 2014. **48**(0): p. 55-59.

301. Xu, L., L. Ni, W. Shi, and J. Guan, *Photocatalytic Activity for Hydrogen Evolution over Well-Dispersed Heterostructured In2O3/Ta2O5 Composites.* Chinese Journal of Catalysis, 2012. **33**(7–8): p. 1101-1108.

302. Lawes, G., *Scanning electron microscopy and X-ray microanalysis.* 1987.

303. Everett, D., R. Haul, L. Moscou, R. Pierotti, J. Rouquerol, and T. Siemieniewska, *Reporting physisorption data for gas solid systems with special reference to the determination of surface-area and porosity (recommendations 1984).* Pure Appl. Chem, 1985. **57**: p. 603.

304. Thommes, M., *Physical adsorption characterization of nanoporous materials.* Chemie Ingenieur Technik, 2010. **82**(7): p. 1059-1073.

305. Shinde, K.N., S. Dhoble, H. Swart, and K. Park, *Basic mechanisms of photoluminescence,* in *Phosphate Phosphors for Solid-State Lighting*. 2012, Springer. p. 41-59.

306. Smith, B.C., *Fundamentals of Fourier transform infrared spectroscopy*. 2011: CRC press.

307. Niemantsverdriet, J.W., *Spectroscopy in catalysis*. 2007: John Wiley & Sons.

308. Dinh, C.-T., Y. Seo, T.-D. Nguyen, F. Kleitz, and T.-O. Do, *Controlled Synthesis of Titanate Nanodisks as Versatile Building Blocks for the Design of Hybrid Nanostructures.* Angewandte Chemie International Edition, 2012. **51**(27): p. 6608-6612.

309. Chu, S., C. Wang, J. Feng, Y. Wang, and Z. Zou, *Melem: A metal-free unit for photocatalytic hydrogen evolution.* International Journal of Hydrogen Energy, 2014. **39**(25): p. 13519-13526.

310. Zhu, B., P. Xia, W. Ho, and J. Yu, *Isoelectric point and adsorption activity of porous g-C_3N_4.* Applied Surface Science, 2015. **344**: p. 188-195.

311. Tachibana, Y., L. Vayssieres, and J.R. Durrant, *Artificial photosynthesis for solar water-splitting.* Nature Photonics, 2012. **6**(8): p. 511-518.

312. Dong, G., Y. Zhang, Q. Pan, and J. Qiu, *A fantastic graphitic carbon nitride (g-C_3N_4) material: Electronic structure, photocatalytic and photoelectronic properties.* Journal of Photochemistry and Photobiology C: Photochemistry Reviews, 2014. **20**: p. 33-50.

313. Zhao, Z., Y. Sun, and F. Dong, *Graphitic carbon nitride based nanocomposites: a review.* Nanoscale, 2015. **7**(1): p. 15-37.

314. Wang, X., J. Chen, X. Guan, and L. Guo, *Enhanced efficiency and stability for visible light driven water splitting hydrogen production over $Cd_{0.5}Zn_{0.5}S/g$-C_3N_4 composite photocatalyst.* International Journal of Hydrogen Energy, 2015. **40**(24): p. 7546-7552.

315. Yu, J., S. Wang, J. Low, and W. Xiao, *Enhanced photocatalytic performance of direct Z-scheme g-C_3N_4-TiO_2 photocatalysts for the decomposition of formaldehyde in air.* Physical Chemistry Chemical Physics, 2013. **15**(39): p. 16883-16890.

316. Miranda, C., H. Mansilla, J. Yáñez, S. Obregón, and G. Colón, *Improved photocatalytic activity of g-C_3N_4/TiO_2 composites prepared by a simple impregnation method.* Journal of Photochemistry and Photobiology A: Chemistry, 2013. **253**(Supplement C): p. 16-21.

317. Obregón, S. and G. Colón, *Improved H_2 production of Pt-TiO_2/g-C_3N_4-MnO_x composites by an efficient handling of photogenerated charge pairs.* Applied Catalysis B: Environmental, 2014. **144**(Supplement C): p. 775-782.

318. Liu, L., Y. Qi, J. Hu, Y. Liang, and W. Cui, *Efficient visible-light photocatalytic hydrogen evolution and enhanced photostability of core@shell Cu_2O@g-C_3N_4 octahedra.* Applied Surface Science, 2015. **351**(Supplement C): p. 1146-1154.

319. Yu, J., S. Wang, B. Cheng, Z. Lin, and F. Huang, *Noble metal-free Ni(OH)2–g-C3N4 composite photocatalyst with enhanced visible-light photocatalytic H2-production activity.* Catalysis Science & Technology, 2013. **3**(7): p. 1782.

320. Martha, S., A. Nashim, and K.M. Parida, *Facile synthesis of highly active g-C3N4 for efficient hydrogen production under visible light.* Journal of Materials Chemistry A, 2013. **1**(26): p. 7816-7824.

321. Dong, F., L. Wu, Y. Sun, M. Fu, Z. Wu, and S.C. Lee, *Efficient synthesis of polymeric g-C_3N_4 layered materials as novel efficient visible light driven photocatalysts.* Journal of Materials Chemistry, 2011. **21**(39): p. 15171-15174.

322. Li, Y., J. Zhang, Q. Wang, Y. Jin, D. Huang, Q. Cui, and G. Zou, *Nitrogen-Rich Carbon Nitride Hollow Vessels: Synthesis, Characterization, and Their Properties.* The Journal of Physical Chemistry B, 2010. **114**(29): p. 9429-9434.

323. Ge, L., C. Han, and J. Liu, *In situ synthesis and enhanced visible light photocatalytic activities of novel PANI-g-C3N4 composite photocatalysts.* Journal of Materials Chemistry, 2012. **22**(23): p. 11843-11850.

324. Cao, S., J. Low, J. Yu, and M. Jaroniec, *Polymeric photocatalysts based on graphitic carbon nitride.* Adv Mater, 2015. **27**(13): p. 2150-76.

325. Wang, X.-j., W.-y. Yang, F.-t. Li, Y.-b. Xue, R.-h. Liu, and Y.-j. Hao, *In Situ Microwave-Assisted Synthesis of Porous N-TiO2/g-C3N4Heterojunctions with Enhanced Visible-Light Photocatalytic Properties.* Industrial & Engineering Chemistry Research, 2013. **52**(48): p. 17140-17150.

326. Li, X., J. Yu, J. Low, Y. Fang, J. Xiao, and X. Chen, *Engineering heterogeneous semiconductors for solar water splitting.* J. Mater. Chem. A, 2015. **3**: p. 2485-2534.

327. Yin, S., J. Han, T. Zhou, and R. Xu, *Recent progress in g-C_3N_4 based low cost photocatalytic system: activity enhancement and emerging applications.* Catal. Sci. Technol., 2015. **5**: p. 5048-5061.

328. Wang, X., S. Blechert, and M. Antonietti, *Polymeric Graphitic Carbon Nitride for Heterogeneous Photocatalysis.* ACS Catalysis, 2012. **2**(8): p. 1596-1606.

329. Zheng, Y., L. Lin, B. Wang, and X. Wang, *Graphitic Carbon Nitride Polymers toward Sustainable Photoredox Catalysis.* Angewandte Chemie - International Edition, 2015. **54**: p. 12868-12884.

330. Zhang, J., Y. Chen, and X. Wang, *Two-dimensional covalent carbon nitride nanosheets: synthesis, functionalization, and applications.* Energy Environ. Sci., 2015. **8**: p. 3092-3108.

331. Khabashesku, V.N., J.L. Zimmerman, and J.L. Margrave, *Powder synthesis and characterization of amorphous carbon nitride.* Chemistry of Materials, 2000. **12**: p. 3264-3270.

332. Seredych, M., S. Łoś, D.A. Giannakoudakis, E. Rodríguez-Castellón, and T.J. Bandosz, *Photoactivity of g-C_3N_4/S-Doped Porous Carbon Composite: Synergistic Effect of Composite Formation.* ChemSusChem, 2016. **290671**: p. 1-6.

333. Martin, D.J., K. Qiu, S.A. Shevlin, A.D. Handoko, X. Chen, Z. Guo, and J. Tang, *Highly efficient photocatalytic H_2 evolution from water using visible light and structure-controlled graphitic carbon nitride.* Angewandte Chemie (International ed. in English), 2014. **53**: p. 9240-5.

334. Wang, Y., J. Hong, W. Zhang, and R. Xu, *Carbon nitride nanosheets for photocatalytic hydrogen evolution: remarkably enhanced activity by dye sensitization.* Catal. Sci. Technol., 2013. **3**: p. 1703-1711.

335. Wang, X., G. Zhang, Z.-a. Lan, L. Lin, and S. Lin, *Overall Water Splitting by Pt/g-C_3N_4 Photocatalysts without Using Sacrificial Agent.* Chem. Sci., 2016. **00**: p. 1-5.

336. Shimura, K. and H. Yoshida, *Heterogeneous photocatalytic hydrogen production from water and biomass derivatives.* Energy & Environmental Science, 2011. **4**: p. 2467.

337. Liang, Q., Z. Li, Z.-H. Huang, F. Kang, and Q.-H. Yang, *Holey Graphitic Carbon Nitride Nanosheets with Carbon Vacancies for Highly Improved Photocatalytic Hydrogen Production.* Advanced Functional Materials, 2015: p. 6885-6892.

338. Fina, F., H. Ménard, and J.T.S. Irvine, *The effect of Pt NPs crystallinity and distribution on the photocatalytic activity of Pt-g-C_3N_4.* Physical chemistry chemical physics : PCCP, 2015. **17**: p. 13929-36.

339. Cao, S., J. Jiang, B. Zhu, and J. Yu, *Shape-dependent photocatalytic hydrogen evolution activity over a Pt nanoparticle coupled g-C_3N_4 photocatalyst.* Phys. Chem. Chem. Phys., 2016. **18**: p. 19457-19463.

340. Xie, Y.P., Z.B. Yu, G. Liu, X.L. Ma, H.-M. Cheng, A. Kudo, Y. Miseki, X. Chen, S. Shen, L. Guo, S.S. Mao, G. Liu, P. Niu, H.M. Cheng, X. Zong, H. Yan, G. Wu, G. Ma, F. Wen, L. Wang, C. Li, X. Zong, J. Han, G. Ma, H. Yan, G. Wu, C. Li, H. Yan, J. Yang, G. Ma, G. Wu, X. Zong, Z. Lei, J. Shi, C. Li, J. Yang, H. Yan, X. Wang, F. Wen, Z. Wang, D. Fan, J. Shi, C. Li, J. Yang, D. Wang, H.X. Han, C. Li, L. Huang, X. Wang, J. Yang, G. Liu, J. Han, C. Li, C. Li, L. Han, R. Liu, H. Li, S. Zhang, G. Zhang, Z. Wu, G. Zhao, Y. Zhang, H. Tian, D. Li, N.N. Hewa-Kasakarage, P.Z. El-Khoury, A.N. Tarnovsky, M. Kirsanova, I. Nemitz, A. Nemchinov, M. Zamkov, Y. Tak, H. Kim, D. Lee, K. Yong, S. Liu, N. Zhang, Z.R.

Tang, Y.J. Xu, L. Wang, H.W. Wei, Y.J. Fan, X.Z. Liu, J.H. Zhan, J. Huang, K.L. Mulfort, P. Du, L.X. Chen, Q. Shen, J. Kobayashi, L.J. Diguna, T. Toyoda, J. Du, J. Qi, D. Wang, Z. Tang, R.G. Chaudhuri, S. Paria, P. Reiss, M. Protière, L. Li, X. Lai, J.E. Halpert, D. Wang, J. Zhang, J. Yu, M. Jaroniec, J.R. Gong, Y. Wang, J. Wu, J. Zheng, R. Xu, R. Li, F. Zhang, D. Wang, J. Yang, M. Li, J. Zhu, X. Zhou, H. Han, C. Li, M. Harada, H. Einaga, S. Anandan, M. Miyauchi, K.S. Kim, N. Winograd, R.E. Davis, M. Harada, K. Okamoto, M. Terazima, M. Liang, J. Chen, G. Ramakrishna, A.K. Singh, D.K. Palit, H.N. Ghosh, W.G. Becker, A.J. Bard, D. Denzler, M. Olschewski, K. Sattler, L. Huang, J.H. Yang, X.L. Wang, J.F. Han, H.X. Han and C. Li, *CdS–mesoporous ZnS core–shell particles for efficient and stable photocatalytic hydrogen evolution under visible light.* Energy & Environmental Science, 2014. **7**: p. 1895.

341. Cheng, F., J. Yan, C. Zhou, B. Chen, P. Li, Z. Chen, and X. Dong, *An alkali treating strategy for the colloidization of graphitic carbon nitride and its excellent photocatalytic performance.* Journal of Colloid and Interface Science, 2016. **468**: p. 103-109.

342. Li, S., G. Dong, R. Hailili, L. Yang, Y. Li, F. Wang, Y. Zeng, and C. Wang, *Effective photocatalytic H_2O_2 production under visible light irradiation at g-C_3N_4 modulated by carbon vacancies.* Applied Catalysis B: Environmental, 2016. **190**: p. 26-35.

343. Yan, S.C., Z.S. Li, and Z.G. Zou, *Photodegradation performance of g-C_3N_4 fabricated by directly heating melamine.* Langmuir : the ACS journal of surfaces and colloids, 2009. **25**: p. 10397-401.

344. Zhao, H., H. Yu, X. Quan, S. Chen, Y. Zhang, H. Zhao, and H. Wang, *Fabrication of atomic single layer graphitic-C_3N_4 and its high performance of photocatalytic disinfection under visible light irradiation.* Applied Catalysis B: Environmental, 2014. **152-153**: p. 46-50.

345. Li, Y., R. Jin, Y. Xing, J. Li, S. Song, X. Liu, M. Li, and R. Jin, *Macroscopic Foam-Like Holey Ultrathin g-C_3N_4 Nanosheets for Drastic Improvement of Visible-Light Photocatalytic Activity.* Advanced Energy Materials, 2016: p. 1601273.

346. Lewis, N.S. and G. Crabtree, *Basic Research Needs for Solar Energy Utilization: report of the Basic Energy Sciences Workshop on Solar Energy Utilization, April 18-21, 2005*. 2005, US Department of Energy, Office of Basic Energy Science.

347. Panwar, N.L., S.C. Kaushik, and S. Kothari, *Role of renewable energy sources in environmental protection: A review.* Renewable and Sustainable Energy Reviews, 2011. **15**: p. 1513-1524.

348. del Valle, F., A. Ishikawa, K. Domen, J.A. Villoria de la Mano, M.C. Sánchez-Sánchez, I.D. González, S. Herreras, N. Mota, M.E. Rivas, M.C. Álvarez Galván, J.L.G. Fierro, and R.M. Navarro, *Influence of Zn concentration in the activity of $Cd_{1-x}Zn_xS$ solid solutions for water splitting under visible light.* Catalysis Today, 2009. **143**: p. 51-56.

349. Ikeda, S., T. Nakamura, T. Harada, M. Matsumura, A. Kudo, H. Araki, A. Takeuchi, A. Holzing, S. Jost, R. Hock, T. Vos, J. Schulze, and A. Kirbs, *Multicomponent sulfides as narrow gap hydrogen evolution photocatalysts.* Physical Chemistry Chemical Physics, 2010. **12**: p. 13943.

350. Meissner, D., R. Memming, and B. Kastening, *Photoelectrochemistry of cadmium sulfide. 1. Reanalysis of photocorrosion and flat-band potential.* The Journal of Physical Chemistry, 1988. **92**: p. 3476-3483.

351. Gaya, U., *Heterogeneous Photocatalysis Using Inorganic Semiconductor Solids.* 2013. **21**: p. 213.

352. Chan, C.-C., C.-C. Chang, C.-H. Hsu, Y.-C. Weng, K.-Y. Chen, H.-H. Lin, W.-C. Huang, and S.-F. Cheng, *Efficient and stable photocatalytic hydrogen production from water splitting over $Zn_xCd_{1-x}S$ solid solutions under visible light irradiation.* International Journal of Hydrogen Energy, 2014. **39**: p. 1630-1639.

353. Li, Q., H. Meng, P. Zhou, Y. Zheng, J. Wang, J. Yu, and J. Gong, *$Zn_{1-x}Cd_xS$ Solid Solutions with Controlled Bandgap and Enhanced Visible-Light Photocatalytic H_2- Production Activity.* ACS Catalysis, 2013. **3**: p. 882.

354. Mei, Z., M. Zhang, J. Schneider, W. Wang, N. Zhang, Y. Su, B. Chen, S. Wang, A.L. Rogach, and F. Pan, *Hexagonal $Zn_{1-x}Cd_xS$ $(0.2 \leq x \leq 1)$ solid solution photocatalysts for H_2 generation from water.* Catal. Sci. Technol., 2017: p. 2-7.

355. Acar, C., I. Dincer, and G.F. Naterer, *Review of photocatalytic water-splitting methods for sustainable hydrogen production.* International Journal of Energy Research, 2016. **40**: p. 1449-1473.

356. Hisatomi, T., K. Takanabe, and K. Domen, *Photocatalytic Water-Splitting Reaction from Catalytic and Kinetic Perspectives.* Catalysis Letters, 2014. **145**: p. 95-108.

357. XING, C., Y. ZHANG, W. YAN, and L. GUO, *Band structure-controlled solid solution of $Cd_{1-x}Zn_xS$ photocatalyst for hydrogen production by water splitting.* International Journal of Hydrogen Energy, 2006. **31**: p. 2018-2024.

358. Zhang, K., D. Jing, C. Xing, and L. Guo, *Significantly improved photocatalytic hydrogen production activity over $Cd_{1-x}Zn_xS$ photocatalysts prepared by a novel thermal sulfuration method.* International Journal of Hydrogen Energy, 2007. **32**: p. 4685-4691.

359. Liu, G., L. Zhao, L. Ma, and L. Guo, *Photocatalytic H_2 evolution under visible light irradiation on a novel $Cd_xCu_yZn_{1-x-y}S$ catalyst.* Catalysis Communications, 2008. **9**: p. 126-130.

360. ZHANG, X., D. JING, M. LIU, and L. GUO, *Efficient photocatalytic H_2 production under visible light irradiation over Ni doped $Cd_{1-x}Zn_xS$ microsphere photocatalysts.* Catalysis Communications, 2008. **9**: p. 1720-1724.

361. Liu, G., Z. Zhou, and L. Guo, *Correlation between band structures and photocatalytic activities of $Cd_xCu_yZn_{1-x-y}S$ solid solution.* Chemical Physics Letters, 2011. **509**: p. 43-47.

362. Wang, X., G. Liu, Z.-G. Chen, F. Li, G.Q. (Max) Lu, and H.-M. Cheng, *Efficient and stable photocatalytic H2 evolution from water splitting by (Cd0.8Zn0.2)S nanorods.* Electrochemistry Communications, 2009. **11**: p. 1174-1178.

363. Wang, L., W. Wang, M. Shang, W. Yin, S. Sun, and L. Zhang, *Enhanced photocatalytic hydrogen evolution under visible light over $Cd_{1-x}Zn_xS$ solid solution with cubic zinc blend phase.* International Journal of Hydrogen Energy, 2010. **35**: p. 19-25.

364. Shen, L., L. Yu, H.B. Wu, X.-Y. Yu, X. Zhang, and X.W.D. Lou, *Formation of nickel cobalt sulfide ball-in-ball hollow spheres with enhanced electrochemical pseudocapacitive properties.* Nature Communications, 2015. **6**: p. 6694.

365. Shen, L., L. Yu, X.-Y. Yu, X. Zhang, and X.W.D. Lou, *Self-Templated Formation of Uniform $NiCo_2O_4$ Hollow Spheres with Complex Interior Structures for Lithium-Ion Batteries and Supercapacitors.* Angewandte Chemie International Edition, 2015. **54**: p. 1868-1872.

366. Tejos R, M., B.G. Rolón, R. Del Río, and G. Cabello, *Investigation and optical evaluation of precursors for the photodeposition of nanosized ZnS amorphous thin films.* Journal of the Chilean Chemical Society, 2007. **52**: p. 1257-1260.

367. McNaught, A.D., A. Wilkinson, and I.U.o.P.a.A. Chemistry., *Compendium of chemical terminology : IUPAC recommendations.* 1997.

368. Gold, V. and I.U.o.P.a.A. Chemistry., *Compendium of chemical terminology : IUPAC recommendations.* 1987: p. 456.

369. Pauling, L., *The nature of the chemical bond and the structure of molecules and crystals: an introduction to modern structural chemistry.* 1960.

370. Zhong, H., Z. Ni, Y. Wang, M. Ye, Z. Song, Y. Pan, R. Quhe, J. Yang, L. Yang, J. Shi, and J. Lu, *Interfacial Properties of Monolayer and Bilayer MoS_2 Contacts with Metals: Beyond the Energy Band Calculations.* Scientific Reports, 2015. **6**: p. 21786.

371. Choi, S., Z. Shaolin, and W. Yang, *Layer-number-dependent work function of MoS_2 nanoflakes.* Journal of the Korean Physical Society, 2014. **64**: p. 1550-1555.

372. Chen, R., K. Li, X.-S. Zhu, S.-L. Xie, L.-Z. Dong, S.-L. Li, and Y.-Q. Lan, *In situ synthesis of porous ZnO-embedded $Zn_{1-x}Cd_xS/CdS$ heterostructures for enhanced photocatalytic activity.* CrystEngComm, 2016. **18**: p. 1446-1452.

List of publications

Journal publications

Nanocomposite heterojunctions as sunlight-driven photocatalysts for hydrogen production from water splitting (review paper)

Mohammad Reza Gholipour, Cao-Thang Dinh, Francois Béland, Trong-On Do

Nanoscale, 7 (2015) 8187-8208.

Graphitic Carbon Nitride-Titanium Dioxide Nanocomposite for Photocatalytic Hydrogen Production under Visible Light

Mohammad Reza Gholipour, Francois Béland, Trong-On Do

International Journal of Chemical Reactor Engineering, 14 (2016) 851-858.

Nitride Nanosheets as an Efficient Photocatalyst for Hydrogen Production under Visible Light Irradiation

Mohammad Reza Gholipour, Francois Béland, Trong-On Do

ACS Sustainable Chemistry & Engineering, 5 (2016) 213-220.

Hollow Microsphere of $Zn_xCd_{1-x}S$ Solid Solution with Noble-metal-free Co-catalyst for Hydrogen Evolution with High Quantum Efficiency in Visible Light

Mohammad Reza Gholipour, Chinh Chien Nguyen, Francois Béland, Trong-On Do

Submitted to ChemCatChem, September 2017

Conference presentations

Post-calcined Carbon Nitride Nanosheets as an Efficient Photocatalyst for Hydrogen Production Under Visible Light Irradiation

Mohammad Reza Gholipour, Francois Béland, Trong-On Do

NANO 2016 XIIIth International Conference on Nanostructured Materials, August 7-12, 2016, Québec, Canada

Post-calcined Carbon Nitride Nanosheets as an Efficient Photocatalyst for Hydrogen Production Under Visible Light Irradiation

Mohammad Reza Gholipour, Francois Béland, Trong-On Do

66th Canadian Chemical Engineering Conference, October 16-19, 2016, Québec, Canada

Nanocomposite of graphitic carbon nitride and titanate for photocatalytic hydrogen production under visible light

Mohammad Reza Gholipour, Francois Béland, Trong-On Do

CCVC Conference, May 2014, Quebec, Canada